Two- and Three-Particle azimuthal Correlations of high-p_t charged Hadrons in Pb+Au Collisions at 158 GeV per Nucleon

Dissertation
zur Erlangung des Doktorgrades der Naturwissenschaften

vorgelegt beim Fachbereich Physik der Johann Wolfgang Goethe-Universität Frankfurt am Main

von
Stefan Kniege
aus Steinau-Ulmbach

Frankfurt am Main, 2009
(D 30)

Vom Fachbereich Physik der Johann Wolfgang Goethe-Universität als Dissertation angenommen.

Dekan:	Prof. Dr. Dirk Rischke
Gutachter:	Prof. Dr. Harald Appelshäuser
	Prof. Dr. Reinhard Stock
Datum der Disputation:	20.04.2009

Zusammenfassung

Ein wesentliches Ziel der Physik mit schweren Ionen ist die Untersuchung der Zustände von Kernmaterie bei hohen Dichten bzw. Temperaturen. Solche Zustände lassen sich durch Kollisionen von hochenergetischen schweren Ionen in Teilchenbeschleunigern wie dem Super Proton Synchrotron SPS am Europäischen Kernforschungszentrum CERN in Genf erzeugen und untersuchen.

Die vorliegende Arbeit beschäftigt sich mit der Analyse des Einflusses des in einer solchen Kollision erzeugten Mediums auf hochenergetische Teilchen, welche dieses Medium durchqueren. Hierzu werden Korrelationen zwischen Teilchen mit hohem Transversalimpuls p_t als Funktion der Zentralität der Kollisionen und der Ladung der beteiligten Teilchen untersucht. Ziel ist es, hierdurch eine experimentelle Grundlage für die theoretische Beschreibung der Eigenschaften des Mediums in solchen Kollision bereitzustellen.

Unter Normalbedingungen liegt Kernmaterie in Form gebundener Zustände aus Quarks und Gluonen (Partonen) vor. Diese lassen sich zwar in elementaren Reaktionen als Bausteine der Nukleonen nachweisen, eine direkte Beobachtung isolierter Quarks ist hingegen nicht möglich. Dies liegt an einer Besonderheit der starken Wechselwirkung, die neben der elektromagnetischen Kraft, der schwachen Wechselwirkung und der Gravitation das Quartett der elementaren Wechselwirkungen in der Natur vervollständigt. Die der starken Wechselwirkung entsprechende Ladung wird als Farbladung (color charge) bezeichnet. Sie liegt in drei Ausprägungen (rot, grün, blau) vor und erlaubt (farb-) ladungsneutrale gebundene Zustände aus zwei (Mesonen) bzw. drei Quarks (Baryonen).

Gluonen sind die Vermittler der starken Wechselwirkung zwischen den Quarks. Im Gegensatz zu Photonen als Austauschteilchen der elektromagnetischen Wechselwirkung sind sie selbst Träger der Farbladung und können somit wiederum mit (farb-)geladenen Teilchen wechselwirken. Dies hat zur Folge, dass die Feldstärke zwischen den Quarks nicht wie im Fall der elektromagnetischen Kraft quadratisch mit dem Abstand abfällt, sondern für große Abstände konstant bleibt. Die Energie, die notwendig ist, um zwei Quarks zu trennen, steigt somit für große Abstände linear an. Übersteigt die im Farbfeld zweier Quarks gespeicherte Energie diejenige Energie, welche zur Erzeugung eines Quark-Antiquark Paares notwendig ist, kann ein solches Paar neu erzeugt werden. Diese Quarks bilden mit den ursprünglichen Quarks wiederum farbneutrale Zustände. Die Quarks sind somit in den gebundenen Zuständen der Hadronen (Mesonen, Baryonen) eingeschlossen (confinement). Bei sehr hohen Kollisionsenergien entstehen durch die beschriebene Fragmentierung des Farbfeldes (string) zwischen den Quarks kollimierte Strahlen (Jets) von Teilchen.
Bei kleinem Abstand bzw. hohem Impulsübertrag verringert sich die Kopplungsstärke der starken Wechselwirkung jedoch (asymptotische Freiheit), was bei extrem hohen Dichten bzw. Temperaturen zu einem Phasenübergang von hadronischer Materie zu einem partonischen Zustand aus freien Quarks und Gluonen (Quark-Gluon-Plasma, QGP) führen kann.

Eine direkte Beobachtung dieses Zustandes ist aufgrund des confinement hingegen nicht möglich. Durch die Expansion des Systems nach einer Kollision wer-

den die Quarks und Gluonen innerhalb weniger 10^{-23} s wiederum in Hadronen gebunden. Nur diese gebundenen Zustände aus Quarks können in Detektoren nachgewiesen werden.

Der Übergang von der partonischen in die hadronische Phase geschieht über die Rekombination von Partonen zu Hadronen oder bevorzugt bei hohen Partonenergien durch die oben beschriebene Fragmentierung des Farbfeldes zwischen zwei Partonen.

Die Herausforderung besteht nun darin, Observablen zu finden und zu untersuchen, welche es ermöglichen, Rückschlüsse auf den Zustand des Mediums in der frühen Phase vor der Hadronisierung zu ziehen. Hierbei werden unterschiedliche Ansätze verfolgt.

Zum einen werden Observablen untersucht, die nicht durch die Expansion des Systems und die anschließende Hadronisierung gestört werden. Hier handelt es sich z.B. um die Untersuchung direkter, in elementaren Reaktionen erzeugter Photonen. Die Wahrscheinlichkeit einer Wechselwirkung dieser Photonen mit dem Medium ist sehr gering. Somit konservieren direkte Photonen Informationen über den Zustand der Materie zum Zeitpunkt ihrer Produktion.

Ein anderer Ansatz ist die Untersuchung der Wechselwirkung der Teilchen mit dem Medium, um damit Rückschlüsse auf den Zustand des Mediums zuzulassen. Dieser Ansatz wird in der vorliegenden Arbeit verfolgt.

Es wird untersucht, welche Signatur die Wechselwirkung von Partonen aus harten Quark-Quark Stößen mit dem sie umgebenden Medium im hadronischen Endzustand hinterlässt.

Die Energie- sowie die Orts- und Impulsverteilung von Hadronen, welche aus solchen Quark-Quark Stößen entstehen, hängt von der Wechselwirkung der Partonen mit dem sie umgebenden Medium ab. Theoretische Rechnungen zeigen deutliche Unterschiede des Energieverlustes farbgeladener Teilchen in einem partonischen Medium (QGP) im Vergleich zu einem farbneutralen hadronischen Medium voraus. Verschiedene Mechanismen, wie der Energieverlust durch elastische Kollisionen und Energieverlust durch die Abstrahlung von Gluonen, werden in der Literatur diskutiert.

Der Energieverlust der Partonen führt zur Unterdrückung der Produktion von Hadronen mit hohem Transversalimpuls. Als Referenz dienen hier die Daten von Proton-Proton Reaktionen, in welchen Partonen aus harten Stößen nicht durch ein sie umgebendes Medium beeinflusst werden. Diese Unterdrückung kann durch den "Nuklearen Modifikationsfaktor" R_{AA} quantifiziert werden, in dem die Multiplizität der Teilchen in Schwerionenkollisionen mit der Multiplizität in Proton-Proton Kollisionen verglichen wird. Die Proton-Proton Daten werden hierfür mit der Anzahl der möglichen Nukleon-Nukleon Stöße in den Schwerionenkollisionen skaliert.
Stellt eine Schwerionenkollision nur eine Überlagerung von Nukleon-Nukleon Kollisionen dar, wäre R_{AA} gleich eins. Am Relativistic Heavy Ion Collider (RHIC) wurden in Au-Au Kollisionen bei $\sqrt{s_{NN}}$=200 GeV ($\sqrt{s_{NN}}$: Schwerpunktsenergie im Nukleon-Nukleon System) Werte von $R_{AA} \approx 0.2$ gemessen, was einer Unterdrückung um einen Faktor 5 entspricht. Eine Unterdrückung

direkter Photonen wurde hingegen nicht beobachtet. Bei der höchsten SPS Energie von $\sqrt{s_{NN}}$=17.2 GeV liegt R_{AA} für Hadronen nahe eins, jedoch ist eine Verringerung des Faktors mit höher werdenden Zentralitäten der Kollisionen zu beobachten. Dies lässt sich auf einen stärker werdenden Einfluss des Mediums bei höheren Dichten bzw. bei längeren Wegstrecken der Partonen im Medium zurückführen. Des Weiteren sagen theoretische Rechnungen unter Einbeziehung von nuklearen Effekten im Anfangszustand vor harten Parton-Parton Kollisionen eine Erhöhung der Multiplizität bei hohen Transversalimpulsen voraus. Ohne Mediumeffekte im Endzustand würden somit Werte von R_{AA} größer als eins erwartet.

Die Unterdrückung von Hadronen mit hohem Transversalimpuls resultiert aus dem Energieverlust von Partonen im Medium einer Schwerionenkollision. Somit ändert sich die Form als auch die Energie der oben beschriebenen Jets von Hadronen in Kern-Kern (A-A) Kollisionen relativ zu den Erwartungen aus Nukleon-Nukleon (p-p, n-n, n-p, p-n) Kollisionen.

In elementaren Proton-Proton Kollisionen lassen sich solche Jets direkt über die Identifizierung von Gruppen (cluster) von Hadronen nachweisen. In Schwerionenkollisionen hingegen ist dies aufgrund des großen hadronischen Untergrundes sehr schwierig. Es wird daher in dieser Arbeit ein anderer Zugang zur Analyse der Jetereignisse gewählt.
Unter der Annahme, dass die Partonen vor ihrer Kollision keinen Transversalimpuls besitzen, sollten die Partonen und die damit aus ihnen entstehenden Jets in entgegengesetzter Richtung in der transversalen Ebene emittiert werden. Somit ergeben sich Korrelationen zwischen den Teilchen solcher Jets (Jetkorrelationen) im azimutalen Winkel ϕ. Sucht man in einer Kollision eines dieser Jetteilchen (Trigger) und bildet die Winkeldifferenzen $\Delta\phi$ mit anderen Teilchen (assoziierte Teilchen) in diesem Ereignis, ergibt sich eine charakteristische Signalverteilung mit einer Erhöhung nahe dem Trigger ($\Delta\phi \approx 0$, near-side) und in entgegengesetzter Richtung ($\Delta\phi \approx \pi$, away-side).

Ein wesentlicher Bestandteil dieser Arbeit ist die Analyse der Struktur der azimutalen Korrelationen auf der near- und der away-side.

Die analysierten Daten wurden mit dem CERES Detektor am CERN SPS aufgenommen. Eine wesentliche Komponente des CERES Experimentes ist eine zylindrische Zeit-Projektionskammer (Time Projection Chamber, TPC). Diese besitzt eine homogene Nachweiswahrscheinlichkeit für geladene Teilchen über den gesamten azimutalen Winkelbereich und ist somit besonders für die Analyse der azimutalen Korrelationen geeignet. Im Jahr 2000 wurde ein Datensatz mit hoher Statistik (30 Mio. Ereignisse) bei maximaler SPS Energie und unterschiedlichen Zentralitäten der Kollisionen aufgenommen. Dieser Datensatz dient als Grundlage für die Analyse der Korrelationen in dieser Arbeit.

Korrelationen, die aufgrund der beschränkten Nachweiswahrscheinlichkeit (Effizienz) der Teilchen im Detektor bei unterschiedichen Winkeln entstehen, werden in einer "Mixed-Event" Verteilung berücksichtigt. Hier werden Trigger und assoziierte Teilchen aus unterschiedlichen Ereignissen kombiniert. Diese Paare zeigen die gleichen Korrelationen aufgrund der Effizienz des Detektors

wie Paare im Signal, jedoch nicht die physikalischen Korrelationen. Teilt man nun die Signalverteilung durch die Mixed-Event Verteilung, erhält man eine Korrelationsfunktion, welche nur die physikalischen Korrelationen unter den Teilchen in der Signalverteilung widerspiegelt.

Für nicht zentrale (periphere) Kollisionen ergeben sich aufgrund der Asymmetrie des Überlappbereiches der Kerne Korrelationen der Teilchen im azimutalen Winkel mit der Reaktionsebene der Kollision. Diese Ebene wird durch die Strahlachse und die Verbindungslinie durch die Mittelpunkte der Kerne aufgespannt. Der als elliptische Fluss bezeichnete Effekt ist den Jetkorrelationen überlagert und muss empirisch korrigiert werden.
Die Stärke des elliptischen Flusses in den untersuchten Reaktionen ist aus früheren Analysen bekannt, allerdings nicht ausreichend detailliert für die hier verwendeten Impulsschnitte und Teilchenkombinationen.
Der elliptische Fluss wird daher in dieser Arbeit in einer Reaktionsebenenanalyse separat bestimmt. Die Kalibrierung der Reaktionsebene und die Bestimmung des Flusses werden für Ereignisse mit und ohne Triggerteilchen und für Teilchen unterschiedlicher Transversalimpulsbereiche durchgeführt.
Dies erlaubt neben einer möglichst genauen Korrektur der Jetkorrelationen auf überlagerte Flusseffekte eine Abschätzung der systematischen Unsicherheit, die durch diese Korrektur eingeführt wird.

Unter der Annahme, dass die physikalischen Korrelationen nur durch den Fluss oder die Jetkorrelationen gegeben sind (Zwei-Quellen-Modell), wird der Beitrag des elliptischen Flusses von der gemessenen Korrelationsfunktion abgezogen. Hierbei wird des Weiteren angenommen, dass die Anzahl der Jetteilchen bei einer bestimmten Winkeldifferenz gleich null ist. Dies entspricht der Annahme einer Trennung der Jets auf der near- und der away-side. Diese "Zero Yield At Minimum" (ZYAM) Bedingung wird verwendet, um den Flussbeitrag an die Korrelationsfunktion anzupassen und abzuziehen. Somit erhält man nach Normierung der verbleibenden Korrelationsfunktion die Anzahl der Jetteilchen pro Triggerteilchen und Ereignis (conditional yield) bei einer gegebenen azimutalen Winkeldifferenz. Aus der Analyse ergibt sich somit ein Muster der Jetkorrelationen in Schwerionenkollisionen.

Der Verwendung des Zwei-Quellen-Modells liegt die Annahme zugrunde, dass Korrelationen eines Jettriggers mit der Reaktionsebene die gleiche Stärke zeigen, wie die Korrelationen von Triggerteilchen, die nicht aus Jetereignissen stammen. In einer Monte Carlo Studie werden die Auswirkungen der Abweichung von dieser Annahme auf die Ergebnisse sowie systematische Unsicherheiten in den einzelnen Analyseschritten näher untersucht. Es zeigt sich, dass die Unsicherheiten des yields in zentralen Kollisionnen sehr gering sind, sich in periphären Kollisionen jedoch Verzerrungen der Struktur des gemessenen yields auf der away-side ergegeben können.
Des Weiteren wird in Detektorsimulationen der Einfluss der beschränkten Zweispurauflösung auf die gemessenen Korrelationen bestimmt sowie die Impulsauflösung der verwendeten Spuren untersucht.

Für hohe Transversalimpulse des Triggers und der assoziierten Teilchen wurde am RHIC ein Verschwinden des conditional yield auf der away-side in zentralen

Au-Au Kollisionen beobachtet. Dies lässt sich in einem als Oberflächentendenz (surface bias) bezeichneten Szenario verstehen. Durch den hohen verlangten Transversalimpuls werden bevorzugt Teilchen als Trigger gewählt, die aus Partonen stammen, die keinen großen Energieverlust erleiden und somit nahe der Oberfläche emittiert werden. Man triggert somit auf Kollisionen nahe der Oberfläche. Das Parton auf der away-side hingegen muss einen großen Bereich des Mediums durchqueren, was zu höherem Energieverlust und somit zur Unterdrückung der Teilchen mit hohem Transversalimpuls und einer Verschiebung hin zu niedrigeren Impulsen führt.
Zu niedrigeren Transversalimpulsen der assozierten Teilchen werden bei RHIC wiederum Teilchen auf der away-side beobachtet, jedoch zeigt der yield dort ein ausgeprägtes Minimum welches für Vakuumfragmentierung nicht erwartet wird und durch weiter unten beschriebene Mediumeffekte hervorgerufen werden kann.

Für zentrale Kollisionen wird in dieser Arbeit bei SPS Energie eine Struktur des conditional yield gemessen, die ähnlich den Beobachtungen am RHIC ein Minimum auf der away-side zeigt.
Eine Analyse des conditional yield als Funktion des Transversalimpulses der assozierten Teilchen zeigt eine Veränderung der Struktur auf der away-side. Bei Transversalimpulsen bis etwa 1.5 GeV/c zeigt sich eine breite Verteilung mit einem Maximum bei $\Delta\phi = \pi$. Über 1.5 GeV/c Transversalimpuls zeigt sich eine Doppelhöckerstruktur mit einem Minimum bei $\Delta\phi=\pi$. Diese Beobachtung ändert sich nur geringfügig bei Variation des Transversalimpuls des Triggers im Bereich von $1.0<p_t<4.5$ (GeV/c). Der integrierte yield auf der near-side ist deutlich geringer als auf der away-side. Dies kann durch den "trigger bias" verstanden werden. Aufgrund des hohen verlangten Transversalimpulses trägt der Trigger einen großen Anteil der gesamten Energie auf der near-side. Es entstehen somit nur wenige weitere Teilchen mit hohem p_t die auf der near-side als assoziierte Teilchen registriert werden.

Des Weiteren zeigt sich, dass der yield auf der near-side sowohl für positive als auch für negative Trigger bei ungleicher Kombination der Ladung von Trigger und assoziierten Teilchen dominiert. Auf der away-side hingegen dominieren positive assoziierte Teilchen den yield unabhängig von der Ladung des Triggers. Dies lässt sich auf der near-side auf lokale Ladungserhaltung in der Fragmentierung zurückführen, während auf der away-side der yield durch die positive Nettoladung des Systems bestimmt ist.

Um dies zu verifizieren werden die yields mit den Erwartungen aus Nukleon-Nukleon Kollisionen verglichen. Ein direkter Vergleich der yields ist hingegen nicht möglich, da erwartet wird, dass ein Großteil der Trigger nicht von Jets, sondern aus dem hadronischen Untergrund stammt. Im Verhältnis der yields von positiven und negativen assozierten Teilchen für eine gegebene Triggerladung kürzt sich dieser Beitrag jedoch heraus. Somit können diese yield-Verhältnisse mit den Verhältnissen aus elementaren Kollisionen verglichen werden.

Hierfür werden Ereignisse für n-n, p-p, p-n und n-p Kollisionen mit dem Ereignisgenerator PYTHIA simuliert. Diese werden entsprechend der Verhältnisse

der möglichen Nukleon-Nukleon Kombinationen in Pb-Au Kollisionen skaliert. Es zeigt sich, dass die yield-Verhältnisse auf der near-side den Verhältnissen in Nukleon-Nukleon Kollisionen entsprechen. Dieses Ergebnis lässt sich im Rahmen des oben beschriebenen surface bias verstehen. Wenn, wie angenommen, durch den hohen verlangten Transversalimpuls des Triggers Kollisionen nahe der Oberfläche untersucht werden, entsprechen die nahe dem Trigger beobachteten Korrelationen der Fragmentierung ins Vakuum, und damit den Verhältnissen in elementaren Kollisionen.
Auf der away-side hingegen wird unabhängig von der Ladung des Triggers in den Daten ein Verhältnis beobachtet, welches dem Ladungsverhältnis im hadronischen Untergrund entspricht. Die Ladungszusammensetzung des yields unterscheidet sich also nicht von den Verhältnissen im Medium, weichen im Falle positiver Trigger jedoch deutlich von den PYTHIA Ergebnissen ab. Dies legt die Vermutung nahe, dass das Parton einen Großteil seiner Energie an das Medium abgegeben hat, und dass die beobachteten Teilchen dem Medium entstammen und nicht aus der Fragmentierung des primären Partons. Die away-side reflektiert somit die "Antwort" des Mediums auf ein dieses Medium durchquerendes Parton.

Die "Antwort" des Mediums auf die es durchquerenden Partonen wird im Rahmen von Drei-Teilchen-Korrelationen näher untersucht. Die beobachtete Doppelhöckerstruktur auf der away-side lässt sich durch verschiedene Szenarien erklären. Wenn Jets in einem Ereignis durch Kollisionen abgelenkt werden, ergibt sich in der Korrelationsfunktion ein Maximum auf der away-side, welches von $\Delta\phi = \pi$ verschoben ist. Theoretisch kann eine solche Ablenkung durch die Emission von Gluonen unter großen Winkeln relativ zum ursprünglichen Parton erklärt werden. Eine Verschiebung des Maximums ergibt sich ebenfalls, falls mehrere Hadronen in einem Ereignis in einem Kegel um das Parton auf der away-side emittiert werden. Ein solches Muster kann sich durch ein Parton ergeben, welches sich mit einer Geschwindigkeit größer als der Schallgeschwindigkeit im Medium bewegt, und hierdurch eine Schockwelle (Machkegel) in diesem Medium auslöst. Über den Winkel eines solchen Machkegels lässt sich die Schallgeschwindigkeit innerhalb des Mediums bestimmen. Es liesse sich somit eine wichtige Größe zur Bestimmung des Zustandes des Mediums über diese Analyse berechnen. Die oben beschriebenen unterschiedlichen Szenarien führen zu ähnlichen Zwei-Teilchen-Korrelationen, können jedoch in der Analyse der Drei-Teilchen-Korrelationen unterschieden werden.

Man untersucht hierbei die Korrelationen von zwei assoziierten Teilchen zu einem Trigger in einem Ereignis. Die Effizienz wird wie auch bei den Zwei-Teilchen-Korrelationen durch eine Mixed-Event Verteilung, in der alle drei Teilchen aus unterschiedichen Ereignissen stammen, untersucht.
In einem Szenarium, in dem die Partonen abgelenkt werden, bevor sie ähnlich den Verhältnissen im Vakuum fragmentieren, ergäben sich Korrelationen unter den assoziierten Teilchen die sehr nahe im azimutalen Winkel lägen. Bei der kegelförmigen Emission hingegen ergeben sich neben kleinen Winkeln zwischen den assoziierten Teilchen ebenfalls große Winkel, die als Inseln in einer zweidimensionalen Darstellung identifiziert werden können.

In der vorgelegte Analyse kann im Rahmen der systematischen Unsicherheiten kein Signal der Drei-Teilchen-Korrelationen extrahiert werden. Dies kann durch Überschlagsrechnungen basierend auf den gemessenen Zwei-Teilchen Ergebnissen und der Anzahl der Ereignisse, die zur Analyse zur Verfügung stehen, plausibilisiert werden.

Ab 2009 werden die Analysemöglichkeiten erheblich verbessert, wenn Pb-Pb Kollisionen bei 5.5 TeV Schwerpunktsenergie im ALICE Experiment als Bestandteil des CERN Large Hadron Collider (LHC) untersucht werden.
Durch die verbesserte Teilchenidentifikation können nicht nur ladungsabhängige Korrelationen sondern auch Korrelationen verschiedener Teilchensorten untersucht werden. Hinzu kommen eine verbesserte Impulsauflösung, eine höhere Streurate für Teilchen mit hohen Transversalimpulsen sowie eine insgesamt höhere Anzahl der registrierten Ereignisse, was ebenfalls die Analyse der Drei-Teilchen-Korrelationen ermöglichen sollte.
Ein wesentlicher Bestandteil des ALICE Experimentes ist eine TPC, welche im Jahr 2006 in Betrieb genommen wurde.

Basierend auf früheren Arbeiten wird parallel zur Analyse der Korrelationen ein Online Monitor für die Kontrolle der Funktionsfähigkeit der ALICE-TPC entwickelt. Ziel ist sowohl die Verifizierung der Funktionalität der einzelnen Elektronikkomponenten der TPC als auch die Kontrolle wesentlicher Parameter des Betriebes der TPC. Nach dem Zusammenbau der TPC wird zunächst die Kontrolle der einzelnen Elektronikkomponenten durchgeführt und die endgültige Zuordnung der einzelnen Komponenten der TPC festgelegt. Nach dieser Endmontage werden die einzelnen Sektoren der TPC in verschiedenen Durchläufen mit kosmischen Strahlen, einem Laser-Kalibrierungsystem und einem Kalibrierpulser getestet. Hier dient der Online Monitor als Standard-Softwaremodul, welches während des Betriebes der TPC verwendet wird, um die Visualisierung der Daten zu gewährleisten. Der Monitor wird schließlich in das offizielle Analysepaket des Experimentes AliROOT eingefügt, und kann basierend auf verschiedenen Datenformaten sowohl online als auch offline zur Datenvisualisierung verwendet werden.
Die notwendigen Schritte zur Benutzung des Monitors und die einzelnen Merkmale des Monitors werden im Anhang der Arbeit erläutert. Die wesentlichen Funktionen des Monitors werden hierbei unter Bezugnahme auf Resultate der Tests während der Inbetriebnahme genauer beschrieben.

Two- and Three-Particle azimuthal Correlations of high-p_t charged Hadrons in Pb+Au Collisions at 158 GeV per Nucleon

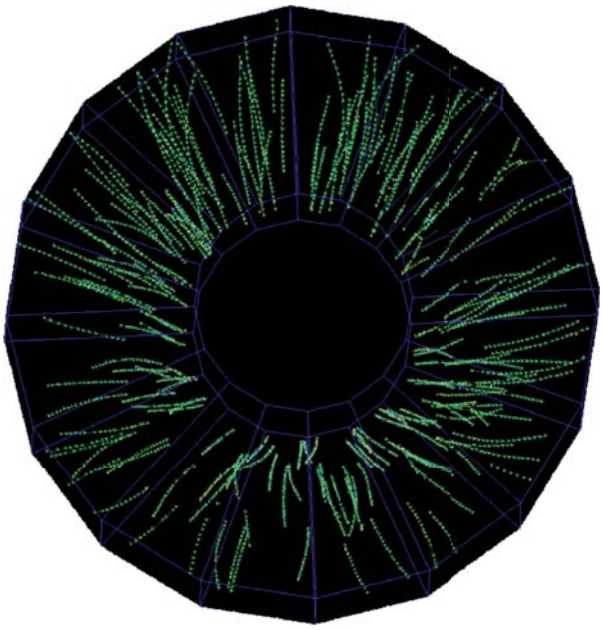

A Dissertation presented to the
Faculty of Physics
of the
Johann Wolfgang Goethe-Universität
Frankfurt am Main

by
Stefan Kniege

Contents

1 Introduction

A major objective of studying heavy ion collisions at high energy is the investigation of nuclear matter at extreme densities and temperatures.
Under normal conditions nuclear matter consists of nucleons, which are bound states of more elementary particles, the quarks and gluons, or more general, partons. These particles can be identified as the constituents of nucleons but can not be observed as isolated particles. This arises due to a peculiarity of the strong force which accomplishes besides the electromagnetic force, the weak interaction, and the gravitation the quartet of elementary forces in nature.

The charge corresponding to the strong force is called color charge. It can be found in three complementary states allowing for color neutral bound states of two (meson) or three (baryon) quarks. Gluons act as exchange particles mediating the strong force and are in contrast to the photon as the exchange particle of the electromagnetic force carrier of the color charge themselves. This leads to a linearly increasing potential between colored objects for large distances as compared to the hadronic dimensions. If the energy stored in the color field (string) between colored objects crosses the threshold for the production of a quark anti-quark pair those particles can be created and combine with the original quarks to color neutral objects. This leads to the confinement of quarks and gluons in color neutral hadronic states of baryons and mesons.

The interaction between colored objects is described by the coupling constant α_s which decreases with decreasing distance of the partons (asymptotic freedom [1]) as predicted by Quantum Chromo Dynamics (QCD), the theory describing the strong interaction.
Particles inside the hadrons can thus be understood as quasi-free particles. The point like nature of the constituents of the nucleons could be proven in collisions of electrons on protons in the late 1960's.

Knowing the characteristics of the strong force the question arises if there exists a state of quasi-free quarks and gluons (Quark-Gluon-Plasma, QGP) extended over a scale larger than the size of the nucleons. Examples for such extended regions are the state of the early universe or the high density region in the interior of neutron stars. A unique opportunity of investigating these different states of matter is the study of collisions of heavy nuclei in accelerator facilities as the Super Proton Synchrotron (SPS) at CERN (Centre Européenne pour la Recherche Nucléaire).

The theoretical calculation of properties of strongly interacting matter is complicated by the change of the coupling constant with distance or momentum transfer between colored objects (running coupling constant). Calculations of the interactions between colored objects in terms of an expansion of the cross section with respect to the coupling constant only converge for small values of

α_s (perturbative QCD).
Lattice QCD calculations try to circumvent these limitations discretising space time on a lattice. These calculations predict a phase transition from the hadronic phase of matter to a partonic Quark-Gluon-Plasma phase at energy densities $\epsilon = 1$ GeV/fm^3 [2][3]. A steep rise in the energy density scaled by the temperature ϵ/T^4 indicates this phase transition (Figure 1.1).

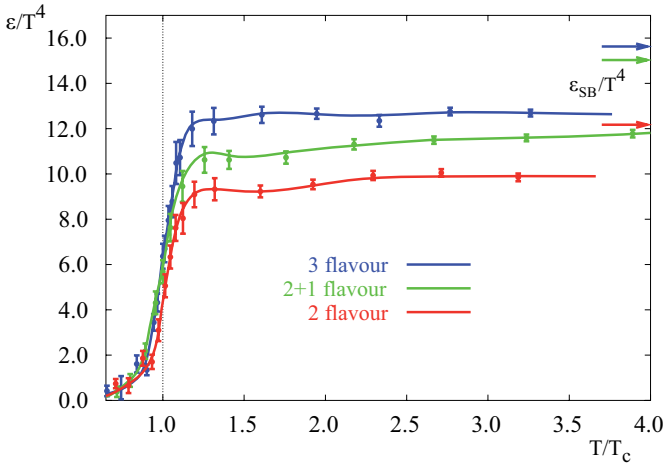

Figure 1.1: Lattice QCD calculations for the energy density ϵ divided by the temperature T to the 4th as a function of the temperature for different types (flavours) of partons in nuclear matter. Predictions for an ideal Stefan Boltzmann gas are indicated by arrows [3].

The necessary energy densities corresponding to a critical temperature of the phase transition of T_{crit}=170 MeV should be reachable in heavy ion collisions with a center of mass energy in excess of $\sqrt{s_{NN}}$= 10 GeV [3]. Analyzing the collisions of Pb-Au ions at top SPS energies of $\sqrt{s_{NN}}$= 17.2 GeV should thus make it possible to investigate nuclear matter in the deconfined phase.

1.1 Phase diagram of nuclear matter

The equation of state of nuclear matter can be characterized by the nuclear density (here described by the baryonic density or the baryochemical potential μ_B) and the temperature of the system. In the phase diagram (Figure 1.2) the different phases of nuclear matter (hadron gas, Quark-Gluon-Plasma) are shown corresponding to the possible nuclear states. A main goal of heavy ion physics is to probe this phase diagram and to access information about the deconfined phase of nuclear matter. Due to the confinement of the partons in hadrons a direct observation of the partonic phase is however not possible.

In heavy ion collisions different states of the system are distinguished starting from a possibly thermalized Quark-Gluon-Plasma phase in the early stage of

the collision. The system expands and hadronizes to a system of inelastically interacting hadrons. The *chemical freezeout* defines the moment when the inelastic interactions of the hadrons stop and the composition of the hadronic medium is defined. The *thermal freezeout* defines the final stage of the collision when the elastic collisions cease and the momenta of the particles are fixed. This is the state of the system that is measured in the experiment.

Assuming that the system is thermalized in the early stage of the collision, statistical models can connect the particle composition after the chemical freezeout to the temperature T and the baryochemical potential μ_B of the system at this point. It is shown that the measured particle abundances can be described by the statistical models to good accuracy [4]. Examples of the extracted temperatures and densities at chemical freezeout are shown in the red points in Figure 1.2.

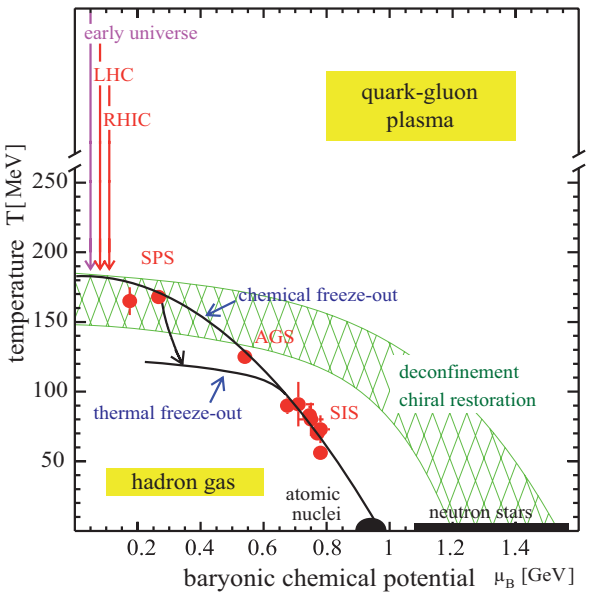

Figure 1.2: Phase diagram of nuclear matter. Chemical freezeout points (red points) at different energies are determined by the analysis of the composition of the hadronic final state [4].

The baryochemical potential μ_B corresponds to the difference of baryons and anti-baryons in the system. Depending on the energy in the collisions and the size of the nuclei different regions in T and μ_B can be reached in the collisions. For the top SPS energy the analysis of the measured hadronic composition of the fireball results in $T = 160 \pm 5$ MeV and $\mu_B = 240 \pm 18$ MeV [5] which is very close to the assumed phase boundary to the deconfined phase which poses an upper limit for this measurement.
The energy density estimated by measurements of the energy transferred perpendicular to the beam direction is about 3 GeV/fm^3 [6] and thus higher than the energy density necessary to reach the deconfined phase. This together with

the measured temperature at chemical freezeout close to the phase boundary hints to the crossing of the phase boundary in heavy ion collisions at the top SPS energy.
For low collision energies the nuclei are supposed to be stopped in the collision which leads to a large net-baryon (baryons - anti-baryons) density and hence to a large baryochemical potential μ_B in the collision zone. In contrast to this picture the nuclei are supposed to traverse each other only depositing part of its energy in the collision zone at higher collision energies. This leads to high temperatures however very small baryochemical potential in the collision zone.

Extreme states of matter as in the interior of neutron stars and the early universe with μ_B=0 and T$\rightarrow\infty$ can thus be reproduced in experiments.

1.2 Observables

Besides the observation of event characteristics such as the particle ratios and the transverse energy, other hadronic and non-hadronic observables can be investigated to characterize the medium created in heavy ion collisions.

Correlations among identical bosons (Bose-Einstein correlations) in phase space due to quantum statistical effects can help to determine the size of the fireball at thermal freezeout and the lifetime of the expanding system [7][8][9][10]. The measured length scale depends on the size and expansion dynamics of the system and can help to better understand the shape of the transverse momentum (p_t) spectra of the produced particles. At low transverse momenta the shape of these spectra is determined by the temperature in the source as well as the collective expansion of the system and resonance decays. Blastwave models [11] which parametrize the particle emitting source can be used to combine the information from correlations and particle spectra to unambiguously determine thermal freezeout temperature and transverse collective expansion of the system.

The anisotropy of the collision zone in non-central collisions leads to a pressure gradient in the system which is larger in the reaction plane than perpendicular to it. The reaction plane is the plane spanned by the beam-axis and the line connecting the center of the colliding nuclei. This asymmetry leads to a modulation of the observed angular distribution of the particles with respect to the reaction plane. This effect is denoted as elliptic flow [12][13][14]. It was shown that the strength of the measured elliptic flow scales with the valence quark content of the particles [15][16][17]. This hints to the flow being developed in an early stage of the collision prior to hadronisation. Measuring the flow in the collisions can thus give insight to the early stage of the collisions in the deconfined phase.

Color screening effects in the Quark-Gluon-Plasma analogous to Debey screening in an electromagnetic plasma can lead to the reduction of the production of bound states of $c\bar{c}$-pairs (J/ψ) relative to the observations in elementary collisions [18]. Depending on the collision energy J/ψ-suppression was observed in experiments [19] and can help investigate the color interaction of partons in a

deconfined phase.

Finally hard probes, i.e. particles with high transverse momentum, can serve as a measure to characterize the early state of the medium in heavy ion collision prior to hadronization.

1.3 Particle production at high transverse momentum

Hadron production with high transverse momenta in nucleus nucleus collisions can be described by the fragmentation of the color field (string) between partons originating from hard interactions. This effect can be illustrated as the break-up of the string between two strongly coupled particles by the creation of quark-anti-quark pairs and the combination of the newly produced particles with the initial quarks. The momenta of the fragmenting hadrons are determined by the momentum of the initial partons. At high collision energy fragmentation leads to the formation of a collimated jet of particles around the axis defined by the trajectory of the initial partons. For nucleon-nucleon collisions the production of hadrons with high p_t can be described by the parton distribution function inside the nucleons, the elementary cross section of the parton-parton interactions in the collisions of the nucleons, and the fragmentation function $D_{C/c}(z)$ of partons in the vacuum (Figure 1.3). The fragmentation function is defined as

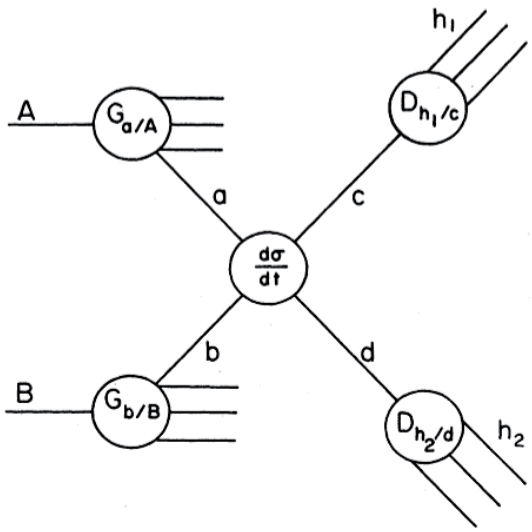

Figure 1.3: Schematic diagram of hadron production in nucleon-nucleon collisions. The assumed factorization of the fragmentation function D, the elementary cross section of parton parton interaction $d\sigma/dt$ (derivative with respect to the Mandelstam variable t) and the parton distribution function G are used to calculate the final hadronic abundances of particles [20].

the probability of finding a hadron C carrying a momentum fraction z of the fragmenting parton c. The low p_t region to the fragmentation function however can not be calculated using perturbative QCD. The fragmentation function has to be extracted from fits to fragmentation functions measured in elementary collisions as (e^-+e^+) [21][22].
The parton-parton cross section is calculated using perturbative QCD. Due to the above mentioned limitations of perturbative QCD this poses a lower bound to the p_t region the calculation is possible for.
The parton distribution function (PDF) $G_{b/B}(x, Q^2)$ defining the fraction of momentum x a parton b is carrying of the momentum of the initial nucleon B is used to describe the momentum distribution the incident partons in the elementary collisions. The PDF also depends on the scale of the momentum transfer Q^2 in the collisions. The PDF can not be calculated and has to be determined from experiments.
Under the assumption that the three terms factorize, that is are independent of each other, the cross section for hadron production in elementary nucleon-nucleon collisions can be described by [20]:

$$\frac{d\sigma}{dydp_t^2} = \sum_{abcd} \int dx_a dx_b G_{a/A}(x_a, Q^2) G_{b/B}(x_b, Q^2) D_{C/c}(z_c) \frac{s}{\pi z_c^2} \frac{d\sigma}{dt}(ab \to cd) \tag{1.1}$$

1.3.1 Parton energy loss

In the presence of nuclear matter the cross section as described by Eq. (1.1) is altered in several respects:

- Initial state effects like shadowing and anti-shadowing [23] alter the parton distribution functions in the nuclei.
- Soft gluon radiation of partons prior to hard collisions leads to increased transverse momentum of partons in the nuclei. This effect is denoted as k_t-smearing [24] and leads to an enhanced particle production with high-p_t compared to calculations where the partons are assumed to have no initial transverse momentum before hard collisions.
- Energy loss of partons in the medium after hard collisions (final state) alters the fragmentation function and suppresses the production of high-p_t particles since the parton distributes part of its energy to the medium.

Different mechanisms describing the energy loss of partons in the medium created in a heavy ion collision are investigated.

An early study is based on elastic collisions of partons in the medium [25]. As a consequence of the collisions the possible extinction of high-p_t jets was assumed as a signature for the creation of the Quark-Gluon-Plasma. However the energy loss calculated was too low to account for the observed suppression of high p_t particles.

Energy loss by gluon radiation [26][27] is supposed to be the major source of

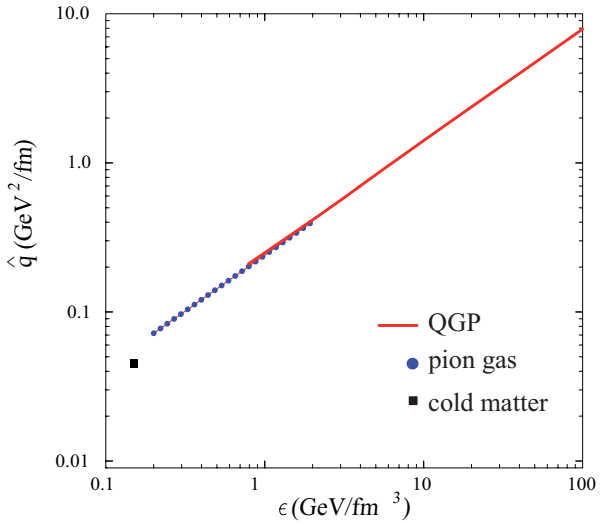

Figure 1.4: Transport parameter $\hat{q}$ as a function of the energy density ϵ for cold nuclear matter, a pion gas and the Quark-Gluon-Plasma [29].

energy loss of the particles in the medium. The probability for the radiation of a gluon from a parton traversing the colored medium depends on the path length of the particle in the medium. The radiated gluons themselves interact with the colored medium where the probability of the interaction depends on the mean free path or the gluon density and the path length L of the gluons in the medium. This leads to a quadratic dependence of the energy loss of a parton traversing the medium [27],[28]:

$$\Delta E = \frac{\alpha_s N_c}{4} \hat{q} L^2, \tag{1.2}$$

N_c denoting the number of color degrees of freedom in the medium. The transport coefficient $\hat{q}$ describes the mean transverse momentum transfer squared per unit mean free path of the particle traversing the medium:

$$\hat{q} = \frac{\langle q^2 \rangle}{\lambda} = \rho \int d^2q q^2 \frac{d\sigma}{d^2q}, \tag{1.3}$$

ρ describing the density of the medium. The transport coefficient $\hat{q}$ incorporates the properties of the medium and the cross section for the interaction of the particles with the medium. It can be connected to the gluon distribution and the density in the medium. The dependence of the transport coefficient on the energy density ϵ in the system is shown in Figure 1.4.
In cold nuclear matter with $\rho = 0.15/fm^3$ and assuming $\alpha_s = 0.5$ and a path length in the medium of 10 fm the energy loss of a parton results in [27]:

$$\Delta E \approx 2 \text{ GeV} \left(\frac{L}{10 \text{ fm}} \right)^2. \tag{1.4}$$

For hot nuclear matter with T=250 MeV and α_s=0.13 the energy loss would be drastically enhanced to:

$$\Delta E \approx 30 \text{ GeV} \left(\frac{L}{10 \text{ fm}} \right)^2 \tag{1.5}$$

According to [27] the exact numbers presented should be taken with caution since they are based on estimates. However the calculations show the importance of radiative energy loss in a high density environment in heavy ion collisions.

1.3.2 Results from RHIC

A consequence of energy loss of partons in the medium of heavy ion collisions is the reduced production of high-p_t particles [31, 32] as compared to p-p collisions.
This can be characterized by the nuclear modification factor R_{AB} which compares the multiplicity in A-A collisions at a given p_t to the multiplicity in p-p scaled by the number of binary collisions $\langle n_{coll} \rangle$:

$$R_{AB}(p_t, y) = \frac{d^2 N_{AB}/dp_t dy}{\langle n_{coll} \rangle \, d^2 Npp/dp_t dy} \tag{1.6}$$

If a nucleus-nucleus collision were just a superposition of nucleon-nucleon collisions R_{AB} should be 1. However, as seen in Figure 1.5, particle production is strongly suppressed in central heavy ion collisions relative to the expectations from p-p.

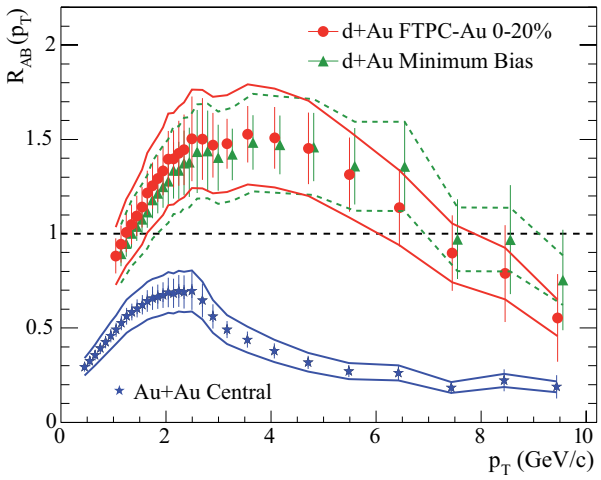

Figure 1.5: Nuclear modification factor R_{AB} for charged hadrons $((h^+ + h^-)/2)$ in d-Au compared to Au-Au collisions at $\sqrt{s_{NN}}$=200 GeV (STAR [30]).

The impact of particles traversing a hadronic medium and initial state effects can be studied by R_{AB} in d+Au. Here a factor close to or above 1 is observed. This indicates the enhancement due to the initial state effects discussed above. However no large energy loss in the hadronic medium as compared to the medium in Au-Au is observed.

R_{AB} can not achieve arbitrarily small values due to contribution from nucleon-nucleon collisions in the diffuse surface of heavy ion collisions. Here particles can escape undisturbed to the vacuum. This gives a contribution similar to expectations from vacuum fragmentation in p-p which is encoded in the denominator of Eq. (1.6).
The measured value of R_{AB} is very close to the limit of 0.15 [33] at high-p_t, indicating surface emission of particles at high-p_t or an opacity of the medium for high-p_t hadrons in high energy heavy ion collisions respectively. We will return to this aspect later, discussing azimuthal correlation measurements.
Another cross check if the observed suppression is indeed a final state effect in the medium can be done studying R_{AB} of direct photons which do not interact strongly with the medium. Assuming binary collision scaling of the production of hard direct photons created in the collisions, R_{AB} should be equal to 1 which is observed independently of the transverse momentum of the particles [34].

1.3.3 Results from SPS

Similar observations are made at SPS energy. Due to the lack of p-p reference data for all energies an alternative definition of the nuclear modification factor is used. The comparison of the multiplicity in central collisions N_C relative to peripheral collisions N_P is used as a measure for the nuclear effects on particle production:

$$R_{CP}(p_t, y) = \frac{\langle n_{coll} \rangle_P \, d^2N_C/dp_t dy}{\langle n_{coll} \rangle_C \, d^2N_P/dp_t dy} \tag{1.7}$$

An advantage of this method is that systematic effects entering the results of the multiplicity are similar for both centrality samples and hence cancel in the construction of R_{CP}. The value for protons reported from NA49 [35] are significantly higher than for pions and above 1. This can be partly attributed to the higher impact of transverse flow on protons. In addition, the particle creation mechanism changes from the recombination to the fragmentation dominated regime in the region of p_t higher than about 4 GeV/c [36]. The recombination favors the creation of baryons at high p_t due to the larger mass of the constituents, in contrast to fragmentation, which favors the formation of two-quark states. This is also observed at RHIC energy as shown in the right panel of Figure 1.6.
Albeit the magnitude of R_{CP} being different going from SPS to RHIC energies due to the assumed smaller energy loss of partons in the medium at SPS, the gross features observed at RHIC are also reflected in the SPS data.

Studying the centrality dependence of R_{AB} using an extrapolation from existing p-p data as reference, a decrease of R_{AB} with increasing centrality could be measured [37]. In addition, model calculations only including initial state

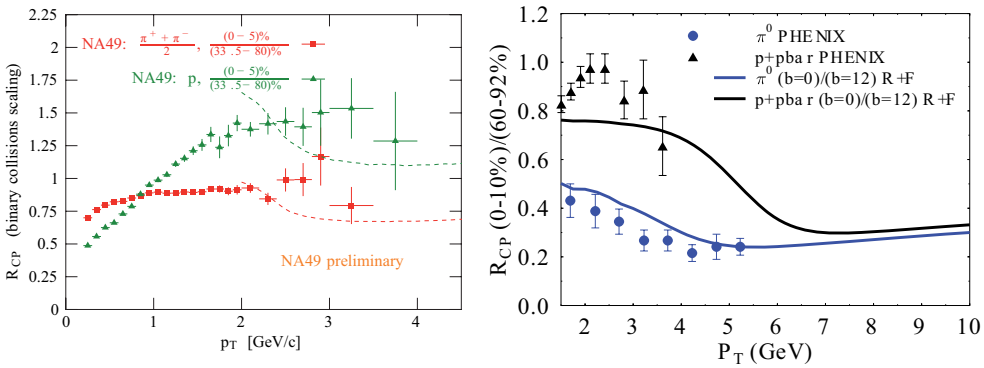

Figure 1.6: Nuclear modification factor R_{CP} for protons and charged pions at SPS from NA49 (left) [35] at $\sqrt{s_{NN}}$= 17.2 GeV and PHENIX measurements for neutral pions and protons at $\sqrt{s_{NN}}$= 17.2 GeV (right) [30].

effects show values of R_{AB} significantly higher than the measured values. This hints to a strong impact of the medium on high-p_t particles also at SPS energy.

1.4 Azimuthal correlations

A major step in understanding the observed impact of the medium would be the measurement of the fragmentation function (FF) modified by the medium. In elementary collisions these FFs can be measured by isolating the hadrons which belong to a jet by calorimetric measurements. Using cone finding algorithms the hadrons belonging to jets can be identified and the fraction of the total momentum of the hadrons in the jet, which is identified as the momentum of the initial parton, can be measured. A picture of a reconstructed jet in p-$\overline{\text{p}}$ collisions at $\sqrt{s}$= 1.8 TeV recorded by the CDF collaboration [38] is shown in the right panel of Figure 1.7.

A clear structure of the di-jet can be identified. In the p_t-range accessible at RHIC and especially at SPS those di-jet structures are overlaid by a large hadronic background in heavy ion collisions, which makes it impossible to reconstruct jets on an event-by-event basis.

To circumvent the problem of the background contribution in single events the jet structure can be studied on a statistical basis.

For a given event a trigger is defined as a particle with a relatively high transverse momentum. For this trigger particle the correlations in relative azimuthal angle $\Delta\phi$ with associated particles (mostly from a lower p_t range) in the event are measured. Assuming that the trigger particle originates close to a fragmenting parton and averaging over many events, this will reveal the jet structure in the given associate p_t range in the collisions.

The measured correlations also contain the correlations due to the acceptance of the detector and other physical correlations arising e.g. due to the elliptic flow evolving in non-central collisions. Those effects have to be accounted for in order to extract the jet-like yield contribution of the associated particles.

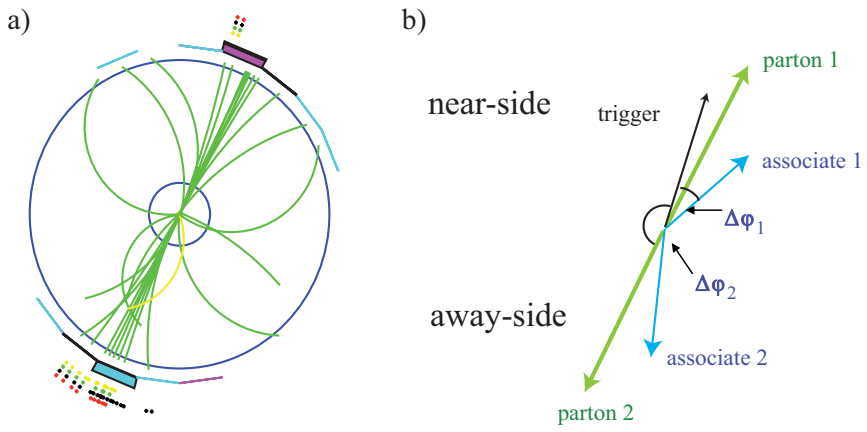

Figure 1.7: a): Example of a reconstructed jet event in p-$\overline{\text{p}}$ collisions [38]. b): Schematic diagram for the identification of jets by measuring azimuthal correlations between a high-p_t trigger particle and associated particles in an event.

It can not be assumed that all selected trigger particles stem from jets. The extracted yield therefore only measures a yield averaged over jet-like and non-jet like trigger particles. The measured yield can thus only recover the shape of the fragmentation function, not the absolute yield. An ansatz to recover the actual number of jet-like trigger particles in the event sample will be discussed in section 3.2.2. Triggering on an outgoing hadron from collisions close to the surface can lead to the observation of one jet fragmenting into the vacuum while the second jet has to traverse the medium, suffering energy loss and hence redistributing part of its energy to the medium. In such a scenario the region close to the trigger particle (near-side, $\Delta\phi = \phi_T - \phi_A \approx 0$) shows features of vacuum fragmentation while the away-side ($\Delta\phi \approx \pi$) will reflect the interactions of the particles with the medium. This scenario corresponds to the surface bias discussed above which is assumed to be dominant at high-p_t at RHIC energy. A recent compilation of the extracted per trigger yields of associated particles for different combinations of trigger and associated p_t is shown in Figure 1.8.
One of the striking results of the early RHIC measurements was the disappearance of the away-side in triggered correlations for trigger and associated particles with relatively high transverse momenta [39, 40, 41] as shown Figure 1.8. In Au-Au collisions the yield on the near-side matches the expectation from p-p collisions to good accuracy while no associate particles were found in the given p_t range on the away-side.
This again demonstrates the high energy loss of particles in the medium and confirms the expectations that on the near-side the trigger condition mostly selects hadrons emerging from collisions close to the surface of the interaction zone. The particles on the away-side on the other hand have to traverse in the extreme case twice the radius of the collision zone and - depending on the density of the medium - lose a significant part of their energy which transforms into hadrons at lower p_t.

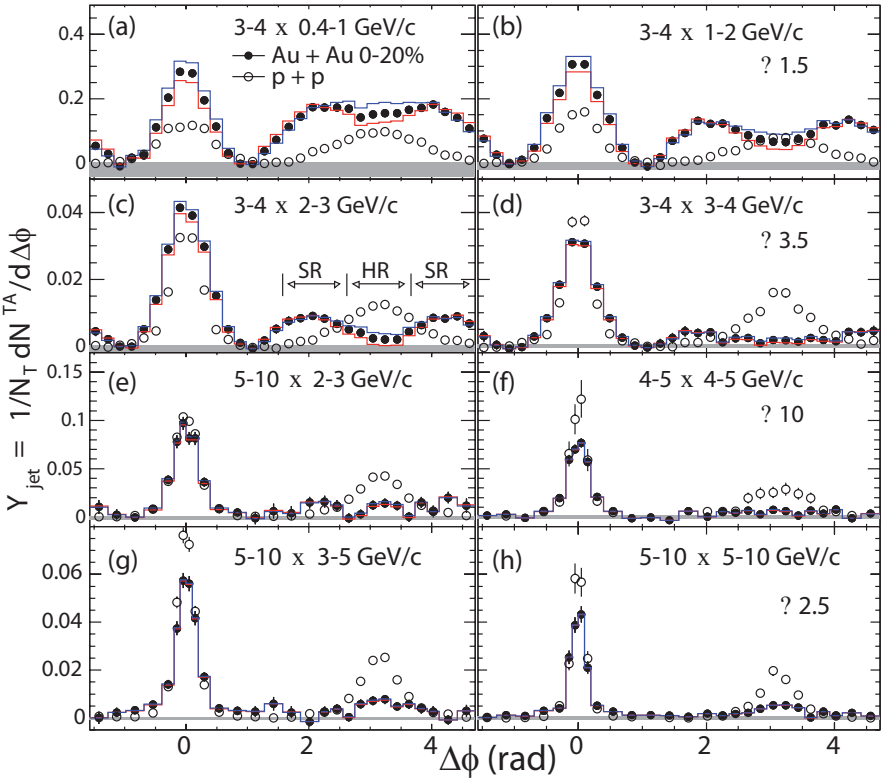

Figure 1.8: Compilation of triggered azimuthal correlations in p-p compared to A-A collisions for different trigger- and associated p_t regions (trigger x associate) at $\sqrt{s_{NN}}$= 200 GeV beam energy (PHENIX) [42].

At SPS energy the CERES collaboration reported a significant broadening of the away-side peak in Pb-Au [40] collisions using non-triggered events, that is studying the correlations of all particles in an event above a given p_t threshold. Extending the RHIC analysis to lower p_t, broadening has also been observed at RHIC [41]. Moreover, the away-side exhibited a double-humped structure which was connected to interactions of the partons with the medium. Such a structure is also observed in triggered correlations at top SPS energy as a result of this thesis.

Different scenarios for the mechanism of the energy transfer and the response of the medium to the transferred energy are studied.

In case the particle is traversing the medium with a speed higher than the speed of sound in that medium, mach cone shock waves [43] can develop in the medium. The angle of the emitted particles θ_M can be related to the speed of sound c_s in the medium which is an important quantity characterizing the equation of state of the system:

$$\sin(\theta_M) = \frac{c_s}{v_p}. \tag{1.8}$$

Approximating the parton velocity v_p with the speed of light v_p=c, the speed of sound can be extracted from the measured mach angle.
In addition, the emission of Cerenkov light [44] or large angle gluon radiation [45] could lead to the particles being emitted under a cone of a given angle relative to the initial parton.
A further effect shifting the maximum of the two-particle jet yield on the away-side could be the deflection of parton by a certain angle prior to hadronisation or the impact of the transverse flow on the partons in the medium [46].
The path length dependence of the energy loss of partons in the medium could favor jets traversing out of the medium rather than inwards [47].

The latter scenarios lead to a different structure of hadron emission event-by-event as compared to cone like scenarios where large angles among the associate particles are observed.
In case of a pure deflection of partons prior to fragmentation, the fragmentation products can still be emitted in a narrow region in coordinate space as in the case of vacuum fragmentation.
The resulting two-particle correlations however can look similar in both scenarios. The two-particle analysis alone can not distinguish these effects. A study of three-particle correlations, i.e. the correlations among a trigger particle and two associated particles, can help to shed light on the genuine jet shape event-by-event.

1.5 Scope of the thesis

In this thesis, two- and three-particle azimuthal correlations of high-p_t charged particles are investigated. The correlations are analyzed depending on the transverse momentum p_t and the charge of the particles for different centralities of the collisions. A two dimensional view of the two-particle correlations is obtained by analyzing the correlations in relative azimuthal angle $\Delta\phi$ and the difference in pseudo rapidity $\Delta\eta$. The analysis is again performed for different charges and p_t regions of trigger and associate particles.

The data analyzed are recorded with the CERES spectrometer as part of the CERN SPS. In the year 2000, 30 million events were recorded in a high statistics run at different centralities at top SPS energy. CERES is equipped with a cylindrical Time Projection Chamber (TPC) with full coverage in azimuth and is hence well suited for the analysis of azimuthal correlations.
The measured correlations are corrected for the limited two-track resolution which is measured via mixed event studies, as well as determined via Monte Carlo simulations. In addition, the resolution in the azimuthal- and the polar angle as well as the transverse momentum resolution are determined by Monte Carlo studies.
The elliptic flow parameter v_2 used to subtract the flow contribution to the correlations is determined in a separate reaction plane analysis for the specific settings of the analysis.
The two-particle correlation results are compared to results from simulations

performed with the PYTHIA event generator in order to compare the A-A measurements to expectations for vacuum fragmentation from elementary collisions.
Due to the limited statistics the three-particle correlation analysis is only performed in one centrality bin.

The next generation of heavy ion physics experiments at the Large Hadron Collider (LHC) will provide collisions of heavy ions at up to a center of mass energy of $\sqrt{s_{NN}} = 5.5$ TeV with sufficient statistics to also allow for a more detailed analysis of three-particle correlations.
One experiment especially designed to study heavy ion collisions at the LHC is the ALICE (A Large Ion Collider Experiment) experiment. It is equipped with a large TPC allowing for particle identification and momentum measurements with high precision.
In parallel to the correlation analysis, a monitoring program is developed to monitor online the data stream coming from the TPC. In a commissioning phase the monitoring program is used to test the functionality of the TPC and to check basic performance parameters of the operating TPC. The program is finally added to the official software package of the ALICE experiment AliROOT. In an appendix this monitoring program is presented and the main features of the monitor are discussed in the context of results recorded during the commissioning runs.

2 Analysis method for two- and three-particle correlations

In this section analyses methods used for the two- and three-particle correlation analyses are presented. In Monte Carlo studies the feasibility and systematic uncertainties of the model assumptions are investigated.

The correlations are analyzed by studying the differences in the azimuthal angles $\Delta\phi$ of high-p_t trigger particles with associate particles from the same event but different p_t region.

A basic assumption for the analysis of the two- as well as the three-particle correlations is that the sources of the correlations are twofold (two-source model). Either an associated particle is jet-like correlated to the trigger or it stems from the underlying event.

Particles from the underlying event are correlated to the reaction plane of the collisions for non-central collisions (elliptic flow). This leads to correlations among two flowing particles with the same functional form as the correlations to the reaction plane. The flow strength encoded in the parameter v_2 is determined in a separate reaction plane analysis.

The flow contribution to the correlations is subtracted from the measured correlations by the Zero Yield At Minimum (ZYAM) [41] method. This method assumes that the jets on the near- and the away-side are separated by a point where no jet-like associate particles are observed, that is where the jet yield is zero.

Correlations arising due to the non-uniformity of the acceptance in the azimuthal angle ϕ are taken into account by a mixed-event technique, combining trigger and associate particles from different events.

An inconsistency in the two-source model arises if the occurrence of a jet-trigger is not correlated to the reaction plane. This results in uncorrelated pairs by combining jet-triggers with particles from the underlying event. Averaging over many events results in a random component in the $\Delta\phi$ distribution of trigger-associate pairs.
However it can be argued that this random component is implicitly accounted for by the measured v_2 parameter which is subject to the same random component in the trigger-p_t range.

Monte Carlo studies based on a simple two-source model are performed for the two- as well as for the three-particle analysis to test the methods applied and to study the impact of the afore mentionend limitations of the two-source model.

2.1 Two-particle correlations

According to the two-source model the $\Delta\phi$ distribution of associates per trigger $J_2(\Delta\phi)$ is assumed to be composed of two components, the jet-like $\hat{J}_2(\Delta\phi)$ and the flow-like contribution $B_2(\Delta\phi)$ which is also denoted as background in the two-particle analysis:

$$J_2(\Delta\phi) = \frac{dN_A}{d(\Delta\phi)} = \hat{J}_2(\Delta\phi) + B_2(\Delta\phi) \tag{2.1}$$

$$B_2(\Delta\phi) = \frac{dN_b}{d(\Delta\phi)} \tag{2.2}$$

$$\hat{J}_2(\Delta\phi) = \frac{dN_{jet}}{d(\Delta\phi)} \tag{2.3}$$

We assume that the number of associates in a triggered event is build up of $N_A = N_b + N_{jet}$ associate particles where N_b denotes the number of background associates and N_{jet} the number of jet-like associates per trigger, respectively. $\hat{J}_2(\Delta\phi)$ is denoted as conditional yield and corresponds to the number of jet-like associates per trigger particle at a given angle $\Delta\phi$ relative to the trigger.
The background component B_2 shows the correlations due to the elliptic flow in the events. We start by evaluating the functional form of this component.

2.1.1 Two-particle flow modulation

The azimuthal distribution of single (background) particles with respect to the reaction plane angle Ψ is described by:

$$\frac{dN_b}{d\phi} = \frac{N_b}{2\pi}\left(1 + 2v_2^b \cos 2(\phi - \Psi)\right), \tag{2.4}$$

The strength of v_2^b depends on p_t and the mass of the particles as well as on the centrality of the collision. The distribution of trigger-background pairs separated by a given $\Delta\phi$ where both particles are correlated to the reaction plane reads:

$$\begin{aligned}\frac{d^4N}{d\Psi d\phi_T d\phi_b d(\Delta\phi)} &= \frac{1}{2\pi}\cdot\frac{N_T}{2\pi}\left(1 + 2v_2^T \cos 2(\phi_T - \Psi)\right) \\ &\cdot \frac{N_b}{2\pi}\left(1 + 2v_2^b \cos 2(\phi_b - \Psi)\right)\cdot\delta(\Delta\phi - (\phi_b - \phi_T)),\end{aligned} \tag{2.5}$$

N_b, v_2^b and N_T, v_2^T corresponding to the total number and the elliptic flow values of background particles and triggers, respectively. The first prefactor $1/2\pi$ stems from the assumed flat distribution of the reaction plane angle.
Integrating over Ψ, ϕ_T, and ϕ_b and normalizing to the number of triggers N_T we obtain:

$$\frac{1}{N_T}\frac{dN}{d(\Delta\phi)} = \frac{dN_b}{d(\Delta\phi)} = \frac{N_b}{2\pi}\left(1 + 2v_2^T v_2^b \cdot \cos 2(\Delta\phi)\right). \tag{2.6}$$

Due to the small number of jet-like associate particles ($\ll$1) relative to the background particles ($\approx$10) the v_2^b paremater is taken as determined from all

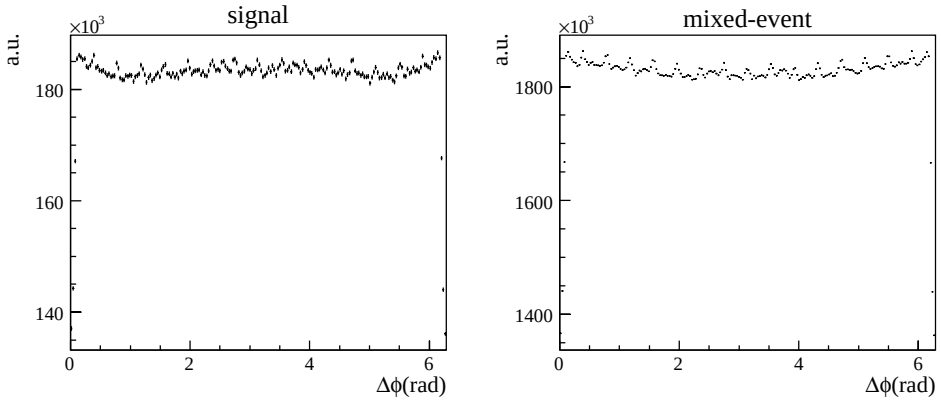

Figure 2.1: Signal-(left) and mixed-event distribution (right) of the difference in the azimuthal angle $\Delta\phi$ for trigger-associate pairs with $2.5<p_t(\mathrm{T})<4.0$ GeV/c and $1.0<p_t(\mathrm{A})<2.5$ GeV/c.

associate particles v_2^A. With this we obtain for the background component B_2 from Eq. (2.2):

$$B_2 = \frac{dN_b}{d(\Delta\phi)} = \frac{N_b}{2\pi}\left(1 + 2v_2^T v_2^A \cdot \cos 2(\Delta\phi)\right). \tag{2.7}$$

2.1.2 Extraction of the conditional yield

In real events the signal distribution $J_2(\Delta\phi)$ (Eq. (2.1)) contains physical correlations but also correlations due to the non-uniform efficiency of the TPC. This arises mainly due to the segmentation of the TPC in 16 read out chambers. The effect can be studied by mixed event distributions $M_2(\Delta\phi)$ where trigger and associated particles are taken from different events.
Those distributions show the same efficiency effects as the signal but not the physical correlations. Examples of signal- and mixed-event distribution with very fine binning in $\Delta\phi$ are shown in Figure 2.1. To correct for the efficiency effects the signal distribution is divided by a mixed event distribution.
To reduce the statistical uncertainty in the mixed-event distribution ten mixed events are created for each signal event. The resulting correlation function $C_2(\Delta\phi)$ is normalized to the number of entries in the signal and mixed-event distribution:

$$C_2(\Delta\phi) = \frac{\int_{\Delta\phi} M_2(\Delta\phi)}{\int_{\Delta\phi} J_2\Delta\phi)} \cdot \frac{J_2(\Delta\phi)}{M_2(\Delta\phi)}, \tag{2.8}$$

In case of a flat background the correlation function describes up to a constant factor the probability distribution for the detection of an associate particle at a given $\Delta\phi$ relative to the trigger [48].

In the two-source approach the correlation function is decomposed in jet-like correlations $C_{2,j}$, and the correlations arising due to the elliptic flow of the

source $C_{2,f}$:

$$\begin{aligned} C_2(\Delta\phi) &= C_{2,j}(\Delta\phi) + C_{2,f}(\Delta\phi) \\ &= C_{2,j}(\Delta\phi) + b \cdot (1 + 2 < v_2^T >< v_2^A > \cos(2\Delta\phi)). \end{aligned} \tag{2.9}$$

Here the approximation $< v_2^T v_2^A > \approx < v_2^T >< v_2^A >$ is used and the v_2 values are calculated separately for the trigger and associate p_t range. The form of the flow modulation $C_{2,f}$ in the correlation function is given by Eq. (2.7) with the parameter b corresponding to the probability of finding a flowing particle among the associates $b{=}N_b/N_A$. This probability however is not a priori known.

To extract the flow contribution the ZYAM method is used. The correlation function is fit with a polynomial of 6th order in the range $0.2{<}\Delta\phi{<}1.5$.
The flow contribution $C_{2,f}$ is increased by the parameter b until it touches a point of the fit to the correlation function. An example of the fit to the correlation function and the adjusted flow background for a simulation is shown in Figure 3.3.
The jet-like contribution $C_{2,j}$ is obtained by subtracting the adjusted flow contribution from the measured correlation function. Up to statistical fluctuations the such constructed jet contribution is zero at its minimum by construction. The jet contribution $C_{2,j}$ normalized to the integral of the correlation function corresponds to the probability of finding a jet-like associate at a given $\Delta\phi$ from the trigger. Scaling this term by the total amount of associates per trigger we obtain the conditional yield as the number of jet-associated particles per trigger at a given $\Delta\phi$:

$$\hat{J}_2(\Delta\phi) = \frac{1}{N_T}\frac{dN_{jet}^{TA}}{d\Delta\phi} = \frac{C_{2,jet}(\Delta\phi)}{\int (C_2(\Delta\phi')d(\Delta\phi'))}\frac{N^{TA}}{N_T}, \tag{2.10}$$

N^{TA} being the total number of associated particles in all triggered events ($N_A{=}N^{TA}/N_T$). In the following chapters the subscript $_{jet}$ will be omitted in the notation of the conditional yield.

The p_t-dependent elliptic flow coefficients for positive and negative triggers (v_2^T) and associated (v_2^A) are measured by a separate reaction plane analysis as discussed in section 8. Implications and constraints due to the model applied are investigated in section 3.

2.2 Three-particle correlations

2.2.1 Principle of the analysis

The analysis of the three-particle correlations is based on methods presented in [49]. As for the analysis of the two-particle correlations a two-source model of the correlations is assumed.
The efficiency effects are again taken into account by a mixed event technique and are discussed at the end of this section and in detail for the different background components in the result section 10.
As in the previous section the signal of the two-particle $\Delta\phi$ distribution is

assumed to be composed of two components, the jet-like $\hat{J}_2(\Delta\phi)$ and the flow-like components $B_2(\Delta\phi)$. The genuine jet-like yield $\hat{J}_2(\Delta\phi)$ is determined as described in the last section and used as an input for the three-particle analysis. Combining two associated particles which are correlated to a trigger according to (Eq. (2.1)) we obtain for the three-particle correlation signal:

$$\begin{aligned} J_3(\Delta\phi_1,\Delta\phi_2) &= \Big(\hat{J}_2(\Delta\phi_1)+B_2(\Delta\phi_1)\Big)\otimes\Big(\hat{J}_2(\Delta\phi_2)+B_2(\Delta\phi_2)\Big) \\ &= \hat{J}_2(\Delta\phi_1)\otimes\hat{J}_2(\Delta\phi_2) \\ &+ \hat{J}_2(\Delta\phi_1)\cdot B_2(\Delta\phi_2)+B_2(\Delta\phi_1)\cdot\hat{J}_2(\Delta\phi_2) \\ &+ B_2(\Delta\phi_1)\otimes B_2(\Delta\phi_2), \end{aligned} \tag{2.11}$$

$\Delta\phi_1{=}\phi_1-\phi_T$ and $\Delta\phi_2{=}\phi_2-\phi_T$ being the differences in the azimuthal angles of two particles with respect to the trigger.

- The first term in the RHS of Eq. (2.11) is denoted as $\hat{J}_3(\Delta\phi_1,\Delta\phi_2)$ and corresponds to the genuine three-particle jet-like correlation. The product is denoted by $\otimes$ to emphasize that this is not simply the product of the two-particle jet-yields.

- The second term corresponds to the case where one particle is jet-like correlated to the trigger whereas the second particle is correlated with the underlying event (flow). It is denoted as Hard-Soft background and abbreviated by $\hat{J}_2\otimes B_2$. Since the two terms are uncorrelated it is just the product of the two terms.

- The third term is denoted as $B_3(\Delta\phi_1,\Delta\phi_2)$ and is called the Soft-Soft term since it accounts for all three particles being flow-like correlated to the trigger particle.
  In addition, two-particle correlations among the associates that are not correlated to the trigger (e.g. from additional jets in triggered events) are considered in the analysis in this background component. In this respect $B_3(\Delta\phi_1,\Delta\phi_2)$ deviates from the pure flow correlations of triplets as described by $B_2(\Delta\phi_1)\otimes B_2(\Delta\phi_2)$. [1]

Subtracting the Hard-Soft and Soft-Soft background terms the genuine jet correlations can be extracted from the measured three-particle distribution as:

$$\begin{aligned} \hat{J}_3(\Delta\phi_1,\Delta\phi_2) &= J_3(\Delta\phi_1,\Delta\phi_2) \\ &- \Big(\hat{J}_2(\Delta\phi_1)\cdot B_2(\Delta\phi_2)+B_2(\Delta\phi_1)\cdot\hat{J}_2(\Delta\phi_2)\Big) \\ &- B_3(\Delta\phi_1,\Delta\phi_2). \end{aligned} \tag{2.12}$$

[1] Particles from additional jets would result in an additional random component in the two-particle correlations altering the definition from Eq. (2.11). If however the random component is already accounted for by B_2 by a reduced measured v_2 it can consistently be incorporated in the Hard-Soft background component (see secition 3.1).

2.2.2 Background contributions: Trigger-Flow

We start with the calculation of the background terms evaluating the contributions where trigger as well as associated particles stem from the underlying event which is subject to the anisotropic flow in the collision. This term is part of the background component $B_3(\Delta\phi_1, \Delta\phi_2)$ from Eq. (2.12).
Only terms up to the second harmonic v_2 of the $\Delta\phi$ distribution of the particles with respect to the reaction plane are taken into account. For details including the fourth harmonic v_4 see [49].

For two associates separated to a trigger by $\Delta\phi_1$ and $\Delta\phi_2$ and all three particles being correlated to the reaction plane we obtain equivalently to Eq. (2.5):

$$\begin{aligned}\frac{d^6N}{d\Psi d\phi_T d\phi_1 d\phi_2 d(\Delta\phi_1) d(\Delta\phi_2)} = \\ \frac{1}{2\pi}\cdot\frac{N_T}{2\pi}\left(1+2v_2^T\cos 2(\phi_T-\Psi)\right) \\ \cdot\frac{N_1}{2\pi}\left(1+2v_2^1\cos 2(\phi_1-\Psi)\right)\cdot\delta(\Delta\phi_1-(\phi_1-\phi_T)) \\ \cdot\frac{N_2}{2\pi}\left(1+2v_2^2\cos 2(\phi_1-\Psi)\right)\cdot\delta(\Delta\phi_2-(\phi_2-\phi_T)),\end{aligned} \tag{2.13}$$

N_1 and N_2 corresponding to the number of two sets of background particles. Integration over Ψ, ϕ_T, ϕ_1, and ϕ_2 and normalizing to the number of trigger particles we obtain for the backround term characterizing flowing triplets of trigger and associates:

$$\begin{aligned}B_2(\Delta\phi_1)\otimes B_2(\Delta\phi_2) = \\ \int_0^{2\pi}\int_0^{2\pi}\int_0^{2\pi}\int_0^{2\pi} d\phi_T d\Psi d\phi_1 d\phi_2 \frac{d^6N}{d\Psi d\phi_T d\phi_1 d\phi_2 d(\Delta\phi_1) d(\Delta\phi_2)} = \\ \frac{N_1N_2}{(2\pi)^2}(1+2v_2^Tv_2^1\cos 2(\Delta\phi_1)+2v_2^Tv_2^2\cos 2(\Delta\phi_2)+2v_2^1v_2^2\cos 2(\Delta\phi_1-\Delta\phi_2)).\end{aligned} \tag{2.14}$$

For samples from the same set of associates the normalization factor N_1N_2 reduces to $N_b(N_b-1)$, N_b being the number of background particles in a triggered event as introduced in the last section. In case no additional two particle correlations from e.g. additional jets in triggered events are present this component determines the complete Soft-Soft background contribution $B_3(\Delta\phi_1, \Delta\phi_2)$.

2.2.3 Background contributions: Hard-Soft

The Hard-Soft background is constructed according to:.

$$\begin{aligned}\hat{J}_2\otimes B_2 &= \hat{J}_2(\Delta\phi_1)\cdot\frac{N_b}{2\pi}\left(1+2v_2^Tv_2^A\cdot\cos 2(\Delta\phi_2)\right) \\ &+ \hat{J}_2(\Delta\phi_2)\cdot\frac{N_b}{2\pi}\left(1+2v_2^Tv_2^A\cdot\cos 2(\Delta\phi_1)\right),\end{aligned} \tag{2.15}$$

where $\hat{J}_2(\Delta\phi_1)$ and N_b correspond to the conditional yield and the number of background associates as determined from the two-particle analysis.

2.2.4 Background contributions: Soft-Soft

In an event containing more than one jet correlations among associates of the jet not selected by the trigger will give a contribution to the three-particle correlations which is however uncorrelated to the trigger particle. This contribution is taken into account by combining a trigger particle with two associated particles from a different event containing both associated particles. No trigger criterion is required for the events the associated particles are taken from but otherwise the same event selection criteria are applied as for triggered events. This class of events is called inclusive event sample.
The assumption behind this choice for the mixed event sample is a Poissonian distribution of jets in inclusive events. If this assumption holds, the probability of finding associates from additional jets in a jet event is equal to the probability of finding any jet-associates in inclusive events. These correlations can be reproduced by combining a trigger with two associated particles from an inclusive event:

$$B_3^{inc}(\Delta\phi_1, \Delta\phi_2) = \frac{1}{N_T} \int_0^{2\pi} d\phi_T \left(\frac{d^3 N_{inc}(\phi_T, \Delta\phi_1, \Delta\phi_2)}{d\phi_T d(\Delta\phi_1) d(\Delta\phi_2)} \right) \tag{2.16}$$

In addition to the contribution from additional jets the such constructed background already accounts for flow-like correlations among the associates not correlated to the trigger. This corresponds to the third term in the RHS of Eq. (2.14) which only depends on the angular differences between the two associates. In other words the such constructed background component already contains part of the Trigger-Flow correlation as described by Eq. (2.14).
In order to fully describe the trigger-flow correlations the first and the second term in Eq. (2.14) have to be added to the mixed event inclusive sample in the form:

$$B_3^{inc,tf}(\Delta\phi_1, \Delta\phi_2) = \frac{< N_{inc}(N_{inc}-1) >}{(2\pi)^2} (2 v_2^T v_2^1 \cos 2(\Delta\phi_1) + 2 v_2^T v_2^2 \cos 2(\Delta\phi_2)), \tag{2.17}$$

where N_{inc} corresponds to the number of particles in inclusive events.
$< N_{inc}(N_{inc}-1) >$ is as well the level obtained by sampling the mixed event inclusive distribution $\frac{d^3 N_{inc}(\phi_T, \Delta\phi_1, \Delta\phi_2)}{d\phi_T d(\Delta\phi_1) d(\Delta\phi_2)}$ from Eq. (2.16) which contains the remaining trigger-flow correlations.
Using these notations the complete Soft-Soft background results in:

$$B_3(\Delta\phi_1, \Delta\phi_2) = B_3^{inc}(\Delta\phi_1, \Delta\phi_2) + B_3^{inc,tf}(\Delta\phi_1, \Delta\phi_2). \tag{2.18}$$

2.2.5 Normalization and construction of the yield

Du to the usage of inclusive events as a reference the background level has to be scaled in order to account for differences in the multiplicity of inclusive and triggered events. The inclusive distributions has to be scaled by a in order to meet the background level in triggered events as determined by the ZYAM method:

$$a = < N_b > / < N_{inc} > . \tag{2.19}$$

With this notation the scaling factor for the Soft-Soft background where to associates from inclusive events are combined with a trigger is given by:

$$\frac{< N_b(N_b-1) >}{< N_{inc}(N_{inc}-1) >} \approx a^2 \tag{2.20}$$

Equality holds if the multiplicity is Poissonian like distributed. For deviations from this scenario a second scaling factor b_3 is introduced which is determined via a Zero Yield At Minimum condition for the three-particle jet-yield. The Hard-Soft component is subtracted from the measured correlation function. The Soft-Soft term added by the Trigger-Flow component is then adjusted to the correlation function by the ZYAM method and subtracted. For the final expression of the three-particle jet-like yield we obtain:

$$\begin{aligned} \hat{J}_3(\Delta\phi_1,\Delta\phi_2) &= J_3(\Delta\phi_1,\Delta\phi_2) \\ &- (\hat{J}_2(\Delta\phi_1)\cdot\frac{N_b}{2\pi}\left(1+2v_2^T v_2^A\cdot\cos 2(\Delta\phi_2)\right) \\ &\quad +\hat{J}_2(\Delta\phi_2)\cdot\frac{N_b}{2\pi}\left(1+2v_2^T v_2^A\cdot\cos 2(\Delta\phi_1)\right)) \\ &- b_3 a^2\left(B_3^{inc}(\Delta\phi_1,\Delta\phi_2)+B_3^{inc,tf}(\Delta\phi_1,\Delta\phi_2\right). \end{aligned} \tag{2.21}$$

2.2.6 Histogramming and efficiency correction

To construct the three-particle signal distribution two-dimensional histograms are filled with the two angular differences $\Delta\phi_1$ and $\Delta\phi_2$ of associated particles to the trigger particle. Each associated particle from an event is combined with all other associates from the same event. The signal distribution is therefore by definition symmetric to the diagonal of the correlation function $\Delta\phi_1 = \Delta\phi_2$. In the signal distribution the physical correlations are overlaid by the effects due to the single track acceptance.
In order to visualize the physical correlations and to account for the acceptance effects in the signal as well as in the different background terms the terms are divided by a mixed-event distribution where all three particles are taken from different events. This cancels the efficiency effects but otherwise only introduces a normalization factor which is equal for all the components and taken out again after the division.
For the mixed-event reference distribution each associated pair is counted explicitly twice in order to ensure the symmetry of the distribution.

3 Monte Carlo studies for two- and three-particle correlations

In order to test the applicability of the model assumptions introduced in the last section, a simple Monte Carlo (MC) study is performed investigating different forms of jet-like correlations. Two- as well as three-particle correlations are investigated.

The input is chosen as to reproduce the measured two-particle conditional yield, the number of associated particles and the flow modulation determined for trigger and associates with $2.5<p_t(\mathrm{T})<4.0$ GeV/c and $1.0<p_t(\mathrm{A})<2.5$ GeV/c. The trigger event sample is divided into sub samples of events where the trigger is from a jet (characterized by a jet trigger probability p_{jet}) and non-jet events (Figure 3.1).
In all events containing a jet the trigger is taken from the jet and there are no additional jets in these events.

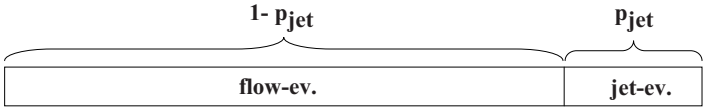

Figure 3.1: Event sample for MC study.

The number of jet-associated particles is assumed to be Poissonian distributed in a jet-event. The number of background particles is assumed to be fixed.
Two topologies for the jet-like structure are investigated. A double-humped structure of the jet-like yield as observed in the data and a deflected jet structure where the peak of the distribution is off π by approx. 1 rad (Figure 3.2).
The deflected jet structure is used alternating in order to reproduce on average the measured conditional yield. For the two-particle analysis these two scenarios are by construction not distinguishable. For this analysis only the first topology is analyzed.
The events are constructed generating randomly a trigger and associated particles. For non-jet events trigger and associated particles are correlated with the reaction plane. The v_2 values are chosen as in the data for two different centrality bins. In jet-events, the trigger is chosen to be random to the reaction plane.

The yield per jet-trigger y_{jet} is obtained by dividing the yield per trigger y_{trig} by the probability to find a jet-trigger p_{jet} in the event sample:

$$y_{jet} = y_{trig}/p_{jet}. \tag{3.1}$$

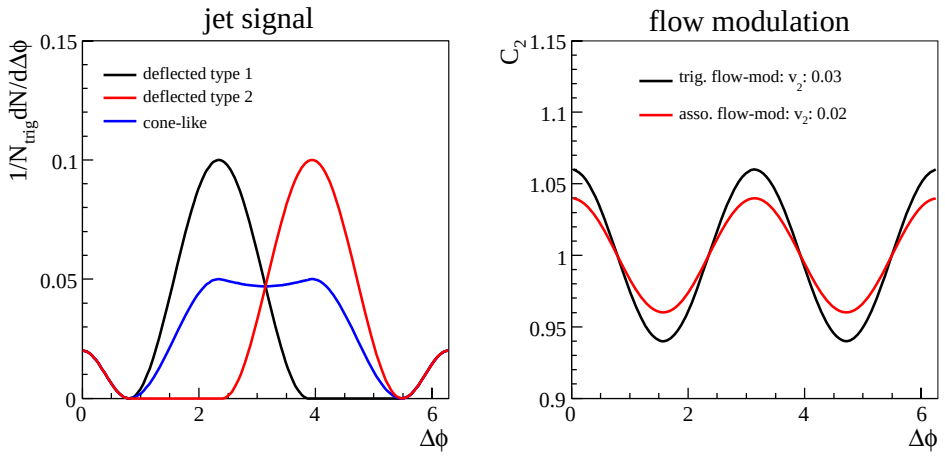

Figure 3.2: Monte Carlo input for jet-(left) and flow-like (right) correlations. The jet-like contribution is either the same in all events (blue line) which would be obtained by e.g. conical emission, or alternating (red, black) which corresponds to a scenario of deflected jets. The total yield is tuned to match the conditional yield observed in the data.

With the such defined yield for a jet-trigger the yield per trigger used as an input is reproduced averaging over jet-and non-jet events.
Two settings for the elliptic flow of trigger and associated particles corresponding to the values extracted for the centrality (0.5)% and (10-20)% are investigated. The specifications of the toy model are summarized in the following table:

Table 3.1: Specifications of the Monte Carlo toy model.

quantity	**value**	**description**
n_{flow}	15	number of flowing associates per event (fixed)
y_{trig}	0.17	integrated conditional yield (Poissonian distr.)
p_{jet}	0.1	prob. for a jet-trigger in the event sample
y_{jet}	1.7	jet-yield per jet-trigger (Poissonian distr.)
v_2^T	0.03(0.1)	trigger v_2 values for (0-5)% ((10-20)%) centrality
v_2^A	0.02(0.07)	associate v_2 values for (0-5)% ((10-20)%) centrality

3.1 Monte Carlo studies for two-particle correlations

The two-particle correlation function is obtained as the normalized ratio of a signal- and a mixed-event distribution as described in 2.1.
Due to the trigger being not correlated to the reaction plane we obtain a random component in the correlation function which corresponds to the combinations of trigger and background particles in jet-events.

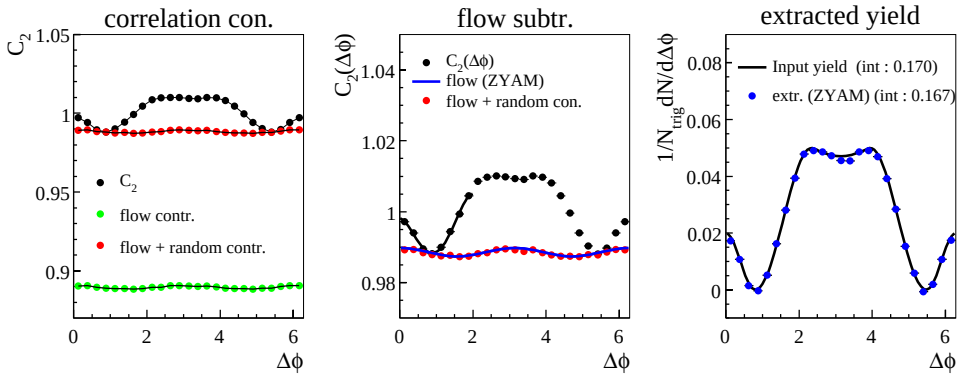

Figure 3.3: Monte Carlo toy model with the settings for central collisions. Left panel: Correlation function with different contributions (flow, random, jet) indicated. Middle panel: Correlation function with flow adjusted by ZYAM (blue line) and actual background component (red circles). Right panel: Conditional yield used as input compared to extracted yield using the ZYAM method. The black line in the middle panel shows a fit to the correlation function in order to adjust the flow contribution via ZYAM.

Since the background (flow) particles dominate the events the random component is approximately given by the ratio of jet-trigger events in the event sample. This is given by the jet-trigger probability p_{jet}. In the toy model the particles can be flagged and the different components of the correlation function can be decomposed.

This is shown in the left panel of Figure 3.3. In the middle panel of Figure 3.3 the correlation function and the non-jet contribution are shown together with the flow as determined via the ZYAM method.

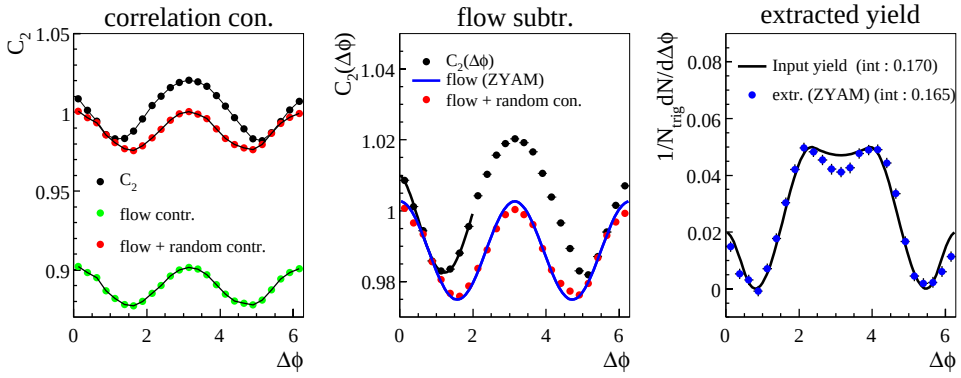

Figure 3.4: Same as Figure 3.3 with v_2 values similar to values expected for the most peripheral bin in the real data analysis ($v_2^T = 0.1$, $v_2^A = 0.07$)

An uncertainty arises due to the fact that the assumed flow strength used in the ZYAM method is diluted in the data by the random component by 10%. As the flow modulation is very small for the central bin, the yield per trigger which was used as the input (line in left panel of Figure 3.3) is well reproduced by subtracting the flow component determined via ZYAM.

If, however, the flow modulation is stronger a 10% deviation can lead to a significant change in the shape of the extracted jet-yield component. The relative change of the modulation due to the random component is the same as in the first example. However, since the flow component is subtracted from the correlation function the absolute change of the modulation is relevant for the extracted yield.

For the example in Figure 3.4 the flow values for the trigger- and associate particles are taken as determined for the centrality $\sigma/\sigma_{geom} = (10-20)\%$. For a better comparison the same input conditional yield has been taken in both examples. The integrated yield extracted in this scenario does not vary much from the input however the shape on the away-side around $\Delta\phi = \pi$ deviates considerably from the shape of the input distribution.

As mentioned at the beginning of this section the data analysis for the elliptic flow might already incorporate a trigger being random to the reaction plane. If, as assumed, each 10th trigger particle stems from a jet and is not correlated to the reaction plane, this might already be reflected in the correlations of trigger particles with the reaction plane. In this case the measured flow modulation would in fact be:

$$v_2^T(meas) = 0.9 \cdot v_2^T \tag{3.2}$$

For the example in Figure 3.5 the same v_2 values as for Figure 3.4 are used however explicitly accounting for the trigger being random to the reaction plane. In the construction of the events a higher trigger v_2 is used as actually measured (Eq. (3.2)) and used in the ZYAM method. Applying this adjustment the yield can be reproduced up to slight variations in the peak on the away-side.

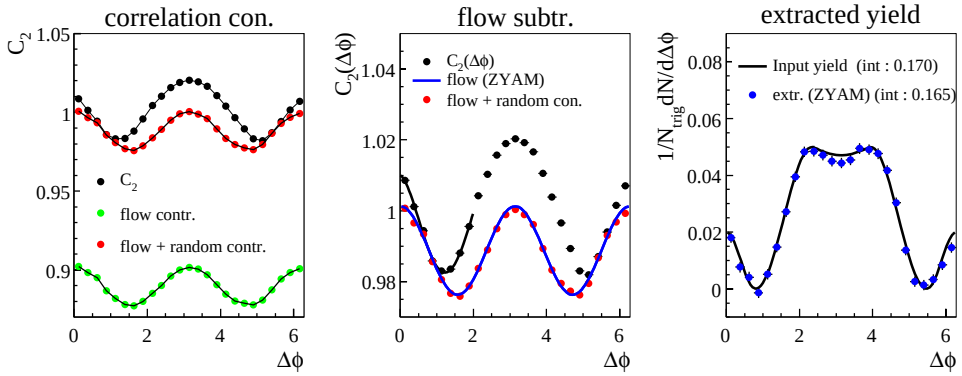

Figure 3.5: Same as in Figure 3.4 under the assumption that the measured v_2 values for the trigger particle already reflects the trigger being random to the reaction plane.

Another technical uncertainty arises due to the adjustment of the flow contribution to the correlation function.
The flow contribution is determined by successively increasing the flow term via the parameter b (Eq. (2.9)) until it reaches an arbitrary point of a fit to the correlation function. A polynomial of 4th order is used in this example to fit the data. The curvature of the measured correlation function increases with increasing modulation of the underlying background. Therefore, the b parameter depends increasingly on the quality of the description of the data by the fit function and the statistical uncertainties in the data. Since the b parameter not only determines the normalization but also scales the modulation the same argument as discussed above holds. A small relative change in the modulation of the flow can have a significant impact on the extracted functional form of the yield.

The path length dependence of the energy loss of partons can lead to a modulation of the trigger particles to the reaction plane which is similar to the correlations due to the elliptic flow in the bulk medium, even if the trigger particle stems from a jet. In this scenario, the random component introduced in this model would vanish. However, it is not clear as to which degree the correspondence of the degree of the ellipticity of bulk matter and high-p_t jet-triggers holds. For very high momenta of the triggers the correlation to the reaction plane can be assumed to be lost due to the smaller impact of the medium on the total momentum of the trigger.
Another uncertainty in this respect arises due to the fact that the fraction of real jet-triggers determining a possible random component in the correlations is not known.

3.2 Monte Carlo studies for three-particle correlations

The three-particle correlations are studied for the two different topologies of jet yields as depicted in Figure 3.2. While generating the signal, the different components (Jet-Jet, Hard-Soft, Soft-Soft, Trigger-Flow) are filled in separate histograms to compare them to the components extracted by the method introduced in section 2.2.1.
In Figure 3.6 signal- as well as the Hard-Soft component (combinations of jet-like and background associates) and the three-particle jet-like correlations are depicted. All components in this section are shown as normalized correlation functions (distributions divided by a mixed event distribution and normalized to the ratio of the integrals of the distributions). The Hard-Soft components are the same for the two-topologies due to the same averaged two-particle jet-yield. The three-particle jet yield however, shows a distinct difference in shape as well as in magnitude. The deflected jet topology shows two associates always being close to each other in the azimuthal angle but separated from $\Delta\phi = \pi$. This leads to two peaks on the diagonal of the correlation function. The cone-like structure also shows off-diagonal components since a broad range in the azimuthal angle and hence in $\Delta\phi$ is covered by the associates in each event. The

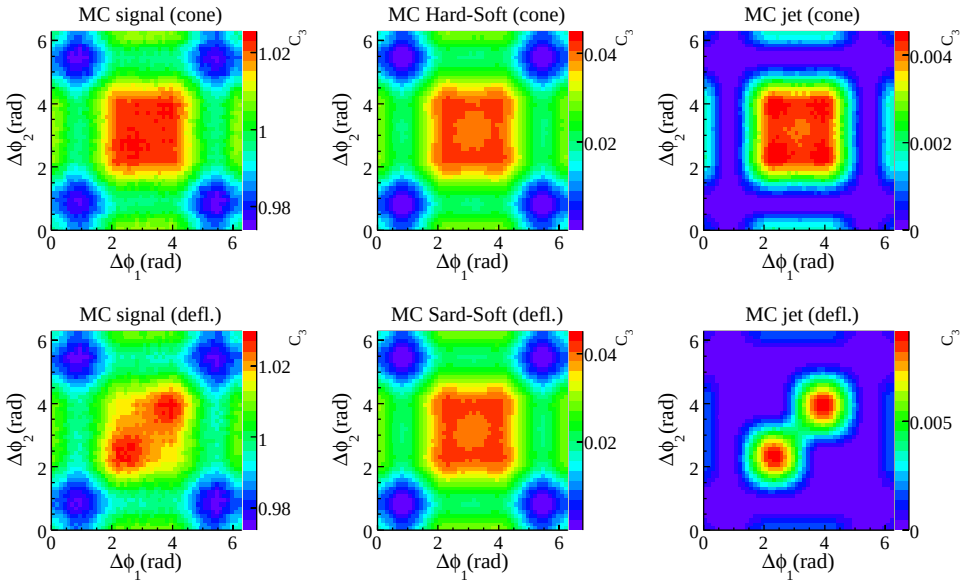

Figure 3.6: Three-particle signal (left), Hard-Soft (middle) and Jet-Jet correlations for the cone (top) and deflected (bottom) scenario.

maximum in the scenario with deflected jets is higher due to the more focused emission of particles than for the cone topology.

3.2.1 Background subtraction

In the generation of the Monte Carlo events each particle is assigned to a given source by a flag (jet, background). Generating the associate pairs they can directly be attributed to a given component of the Monte Carlo signal (Hard-Soft, Soft-Soft, etc). These components are shown in the left column of Figure 3.7. The feasibility of the background subtraction method as described in 2.2.1 is checked by comparing the Monte Carlo components to the components extracted by the background subtraction scheme (Figure 3.7, right column) In the following the different components (rows in Figure 3.7) are discussed:

- **a) : Three-particle correlation Signal**
  The signal distribution is created by combining all trigger-associated triplets in a generated event. The cone topology is used for this example. For the graphical representation the signal is shown in both columns.

- **b) : Hard-Soft background**
  The Hard-Soft background in the Monte Carlo signal matches perfectly the Hard-Soft component as determined by folding the two-particle yield with the flow-modulated background (Eq. (2.15)).

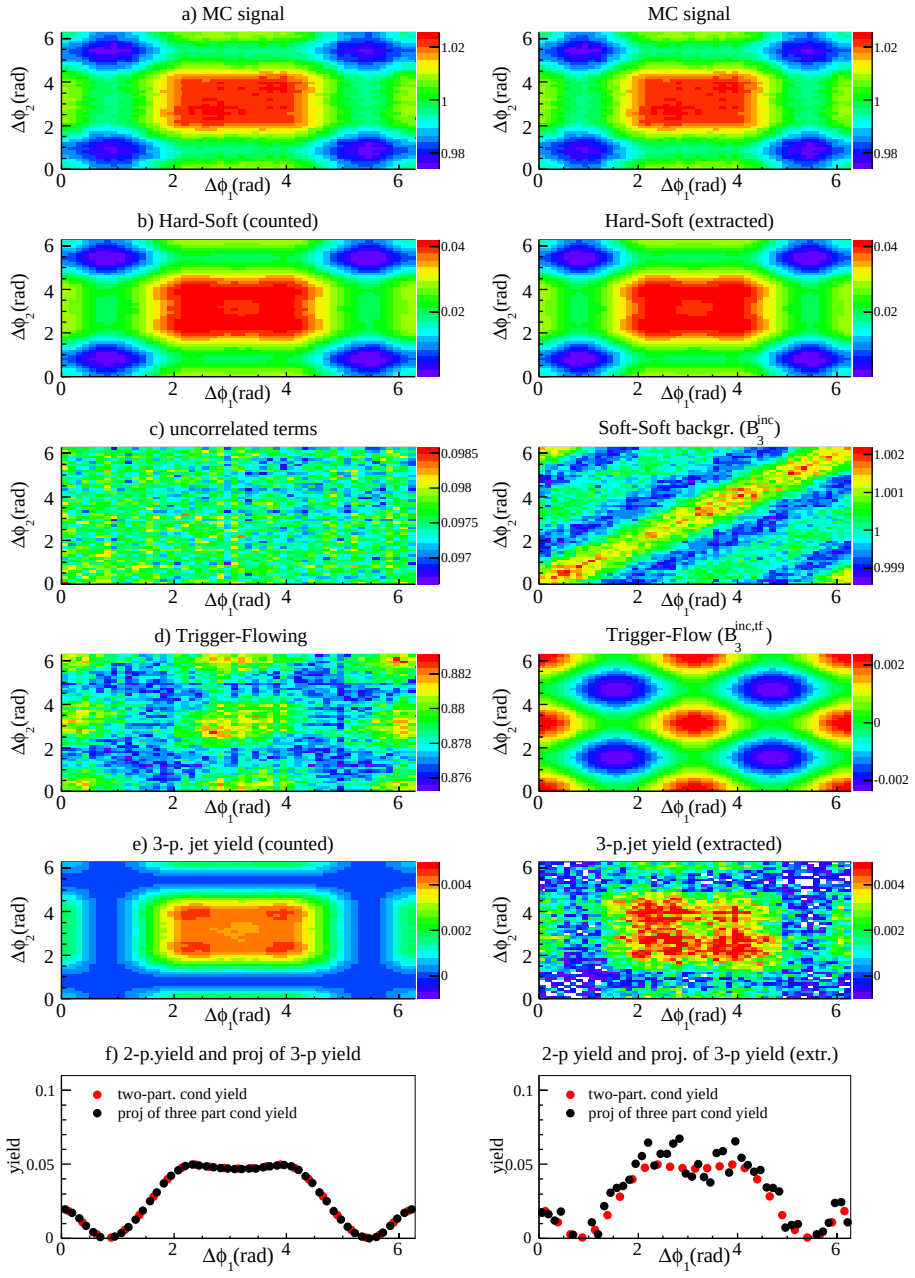

Figure 3.7: Different components of the three-particle Monte Carlo signal (left) compared to the background components as determined for the data analysis (see section 2.2.1 for details). The bottom four panels show a comparison of the three-particle jet-yield to the extracted jet-yield (e) and a comparison of the projection of the three-particle yield to the two-particle conditional yield used as an input (d) (see section 3.2.2 for details of this comparison).

- **c), d) : Soft-Soft background**

  The comparison of the Soft-Soft background is more involved. The way it is constructed it accounts for flowing triplets of trigger and associates and associates not being correlated to the trigger but among each other (additional jets in a jet event).

  The dominant contribution to the Monte Carlo signal is the trigger-flow contribution (d), left) since 90% of the triggers do not stem from jets.

  The flow modulation in the signal is recovered by adding the flow modulation among the associates incorporated in the inclusive mixed event sample B_3^{inc} (c),right) and the trigger-flow modulation $B_3^{inc,tf}$ (d),right). The two flow components add to the total flow correlation as depicted in row d (left). Here all flowing trigger-associate triplets in the MC events are shown. $B_3^{inc,tf}$ only reflects part of the total contribution from three-particle flow modulation.

  The uncorrelated term (c), left) corresponds to the flowing particles in jet events not being correlated to the trigger. This part is reflected by the inclusive sample as well. However, since this term is only visible in 10% of the events and the flow modulation is very small the modulation is covered by the statistical fluctuations.

  In addition to a part of the flow modulation the mixed-event term B_3^{inc} contains as well jet-like correlations among the associates from jet-events. In the mixed-event sample these are by definition not correlated to the trigger. However such correlations - which would arise from additional jets in a jet-event - are not contained in the Monte Carlo signal distribution. Only events containing at most one jet are generated.

  This shows a limitation of the Monte Carlo model or in other words that the background subtraction with the inclusive event method assumes a Poissonian distribution of the number of jets in the events.

- **e), f) : Extracted yield**

  The genuine three-particle jet-yield in the signal is shown in row e) (left). The right panel shows the jet-yield extracted after subtracting the Hard-Soft term from the signal and adjusting the Soft-Soft+Trigger-Flow background to the remaining signal by the ZYAM method.

  Albeit the limitations of the model discussed in the last item the yield can reasonably well be extracted with respect to magnitude as well as to the shape of the yield.
  Projecting the three-particle yield onto one axis the two-particle input conditional yield can be recovered (row f)). However, for the three-particle yield to exactly match the input, a scaling factor has to be applied which will be discussed in the next section.

3.2.2 Comparison of two- and three-particle conditional yield

In the model presented there is a simple relation between the two-particle conditional yield used as an input and the obtained three-particle conditional yield. Assuming that in the trigger sample the jet-trigger occurrence is given by a probability p_{jet} the observed yield per trigger is the actual yield per jet times the probability to find the jet trigger in the sample:

$$y_{trig} = y_{jet} \cdot \frac{n_{jet}}{n_{trig}} = y_{jet} \cdot p_{jet} \tag{3.3}$$

The same argument holds for the three-particle jet yield per jet trigger (prs_{jet}) which has to be scaled by the jet probability in order to obtain the actual pair yield per trigger (prs_{trig}):

$$prs_{trig} = prs_{jet} \cdot p_{jet} \tag{3.4}$$

Under the assumption of a Poissonian distribution of the jet particles in a jet event, the mean number of pairs is just the square of the mean number of associated tracks $< y_{jet}(y_{jet} - 1) >=< y_{jet} >^2$ and hence:

$$\begin{aligned} prs_{trig} &= y_{jet} \cdot y_{jet} \cdot p_{jet} \\ &= y_{jet} \cdot y_{trig}. \end{aligned} \tag{3.5}$$

The conditional two- as well as the three-particle yield (yield per trigger) are measurable quantities so that we can recover via Eq. (3.5) the actual yield of jet-associated particles in a jet-event. Alternatively we can rewrite Eq. (3.5) to:

$$\begin{aligned} prs_{trig} &= y_{jet} \cdot y_{jet} \cdot p_{jet} \\ &= \frac{y_{trig}}{p_{jet}} \frac{y_{trig}}{p_{jet}} \cdot p_{jet} \\ &= \frac{y_{trig}^2}{p_{jet}} \end{aligned} \tag{3.6}$$

and extract the jet probability p_{jet} in the trigger sample using the extracted yields. In the model presented, the jet-probability is $p_{jet} = 0.1$ so the actual yield per jet event is 10 times the integrated conditional yield used as an input:

$$y_{jet} = y_{trig}/p_{jet} = 0.17 \cdot 10 = 1.7 \tag{3.7}$$

According to Eq. (3.5), the ratio between the integrated pair yield and the singles yield per trigger corresponds to the yield per jet which is 1.7 in the example. The comparison of the two-particle conditional yield and the three-particle conditional yield is shown in Figure 3.8. For comparison the three-particle yield is projected onto the x-axis (left). Scaling the three-particle yield by 1/1.7 which is the inverse of the yield per jet $1/y_{jet}$ the three-particle distribution exactly matches the two-particle conditional yield (Figure 3.8, right).

This confirms Eq. (3.5) for the model studied. Summarizing this section, it should be possible (under the assumption of a Poissonian distribution of the

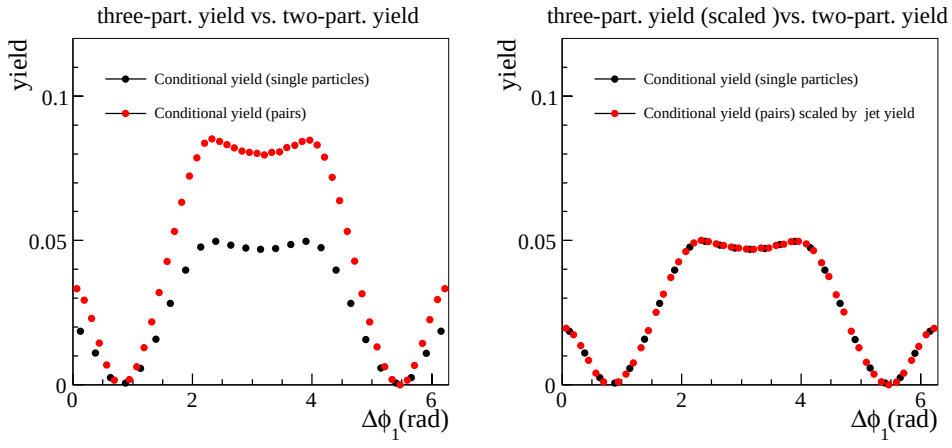

Figure 3.8: Comparison of the projection of the three particle conditional yield to the two-particle conditional yield without (left) and with scaling (right) to the calculated yield per jet according to Eq. (3.5).

jet particles) to infer from the results of the two- and three-particle analysis to the yield per jet-trigger in a jet-event or to the jet probability in the trigger sample.

3.2.3 Systematic uncertainties

The strength of the Hard-Soft background modulation is dominated by the two-particle jet-yield in case of the most central bin which is studied in this example. The modulation of the Hard-Soft background is of the order of a few percent while the flow modulation determined by $v_2^T \cdot v_2^A$ is less than a per mill. Since the jet-like yield is as well of the order of a few per mill, it is crucial to determine the two-particle jet-like yield with a precision of the order of a few percent. These limitations lead to large systematic uncertainties in case of the more peripheral bins. Here the systematic uncertainties in the extraction of the two-particle yield via ZYAM (see section 3.1) grow and the flow modulation is as well of the order of a few per mill and hence as big as the signal to be extracted.

3.2.4 Statistical uncertainties

To estimate the statistical uncertainties a rough calculation of the assumed signal-to-noise ratio for the three-particle correlations is performed for three different scenarios.
The assumed bin content of the three-particle jet-signal is compared to the estimated bin error in the signal distribution which is defined as the square root of the bin content.
It is assumed that the total number of associate particles N (jet+flow) is 15 as approximately in real data. For a fixed conditional yield y_{trig} the probability

p_{jet} for the trigger to be an actual jet-trigger is varied. The smaller the jet-probability the higher the actual yield per jet-trigger y_{jet} is. According to Eq. 3.6 the measured three-particle yield is inversely proportional to the jet-probability keeping the measured conditional yield fixed.

Table 3.2: Signal-to-noise ratio for three-particle correlations for three different scenarios.

quantity \ scenario	1. High statistics: $p_{jet} = 0.1$.	2. Statistics as in data: $p_{jet} = 0.1$.	3. Statistics as in data: $p_{jet} = 1.0$.
N_{trig}	$3 \cdot 10^7$	$2.5 \cdot 10^6$	$2.5 \cdot 10^6$
N	15	15	15
y_{trig}	0.17	0.17	0.17
p_{jet}	0.1	0.1	1.0
y_{jet}	1.7	1.7	0.17
Signal triplets (S) $N_{trig} \cdot N(N-1)$	$6.3 \cdot 10^9$	$5.2 \cdot 10^8$	$5.2 \cdot 10^8$
Jet triplets (J) $N_{trig} \cdot y_{jet}^2 \cdot p_{jet}$	$8.7 \cdot 10^6$	$0.7 \cdot 10^6$	$0.07 \cdot 10^6$
Bins in 2d histo	400	400	400
Bin content (S)	$15.8 \cdot 10^6$	$1.3 \cdot 10^6$	$1.3 \cdot 10^6$
Bin error (S) (1σ) ($\sqrt{\text{Bin content(S)}}$)	3968,6	1145.6	1145.6
Bin content (J)	21675	1806.2	180.6
Signal-to-noise ratio Bin c.(J)/Bin e.(S)	5.46	1.58	0.16

The first scenario in table 3.2 corresponds to a sample of 30 million triggers with a probability for triggers coming from a jet of p_{jet}=0.1 . This corresponds to the sample the decomposition of the signal in the previous section is based on. Assuming a two dimensional histogram with 20 bins on each axis, the bin error in the signal is approximately 4000, whereas the jet contribution in the signal is of the order of 20000. Hence the jet signal-to-noise ratio is 5 and the jet-signal is measurable to good accuracy.

Reducing the number of triggers N_{trig} to the actual number of measured triggers ($2.5 \cdot 10^6$, scenario 2) while keeping the other parameters constant, the signal-to-noise ratio shrinks to 1.5 still allowing for the measurement of the three-particle jet-signal.

If, however, we assume that each of the triggers stems from a jet ($N_{trig} = 2.5 \cdot 10^6$, $p_{jet} = 1.0$, scenario 3) the signal-to-noise ratio is reduced again by a factor of 10 which makes it impossible to distinguish the jet-signal from the statistical fluctuations in the overall signal distribution.

These very basic considerations do not take into account the actual modulation of the conditional yield. As depicted in Figure 3.2, in the scenario with the deflected jets the maximum of the yield is event-by-event twice as high as in the cone-case, however only in each second event at the same position. This leads to a maximum of the three-particle signal in the deflected case being again twice as high ($\frac{2 \cdot 2}{2}$) as in the case of cone-like emission.

In summary, the measurability of the three-particle jet-signal given the two-particle conditional yield and the number of triggers in the sample depends on the actual contribution of jet-triggers in the trigger sample, and the event-by-event shape of the jet-like correlations.

4 The CERES experiment

In this section the CERES experiment is described. After an overview of the detector setup the different detector components are discussed. The main focus is put on the TPC [50] which is the device the data analyzed in this thesis are recorded with. Working principle, the main components, and the data reconstruction scheme are presented.

4.1 Experimental setup

The CERES (Cherenkov Ring Electron Spectrometer) experiment (Figure 4.1) is originally designed to measure low mass e^+-e^- pairs to study medium effects on meson production in Pb-Au collisions at 158A GeV beam energy. As a main result a strong enhancement of intermediate mass electron pairs is observed when compared to a p-p reference. This can be understood to arise from an

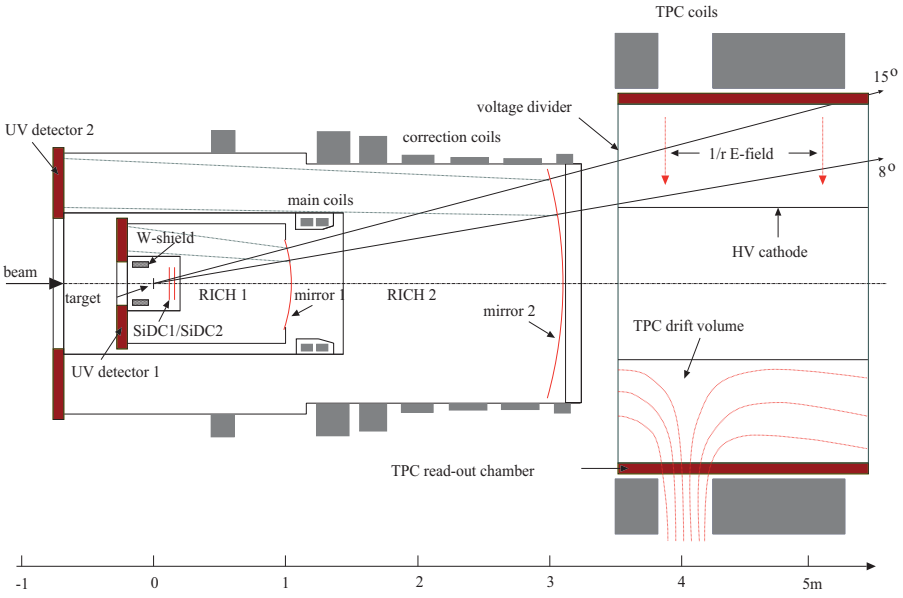

Figure 4.1: Schematic overview of the upgraded CERES experiment. Indicated are the two large Ring Imaging Cherenkov counters (RICH) with mirrors and UV detectors, the target area with the two Silicon Drift Detectors (SDD1/2) and the Time Projection Chamber TPC with field lines for the electric and the magnetic field.

in-medium shift of the ρ-meson mass [51] in the heavy ion collisions.

For the study of electron pairs CERES is equipped with two large Ring Imaging Cherenkov Counters (RICH) which allow to discriminate between electrons and heavier charged particles. The Cherenkov radiation is reflected by two mirrors and read out by UV-gas detectors which are located upstream of the target and thus are not exposed to the large flux of charged particles. This design limits the acceptance of the RICH detectors to $2.1 < \eta < 2.7$.

The momentum of the particles can be reconstructed via the deflection of the tracks due to a momentum kick provided by two super conducting magnets located after the mirror of the first RICH. A set of correction coils allows it to keep the radiator of the first RICH field free and the field lines in the second radiator aligned with the particle trajectories in order not to distort the emission pattern of the Cherenkov light.

In 1998 the CERES spectrometer is upgraded with a Time Projection Chamber (TPC) to increase the mass resolution in order to be able to resolve e.g. ρ/ω mass peaks in the invariant e^+e^- spectrum. The usage of a TPC also extends the capability of the experiment to measure hadronic observables.

4.2 Target area and trigger scheme

To keep the radiation length for electrons and photons small while allowing for a large interaction length for the Pb nuclei in the target, a segmented Au target is used. For the Pb-Au run in the year 2000, a telescope of 13 Au discs of 25 μm thickness and 600 μm diameter is chosen with an equal spacing of 1.98 mm between the discs. This setup prevents the particles produced in the collisions to pass further discs before reaching the detector acceptance of θ= 8-15°.

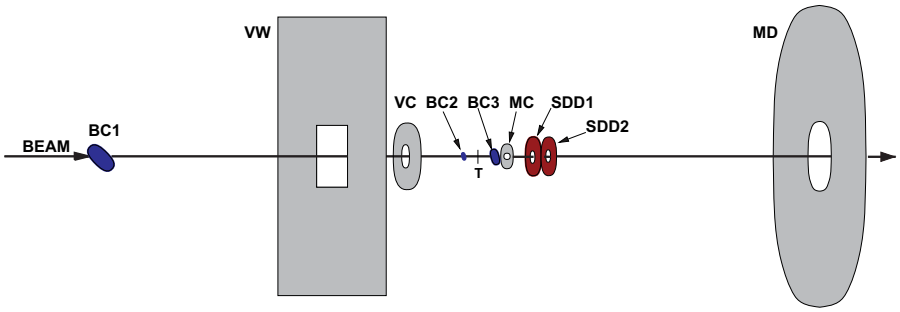

Figure 4.2: Trigger system with Silicon Drift Detectors (the positions of the detectors relative to the target are given in brackets): Cherenkov Beam Counters (BC, BC1: ≈ -60 m , BC2: ≈ -40 m, and BC3: +69 mm), Plastic scintillators Veto Counter (VC: -2.62 m) and Veto Wall (VW: -4.13 m), Multiplicity Counter (MC: +79 mm) and Multiplicity Detector (MD, ≈ 10 m)

.

To start the readout process a trigger signal T_0 is needed which is provided by

a set of Cherenkov type Beam Counters (BC) and a scintillator Multiplicity Counter (MC). To define an interaction the beam counters BC1 and BC2 positioned upstream of the target have to register a beam particle. An interaction is defined by a veto of BC3 which is placed after the target:

$$T_{\text{minimum bias}} = BC1 \times BC2 \times \overline{BC3}$$

In this case no further restriction on the centrality of the collision is made (minimum bias).
The relation between the number of charged particles (multiplicity) produced in a collision and the impact parameter (distance between the centers of beam- and target particle) can be used to trigger on the centrality of the collisions. For this, the MC signal which is proportional to the charged multiplicity is combined with the minimum bias trigger condition:

$$T_{\text{central}} = T_{\text{minimum bias}} \times MC$$

A set of veto counters is used to discard interactions happening before the target.

4.3 The Silicon Drift Detectors

The vertex of the interaction can be precisely determined by a set of two Silicon Drift Detectors [52] (SDD, Figure 4.3) located 10 and 14 cm downstream of the target. The drift field of the detector is created by a voltage divider connected

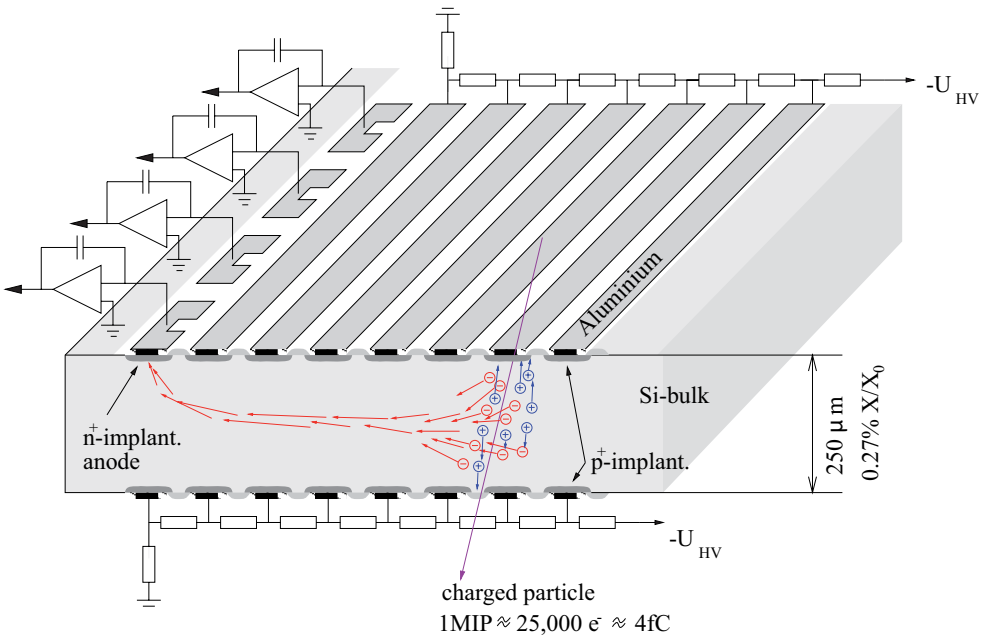

Figure 4.3: Sketch of a Silicon Drift Detector. Electrons released by a charged particle passing the silicon wafer drift towards the segmented anode on the outer radius of the detector.

to radial field rings implanted on a silicon waver. Charged particles traversing the silicon waver create free electrons which drift radially outwards to the edges of the detector which is segmented into 360 anodes.
The radial position can be reconstructed from the drift time information. The detector covers the full range in azimuth and with an inner and outer radius of 4.5 mm and 42 mm respectively a range in pseudo rapidity of $1.6 < \eta < 3.4$.

4.4 The RICH detectors

The main device for electron identification are the two Ring Imaging Cherenkov Counters [53] (RICH). The operating principle is based on the emission of light of charged particles traversing a medium at a speed higher than the speed of light in that medium. The threshold velocity for the emission of light is given by:

$$\beta_{th} = \frac{v_{th}}{c} \geq \frac{1}{n}\,,\ \gamma_{th} = \frac{1}{\sqrt{1-\beta_{th}^2}} \tag{4.1}$$

The Cherenkov light is emitted under the angle Θ_C relative to the trajectory of the particle.

$$\Theta_C = \arccos(\frac{1}{n\beta}) \tag{4.2}$$

The angle can be determined by the radius of the ring projected onto the UV gas-detectors by the Cherenkov light. The gas mixture of 94% helium and 6% methane in the RICH is chosen to obtain a very high γ threshold ($\gamma_{th} > 32$). Only very energetic hadrons (e.g pions) with a momentum higher than 4.5 GeV/c produce Cherenkov light at all. The RICH detectors are therefore practically hadron blind.

4.5 The Time Projection Chamber

The working principle of a TPC is based on the detection of electrons released by a charged particle traversing a gas. These electrons drift in an electric drift-field to a readout plane where the signals are amplified in the high electric field between a cathode and an anode wire plane. The electrons created in an avalanche between the wire planes are collected on the anode wires and the positive ions induce a signal on a segmented pad read out plane close to the wire planes. This allows for the a two dimensional reconstruction of the projection of the trajectory of the particle. The third coordinate of the track is obtained by the known profile of the drift velocity of the electrons in the gas and the time between the collision of the nuclei and the detection of the signal on the pad plane.

The TPC can be operated such that the amplification in the avalanche between cathode and anode wires is proportional to the charge initiating the avalanche. The differential energy loss of particles traversing the gas (dE/dx) can then be reconstructed by measuring the integrated induced charge on the pad planes along the particle trajectories. This characteristic energy loss can be used to

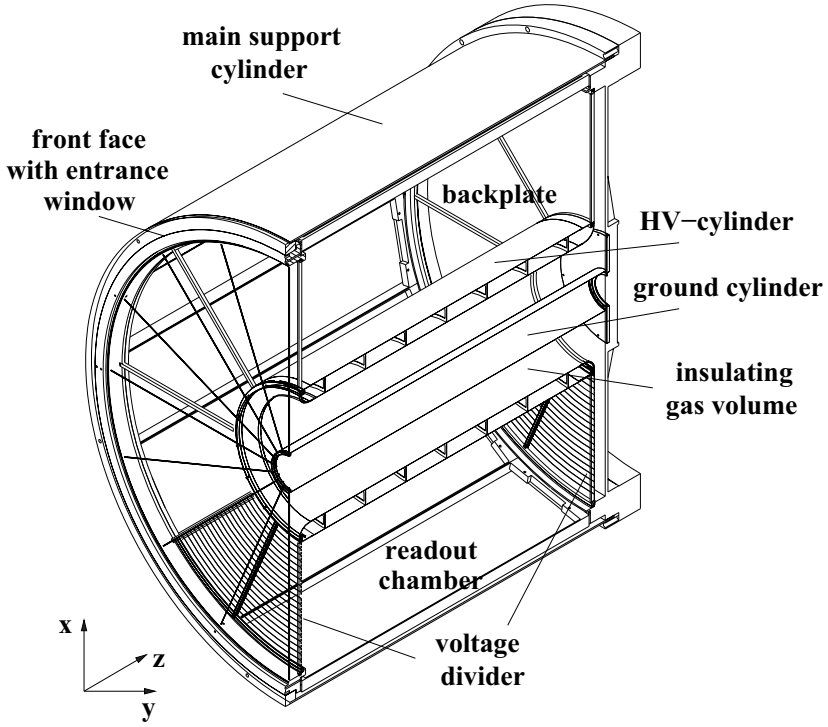

Figure 4.4: The CERES TPC.

determine the velocity of the particles in the gas. Applying a magnetic field the momenta of the particles can be measured by the curvature of the tracks in the field. Combining the measurements of momentum and differential energy loss the mass and thus the type of the particles can be identified.

The design of the CERES TPC (Figure 4.4) is constrained by the requirement of full coverage in azimuth and a similar coverage in η as the RICH detectors. To meet these requirements a cylindrical TPC with radial drift field is chosen. The read out is segmented into a polygon of 16 readout partitions which are mounted on the outer cylinder of the TPC. The wire planes run perpendicular to the beam axis. The pad plane is segmented into 20 pad planes in z direction allowing the measurement of 20 space points per track and 48 pads running in azimuthal direction. The full azimuth is covered by a total of 48*16=768 read out pads. In total the TPC has 15360 readout channels which are read out in 256 time bins per event. The radial electric field is provided by the central electrode with a potential of -30 kV and the cathode wire plane on ground potential. The 1/r dependence of the electric field results in a drift velocity between 2.4 and 0.7 cm/μs.

The magnetic field is provided by two magnet coils with current running in opposite directions. The resulting magnetic field is depicted in Figure 4.1 and increases from 0.18 Tm at θ=8° to 0.38 Tm at θ=15°. The resulting deflection is mainly in azimuthal angle and affects both the trajectories of the tracks as

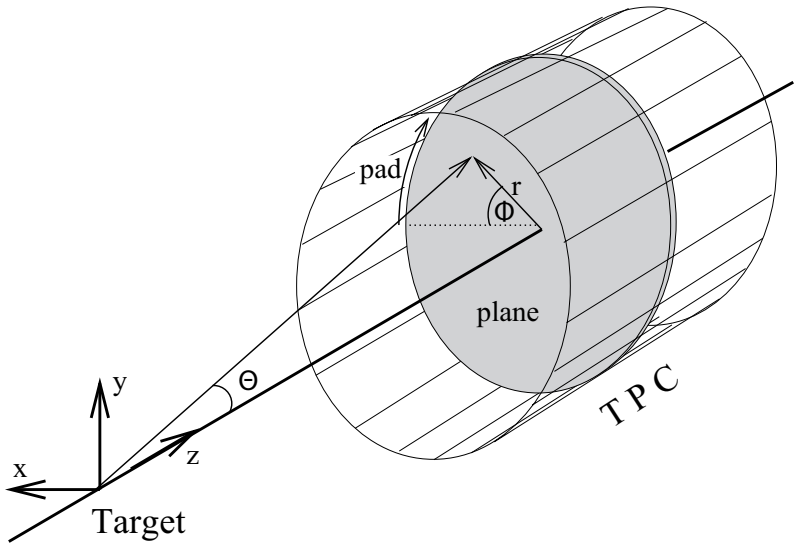

Figure 4.5: The CERES TPC coordinate system (picture taken from [54]).

well as the electrons drifting towards the read out plane. The projections of the trajectories on the readout planes have to be corrected for this effect.

The coordinate system of the TPC (Figure 4.5) is aligned with the z-axis running in beam direction and its origin located in the center of the first disc of the Au target. The x-axis runs horizontally between the boundary of sector 15 and 0. The y-axis forms a right handed coordinate system with the z- and x-axis.

4.6 Data reconstruction

4.6.1 Hit finding

The first step in the reconstruction of TPC tracks is the search for local maxima of the signal induced on the pads for each time-bin and each pad row [55]. For each time bin the maximum in clusters of non-zero ADC values are searched in the pad (azimuthal) direction. In the same way for each pad the time-bins are searched for maxima. Those maxima are denoted as local. Pixels (pad-time combination) corresponding to local maxima in pad- as well as in time direction are denoted as absolute maxima in the TPC.

With this information hits are defined as an area of 5 timebins and three pads around an absolute maximum. The position of a hit is defined by the center of gravity of the pixels in the area. The time $\overline{t}$ and pad $\overline{p}$ coordinate of a hit is defined as:

$$\overline{t} = \frac{\sum_i A_i \cdot \frac{A_{max}}{f_i} \cdot t_i}{\sum_i A_i}, \overline{p} = \frac{\sum_i A_i \cdot \frac{A_{max}}{f_i} \cdot p_i}{\sum_i A_i}, \tag{4.3}$$

Pixels belonging to several hits are flagged with a weight f_i which increases with the number of hits the pixel belongs to (Figure 4.6). The ADC value A_i

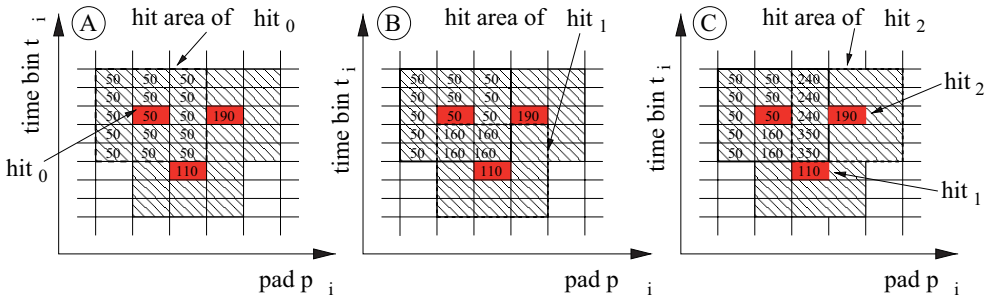

Figure 4.6: Hit areas of three overlapping hits in the time-pad plane. The numbers in squares correspond to the ADC value of the pixels.

for the given pixel is divided by this weight in order to reduce the contribution from overlapping hits to the mean values.

4.6.2 Track finding

The track finding starts with the combination of hits in the middle of the TPC between planes 5 and 15 where the track density is lowest [56]. For a given hit neighboring hits in two up-and downstream pad-planes are searched. With this track segment of up to 5 hits, the curvature in the azimuthal angle ϕ is determined and linearly extrapolated to determine further hits belonging to the track. If no further hits are found the tracks are fitted with a second order polynomial in order to find further missing hits.
Details about the corrections applied during the extrapolation steps can be found in [56].

4.6.3 Track fitting and momentum resolution

Due to the inhomogeneity of the magnetic field and the $E \times B$ effects on the drifting electrons it is not possible to analytically describe the trajectories of the tracks projected onto the pad planes. In order to reconstruct the tracks, reference tables for tracks generated by a detector simulation using the GEANT [57] package are used. Tracks are generated for 32 different angles in ϕ covering the full azimuthal range, 18 different η angles in the range $2.05 < \eta < 2.95$ and 8 different values of momentum in the range $-2 < q/p < 2.0$ $(\mathrm{GeV/c})^{-1}$ where q corresponds to the charge of the generated particles.

Due to the topology of the magnetic field the deflection of the tracks happens to first order only in the azimuthal angle. A two parameter fit is performed to fit the tracks under the constraint that the particles originate from the vertex.

The momenta of the particles are then determined by comparing the deflection in the azimuthal angle ϕ to the deflection of simulated tracks.
For small momenta multiple scatterings and deflections of the particles, especially in the Mirror of RICH2 with an interaction length of 4.7%, play an increasing role. For those tracks a three parameter fit can be performed allowing for an inclination of the tracks at the beginning of the TPC.

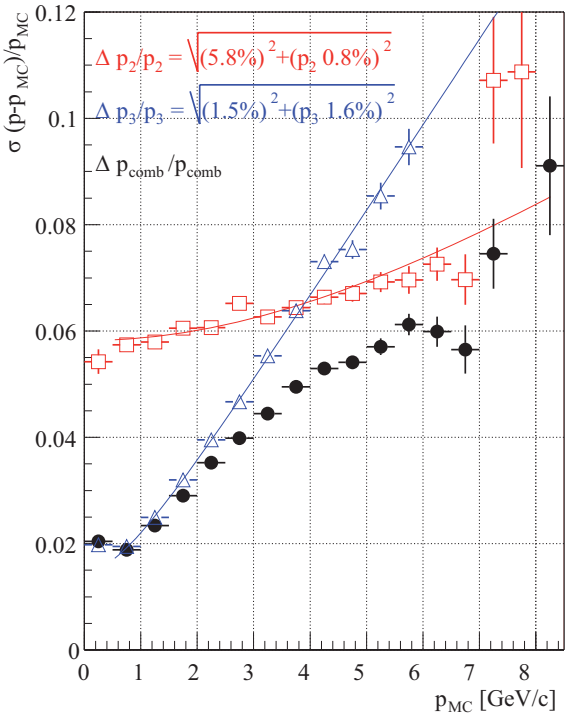

Figure 4.7: Momentum resolution as obtained from Monte Carlo studies for the two-parameter fit including a vertex constraint (triangles) and three parameter fit (squares). The resolution in the combined fit comprising the advantage of both fit methods is shown in full circles.

The momentum resolution as function of momentum is shown in Figure 4.7 for the two- and the three parameter fits, respectively. To combine the advantages from the two- and three- parameter fits a combined momentum is defined as:

$$p_{comb} = \left(\frac{p_2}{\sigma_2^2} + \frac{p_3}{\sigma_3^2}\right) / \left(\frac{1}{\sigma_2^2} + \frac{1}{\sigma_3^2}\right). \tag{4.4}$$

The relative resolution of the such defined momentum is parametrized as function of the momentum and given by:

$$\frac{\Delta p_{comb}}{p_{comb}} = \sqrt{(1\% \cdot p_{comb})^2 + (2\%)^2}. \tag{4.5}$$

5 Data selection

The data are taken from the run period in 2000 which is dominated by events taken with a trigger on high centrality of the collision at $158A$ GeV beam energy. The centrality of the collisions is determined by the correlation between the measured multiplicity in the different detectors and the centrality itself. A detailed study of the calibration procedure and the translation of the measured multiplicities in a fraction of the total geometrical cross section σ_{geom} in a nuclear overlap model can be found in [58][59][60].

5.1 Event selection

The main goal of the event selection is to discard events where tracks from more than one collision enter the sensitive volume of the TPC during the readout cycle (pile up), and the determination of a well defined centrality of the collision.
To remove events with potential pile up of collisions, the information from the beam counters (BC1/BC2) is used and cut to relatively low ADC values for a given event. In addition, a cut on the correlation between the multiplicity in the TPC and the ADC value of the multiplicity counter is applied.
Increased multiplicities in the TPC relative to the multiplicity registrated in the MC or SDD counters can be due to the slowly read out TPC seeing more than one event, however the fast multiplicity counter only registering the first collision of several overlapping events and assigning it to an event. In order to have a well defined centrality of the collision, a cut on the difference of the centrality determined from the Silicon Drift Detector multiplicity and the TPC multiplicity is applied. The set of cuts on the events is given by:

$$\begin{gathered} 0 < \sqrt{BC1^2 + BC2^2} < 6, \\ 0 < |centr_{SD} - centr_{TPC}| < 8, \\ \text{elliptic cut on } mult_{TPC} - mult_{MC}. \end{gathered}$$

Figures showing the different distributions and the impact of the applied cuts on the distributions are given in Appendix A. The event sample which passes the event cuts is divided into three classes of centralities to study the impact of the path length dependence of the high-p_t tracks passing the medium. The centrality is defined as the mean value of the calibrated centralities measured in the TPC and the SDD and is given by:

$$centr = (centr_{TPC} + centr_{SD})/2.$$

The centrality is given in per cent of the total geometric cross section σ/σ_{geom}. The number of binary collisions N_{coll} and the number of participants N_{part} of the Pb-Au collisions are shown in Table 5.1. The quantities are calculated in a

nuclear overlap model using an inelastic nucleon-nucleon coss section of σ_{NN}= 30 mb [60].

Table 5.1: Centrality bins of the data sample .

$\sigma/\sigma_{geom}(\%)$	N_{part}	N_{coll}
$00.0 - 05.0$	346.8	817.2
$05.0 - 10.0$	286.9	654.9
$10.0 - 20.0$	218.1	471.1

The distribution of the centrality for the entire event sample after the event cuts were applied, together with the intervals for the centrality bins is shown in Figure 5.1.

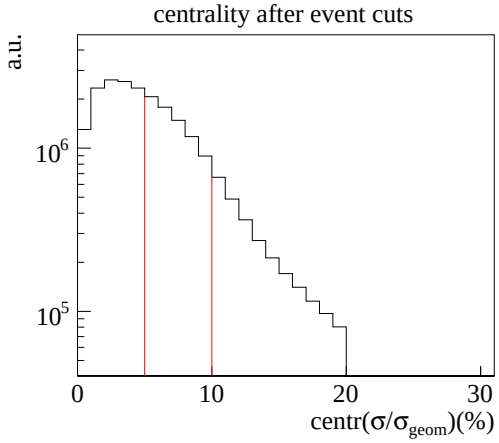

Figure 5.1: Distribution of event centrality after event cuts. The borders of the centrality bins are indicated by the red lines.

5.2 Track selection

A set of standard cuts is applied in order to obtain a data sample of tracks with well defined momenta. The number of fitted hits (nfittedhits) on a track is required to be higher than 12 hits (out of 20). This cut also removes possible contributions from split tracks which can occur if the number of hits on a track is less than half of the possible hits.
Such a contribution could artificially enhance the occurrence of tracks with small $\Delta\phi$ and hence increase the associate yield on the near-side. The standard binning for the analysis is using a trigger particle in the range of $p_t = (2.5 - 4.0)$GeV/c and associates from the range $p_t = (1.0 - 2.5)$ GeV/c. These ranges will be varied in a p_t-scan however in most cases the two particles being combined will stem from different p_t regions with at least one high-p_t particle. The split tracks discussed above will already be reduced due to the difference

in p_t of the two particles, since split track segments will in general have as well similar momenta. The $chi2$ of the fit in the radius R and ϕ has to lie within reasonable limits. No particle identification is applied in the analysis since the discrimination power of the $dEdx$ measurement does not show a sufficient resolution over the full p_t-range investigated.
The track sample is subdivided into positive and negative particles defined by the curvature of the track in the magnetic field. The identification as positive and negative tracks is done via a sign of the momentum of the particles where positive momentum corresponds to positive particles and negative sign to negative particles respectively.
In order to reduce the contamination from secondaries created in the detector material a range of tracks lying well within the acceptance of the TPC is chosen by a cut on the θ angle of the tracks. The set of track cuts is given by:

$$\begin{gathered} 0.14 < \theta(rad) < 0.24 \\ 12 < nfittedhits < 8 \\ 0.0 < chi2R < 3.0 \\ 0.0 < chi2Phi < 4.0 \end{gathered}$$

The distribution of the θ and the ϕ angle of the accepted tracks in the standard associated and trigger range is given in Figure 5.2.

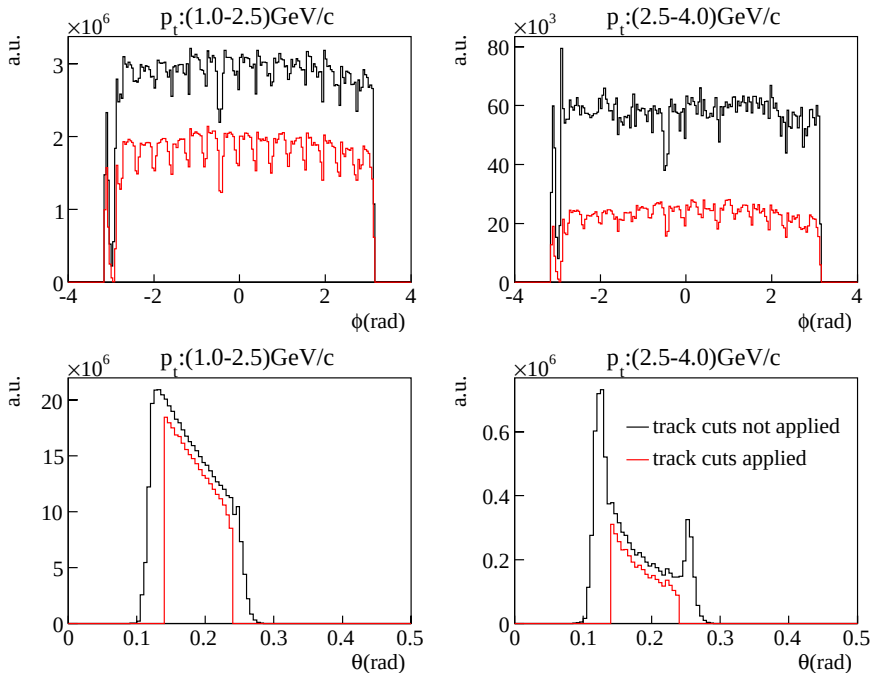

Figure 5.2: Distribution of ϕ and θ before (black) and after (red) event cuts are applied.

The strong decrease in the efficiency in the range $\phi \approx 3.3$ is due to a row of not powered Front End Electronic boards. Close to the edge of this acceptance

hole an increased number of high p_t particles is observed in the trigger region. This increase is only observed in a narrow range in $\theta = 0.14 - 0.16$ and cut out by an additional isolation cut (region cut out is given):

$$0.14 < \theta(rad) < 0.16 \qquad \&\& \qquad 3.35 < \phi(rad) < 2.42$$

Non-vertex tracks can be isolated by a matching criterion between the TPC and the Silicon Drift Detector information of a track. The tracks stored in the data structures are global tracks corresponding to the closest matches of segments from different detectors. The matching criterion for the TPC and SDD segments is the difference in the angles in θ and ϕ of the two segments. In order to estimate the quality of the matching of two tracks the distribution of the difference in the angles is accumulated. The width in θ and ϕ ($\sigma_\theta, \sigma_\phi$) are determined and parametrized.
To obtain a single quality criterion the differences in the measured angles are normalized to the width σ of the distributions and added in quadrature to:

$$\sigma_{SD} = \frac{1}{\sqrt{2}} \sqrt{\left(\frac{\Delta\theta}{\sigma_\theta}\right)^2 + \left(\frac{\Delta\phi}{\sigma_\phi}\right)^2} \tag{5.1}$$

Details of the calibration procedures for the differences in the angles between the segments can be found in [58]. The distribution for the relative differences in the angles normalized to the width according to Eqn. 5.1 is shown in Figure 5.3 for both charges of the particles combined.

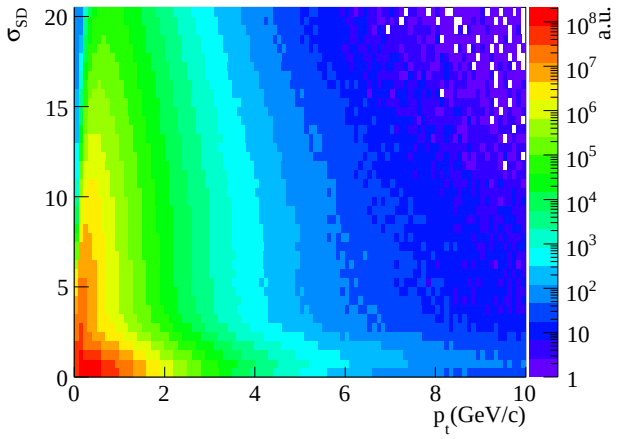

Figure 5.3: Distribution of the normalized difference in the angles of TPC and Silicon track segments versus p_t after track cuts were applied.

A standard cut value for the matching of TPC to SDD track segments is σ_{SD}=2.5. This cut however loses significance at high p_t because the relative contribution of the tracks with high (e.g.> 2.5) and low values of σ_{SD} decreases as can be seen in Figure 5.3. This supports the assumption that the contribution from secondaries is reduced at high p_t.

The matching procedure is assigned with an error due to the random assignment of track segments which actually do not belong to the same physical track. This random component can be reconstructed by combining track segments from the TPC and the SDD from different events. In a feasibility study it is shown that the signal over background ratio does not significantly increase after having applied the cut on the matching at high p_t. This indicates that the discrimination power of the cuts gets worse at high p_t.
An additional complication arises due to the limited efficiency of the Silicon Detector which has to be taken into account applying the matching procedure. For these reasons this cut was not applied for the analysis of the azimuthal correlations.

Additional Figures showing relations between the cut variables used for track selection and the impact of the applied cuts on the distributions are shown in Appendix A.

6 Two-track efficiency

The limited two-track efficiency of the TPC leads to a loss of pairs with small relative distance in the TPC and hence influences the correlation function at small $\Delta\phi$. The resolution of the TPC [61] can be studied via normalized correlation functions $C_2 = N \cdot (Sig/Mix)$ of the opening angle ω or the difference in the polar angle $\Delta\theta$. One approach to account for the inefficiencies is to apply a cut on the inefficiency region in the signal as well as in the mixed-event distribution of the triggered correlations. This however, also implies cutting in the physical signal and might alter the results. An alternative approach is to correct the measured correlation function by the efficiency as determined via simulations not applying a cut to the data sample. Both approaches are discussed in the following chapter.
Throughout this chapter the quality cuts applied to the TPC-tracks for real data as for the Monte Carlo tracks studied are as follows:

$$0.14<\theta<=0.24 \text{ , } 12<\text{nfittedhits}<=20$$

6.1 Efficiency measurement

A detailed study of the efficiency depending on the transverse momentum and the charge of the particles in triggered events is performed. The efficiency is studied via the difference of the polar angle $\Delta\theta$ and the difference in the opening angle $\Delta\omega$ of the two tracks which is defined as $\Delta\omega=\vec{p_1} \cdot \vec{p_2}/p_1 \cdot p_2$
In Figure 6.1, the efficiency as a function of the transverse momentum p_t of the particles is shown for different charge combinations of the particles in triggered events. In the left plots the histograms are filled at the smaller p_t-value of both tracks of a pair. The right panels show the projections of the two dimensional correlation function starting from different p_t values. For small p_t and small opening angles the efficiency loss is overlaid by an enhancement of pairs from conversions or decays in the signal. The effect is more pronounced for unlike-sign combinations of particles. Applying a cut of ω=0.015 restricts the losses due to the limited efficiency to less than 1% independent of p_t and the charge combination of the particles.
Having determined a cut value from the efficiency study the triggered correlation function as the actual observable of interest is studied varying the cut values. This is shown in Figure 6.2, where triggered correlation functions with a successive increase of the cut values in $\Delta\theta$ (left) and ω (right) are shown. Applying a cut on $\Delta\theta$ cuts out a torus in the acceptance over the full range in $\Delta\phi$ whereas the opening angle cut only affects the near-side of the correlation function. For particles in the acceptance of the TPC at $\theta \approx$0.18 the opening angle of 0.02 corresponds to a maximum $\Delta\phi$ of 0.1 thus only affecting the first

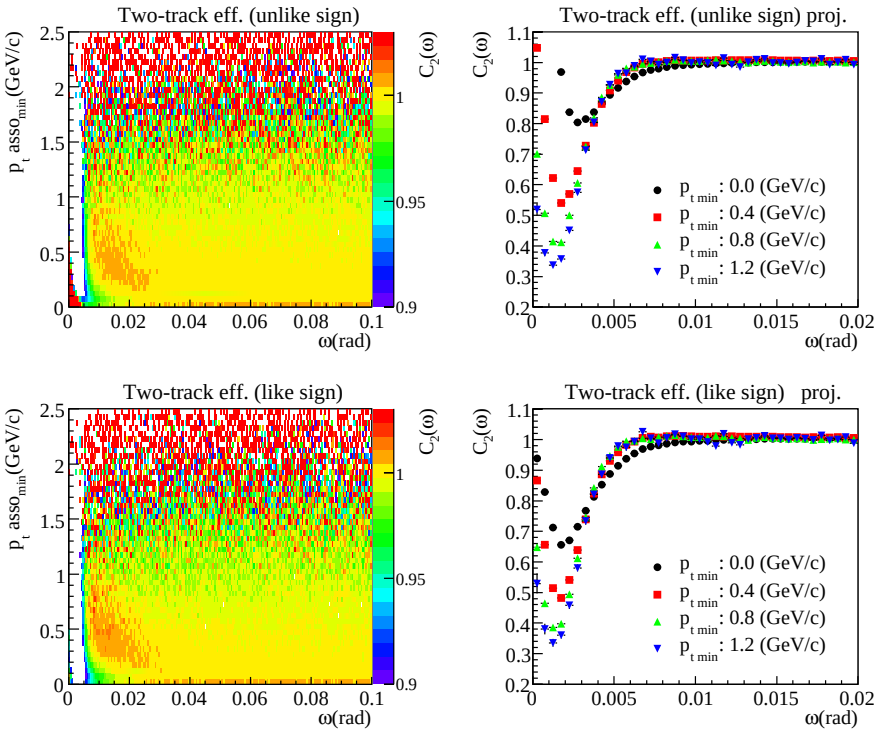

Figure 6.1: Two-track efficiency as function of the opening angle ω and the minimal transverse momentum p_t of the two particles for unlike- (top) and like-sign (bottom) charge combinations.

bin in Figure 6.2. The impact of a variation of both cuts in the $\Delta\phi$-$\Delta\theta$ plane is depicted in Figure 6.3.

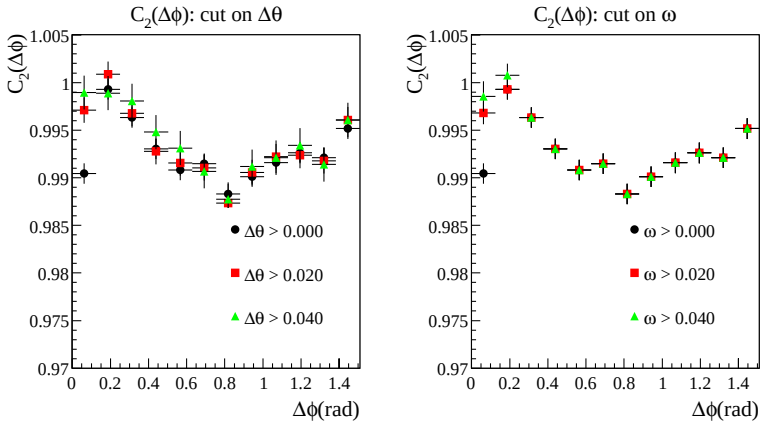

Figure 6.2: Correlation function for trigger-associate pairs (2.5< p_t(T)(GeV/c) <4.0, 1.0< p_t(A)(GeV/c) <2.5) for all charge combinations. Successive cuts on ω and $\Delta\theta$ are shown.

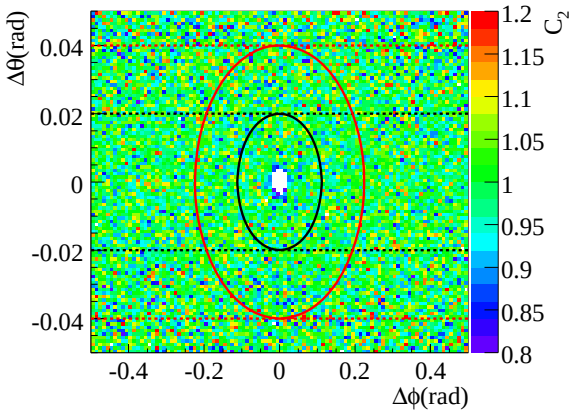

Figure 6.3: 2d-correlation function of trigger-associate pairs without two-track efficiency cut. Indicated by the lines are the regions cut out by applying a cut on the opening angle ω (solid) and $\Delta\theta$ (dashed) of 0.02 (black) and 0.04 (red) respectively.

Assuming a positive correlation of trigger and associates and excluding efficiency losses the maximum is supposed to be located at $\Delta\phi$=0. However, even applying a cut on 20 mrad which is far off the inefficiency region in both cut variables shows the first bin being significantly below the second one. Having a closer look at the correlation function in Figure 6.4 with an already applied cut in $\Delta\theta$ shows that the maximum value of the correlation function is located around $\Delta\phi$=0.15. Cutting out small fractions in $\Delta\phi$ and rebinning the histograms shows an increase of the correlation function towards this maximum.

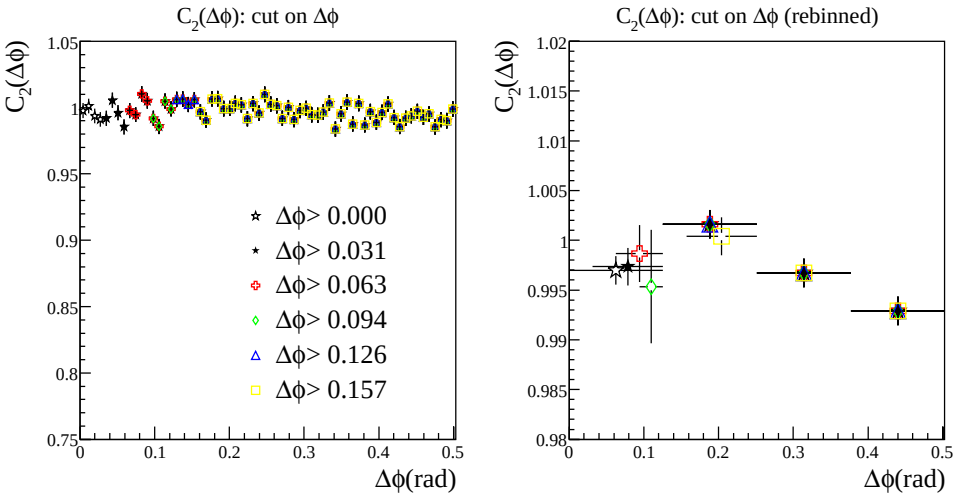

Figure 6.4: Triggered correlation function with successive cut on $\Delta\phi$ for fine- (left) and coarse binning (right).

To avoid cutting on the two-particle observable however still accounting for the inefficiency of the detector a detailed Monte Carlo study of the two-track efficiency is performed.

6.2 Efficiency simulation

To study the two-track efficiency of the detector $2 \cdot 10^6$ events are generated and processed through the reconstruction chain of the experiment.
For each event, $3\pi^+$ and $3\pi^-$ particles are generated with a flat distribution in rapidity $2.0<y<2.8$, processed through the detector by GEANT and embedded in raw Pb-Au events as obtained from the running experiment.
To cover a large area of the transverse momentum the event sample is subdivided in 10 classes with particles of fixed p_t ranging from 0.2-9.2 GeV/c in steps of 1 GeV/c.
To further increase the number of close pairs in the detector the particles are generated in a fixed window of $\Delta\phi$=0.1 in each event. This window is moved in order to equally cover the whole ϕ acceptance of the TPC.

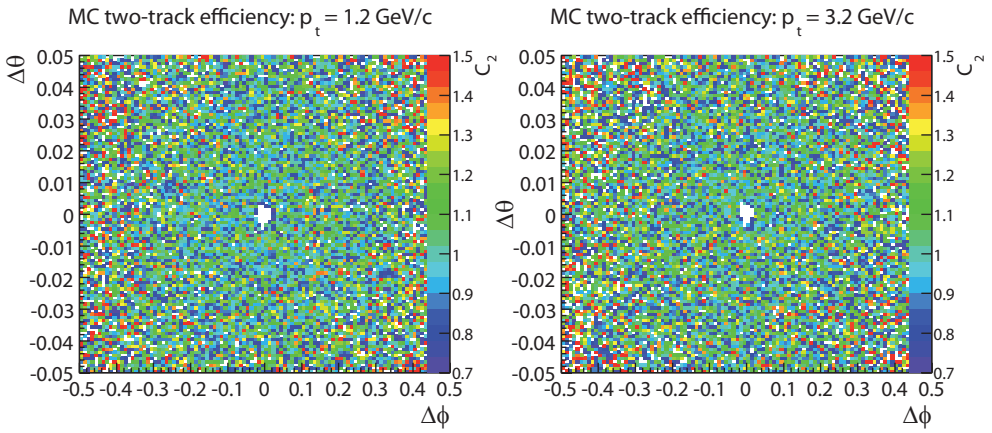

Figure 6.5: Two-track efficiency as determined by simulations for two different p_t values.

After reconstruction of the generated particles the best match of the reconstructed tracks for each Monte Carlo track is searched and stored. The same quality cuts as for the efficiency study of real data discussed in the previous section are applied.
For the accepted tracks, a correlation function C_2 as the ratio of a signal and a mixed event distribution of the difference in the azimuthal angle ϕ and the polar angle θ is acquired. Figure 6.5 shows the correlation functions for two different p_t regions. Since the curvature of the tracks only changes marginally for particles above 1 GeV/c in p_t, no significant differences in the efficiency is observed.
In a next step the two dimensional correlation function is fit with a two dimen-

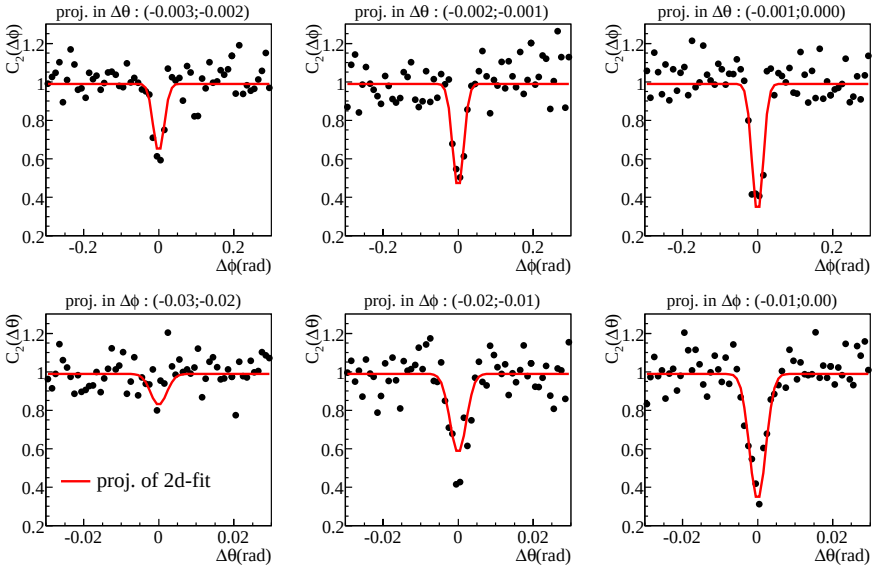

Figure 6.6: Projections of the MC two-track efficiency in slices of $\Delta\phi$ (top) and $\Delta\theta$ bottom. Indicated by the lines are the projections of a 2d-Gaussian fit to the efficiency.

sional Gaussian in order to create a correction histogram to correct the real data.

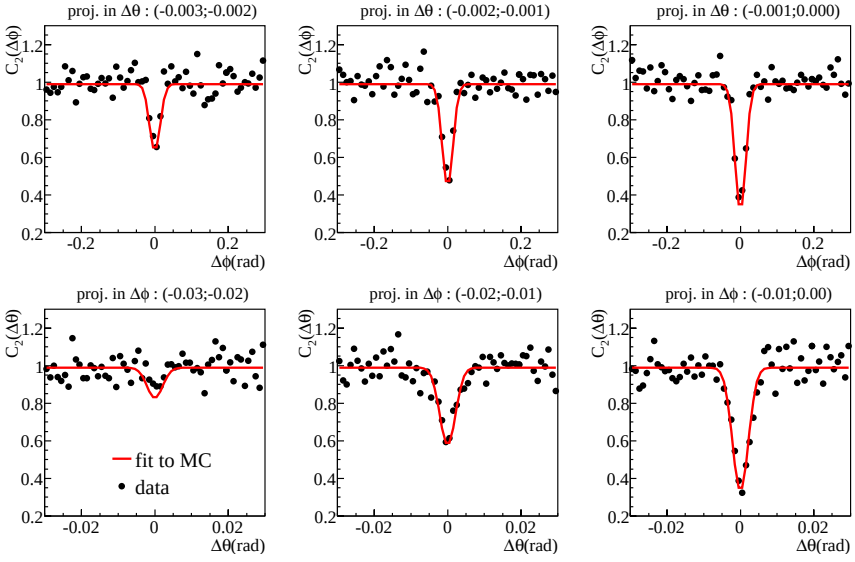

Figure 6.7: Projections of the triggered correlation function in slices of $\Delta\phi$ (top) and $\Delta\theta$ bottom. The red lines show the efficiency as determined by the simulation (Figure 6.6).

The distributions ranging from 1.2-5.2 GeV/c are added to increase statistics. In Figure 6.6, projections of the two dimensional correlation function in slices

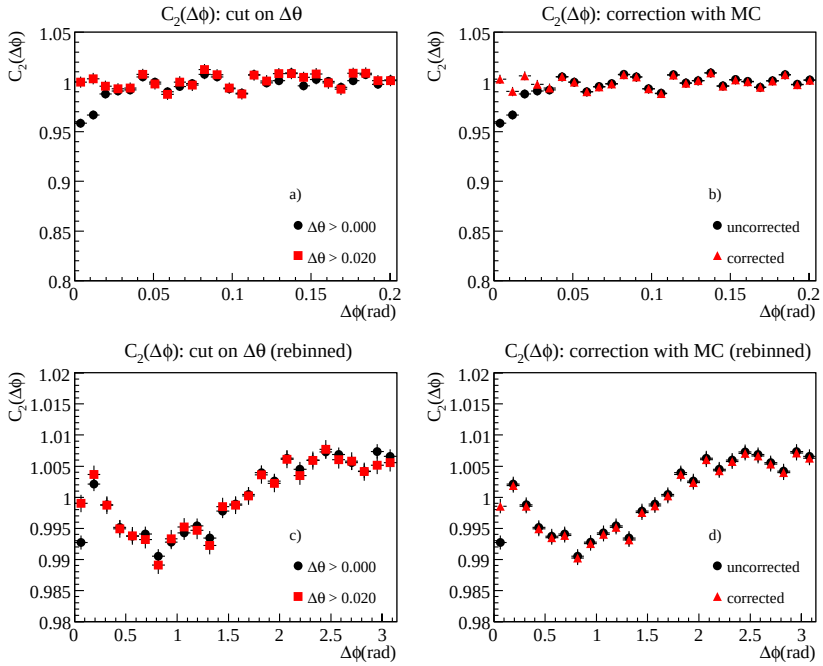

Figure 6.8: a),c): Correlation function with (red squares) and without (black squares) cut on $\Delta\theta$. b),d): Correlation function with (red triangles) correction by two-track inefficiency determined via Monte Carlo simulations compared to the correlation function without cut (black squares). Bottom plots show rebinned versions of the top plots over a wider $\Delta\phi$ range.

of $\Delta\theta$ (top) and $\Delta\phi$ (bottom) are shown.
Up to the projection in $\Delta\phi$=(-0.02, 0.01) the MC efficiency is very well described by the fit. The fitted efficiency is now compared to the real data.
Figure 6.7 shows projections of the triggered correlation function in the same representation as for the MC study and compared to the fit to the MC efficiency.
In azimuthal correlations between triggers of $2.5<p_t(\mathrm{GeV/c})<4.0$ and associated particles in the range $1.0<p_t(\mathrm{GeV/c})<2.5$ no enhancement from decays ore conversions at small $\Delta\phi$ is observed and the data are very well reproduced by the simulation.

Applying the correction to the data results in a correlation function as depicted in 6.8. The triggered correlation function is shown without two-track cut and with correction by the efficiency as determined by the simulation (right). As shown in the top plots the undershoot of the correlation function is removed as in the case of the cut on $\Delta\theta$ (left plots). However in the more coarse picture in the bottom plots the first bin is again significantly lower than the second as in the case of the cut on $\Delta\theta$.
Summarizing this chapter the observation of the first bin being significantly lower than the second can not be altered by either cutting on the opening

angle nor can be accounted for by MC simulations. However cutting out the inefficiency region and the correction with the efficiency as determined via simulations results in similar values of the correlation functions at $\Delta\phi$=0.
No centrality selection is applied in the simulation and the exact p_t- distribution is not reproduced so the MC study can be improved. Statistics could as well be increased to better resolve the edge of the onset of the inefficiency.

However, it cannot be excluded that the origin of the decrease to $\Delta\phi$=0 is due the physical correlation, like e.g. momentum conservation of the fragmentation products in the plane normal to the momentum of the leading parton. This will be discussed again in the context of the $\Delta\phi$-$\Delta\eta$ correlation analysis.

7 Momentum resolution and single-track efficiency

The conditional yield extracted from the two-particle correlations has to be corrected for the limited single track efficiency of the detector.

A further effect influencing the results is the limited momentum resolution of the detector which decreases at high transverse momenta due to the smaller absolute change of the curvature required for the same change in p_t of the tracks.

The resolution of the momenta only affects marginally the correlation function in $\Delta\phi$ since the conditional yield is acquired over a wide range in the transverse momentum and large differences in ϕ. On the other hand, the slope and the shape in the invariant p_t spectrum is significantly affected by the resolution at high-p_t.

This mainly influences the actual mean p_t of the trigger and associated particles entering the analysis.

In order to account for these effects, a Monte Carlo study is performed calculating the single track resolution in polar and azimuthal angle as well as the transverse momentum resolution depending on the polar angle, the number of

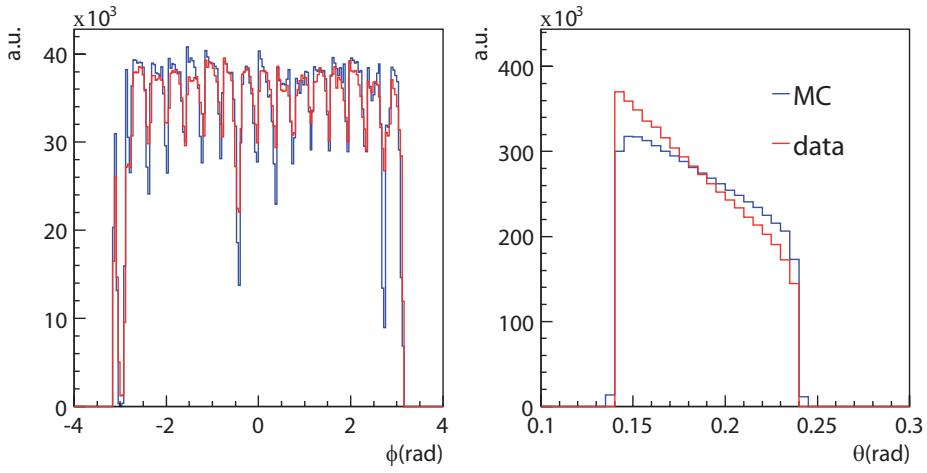

Figure 7.1: Comparison of the distribution of the azimuthal angle ϕ (left) and the polar angle θ (right) for MC and real data. Due to the flat p_t input for the Monte Carlo data sample, the distributions do not exactly match each other.

fitted hits, the charge and the p_t of the particles itself.
The single track efficiency is calculated depending on transverse momentum p_t, the rapidity y and the charge of the particles.
The v_2 values used to subtract the flow contribution to the correlation function depend on p_t of the particles. However, the momentum resolution is not supposed to affect this correction since the v_2 values are extracted depending on p_t themselves and are thus subject to the same uncertainty in the determination of the transverse momentum.

7.1 Monte Carlo input

For the study of the momentum resolution and the efficiency large samples of pions are generated over a wide range in rapidity $2.0<y<2.8$ and transverse momentum $0.0<p_t(\mathrm{GeV/c})<10.0$ and passed through the detector simulation chain. Before reconstruction the tracks are embedded into raw Pb-Au events to match the occupancy in the detector for real events. The azimuthal angle is uniformly covered by the generated particles. Choosing this set of generated particles can not reproduce exactly the distributions as arising in real events due to the different shape of the p_t spectra. The uniform coverage in p_t of the generated particles on the other hand, allows for the determination of the resolution in the very high momentum region as well with sufficient statistics.
A comparison of reconstructed Monte Carlo tracks to the real data with the same kinematic constraints is shown in Figure 7.1.

7.2 Single-track efficiency

The single-track efficiency depending on the charge of the particles is shown in Figure 7.2 as function of p_t and y for the generated pions. The efficiency is defined as the fraction of generated Monte Carlo tracks $n_{mc(match)}$ which have a matched reconstructed track for a given phase space bin:

$$\text{efficiency} = \frac{n_{mc(match)}}{n_{mc}} \tag{7.1}$$

The actual momentum of the reconstructed particles is not taken into account. It is only checked if a matching track for a Monte Carlo particle exists.

The efficiency is approximately 75%-80% for tracks above p_t=1 GeV/c and only marginally varying with p_t. The efficiency drops slightly going to larger rapidities which can be attributed to a larger amount of tracks with a smaller number of hits in the TPC. For the correction of the conditional yield an efficiency of 0.78 was chosen for the associated interval $1.0 < p_t < 2.5$ GeV/c independent of the rapidity (polar angle θ) region.

7.3 Resolution in azimuthal- and polar angle

The resolutions in the azimuthal- and the polar angle are shown in Figure 7.3. No decomposition in positive and negative particles has been done. Since the

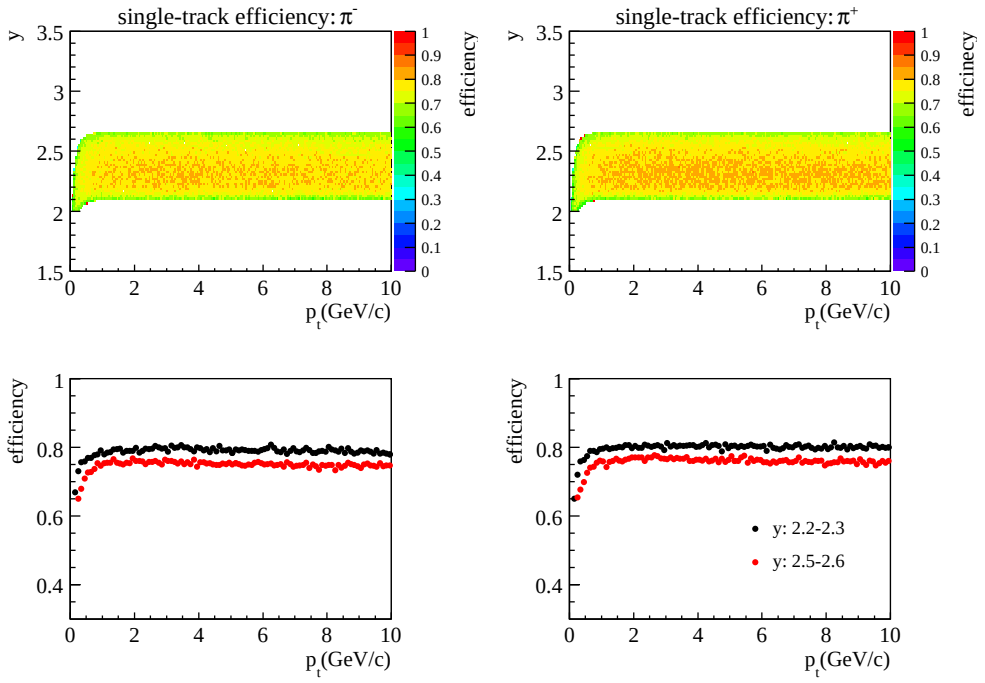

Figure 7.2: p_t and y dependence of the single-track efficiency determined via Monte Carlo simulations for positive (left) and negative (right) pions. The bottom panels show projections of the two dimensional representation over two rapidity slices.

curvature does not significantly change for particles above e.g. 1.0 GeV/c the resolution in the angels is hardly affected by the transverse momentum of the tracks.

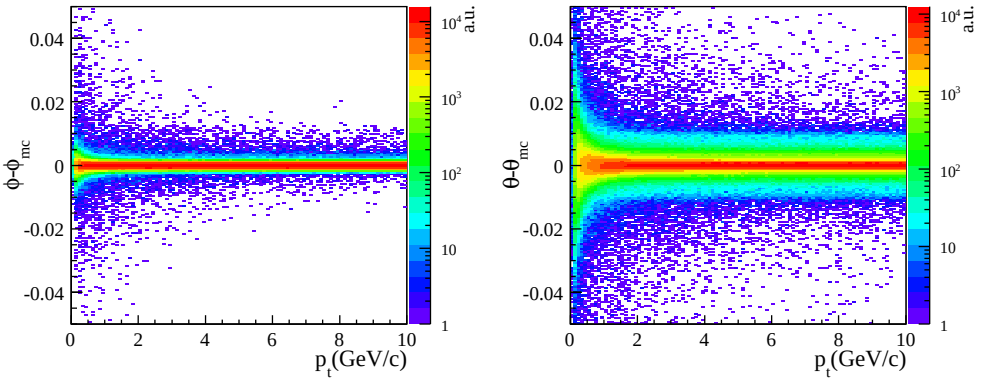

Figure 7.3: Resolution in the azimuthal angle ϕ (left) and the polar angle θ (right) depending on transverse momentum p_t of the particles. The resolution is integrated for positive and negative pions.

For tracks with p_t corresponding to the mean p_t in the associate region ($\langle p_t \rangle$=1.3 GeV/c) and the trigger region ($\langle p_t \rangle$=2.8 GeV/c) the resolution in ϕ and θ is given in the following table:

Table 7.1: ϕ and θ resolution as determined via simulations for selected values of transverse momentum p_t.

p_t (GeV/c)	$\sigma_{\phi-\phi_{mc}}$ (mrad)	$\sigma_{\theta-\theta_{mc}}$ (mrad)
1.3	1.8	0.7
2.8	2.5	0.9

7.4 Transverse momentum resolution

The resolution of the transverse momentum is determined for positive and negative pion samples. It is defined as the width of the distribution of the difference of the reconstructed momentum of the best matched reconstructed track to a Monte Carlo track:

$$\frac{\Delta p_t}{p_t} = \frac{p_t(rec) - p_t(mc)}{p_t(mc)} \tag{7.2}$$

The generated poins are divided into 5 bins in θ from 0.14-0.24, 9 bins for the number of fitted hits from 12-20 and 50 bins in p_t ranging from 0-10 GeV/c. An example of the distribution for $\Delta p_t/p_t$ two different p_t values and sets of number of fitted hits (nfittedhits, n_{fit}) and the θ region is shown in the top panels of Figure 7.4.
For each n_{fit}-θ-p_t-bin of the generated tracks, the distribution is fitted with a Gaussian and the mean and width of the distribution are extracted. The p_t-dependence of the resolution σ and the mean μ of the distributions for two different n_{fit}-θ bins is shown in middle and bottom panels of Figure 7.4.

The resolution decreases significantly to higher momenta with a trend to smaller p_t values indicated by the shift in the mean value of the distribution to negative values.
Assuming that the shift is due to the limited position resolution of the hits a tendency to higher values would be expected due to the nonlinear depencence of the curvature of the tracks on the extracted momentum.

The momentum of the tracks is determined by a characteristic deflection in the ϕ angle which is parameterised for a set of Monte Carlo tracks with p_t values of up to 2 GeV/c. The systematic shift in the momentum to smaller values could thus be a systematic effect accounting for deviations of the shift from the expectations for tracks with high transverse momentum.

The resolution only slightly differs for negative and positive particles. Typical values for the resolution in the standard associate- and trigger-p_t bin are in the range of $5.0\% < \sigma < 15\%$ with a shift of $-5.0\% < \mu < 0.0\%$.

This maximum value of the resolution 15% in the trigger region of $p_t = 3$ GeV/c is in agreement with the value expected from Eq. 7.2. A differential view of the mean and the resolution is shown in Appendix C.

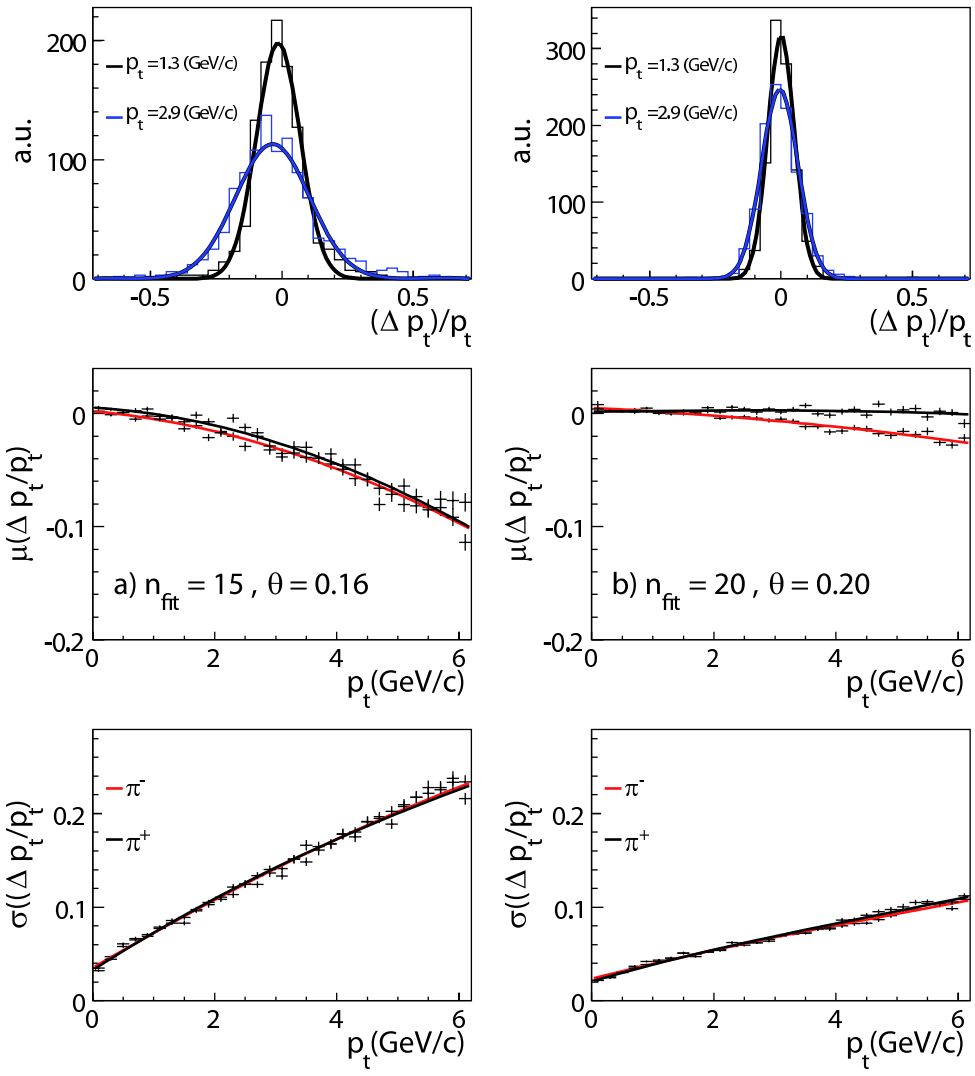

Figure 7.4: Top: distribution of the relative transverse momentum difference $\Delta p/p$ for two different p_t values. Middle: p_t-dependence of the mean values of the distribution in $\Delta p_t/p_t$. Bottom: p_t-dependence of the width of the distribution in $\Delta p_t/p_t$.

8 Elliptic flow analysis

A major uncertainty in the analysis of jet like azimuthal correlations is the assumed contribution to the correlations from the anisotropy of the underlying event. As described in section 2.1 the flow contribution is subtracted in a two-source model, assuming the flow modulation in the correlation function as measured in the data in the p_t ranges of trigger and associated particles. A systematic study of the impact of variations of the flow parameter v_2 on the results is described in 3.

The anisotropy in (transverse) momentum space and hence in the azimuthal angular distribution depends on the transverse momentum of the particles itself. In addition, positive and negative hadrons show a different transverse momentum dependence due to the different dominant types of particles in the positive and negative particle sample. In order to obtain the proper v_2 values for the specific settings, an analysis of the azimuthal anisotropy of the source is performed depending on the centrality of the collisions, the transverse momentum and the charge of the particles.
In the following, a brief summary of principles of the determination of the anisotropy parameter v_2 is given, and a comparison of the results for different analysis settings to estimate the systematic uncertainties is presented. Details of the flow analysis procedure can be found in [62][58].

8.1 Reaction plane determination

The anisotropy of the source in momentum space arises due to the finite impact parameter of the collisions. This leads to different pressure gradients in the reaction plane - which is defined as the plane spanned by the beam direction and the connection betwen the center of the target and the projectile - and perpendicular it. The initial asymmetry in coordinate space transforms to an asymmetry in momentum space with respect to the reaction plane in the final state. To analyze this anisotropy, the dependence of the azimuthal angle ϕ with respect to the reaction plane angle ψ_r of the particles is decomposed in a Fourier series [12]:

$$E\frac{d^3N}{d^3p} = \frac{1}{2\pi}\frac{d^2N}{p_t dp t dy}(1 + \sum_i 2v_n \cos(n(\phi_i - \psi_r)). \tag{8.1}$$

From this distribution, the Fourier coefficients can be calculated as an average over the distribution with respect to the reaction plane:

$$v_n = \langle \cos(n(\phi - \Psi_r) \rangle. \tag{8.2}$$

For a coordinate system with the x-axis lying in the reaction plane we obtain: $\cos(\phi - \Psi_r) = p_x/p_t$ and $\sin(\phi - \Psi_r) = p_y/p_t$. With the sum formulas for sin and cos and the prefactor 2 in the Fourier series the second Fourier coefficient results in:

$$v_2 = \langle \cos(2(\phi - \Psi_r) \rangle = \langle (p_x/p_t)^2 - (p_y/p_t)^2 \rangle, \tag{8.3}$$

which describes the eccentricity of an ellipse. To determine the Fourier coefficients via Eq. 8.2 the reaction plane angle has to be determined first. This can be done by analyzing the anisotropy of the distribution itself. The components of the reaction plane vector are defined as:

$$Q_n^X = \sum_i w_i cos(n\phi_i) \ , \ Q_n^Y = \sum_i w_i sin(n\phi_i). \tag{8.4}$$

With these components we obtain for the reaction plane angle:

$$\Psi_r = \arctan(\frac{Q_n^Y}{Q_n^X})/n. \tag{8.5}$$

The reaction plane angle can be determined from each harmonic of the distribution. With the transverse momentum as the weight, the reaction plane angle for the first harmonic results in the vector sum of the momenta of all particles, reflecting an overall shift in the momenta of the source in a certain transverse direction. This is known as the sidewards flow in a collision. For a random reaction plane such a sidewards flow would result in a shift of the maximum of the distribution of the reaction plane components to a ring of constant radius. No strong effect is observed in the data (Figure 8.1).

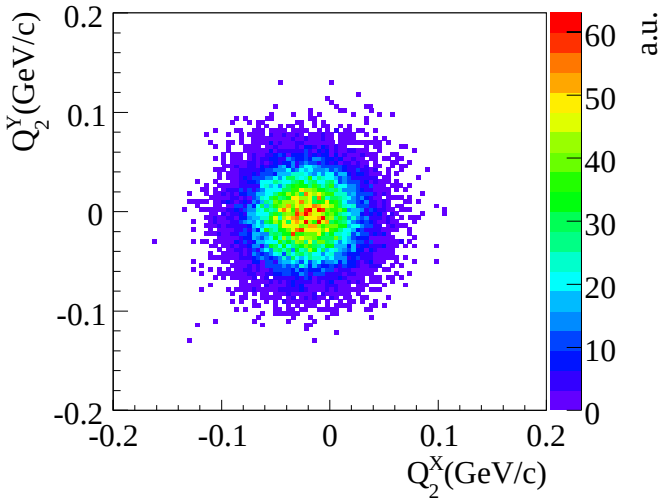

Figure 8.1: Distribution of the components of the reaction plane vector $\vec{Q}_2$ for one unit.

However, the whole distribution is slightly shifted which arises due to the non uniform acceptance of the detector. This leads to a non-uniform distribution of the reaction plane as depicted in Figure 8.3 which has to be corrected for.

8.2 Reaction plane calibration

8.2.1 Recentering of the reaction plane vector components

To remove this non-uniformity a unit by unit correction is applied shifting the components of the reaction plane back to the center by the mean values of the distributions for each unit. This removes the first harmonic of the reaction plane distribution, as it would be the case for the azimuthal distribution of the momenta with respect to the reaction plane on an event by event basis. The second harmonic is removed by scaling the recentered reaction plane vector components by the width of the distributions in Q_2^Y and Q_2^Y. For the recentered reaction plane vector components we obtain:

$$Q_{n\,cal}^{X/Y} = \frac{Q_n^{X/Y} - \mu(Q_n^{X/Y})}{\sigma(Q_n^{X/Y})} \tag{8.6}$$

8.2.2 Calibration for specific settings

A first systematic check specific for the correlation analysis is whether triggering and selecting different charges for the analysis has an impact on the calibration of the reaction plane. For this the reaction plane components are calculated for positive and negative charged hadrons in triggered and non-triggered events for several units (Figure 8.2). The main observation is that the absolute values for the mean and variance are higher for positive than for negative particles.

This, however, can be explained by a combination of statistical effects and the underlying momentum distribution of the particles. The reaction plane components are weighted averages over the momentum components of the particles in an event. Hence, for an isotropic source and in the absence of detector effects, the components approach 0 for an infinite number of particles. All the more the weights are normalized to the total number of particles. This holds as well for the width of the distribution. On the other hand, the fluctuations scale with the transverse momenta of the particles.

Negative particles exhibit a steeper p_t-spectrum and the overall number per event is smaller than for positive particles. Therefore, the two effects described above interfere. In a simple toy model the impact of the number difference and the difference in the slope of the p_t-spectra is modelled. The p_t-spectrum for the same set of cuts as for the calculation of the Q-vector is accumulated in triggered and non triggered events. Based on these distributions, particles with a random distribution in the azimuthal angle are generated. The number of generated particles is chosen to match the corresponding average number of positive and negative particles in an event.

With these settings it is possible to quantitatively describe the difference in

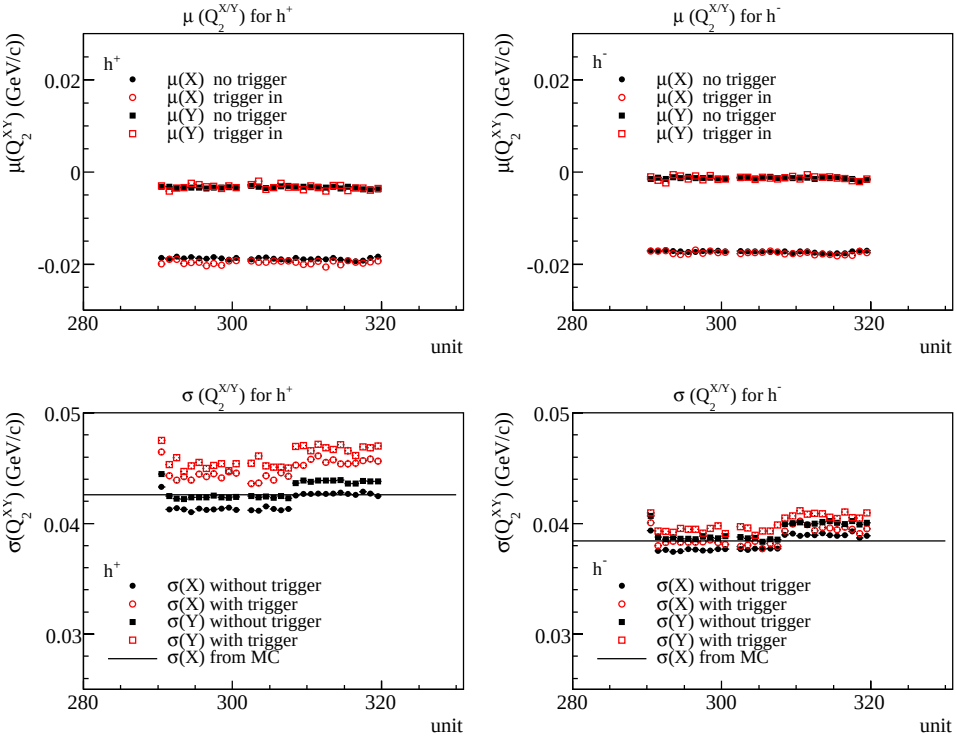

Figure 8.2: Mean and variance of the X and Y components of the reaction plane vector $\vec{Q}_2$ for the second harmonic for positive (left) and negative (right) hadrons in triggered and non-triggered events. Indicated by the line are the results from toy model studies assuming the shape of the p_t distribution as well as the number of positive and negative tracks per event as in the data. Only statistical fluctuations are taken into account.

the width between positive and negative particles for untriggered events. The jump in the width from non-triggered to triggered events however could not be reproduced. This jump might be due to the higher momenta in triggered events and due to high p_t-particles possibly clustering in events, thus leading to higher fluctuations of the width of the reaction plane components.
In the toy model on the other hand, only the average number of particles per event entered the simulation and the p_t distribution was sampled without constraints on the event-by-event distribution of the particles and hence did not significantly increase the width for triggered events.

Based on these findings it is concluded that the main impact on the difference in the calibration for the different settings relevant for the analysis are of statistical nature. No trigger of charge specific calibration steps are taken for the different settings but the calibration quantities are derived from the integrated distributions.

8.2.3 Flattening of the reaction plane distribution

For the following section the calibration is shown as it is determined for the final calibration to determine the elliptic flow. Details of the settings and the applied cuts are described in the next section. The raw reaction plane distribution for the second harmonic is shown in Figure 8.2 (black) together with the reaction plane distribution for the recentered and scaled vector components (blue). The corresponding mean and variance for the recentered $\vec{Q}_2$-vector components is shown in Figure 8.4 for all units.
To remove the remaining non-uniformity a flattening correction is applied [13]. The calculated reaction plane angle is shifted by a correction term $\Delta\Psi_r$:

$$\Psi_r' = \Psi_r - \Delta\Psi_r \tag{8.7}$$

which is determined via the Fourier decomposition of the recentered reaction plane distribution:

$$\Delta\Psi_r = \sum_n (A_n \cos(n\Psi_r) + B_n \sin(n\Psi_r)). \tag{8.8}$$

With

$$A_n = -\frac{2}{n}\langle \sin(n\Psi_r)\rangle \ , \ B_n = \frac{2}{n}\langle \cos(n\Psi_r)\rangle \tag{8.9}$$

we obtain for the corrected reaction plane angle:

$$\Psi_r' = \Psi_r + \sum_n \frac{2}{n}(-\langle \sin(n\Psi_r)\rangle \cos(n\Psi_r) + \langle \cos(n\Psi_r)\rangle \sin(n\Psi_r)). \tag{8.10}$$

The shape of the recentered reaction plane distribution changes with centrality. Therefore, the flattening coefficients are calculated for each centrality bin separately and up to the fourth order. The flattened reaction plane distribution is

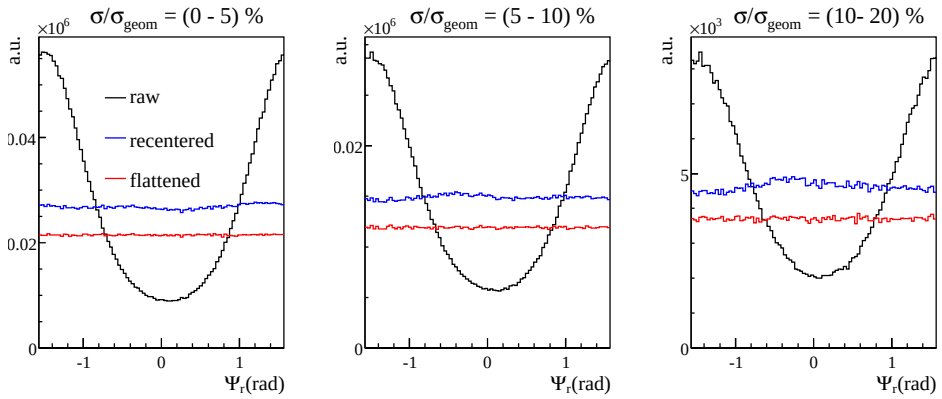

Figure 8.3: Reaction plane distribution in triggered events. Black line: raw distribution. Blue line: distribution after recentering the reaction plane with the unit-by-unit determined calibration factors. Red line: Distribution after the recentering- and flattening correction.

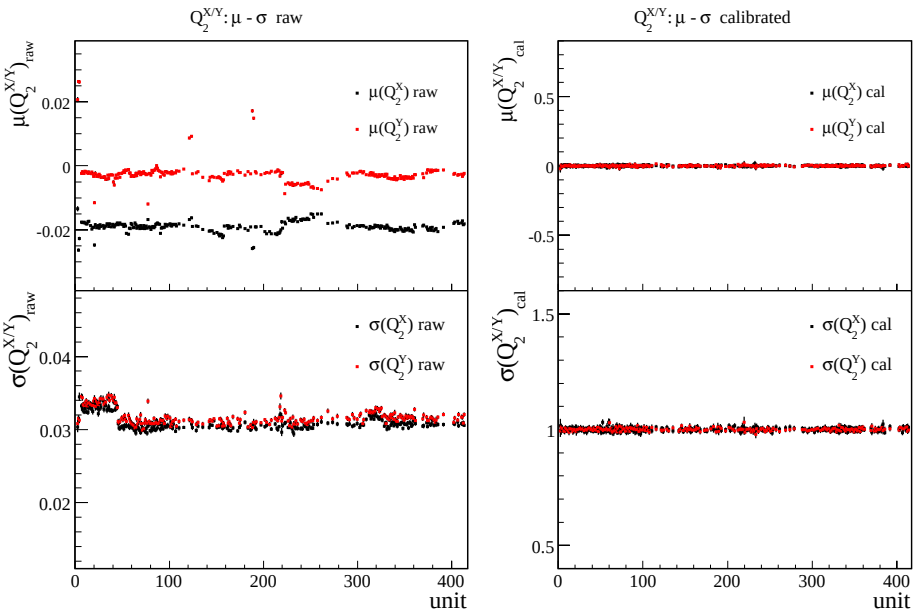

Figure 8.4: Unit-by-unit distribution of the mean and variance of the X- and Y components of the reaction plane vector $\vec{Q}_2$ for the second harmonic before (left) and after (right) recentering of the reaction plane vectors.

shown in red in Figure 8.3.
Since the corrections are very small the flattening does not influence the reaction plane resolution which is needed to correct the measured v_2 values as described in the next section.

8.3 Determination of the elliptic flow

Having determined the calibrated reaction plane and neglecting the sidewards flow v_1 and higher harmonics the elliptic flow v_2 can be calculated via:

$$v_2 = \langle \cos(2(\phi - \Psi_r) \rangle, \tag{8.11}$$

or by a fit of the azimuthal distribution with respect to the reaction plane to the functional form [63]:

$$\frac{dN}{d(\phi - \Psi_r)} = v_0 \cdot (1 + 2v_2 \cos(\phi - \Psi_r)), \tag{8.12}$$

as is done for the presented analysis. The finite multiplicity and limited efficiency of the detector lead to an uncertainty in the determination of the reaction plane resolution which diminishes the measured elliptic flow. The true elliptic flow v_2 is obtained by scaling the measured v_2 (v_2^{obs}) with the reaction plane resolution [12]:

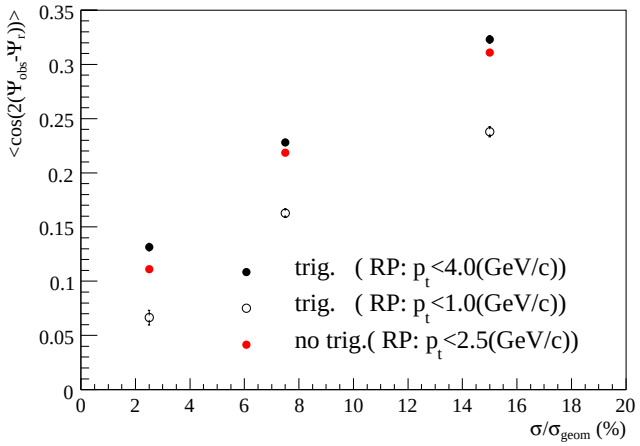

Figure 8.5: Centrality dependence of the correction factors for the limited reaction plane resolution applied to the measured v_2 parameter (Eq. 8.13). Shown are values for triggered and non-triggerred events and different p_t regions for the caclulation of the reaction plane.

$$v_2 = \frac{v_2^{obs}}{\langle \cos(2(\Psi_{obs} - \Psi_r)\rangle}. \tag{8.13}$$

The resolution can be calculated based on reaction plane angles calculated for different harmonics. Details can be found in [12]. For this thesis the resolution is calculated using a sub-event method. Each event is subdivided into two samples of equal size but with otherwise random particles from the event and the reaction planes are calculated for both sub-event samples. The difference in the reaction plane angles of the two sub-event reaction planes can be connected to the reaction plane resolution in the whole event:

$$\langle \cos(2(\Psi_{obs} - \Psi_r)\rangle = \sqrt{2\langle \cos(2(\Psi_{SE1} - \Psi_{SE2})\rangle}. \tag{8.14}$$

An alternative way calculating the reaction plane resolution based on the sub-event method [64][65] is performed for the CERES analysis as well and is described in detail in [58]. The correction factors applied for the measured v_2 values are shown in Figure 8.5.

For the actual flow calculation different setting are chosen to study the impact of high-p_t tracks on the flow as well as on the reaction plane determination. For this the entire event sample is subdivided into triggered and non triggered events.

For the non triggered events the calibration of the reaction plane is performed using all particles below 2.5 GeV/c.

For the triggered events which contain by definition at least one particle above

p_t=2.5 GeV/c the reaction plane is calculated using all particles and only particles below 1 GeV/c. For the later setting all trigger and associate particles used in the standard bin of the correlation analysis are excluded from the calculation. The reduced multiplicity for this setting reduces significantly the reaction plane resolution as shown in Figure 8.5.

For the construction of the distribution of the azimuthal angles with respect to the reaction plane (Eq. 8.12) for each particle the reaction plane is recalculated taking out the contribution from the studied particle in order to remove auto correlations of the particles and the reaction plane.

The extracted v_2 values corrected for the reaction plane resolution are shown in Figure 8.6.

In case of a jet with several high p_t particles in a triggered event, it might not be sufficient to just remove the auto correlations of each single particle to the reaction plane, since the particles from jets are collimated and would shift the reaction plane to the direction of the jet-axis. This effect could lead to an enhanced measured v_2 in triggered events and would be removed by only choosing particles below 1 GeV/c for the caclulation of the reaction plane in triggered events. However as shown in Figure 8.6 no significant change of the extracted v_2 values are observed.

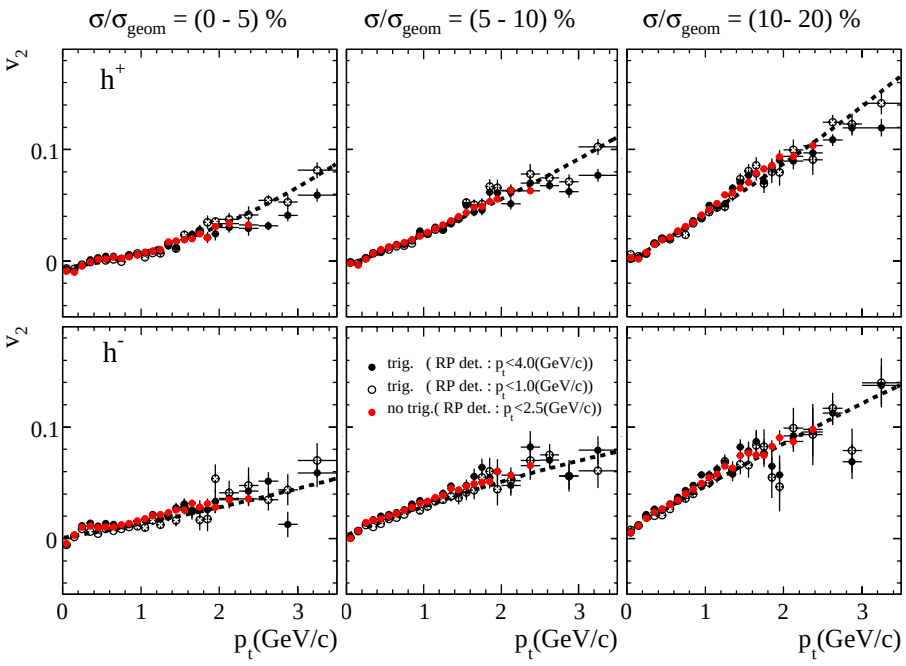

Figure 8.6: p_t-dependence of the elliptic flow parameter v_2 for positive (top) and negative (bottom) hadrons for three different centrality slices. Black circles: triggered events (open symbols with cut on $p_t < 1.0$ GeV/c for the determination of the reaction plane), Red circles: non-triggered events ($p_t < 2.5$GeV/c for the reaction plane determination).

Up to statistical uncertainties the results extracted from non-triggered events using particles below $p_t = 2.5$ GeV/c agree well with the previously discussed studies for triggered events.
For the further analysis, the flow parameter extracted for triggered events with the small p_t range (p_t <1.0 GeV/c) for the determination of the reaction plane is taken as a basis for the subtraction of the flow contribution from the triggered correlation function.
In order to remove the fluctuations in the p_t dependence a polynomial fit is performed, which reasonably describes the data over the whole p_t range for positive and negative particles for all centralities.

9 Results on two-particle correlations

The two-particle correlations are analyzed as a function of the centrality of the collision and depending on the charge and the transverse momenta of the particles.
The centrality serves as a measure for the size of the collision zone and thus as a measure for the path length of the particles traversing the medium.
At SPS the dominant contribution to scatterings with large momentum transfer is from the incoming valence quarks. Therefore, the initial state (net positive charge/baryon density) might be reflected in the extracted two-particle yield. In order to investigate the interplay of the final state medium effects and the initial state, the conditional yield is extracted for different charge combinations of trigger and associated particles.
Thermal hadron production is supposed to fall off steeper with p_t than hadron production by (jet-)fragmentation from hard collisions. Assuming the high-p_t triggered correlations measure the jet-like contribution of hadron production, the jet like yield should be harder than the measured inclusive hadron yield. This is investigated by measuring the integrated jet-like yield on the near- and the away-side as a function of the transverse momentum of the particles, and comparing it to the inclusive p_t distribution and to expectations from vacuum fragmentation as determined from PYTHIA simulations.
The two-particle jet like yield measured as function of $\Delta\phi$ describes the projection of a jet on the axis defined by the trigger. A two dimensional picture of the jet-topology can be recovered by the investigation of correlations in $\Delta\phi$ and $\Delta\eta$, which are as well analyzed as a function of the charge of the particles and differentially in p_t.

9.1 Centrality dependence

During the run period in the year 2000, 30 million Pb-Au events at 158A GeV beam energy were recorded with a trigger on the centrality of 7.5%, and about 3 million events with a trigger on 20% of the total geometric cross section σ_{geom}. In addition, 0.5 million events with a minimum bias trigger on the centrality were recorded [66]. For the presented analysis, this event sample is subdivided into three centrality classes (σ/σ_{geom}=(0.0-5.0)%, (5.0-10.0)%, (10.0-20.0)%). After the event cuts are applied, about 15 million events remain in the most central bin (0-5)%. In this event sample 17% of the events contain a trigger particle in the standard bin of $2.5<p_t(T)(\mathrm{GeV/c})<4.0$. A list of the numbers of accepted events, the trigger probability in the range $2.5<p_t(\mathrm{T})(\mathrm{GeV/c})<4.0$ and the number of associates per trigger event in the range $1.0<p_t(\mathrm{A})(\mathrm{GeV/c})<2.5$

Table 9.1: Centrality classes, number of accepted events N_{ev}, trigger probability N_T/N_{ev}, and number of associates per trigger N_A in the standard p_t bin (see text).

σ/σ_{geom}	N_{part}	N_{coll}	N_{ev}	N_T/N_{ev}	N_A
00.0 – 05.0	340	817.2	$1.5 \cdot 10^7$	0.17	14.5
05.0 – 10.0	280	654.9	$9.7 \cdot 10^6$	0.14	12.2
10.0 – 20.0	220	471.1	$3.7 \cdot 10^5$	0.11	9.9

is shown for the different centrality classes in Table 9.1.
The upper row of Figure 9.1 shows the correlation functions $C_2(\Delta\phi)$ according to Eq. 2.8 and the estimated flow contributions determined via the ZYAM

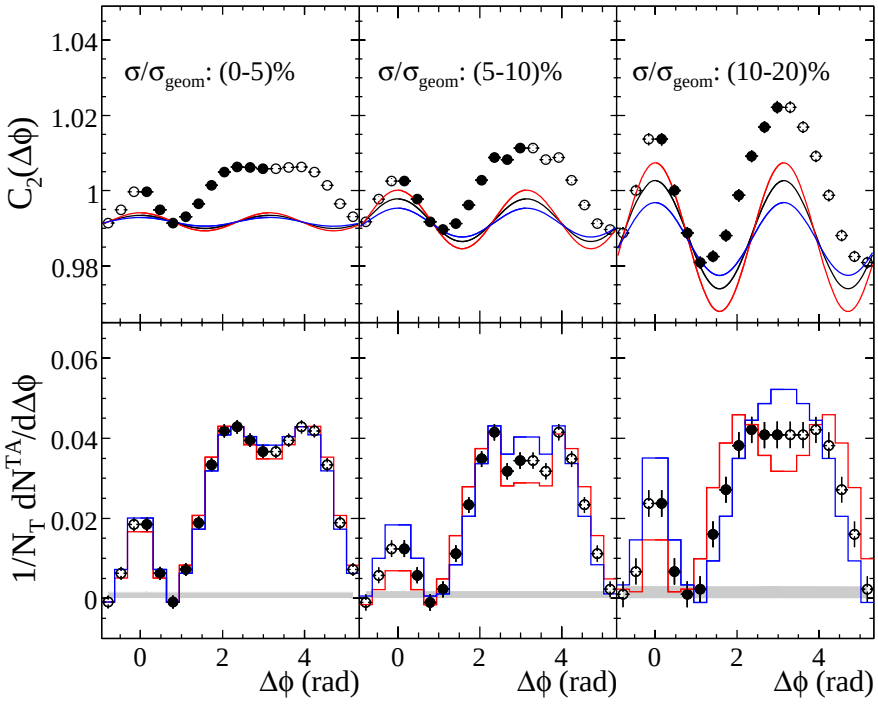

Figure 9.1: Correlation function (top) and conditional yield (bottom) without charge selection for trigger and associates (p_t(T)=(2.5-4.0) GeV/c , p_t(A)=(2.5-4.0) GeV/c) for three different centralities. The blue and red lines show the uncertainty in the flow contribution. The shaded bands show the uncertainty in the flow adjustment with the ZYAM method. The open symbols show reflected measured data points (full symbols).

method for the triggers with p_t(T)=(2.5-4.0) GeV/c and associates in the range p_t(A)=(1.0-2.5) GeV/c. The elliptic flow values v_2 used for the modulation of the flow contribution according to Eq. 2.9 are determined in a separate reaction plane analysis for the specific set of cuts used in the analysis (section 8).
The colored lines in Figure 9.1 correspond to the variation of the v_2 coefficients by the uncertainty in the v_2 parameters which is of the order of 10% in the associate p_t-range and 25% in the trigger p_t-range respectively. The variation is done in a correlated way increasing or decreasing both v_2 values. Hence the variations correspond to a conservative estimate of the uncertainty. The lower row in Figure 9.1 shows the extracted conditional yield corrected for efficiency, as determined in a Monte Carlo study to be 78% for transverse momenta above p_t= 1 GeV/c. The conditional yield shows a double humped structure for the most central bin which is already indicated by the raw correlation function in the upper row of Figure 9.1.
This strong deviation from a Gaussian-shaped form (or single peak shape) as expected for vacuum fragmentation indicates medium effects on the high-p_t particles traversing the medium in the collision. The modulation in the correlation function is more pronounced towards more peripheral collisions. However part of this effect can be attributed to the increasing flow modulation in more peripheral bins.
The estimated relative uncertainty in the elliptic flow parameters is not changed with centrality, however since the flow modulated background is subtracted from the correlation function, the absolute variation of the flow contribution is the relevant quantity determining the uncertainty. The extracted conditional yield has a large uncertainty in the shape on the near- as well as on the away-side for more peripheral bins. For the centrality class σ/σ_{geom}=(10-20) % a double humped structure as well as a Gaussian like shape is consistent with the data within the systematic uncertainty of the measurement.
The double humped structure observed on the away-side for central collisions can arise due to Mach cone shock waves [43], induced by particles traversing the medium by a speed higher than the speed of sound in that medium, induced gluon radiation [44] or Cherenkov-like radiation in the medium [45]. Those scenarios can not be distinguished from an event-by-event deflection of the jets in the medium based on two-particle correlations only, since both scenarios can lead to a similar shape of the correlation function on the away-side. This will be further discussed in the course of the three-particle correlation analysis which can help to shed light on this ambiguity.
The yield on the near-side stays constant within errors over the centrality range and is significantly smaller than the yield on the away-side. This can be partly attributed to the trigger bias which is imposed due to the requirement of a relatively high p_t for the trigger particle. The trigger takes away a large fraction of the total transverse momentum on the near-side which can lead to a suppression of the associates on the near-side relative to the away-side, where no trigger criterion is required.
This strong difference of the absolute yield as well as the integrated yield on near- and away-side only holds investigating the correlation function for all hadrons (positive and negative triggers and associates respectively) combined.

The picture changes investigating different combinations of trigger- and associated charges as discussed in the next chapter.

9.2 Charge dependence

Figure 9.2 shows the conditional yield for different charge combinations of trigger and associated particles for the most central bin. The corresponding correlation functions and the yields for more peripheral bins are shown in Appendix B.1. The dip on the away-side of the yield as described in the last section is also visible in the differential view in Figure 9.2, however the absolute yield on the near- and away-side showing significantly different yields depending on the charge of the particles.

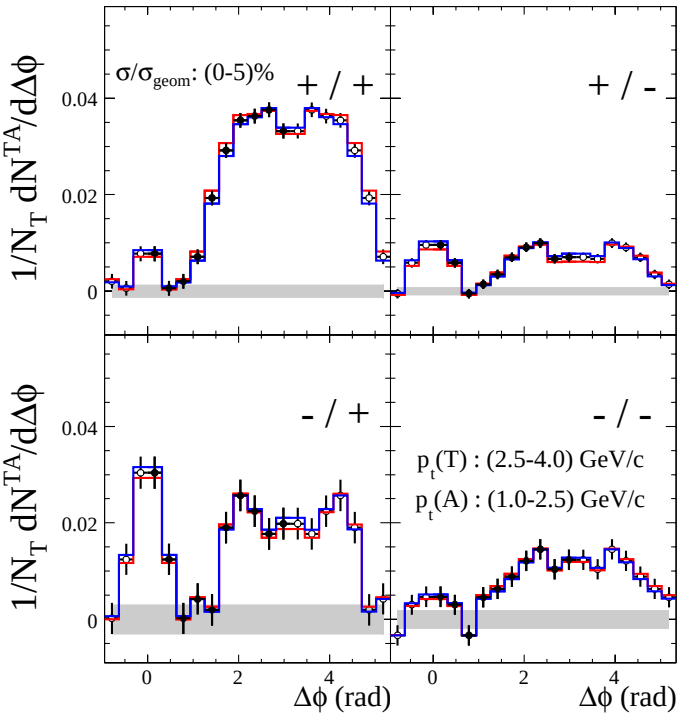

Figure 9.2: Conditional yield for different charges of trigger and associated particles for central Pb-Au collisions. The red and blue lines indicate the uncertainty in the flow contribution. The shaded bands indicate the uncertainty in the ZYAM method.

While the overall trigger sample is dominated by the positive triggers indicated by the smaller error bars, the yield on the near-side is always higher for unlike sign charge combinations of the particles.
This can be understood as to arise from local charge conservation in the fragmentation process and the small overall amount of particles expected for a fragmentation process at SPS energy. This leads to an enhanced probability for

the observation of a positive fragmenting hadron following a negative trigger and vice versa. The yield on the away-side however is not influenced by this effect since no trigger is required here.

The away-side is always dominated by positive particles. This can be understood as to arise due to the positive net charge in the collision and is hence linked to the initial state of the collision. The extracted yield thus reflects qualitatively different features on the near- and the away-side.
If the yield on the near-side features properties of vacuum fragmentation, the yields should be comparable to the expectations from elementary nucleon-nucleon collisions.
However, since the yields are extracted as an average over many events, jet-triggers as well as non-jet triggers enter the event sample and the yield only reflects an average per trigger yield, not the actual per jet-trigger yield which would be needed for a direct comparison.
This caveat can be circumvented by building the ratio of the yield for negative and positive particles R_{np} on the near- and the away-side (n/a) for a given trigger charge:

$$R_{np} = \int_{n/a} \hat{J}_2^{A^-}(\Delta\phi)d\Delta\phi / \int_{n/a} \hat{J}_2^{A^+}(\Delta\phi)d\Delta\phi. \tag{9.1}$$

This ratio can directly be compared to results from elementary collisions.

9.3 Comparison to PYTHIA simulations

The comparison to elementary collisions is made by simulations of nucleon-nucleon collisions with the PYTHIA [67] event generator. The simulations allow to study QCD processes in nucleon nucleon (p-p,n-p,n-n) as well e^+-e^- and e-p collisions. The program calculates the hadron abundances using as an input the parton distribution functions of the colliding particles, the cross-section for the collisions of the elementary partons, and the fragmentation functions as described in the introduction.
For the comparison of Pb-Au to nucleon-nucleon collisions, n-n, p-p, n-p, and p-n collisions are generated. The collisions are simulated in the center of mass frame of the collision with the center of mass energy used as an input. In order to meet the specific settings in the experiment, hadrons as an output from the simulation are boosted to mid-rapidity (y=2.9) at 158A GeV. The same acceptance window for the tracks to be analyzed is chosen as in the data ($0.14<\theta<0.24$). Only protons, pions, kaons and the corresponding anti-particles are considered in the analysis.
For this set of particles, for each PYTHIA event a trigger is searched in the p_t range of p_t(T)=(2.5-4.0) GeV/c as for the real data analysis, and all associated particles in the p_t range of p_t(A)=(2.5-4.0) GeV/c are counted in an event a trigger is found. No background subtraction is necessary for the analysis of the simulated data since no background contribution from a surrounding medium exists.
Under the assumption of binary collision scaling of hard hadron production in

Pb-Au, the PYTHIA results for the different collision systems are scaled by the relative occurrence of n-n, n-p, p-n, and p-p pairs in Au-Pb events.
The per trigger yield for PYTHIA events for different charge combinations of trigger and associate particles in shown in Figure 9.3.

The simulations show that the ZYAM assumption is justified in this p_t regime. Increasing the beam energy, lowering the p_t threshold for the associated particles, or widening the acceptance window on the other hand, shows a yield at minimum increasingly deviating from 0.
The minimum is located at an angle of $\Delta\phi \approx 1.5$ which is higher than for the data. However, this value is not directly comparable to the properties in Pb-Au since the away-side and hence the position of the minimum is supposed to be changed in the environment of a heavy ion collision.
A similar enhancement of unlike sign combinations of trigger-associate pairs as in real data is observed on the near-side for the PYTHIA yield. Similarly the yield on the away-side is slightly higher for positive associates than for negatives in the simulations.

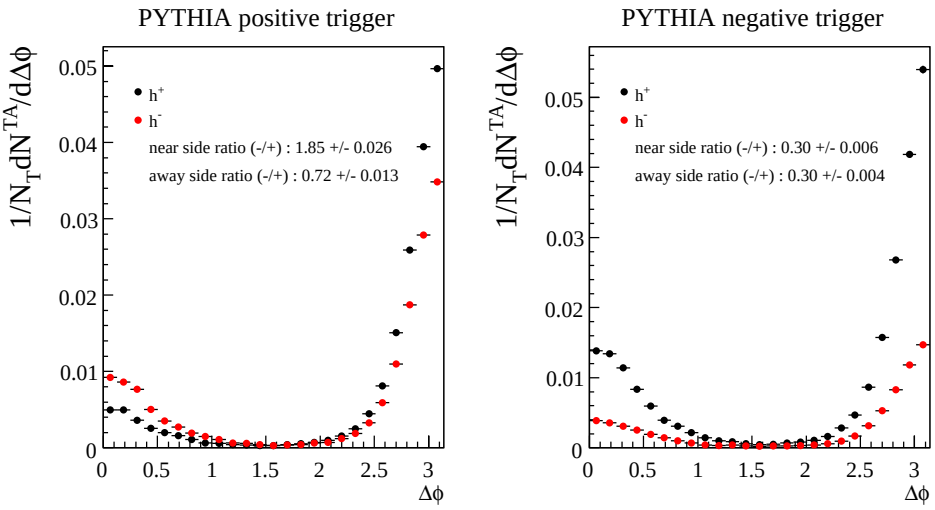

Figure 9.3: Conditional yield for different charges of trigger and associated particles for PYTHIA events (p_t(T)=(2.5-4.0) GeV/c), p_t(A)=(1.0-2.5) GeV/c). The results for p-p, p-n, n-p, and n-n are scaled to match the occurrence of the nucleon-nucleon combinations in Pb-Au collisions.

The resulting yield ratios of negative to positive hadrons obtained from PYTHIA together with the ratios from the data are shown in Figure 9.4. The shaded band corresponds to the range the ratio of the multiplicity of negative to positive hadrons is spanning in the p_t range of the associated particles (p_t(A)=(2.5-4.0) GeV/c). This representation for the medium ratio is chosen since the average p_t of the extracted jet-like yield can not be deduced.

The expected result from a charge ordering in the fragmentation process is an

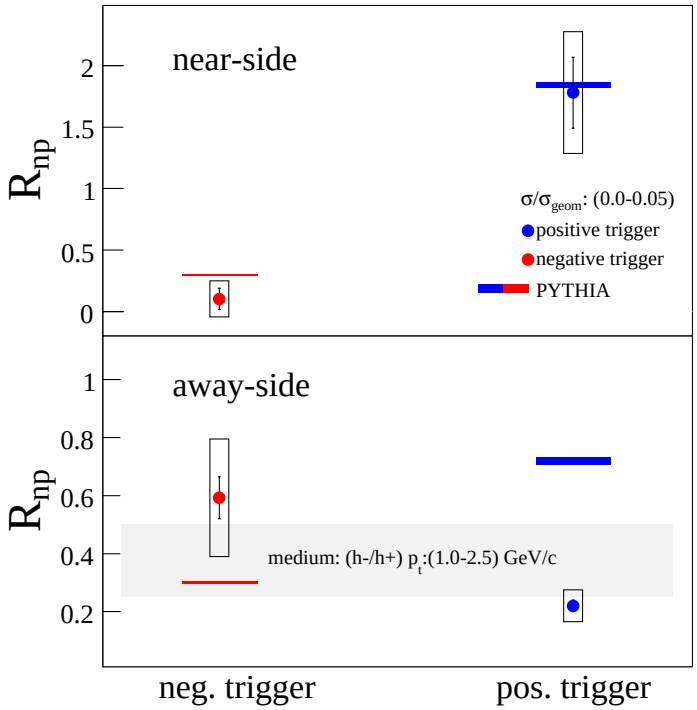

Figure 9.4: Associated yield ratios (negative/positive) on the near- and the away-side. Indicated by the bars are results from PYTHIA simulations for the same kinematic regions and acceptance cuts. The grey band shows the region the ratio of negative to positive associates spans over the associated p_t-range.

increased abundance of negative associates for a positive trigger as compared to positive associated particle and vice versa. Therefore, a ratio bigger than one is expected for positive triggers and smaller than one for negative triggers on the near-side. This is confirmed by the PYTHIA results on the near-side of the correlation function as shown in the top panel of Figure 9.4. The yield ratios from the data agree well with the PYTHIA results emphasizing that at SPS indeed fragmentation processes from hard scatterings are observed in Pb-Au collisions.

On the away-side, PYTHIA results are close to the expectations for the medium for negative triggers whereas the results for positive triggers are closer to 1. The yield ratios for Pb-Au data however are close to the expectation from the bulk medium independent of the trigger charge. In addition, there is a large discrepancy to the PYTHIA results for positive triggers.

The remarkable agreement on the near-side supplements the earlier conclusion that indeed the near-side features fragmentation into the vacuum, emphasizing the picture of surface biased emission of particles. The charge composition on

the away-side however is consistent with the composition of the bulk medium. This can be interpreted as to arise from a parton traversing the medium and boosting the particles inside the medium, leaving the charge composition undisturbed. The excess measured over the bulk medium therefore shows the same charge composition as the medium itself.

9.4 p_t-scan of two-particle correlations

To study the p_t dependence of the jet-like contribution of the hadron production as determind via the two-particle correlations, the integrated yield on the near- and the away-side is determined for different trigger and associate p_t ranges. For this analysis no charge decomposition of trigger and associated particles is performed.

For the trigger interval a p_t range of Δp_t=1.5 GeV/c is chosen starting with a lower bound of 1.0 GeV/c and increasing it by 0.5 GeV/c for 5 trigger p_t bins. The associates are analyzed in 6 non-overlapping bins spanning a p_t range of Δp_t=0.5 GeV/c.

In Figure 9.5 the dependence of the integrated yield on the near- and the away-side is shown as function of the trigger-p_t for different associate-p_t ranges and centralities. The p_t ranges of the triggers is shown in the legend. The corresponding correlation functions and the conditional yields as function of $\Delta\phi$ are shown in Appendix B.2.

Since the trigger particle is by definition chosen to be the particle with the highest p_t in a given interval, there is a bias on the accessible associate p_t in case of overlapping trigger and associate p_t bins. Those bins are depicted in the Appendix by the colored background however omitted for the calculation of the integrated yield. The p_t dependence for the highest trigger p_t bin shows similar features as at lower p_t but are omitted due to large statistical uncertainties.

The yield on the near- as well as on the away-side stays approximately constant over the investigated trigger range showing no significant difference for the different centrality bins. An away-over near-side yield ratio bigger than one is observed for all trigger and associate p_t bins.

A higher trigger p_t requirement corresponds to triggering on harder parton-parton interactions and hence to a larger total transverse momentum. This is transferred to the jet-like particles originating from the fragmentation and can lead to a higher number of jet-like associates at a given associate p_t.
On the other hand the higher trigger p_t poses a stronger trigger bias, given a certain class of parton-parton collisions.
The small observed variation of the extracted yield on the near-side with trigger p_t could thus result from an interplay of the two described effects.

A further effect complicating the comparison is that different event samples are studied for each trigger p_t bin. The extracted yield is a per trigger yield and the ratio of jet-like to non-jet like triggers is as well supposed to change with p_t.

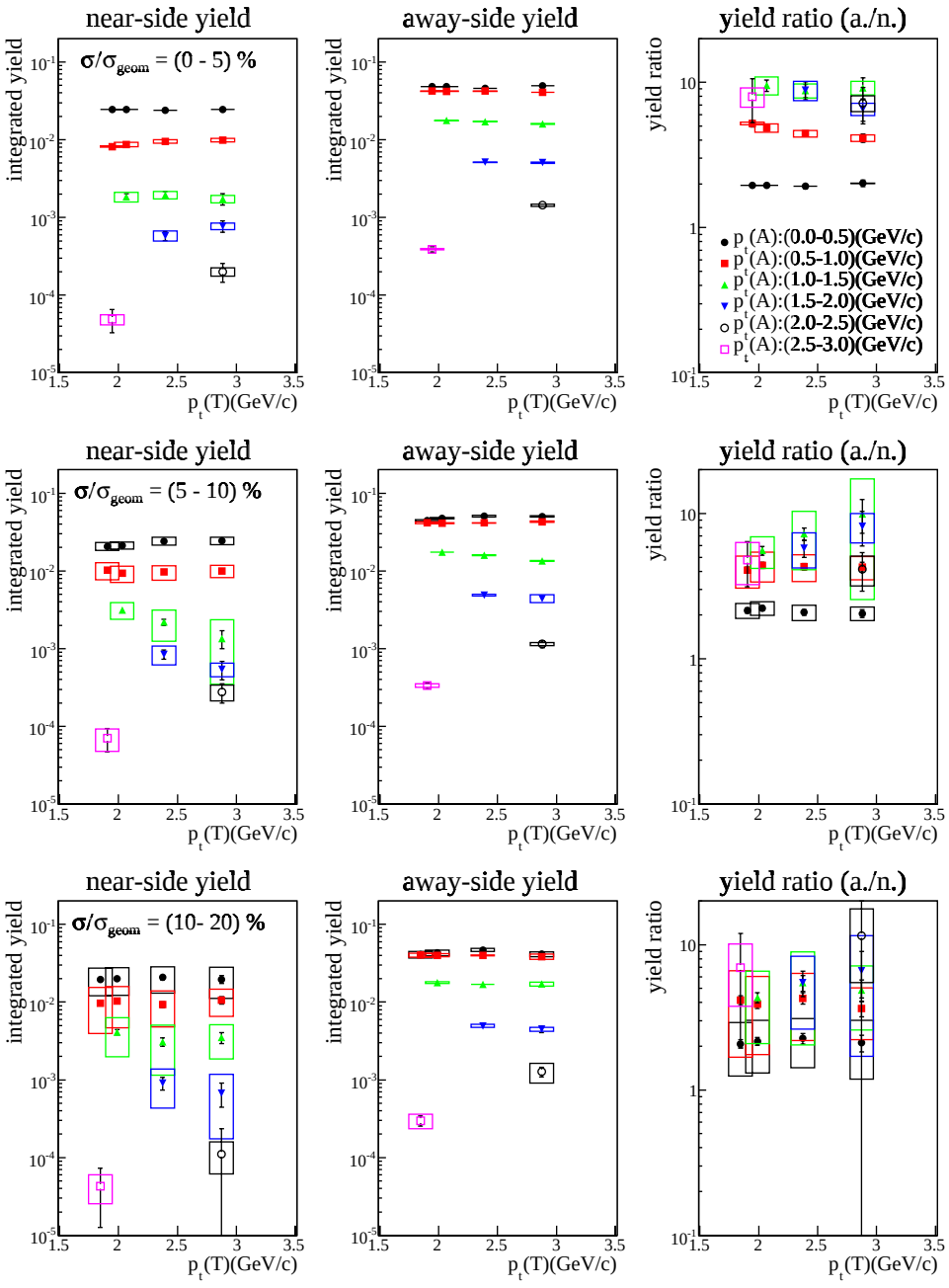

Figure 9.5: Integrated yield on near- (left panels) and away-side (middle panels) as a function of the trigger-p_t for different associate-p_t ranges. The left panels show the ratios of the near- and the away-side yields.

A comparison with less systematical uncertainty can be performed choosing a fixed value for the trigger p_t and varying the associate p_t as is shown in Figure 9.6. The results shown in this Figure correspond to the results from Figure 9.6 however in a different representation. As already seen from Figure 9.5 there is

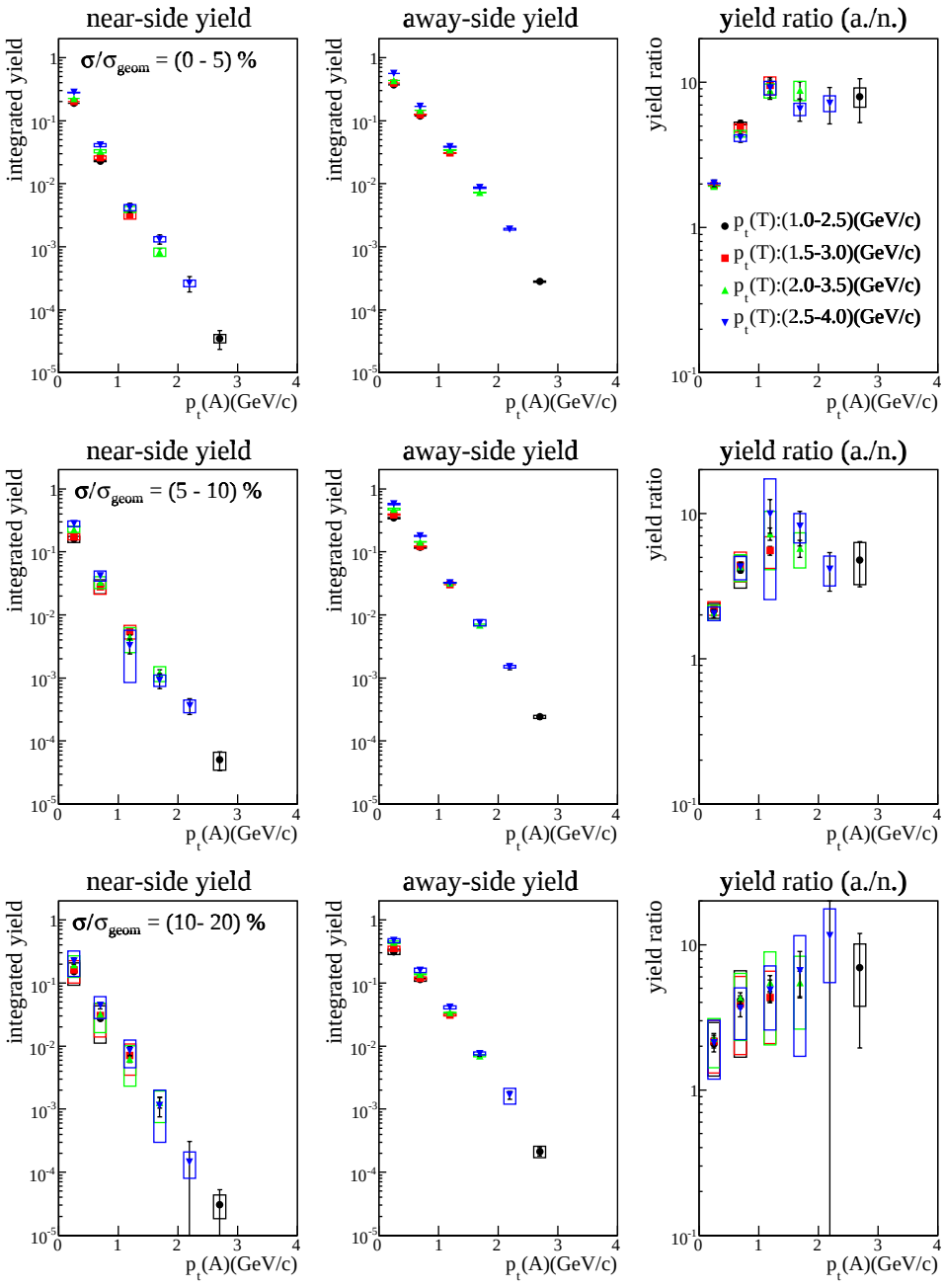

Figure 9.6: Integrated yield on near- (left panels) and away-side (middle panels) as a function of the associate-p_t for different trigger-p_t ranges. The left panels show the ratios of the near- and the away-side yields.

only small dependence on the chosen trigger p_t and centrality. The associated yield falls steeply off with p_t however near- and the away-side showing a slightly different shape which is seen in the ratio of the away-over-near (a./n.) side yield. First the ratio rises steeply however starts to flatten from $p_t \approx 1$ GeV/c. This

observation can again be understood as to arise from an interplay of several effects. Assuming the near-side yield not to be disturbed by medium effects, the trigger bias is assumed to be a major effect alternating the p_t dependence as compared to vacuum fragmentation without any kinematical constraints.
This trigger bias selects an event sample with at least one high-p_t trigger per event. Momentum conservation might lead to the occurrence of an additional number of low p_t associates however high p_t associates might be suppressed. This constraint is not seen on the away-side since no trigger criterion is required. Thus the ratio of away-over-near side grows with p_t.
At about p_t= 1 GeV/c the ratio stops to increase and saturates at about a factor of 10. This can be understood as to arise from the attenuation of high-p_t particles in the medium, which is more pronounced on the away- than on the near-side. The redistribution from high- to low p_t due to multiple scattering or soft gluon radiation would lead to a shift of high p_t particles to lower p_t, however without populating the higher p_t region in the same way. In addition, the near- as well as away-side yield fall off steeply with p_t. Thus, the lower the p_t the smaller the impact from a shift of particles from a given high p_t region is. In total the intermediate p_t region on the away-side is enhanced leading to the observed flat plateau observed from p_t=1 GeV/c on.

Figure 9.7 shows a direct comparison of the p_t-dependence of the near- and the away-side for triggers with p_t=(2.5-4.0) GeV/c and associates with p_t=(2.5-4.0) GeV/c for the most central bin. In the top left plot the integrated yields as well as the p_t distribution for all associated particles (inclusive distribution) is shown. Since the integrated conditional yield is of the order of 0.17 compared to a total number of associates per trigger of approximately 15, the inclusive distribution is dominated by the bulk medium in the collision.
For a better comparison, the data are normalized to agree at $p_t \approx$ 0.8 GeV/c. As discussed before the yield on the away-side is flatter at small p_t however decreasing faster at high p_t. Therefore a direct comparison of the two distributions by this normalization is difficult.
A basic expectation is that the p_t-spectra for fragmenting partons should be harder than the inclusive distribution indicated by the line in the top left panel. In addition, the near-side distribution should be harder than the away-side distribution assuming dominance of vacuum fragmentation on the near-side and medium effects on the away-side.

However the already discussed trigger bias alters this picture. To estimate this effect the p_t-distribution of the integrated yields on the near- and the away-side are determined from PYTHIA simulations (top right panel in Figure 9.7). The yields are again normalized to agree at $p_t \approx$ 0.8 GeV/c.
Contrary to the above mentioned expectation, the near-side is softer than the away-side even in elementary collisions, however the ratio of away-over-near side steadily increases in contrast to the measured yield ratios in Pb-Au saturating at p_t=1 GeV/c.

A direct comparison to the PYTHIA results is shown in the bottom panels of Figure 9.7. As above the results are normalized to agree at $p_t \approx$ 0.8 GeV/c. This arbitrary normalization complicates the comparison however at high associate

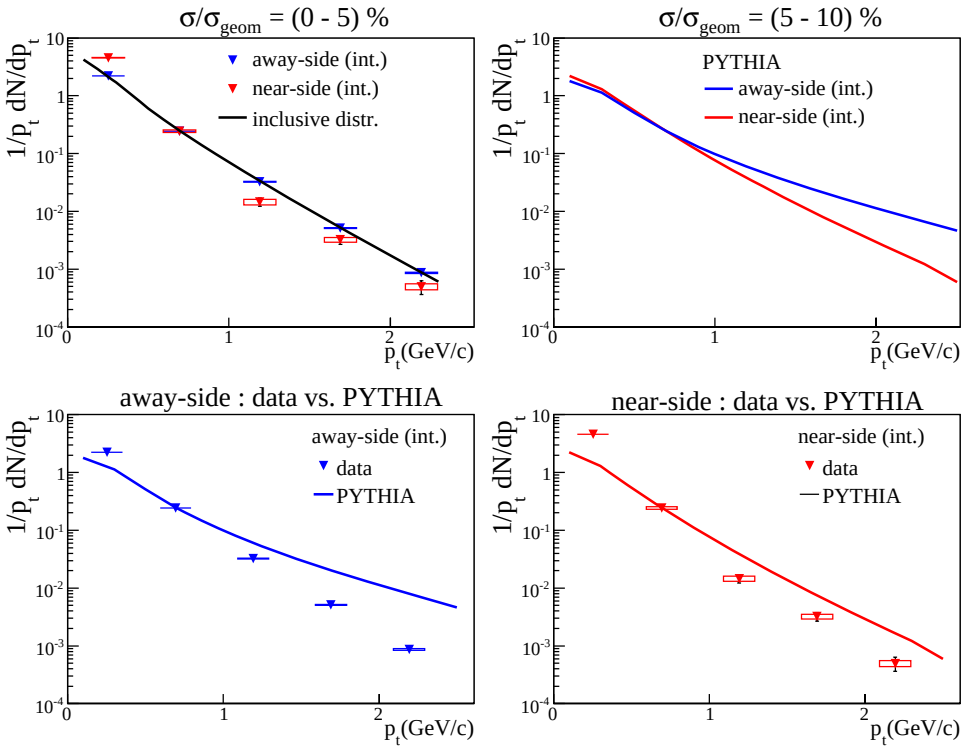

Figure 9.7: Top left: p_t-dependence of the integrated yield of near- and away-side compared to the p_t-distribution of hadrons in the associate range. Top right: Yields as determined by PYTHIA simulations. Bottom panels: comparison of PYTHIA results to yields extracted from the Pb-Au data.

p_t the shape of the conditional yield is more consistent with the PYTHIA results on the near- than on the away-side where the measured conditional yield falls off steeper as compared to the PYTHIA results.

9.5 $\Delta\phi - \Delta\eta$ correlations

A two-dimensional picture of high-p_t jet-like correlations can be obtained by analyzing the two-particle correlations as function of $\Delta\phi$ and $\Delta\eta$ of trigger and associate pairs.

Results for p-p collisions from PHENIX at $\sqrt{s}$=200 GeV [68] show a narrow jet-peak of 0.3 in $\Delta\eta$ on the near-side. The away-side however is washed out over a wider range in $\Delta\eta$. In A-A collisions results from RHIC [68],[69],[70],[71],[72] show a conditional yield which is significantly broadened also on the near-side and does not reach zero yield at high $\Delta\eta$. This phenomenon is denoted as the ridge and is a field of intense investigation. Incerasing the p_t of trigger and associate particles, the peak structure is more pronounced on the near-side in $\Delta\eta$ and the ridge like structure disappears.

The ridge in the $\Delta\eta$ yield is, among others, [73],[74],[75],[76] discussed as to

arise due to momentum kicks jet-partons transfer to the deconfined medium on the near-side [77].

In this thesis the construction of the correlation function in $\Delta\phi - \Delta\eta$ is done in the same way as for the analysis of the $\Delta\phi$ correlations by dividing a signal- by a mixed event distribution. Examples of correlation functions in $\Delta\phi - \Delta\eta$ are shown in the top panels of Figure 9.8. The strength of the flow modulation is assumed to be independent of $\Delta\eta$. The v_2 values and the extracted b parameter describing the level of the flowing background is chosen as determined from the ZYAM method from the two-particle $\Delta\phi$ correlation analysis. The jet like-yield is obtained by subtracting the two-dimensional flow contribution and scaling it by the number of associates per trigger.

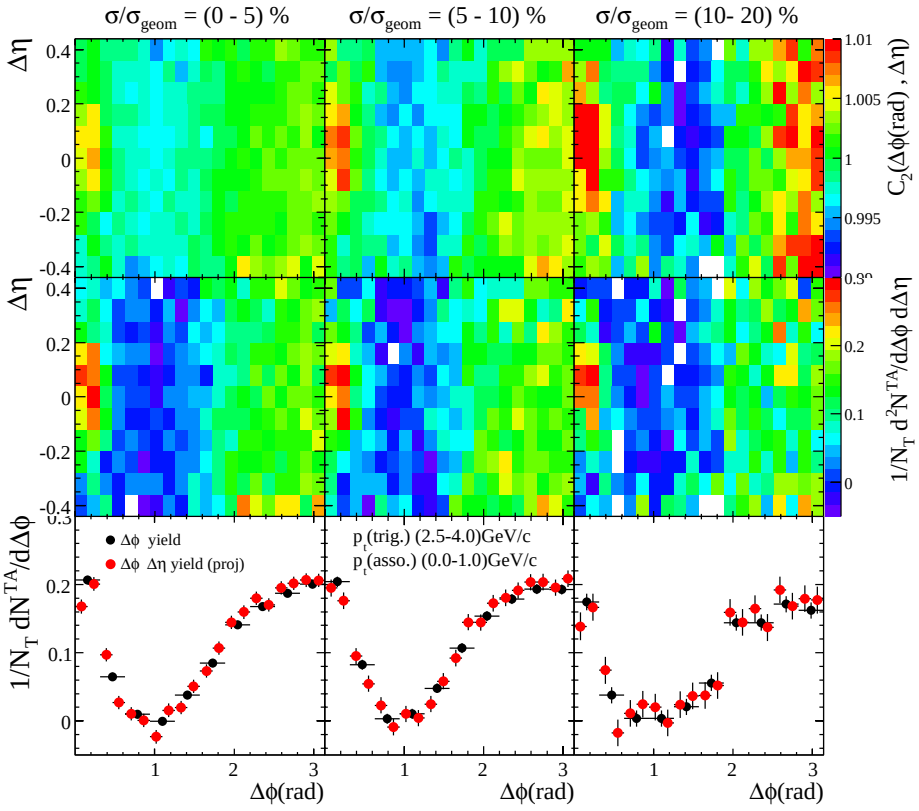

Figure 9.8: Top panels: $\Delta\phi$-$\Delta\eta$ correlation functions for three different centrality bins. Middle panels: corresponding conditional yield. Bottom panels: Comparison of the projection of the $\Delta\phi$-$\Delta\eta$-yield on $\Delta\phi$ to the results from the two-particle $\Delta\phi$ analysis. (p_t(T)=(2.5-4.0) GeV/c, p_t(A)=(0.0-1.0) GeV/c).

Assuming a uniform distribution of the associates in $\Delta\eta$ the yield is normalized to the acceptance window in $\Delta\eta$ and $\Delta\phi$. The acceptance is limited to $\Delta\eta$<0.5. The middle panels of Figure 9.8 show the extracted conditional yield for small p_t values of the associates. The near-side shows a pronounced peak with a

width of approx. 0.25 in $\Delta\eta$. The width on the near-side in $\Delta\phi$ is as well of the order of 0.25. To compare the measured widths in the two variables $\Delta\eta$ is transformed to the corresponding difference in polar angle $\Delta\theta$ in the pair center of mass system for triggers around η=2.3.
The corresponding width in the polar angle is $\Delta\theta$=0.25 as is the width in $\Delta\phi$. In the center of mass frame the near-side has a ringlike shape around the trigger as is expected from symmetry reasons for fragmentation around a jet-axis.

The away-side shows a broad distribution without big variations over the acceptance. The yield on the near-side does not approach 0 in the most central bin but is consistent with 0 in the more peripheral bins at the edge of the acceptance.

As a consistency check the $\Delta\phi - \Delta\eta$ yield is projected on $\Delta\phi$ and compared to the yield as obtained from the $\Delta\phi$ correlation analysis. The projection agrees well with the results from the integrated $\Delta\phi$ analysis. For low p_t-associates no double humped structure is observed on the away-side.

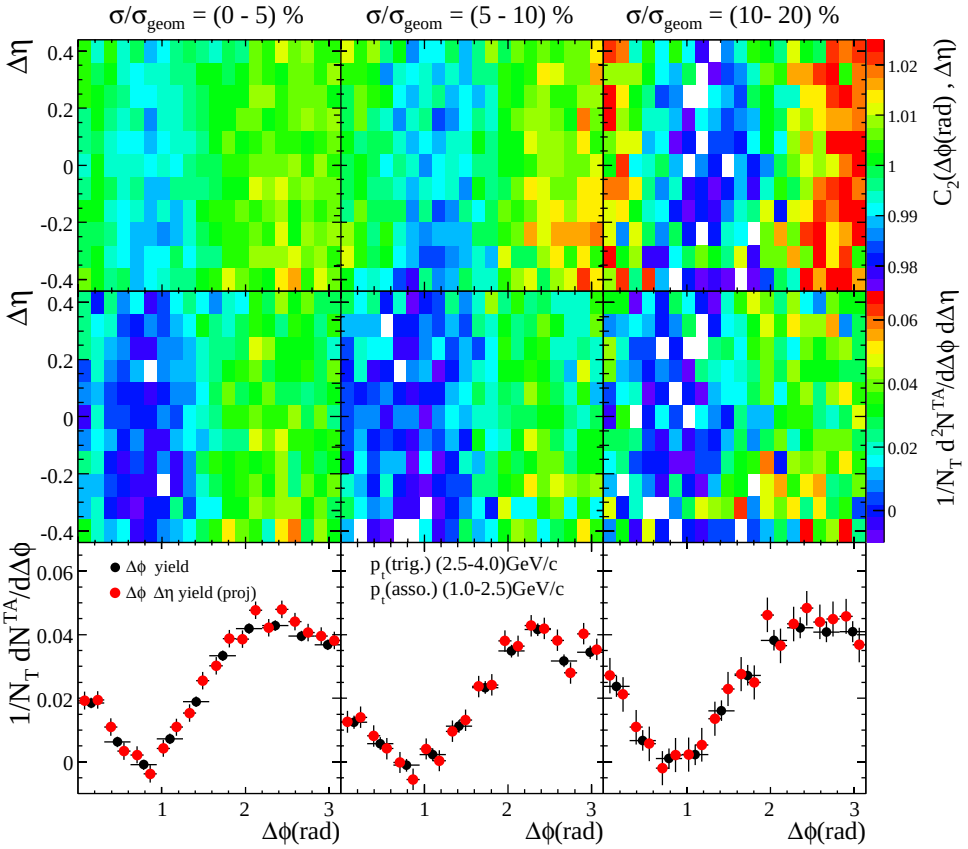

Figure 9.9: Top panels: $\Delta\phi$-$\Delta\eta$ correlation function for three different centrality bins. Middle panels: corresponding conditional yield. Bottom panels: Comparison of the projection of the $\Delta\phi$-$\Delta\eta$-yield on $\Delta\phi$ to the results from the integrated $\Delta\phi$ yield. (p_t(T)=(2.5-4.0) GeV/c, p_t(A)=(1.0-2.5) GeV/c).

Increasing the associate p_t to p_t(A)=(1.0-2.5)GeV/c (Figure 9.9) the peak structure on the near-side is spread over the whole acceptance in $\Delta\eta$. No significant change is observed for the three different centrality bins.
On the away-side a broad distribution in $\Delta\eta$ approximately constant over the whole acceptance is observed as for the lower p_t bin. However, the projections showing the double-humped structure on the away-side. No systematic errors are studied for the $\Delta\eta - \Delta\phi$ yield. A scan of the trigger and the associate p_t as for the integrated analysis of the $\Delta\phi$ correlations is performed depending on the charges of the trigger and associate particles.
The extracted yields for all combinations of trigger and associate charges is shown in Figure 9.10. The yields for increasing associate p_t are scaled in order to show the yields in the same range as for the lowest associate-p_t bin.

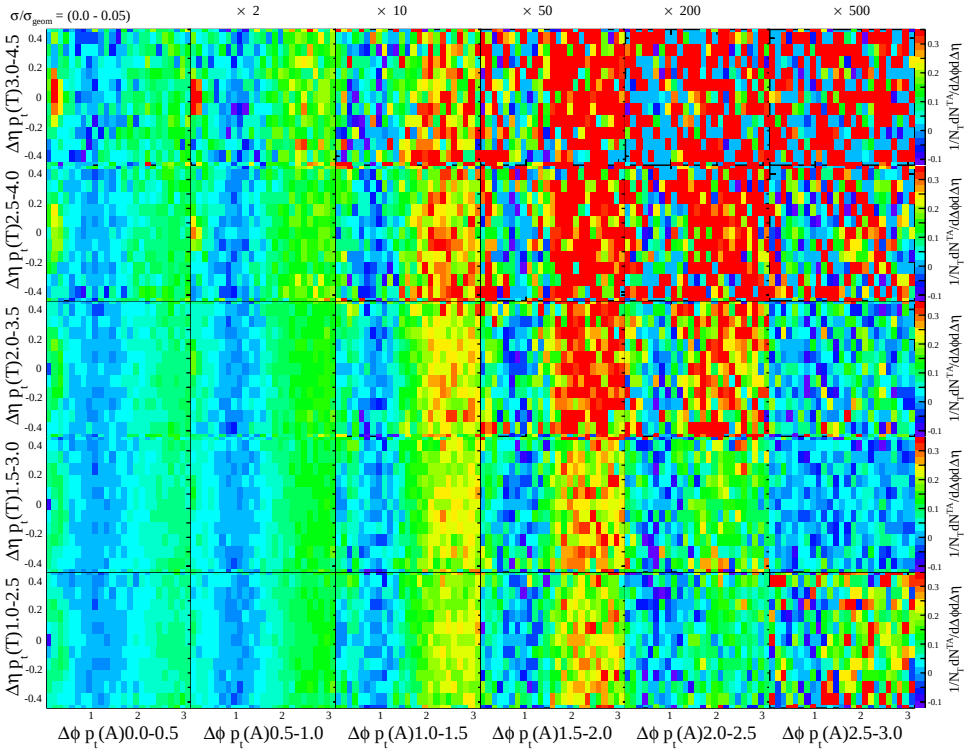

Figure 9.10: $\Delta\phi$-$\Delta\eta$ conditional yield as function of the trigger- and associate p_t range (p_t(A), p_t(T) given in GeV/c) for all charge combinations of trigger and associate particles (σ/σ_{geom}=(0.0-5.0)%)

For small associate p_t the peak on the near-side yield increases with trigger p_t. Due to the increasing statistical uncertainties no such trend can be observed in the high p_t region. The peak on the near-side gets broader with increasing associate p_t. Decomposing trigger and the associate charges the peak on the near-side is only pronounced for unlike combinations of trigger and associate charges. The correlation functions and the extracted yields as function of p_t for the different charge combinations of trigger and associates is shown in Ap-

pendix B.3.
For small trigger and associate p_t a dip is observed on the near-side which spans out to $\Delta\eta$=0.15. This corresponds to a difference in θ which is far off the two-track inefficiency as determined from the difference in the opening angle in section 6 of about 10 mrad. A possible explanation of this dip might be the momentum balance of the fragmentation products relative to the leading parton. If a particle is fragmenting with non-zero transverse momentum relative to the jet-axis this momentum has to be balanced by the following fragmentation products. This effect is more pronounced in case of only a small number of fragmenting particles as is the case at SPS energy.
The pronounced observation of this effect for unlike charge combinations might as well be attributed to the charge correlation in the fragmentation process. Positive and negative particles following closely each other have to balance the

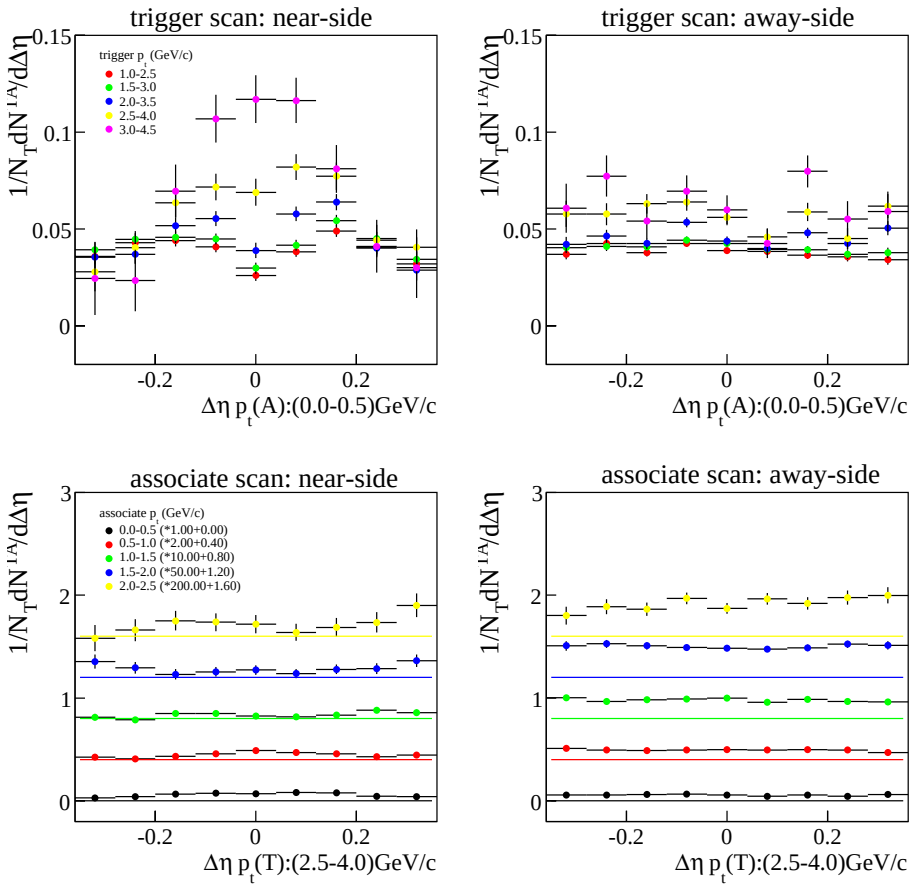

Figure 9.11: Projections of the near- (left) and the away-side (right) on $\Delta\eta$ over 1.0 rad in $\Delta\phi$. Top panels: Dependence on trigger p_t for associate p_t of (0.0-05) GeV/c. Bottom panels: Dependence on associate p_t for triggers with p_t of (2.5-4.0)GeV/c. For better presentation an increasing offset is added to the yield for increasing associate p_t.

transverse momentum of each other. For like-sign combinations this effects is reduced due to possible intermediate particles balancing the momentum.

In Figure 9.11 the projections on the near- and the away-side of the yield from Figure 9.10 are shown for different trigger and associate p_t ranges.
For small associate p_t the near-side evolves from a dip to a pronounced peak for triggers with p_t=(3.0-4.5) GeV/c. This can again be understood as to arise due to energy and momentum conservation. Due to energy conservation the higher the trigger p_t the smaller the momentum transverse to the initial parton direction will be given a fixed parton energy. The momentum to balance and hence the opening angle of following associate particles decreases leading to the observed peak at high trigger p_t.
For all trigger p_t a non-vanishing yield is observed on the edges of the acceptance. As already discussed for the two-dimensional representation, the near-side is broadened for higher associate p_t as shown in the bottom left panel of Figure 9.11. For a better representation the results are scaled and added by an offset. The offset is shown by the colored lines. Due to the large statistical errors for higher associate p_t no clear evolution of the shape of the yield can be observed.

The yield ratios show that the charge composition is consistent with vacuum properties on the near-side in the range p_t(A)=(1.0-2.5)GeV/c and p_t(T)=(2.5-4.0)GeV/c. The basic expectation would be the observation of a peak structure also in $\Delta\eta$ for this kinematical region. It might be that the broad structure is an artifact of an increasing dip on the near-side due to the higher required associate p_t and the kinematical effects discussed above. Those kinematical effects would, on the other hand, not alter the charge composition of the observed particles.

10 Results on three-particle correlations

10.1 Analysis strategy

The procedure to extract the three-particle jet-like correlations described in section 2.2 assumes three-particle signal- and background distributions already being corrected for non-uniformities in the detector efficiency.

The correction procedure the author of [49] follows is based on applying weights to triplets of trigger and associates according to the product of the pair efficiency. The efficiency is determined from the two-particle $\Delta\phi$ distribution of trigger associate pairs for different kinematical regions and for different charges and centralities separately and is normalized to unity. In this way, only the non-uniformity of the efficiency is corrected but not the overall efficiency of the detector.

In this thesis a different approach is followed, dividing the Signal and the background components affected by the efficiency by mixed-event distributions where trigger and associates stem from three different events. Otherwise the same kinematical constraints are used for the mixed event distribution as for the Signal and the background components.

In the following a detailed description of the construction and the decomposition of the three-particle Signal and the background contributions, the efficiency correction and the normalization of the different components is given. The results are presented as function of the charge combination of the associates and the as function of the centrality of the collisions.

10.2 Construction of the Signal and the Background components

10.2.1 Signal distribution

The three-particle Signal is constructed by combining trigger particles with pairs of associated particles taken from the same event. The differences in the azimuthal angles with respect to the trigger particle ($\Delta\phi_1$,$\Delta\phi_2$) are filled in two dimensional histograms (Figure 10.1, left). Projecting the two-dimensional three-particle distribution onto one axis (Figure 10.1,right), the two-particle $\Delta\phi$ distribution as depicted in Figure 2.1 is recovered (scaled by the number of associates at a given $\Delta\phi$). Each triplet is rotated such that the azimuthal angle of the trigger is 0, the azimuthal angles of the associates ranging from $\Delta\phi = 0{-}2\pi$. Each pair of associates is counted twice ($\Delta\phi_1$,$\Delta\phi_2$) and ($\Delta\phi_2$,$\Delta\phi_1$)

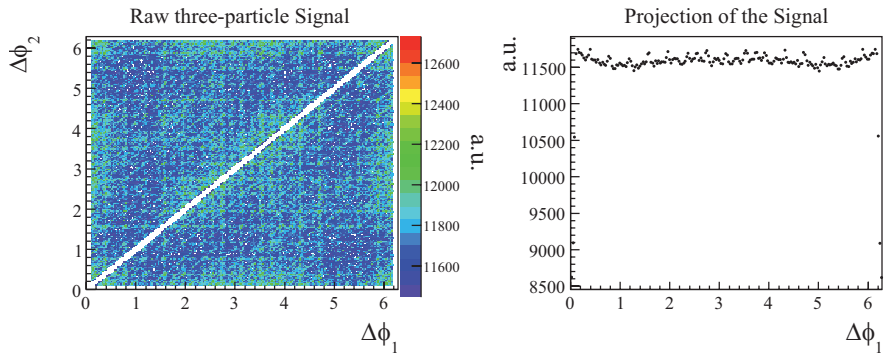

Figure 10.1: Raw three-particle Signal (left) and projection of the Signal distribution on $\Delta\phi_1$ (right).

by looping over all associates from an event and combining the particles with each associate (except the same associate) from the same event. This results in $(N_A(N_A-1))$ pairs of associates for each trigger, N_A being the number of associate particles in on event. Therefore, the signal distribution is by definition symmetric to the diagonal of the distribution $\Delta\phi_1 = \Delta\phi_2$.

10.2.2 Soft-Soft background

For the Soft-Soft background component (Figure 10.2) two associated particles from an event without trigger criterion but otherwise from the same centrality sample as the trigger are combined with a trigger from a different event. As described in detail in section 2.2.4, this distribution accounts in part for the flow correlations. In addition, jet-like correlations among the associates in triggered events from additional jets other than the jet which was triggered on are accounted for by this construction.

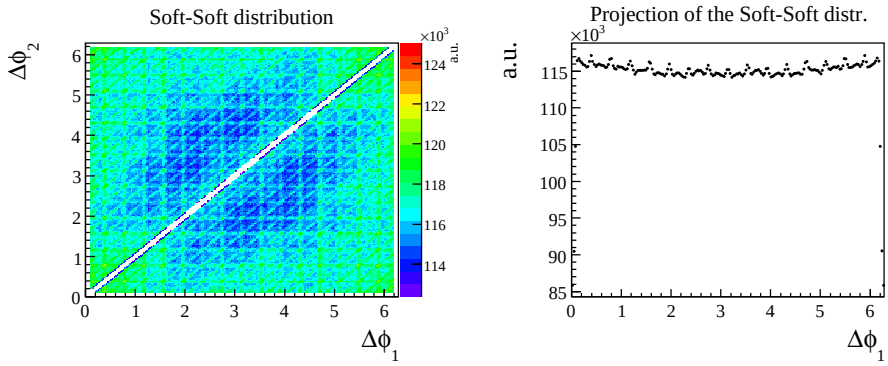

Figure 10.2: Raw three-particle Soft-Soft background distribution (left) and projection on $\Delta\phi_1$ (right).

As for the signal distribution all associate pairs are filled twice. To further

reduce the statistical uncertainties in this distribution for each trigger entering the signal 10 event are used to build up the Soft-Soft distribution.

10.2.3 Trigger-Flow background

The signal contribution where all three particles stem from the background (flow) is already accounted for in part by the Soft-Soft -background as described in the last section. The remaining flow correlation (Eq. (10.1)) is added to the Soft-Soft background such that the Soft-Soft + Trigger-Flow contribution contains the complete flow correlation term according to Eq. (2.14). In order to account for subtle differences between $< v_2^T >< v_2^A >$ and $< v_2^T v_2^A >$ the trigger flow contribution is calculated triplet wise, with v_2 values determined depending on centrality, charge and transverse momentum of the particles. To construct the Trigger-Flow background, triggers combined with two particles from two different inclusive events are filled in a separate histogram. For each triplet a weight w_{tf} is applied in the form:

$$w_{tf} = (2v_2^T v_2^1 \cos 2(\Delta\phi_1) + 2v_2^T v_2^2 \cos 2(\Delta\phi_2)). \tag{10.1}$$

The normalization to the number of associate pairs in inclusive events according to Eq. (2.16) is generated by looping over all associates in mixed inclusive events. The different pair statistics in mixed inclusive events for the Trigger-Flow and inclusive events in the Soft-Soft background is accounted for by applying an additional weight to the Trigger-Flow distribution in the form: $\frac{<N_{inc}(N_{inc}-1)>}{<N_{inc}>^2}$. The resulting Trigger-Flow addon is shown in Figure 10.3. In contrast to the Signal and the Soft-Soft distribution, the symmetrization cannot be obtained by combining each associate from one mixed event with all associates from the second event, since the two events contain different particles. In order to achieve the symmetrization, each pair of associates is filled explicitly twice just alternating the two azimuthal differences filling the histogram. This results in a $2 < N_{inc} >^2$ pairs of associates for each trigger in the mixed event distribution.

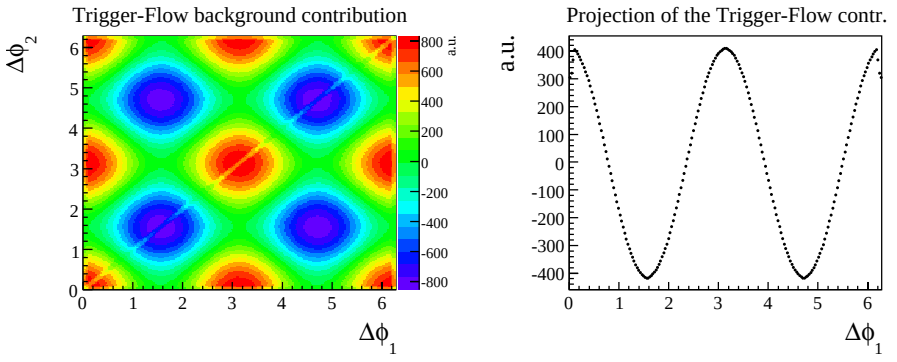

Figure 10.3: Trigger-Flow contribution to the correlation signal (left) and projection on $\Delta\phi_1$ (see text for details).

10.2.4 Hard-Soft background

With the knowledge about the two-particle conditional yield and the background level in triggered events the Hard-Soft background can directly be constructed by the functional form of Eq. 2.15. In order to facilitate the analysis for different bin sizes of the afore discussed histograms, the two-particle conditional yield is fit with a polynomial. Afterwards each bin of a two dimensional histogram with the same bin size as the signal distribution is filled with a weight according to Eq. 2.15.
This term can directly be subtracted from the properly normalized and efficiency corrected signal distribution. If the three-particle signal distribution has only been corrected for non-uniformities in the efficiency as discussed above, the conditional yield taken as an input must not to be corrected for the overall pair efficiency in the form of Eq. 2.10. The Hard-Soft background contribution is shown in Figure 10.4.

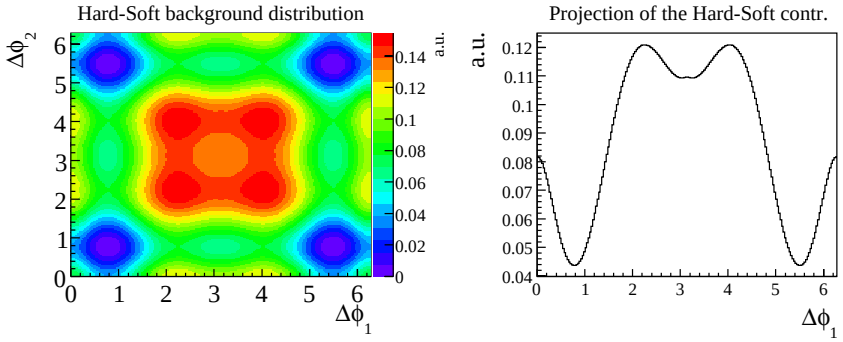

Figure 10.4: Hard-Soft background contribution (left) and projection on $\Delta\phi_1$ (right).

10.3 Efficiency correction and normalization

The efficiency correction is done by dividing the Signal, the Soft-Soft distribution and the Trigger-Flow distribution by mixed event distributions M_3 where all three particles stem from different events. In order to leave the absolute magnitude of the distributions unchanged the distributions are scaled afterwards by the mean bin content μ_{bin} of the mixed event distributions in the form:

$$\mu_{bin} = \frac{\int M_3}{nb_x \cdot nb_y} \tag{10.2}$$

nb_x and nb_y denoting the number of bins of the two dimensional histograms. The mixed event distribution for the signal distribution is constructed from a trigger and two associated particles from two different triggered events.
For the construction of the Soft-Soft and the Trigger-Flow background, associates are taken from inclusive events. For the corresponding mixed-event

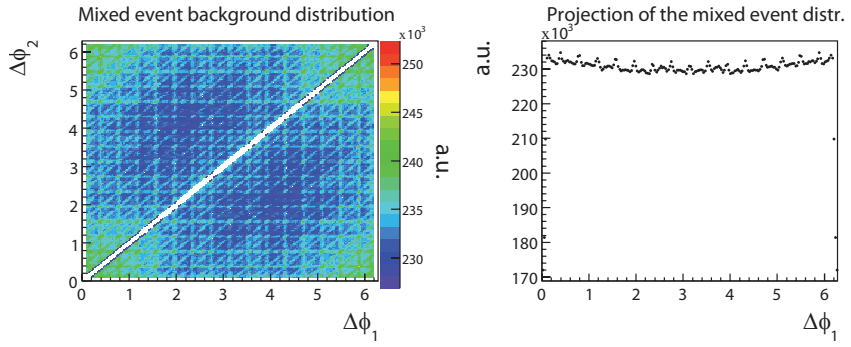

Figure 10.5: Three-particle mixed event reference distribution (left) and projection on $\Delta\phi_1$ (right).

distribution a trigger is therefore combined with two associates from two different inclusive events. However, within statistical uncertainties no differences in the non-uniformity of the two different mixed event samples are observed. An example of the mixed-event reference distribution where trigger and associates are taken from three different triggered events is shown in Figure 10.5.

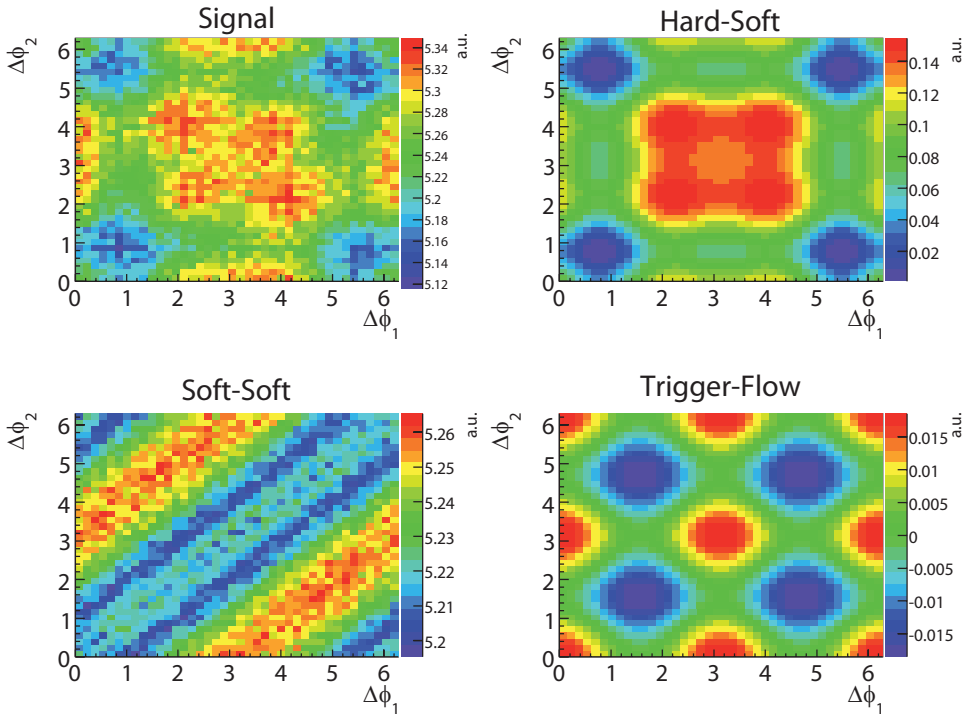

Figure 10.6: Three-particle correlation Signal and background distributions corrected for non uniformities in the acceptance and normalized according to Eq. 10.3.

The efficiency corrected distributions are normalized to the acceptance by $1/(2\pi)^2$ and divided by the bin widths of the two dimensional histograms bw_x and bw_y. The functional form of the efficiency correction of the signal contributions S_3 and the normalization is given by:

$$S_3 = \frac{1}{n_s}\frac{1}{(2\pi)^2}\frac{1}{bw_x bw_y}\frac{1}{N_T}\frac{J_3}{M_3}\frac{\int M_3}{nb_x \cdot nb_y}, \tag{10.3}$$

J_3 and M_3 corresponding to Signal, Soft-Soft and Trigger-Flow (J_3) distributions and the corresponding mixed event distribution (M_3) respectively. The Trigger-Flow distribution is constructed weighting pairs from three different events. As described in section 10.2.3 the symmetrization is achieved by filling each pair explicitly twice into the histogram. The normalization to the mixed event distribution, which is also constructed from three different events is also symmetrized, however the efficiency correction according to Eq. 10.2 leaves the overall level of the distributions unchanged. To account for the symmetrization the factor $n_s = 1; 2$ is applied.
Signal, Soft-Soft- and Trigger-Flow contributions divided by the mixed-event reference distribution and rescaled by the mean bin content of the mixed-event distributions are shown in Figure 10.6.
Projections of the different components over 1.2 rad in $\Delta\phi_2$ are shown in Figure 10.7.

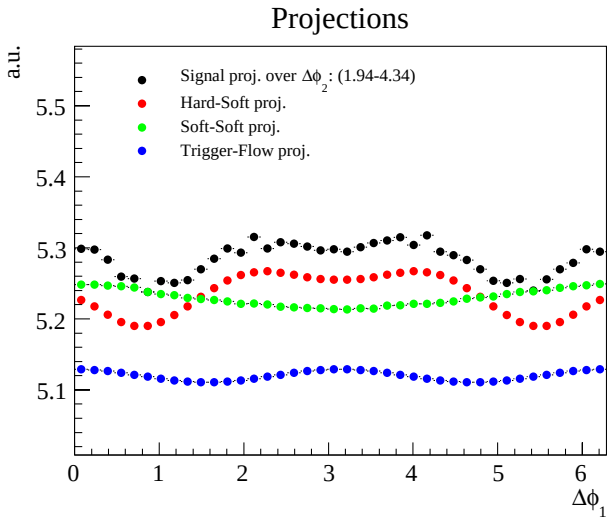

Figure 10.7: Projections of three-particle Signal and the background components from Figure 10.6 on $\Delta\phi_1$ (normalized to the number of bins in the projection range).

Hard-Soft and Trigger-Flow component are added with an offset in order to be able to compare the different modulations in the distributions on the same scale.

10.4 Background subtraction and three-particle jet yield

After normalization and efficiency correction the subtraction of the background components is performed according to Eq. (2.21). The Hard-Soft background is subtracted from the signal distribution. The result is shown in the top left panel of Figure 10.8. The Trigger-Flow contribution is added to the mixed event inclusive distribution (Figure 10.8 top right). The difference in the mixed event inclusive statistics and the triggered events is accounted for by scaling the Soft-Soft + Trigger-Flow component by the ratio of the statistics in triggered and inclusive events according to Eq. (2.20).
In the next step, the Soft-Soft+Trigger-Flow term is adjusted to the Signal-Hard-Soft distribution by a ZYAM method. Assuming Zero Yield At Minimum for the two-particle conditional jet yield it follows that the three-particle conditional yield also has to show Zero Yield At the Minimum of the two-particle conditional yield. For the angle at the minimum of the two-partice conditional yield the yield should by zero for all angles of the second associate and vice versa. This would also hold for the projection of the yield on either axis which would result in a scaled two-particle conditional yield distribution.
The Zero Yield At Minimun condition is determined by the projection of the Signal-Hard-Soft and the Soft-Soft+Trigger-Flow distribution on $\Delta\phi_1$ and $\Delta\phi_2$. The projections are shown in the middle panel of Figure 10.8. The Soft-Soft+ Trigger-Flow component is scaled such that both projections have the same value at a defined minimum. The position of the minimum is determined from the two-particle conditional yield which is $\Delta\phi_{min} = 0.8$. At this position the ratio of the projections is determined. To reduce the impact of statistical fluctuations the ratio is constructed as the mean ratio of the bin contents at $\Delta\phi =$ 0.8 and $\Delta\phi = 2\pi$-0.8 in the $\Delta\phi_1$ and $\Delta\phi_2$ projections.

The scaled Soft-Soft+Trigger-Flow distribution is shown in blue open circles in the middle panel of Figure 10.8. As a systematical check the ZYAM is determined from an area of 0.2 around the minimum $\Delta\phi_{min}$ of the two-particle conditional yield as well. As before the ratio of the mean bin contents in the two distribution is used to scale the Soft-Soft+Trigger-Flow distribution. No significant difference is observed. A stable fit to the projection of the distributions as applied for the determination of the two-particle conditional yield can not be performed. As can already be seen from the projections of the distributions in the middle panel of Figure 10.8 no clear signature in the Signal-Hard-Soft distribution deviating from the Soft-Soft+Trigger-Flow distribution can be observed.

Subtracting the Soft-Soft+Trigger-Flow distribution scaled by the ZYAM condition we obtain the three-particle conditional yield as in the bottom left panel of Figure 10.8. Within the statistical uncertainties no signal can be observed. Projecting the three-particle yield on either axis (bottom right panel in Figure 10.8 an indication of a slight dip at π is observed. However, the statistical fluctuations are to big to draw conclusions about the shape of the two-dimensional three-particle conditional yield.

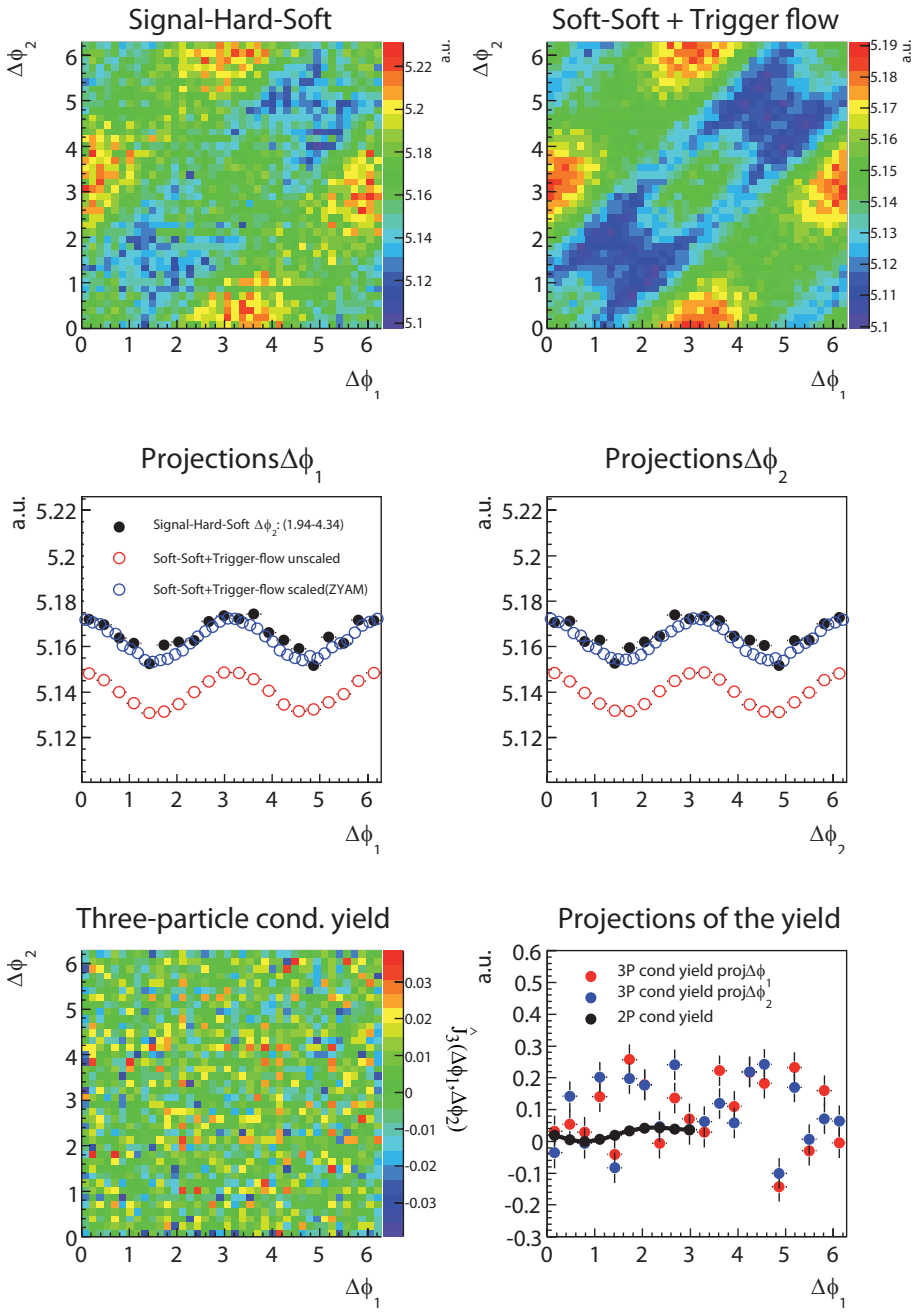

Figure 10.8: Top: Signal subtracted by the Hard-Soft component (left). Soft-Soft background added by the Trigger-Flow component (right). Middle: Projections on $\Delta\phi_{1/2}$ (left/right) of the Signal-Hard-Soft distribution (full black circles) and Soft-Soft + Trigger-Flow distribution unscaled (open red) and scaled according to ZYAM (open blue). Bottom: Three-particle conditional yield obtained by subtracting the scaled (ZYAM) Soft-Soft+Trigger-Flow component from the Signal-Hard-Soft component (left). Projection of the yield on $\Delta\phi_{1/2}$ (red/blue) compared to the two-particle conditional yield (black).

10.5 Centrality dependence of the three-particle jet yield

The centrality dependence of the different signal components is shown in Figure 10.9.

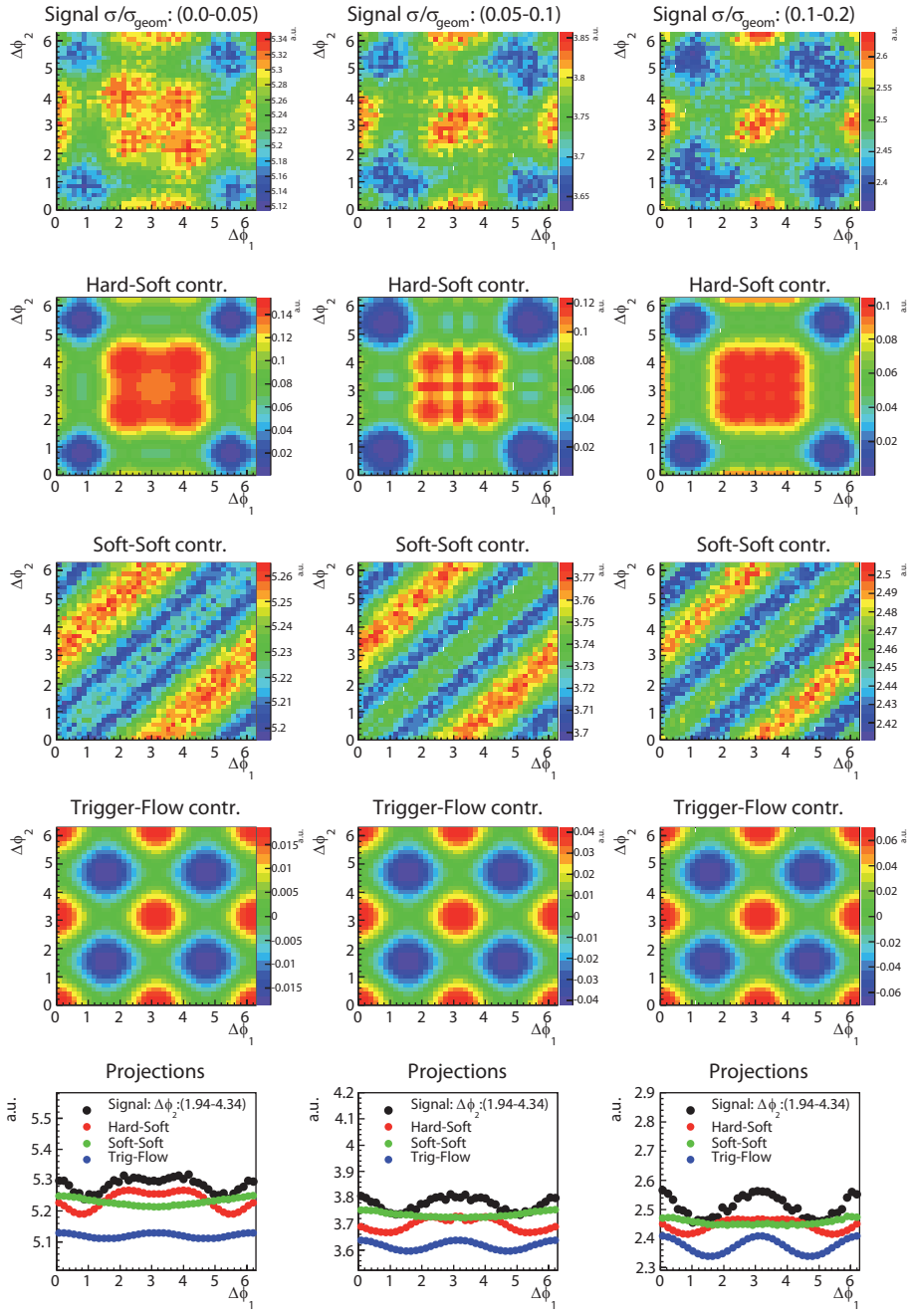

Figure 10.9: Normalized and efficiency corrected Signal and background components for three different centrality classes and projections of the components on $\Delta\phi_1$ (bottom row).

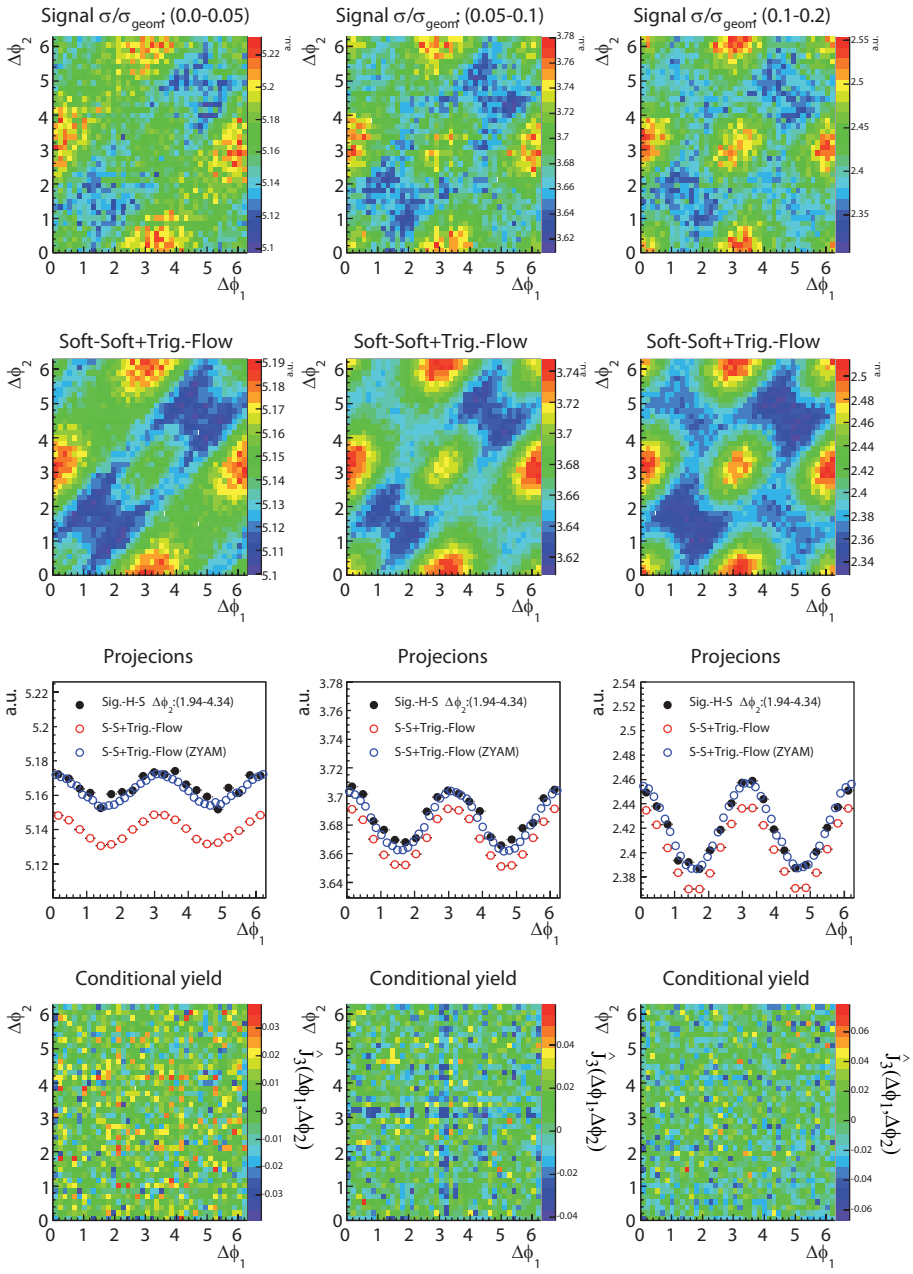

Figure 10.10: Top: Signal-Hard-Soft components for three different centrality classes. Second row: Soft-Soft+Trigger-Flow component. Third row: Projections for scaled and unscaled Soft-Soft+Trigger-Flow contribution (see Figure 10.8) Bottom row: three-particle conditional yield.

As in the case of two-particle correlations the impact of the elliptic flow increases with decreasing centrality. This is clearly observed in the Signal (Figure 10.9, first row) and the Soft-Soft (Figure 10.9, third row) distribution. While for

the most central bin (σ/σ_{geom}=(0-5)%) the Hard-Soft component dominates the flow modulation, the flow modulation is more pronounced in the most peripheral bin (σ/σ_{geom}=(0-5)%, Figure 10.9, right column). With decreasing centrality the signal distribution approaches the shape of a three-particle flow correlation which is shown in the left panel of Figure 3.7 (row d)). Here the complete three-particle flow correlation term is shown. The Trigger-Flow correlation as shown in the fourth row of Figure 10.9 only accounts for part of the three-particle flow correlation.
The increasing flow impact is also seen in the Soft-Soft term which is increasingly symmetric to the diagonal of the distribution. As for the most peripheral bin, the Hard-Soft and Trigger-Flow background are constructed from the known two-particle conditional yield and the p_t- and charge dependent elliptic flow parameters.

The signal distribution subtracted by the Hard-Soft background and the Soft-Soft contribution added by the Trigger-Flow contributions are shown in Figure 10.10. The Soft-Soft+Trigger-Flow contribution now contains the full three-particle flow correlation and resembles closely a pure three particle flow correlation pattern in the most peripheral bin. This indicates again the strong impact of the flow correlation in the analysis. The two components are adjusted by the ZYAM method as described in the last section. The projections of Signal-Hard-Soft and Soft-Soft+Trigger-Flow component used to determine the ZYAM scaling factor are shown in the third row of Figure 10.10.

As for the most central bin, subtracting all two-particle and the tree-particle flow-like correlations no significant pattern in the three-particle conditional yield is observed.

10.6 Charge dependence of three-particle correlations

The three-particle Signal and the three particle Soft-Soft distributions are shown in Figure 10.11 for different charge combinations of the associated particles.

The distinct difference along the diagonal of the distribution can be attributed to the jet-like two-particle correlations. As discussed in section 9.2 like-sign charge combinations of jet-like trigger-associate pairs are suppressed on the near-side as compared to unlike-sign combinations. This is reflected in the Soft-Soft background showing a more pronounced positive correlation along the diagonal of the distribution as compared to the case of the unlike-sign combinations of associate pairs.
This indicates that a significant amount of low-p_t jets is contained in the associate range showing charge correlations as in the case of high-p_t jets which are however uncorrelated to the trigger. Due to the even smaller statistics as in the case considering all charge combinations of trigger associate triplets, no significant signal can be extracted from the measurement.

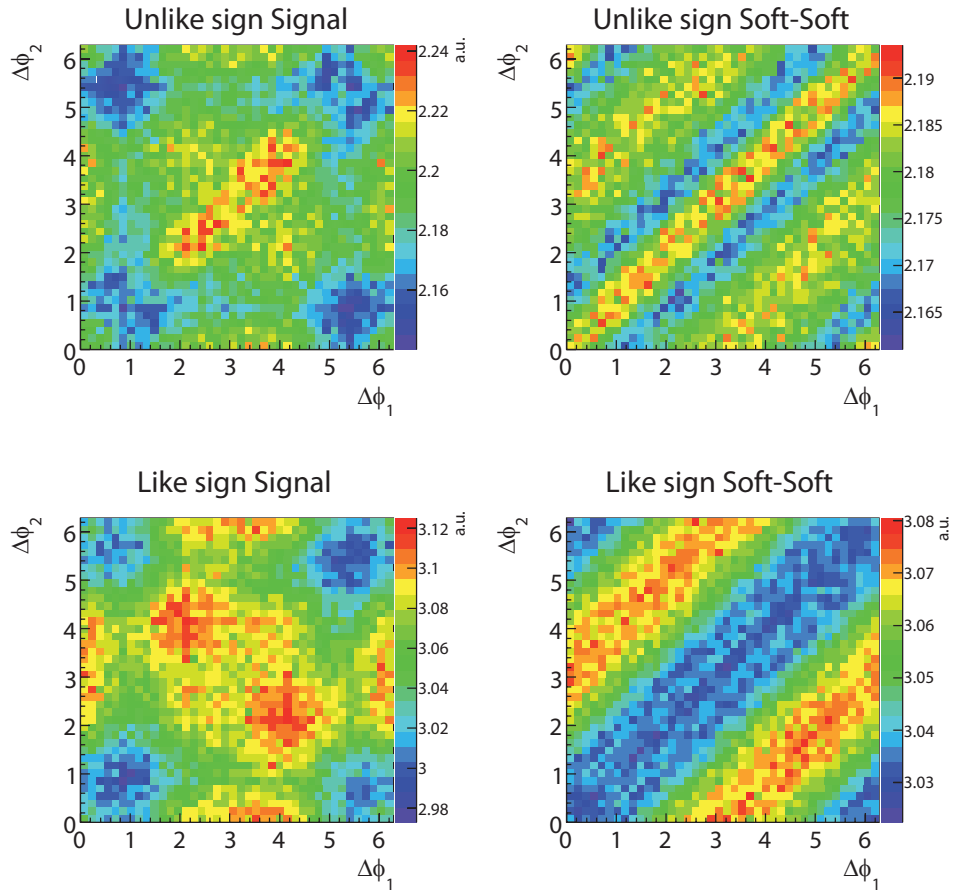

Figure 10.11: Top: Signal- (left) and Soft-Soft component (right) for oppositely charged associates. Bottom: Signal- (left) and Soft-Soft component (right) for like sign charge associates.

10.7 Systematic uncertainties

Besides the limitations posed by the high statistics required to measure a clear three-particle jet yield signal there are several systematical uncertainties connected to the presented analysis.
The major uncertainties are the model used to subtract the background components and the uncertainties in the two-particle results used as an input. The major ingredients to extract the two-particle conditional yield are the elliptic flow, measured by the reaction plane method, and the assumed Zero Yield At Minimum method used to subtract the background components from the correlation signal.

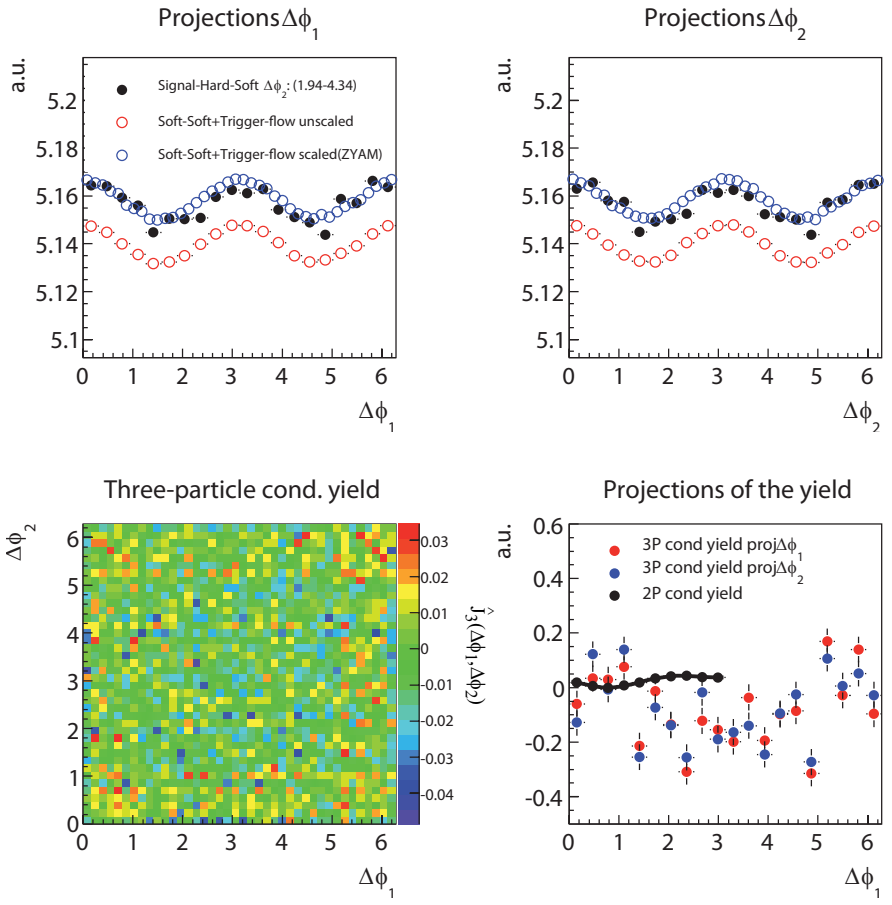

Figure 10.12: Top: Projections of Signal-Hard-Soft- (black) and Soft-Soft+Trigger-Flow contributions scaled (blue) and unscaled (red) by the ZYAM method. Trigger-Flow and Hard-Soft component are scaled by a factor of 0.9 and 1.1 respectively. Bottom: Three-particle conditional yield (left) and yield projected on $\Delta\phi_1$ in comparison to the two-particle conditional yield (right).

The Zero Yield At Minimum condition is maintained in the study. Even with a significant broadening of the vacuum conditional yield due to medium interactions in heavy ion collisions on the away-side, a minimum close to zero can be assumed. This can be seen from PYTHIA simulations (Figure 9.3) where a broad region of very small conditional yield is observed. Relaxing the ZYAM condition would make a systematic study less feasible since further assumptions about the deviation from the ZYAM condition would have to be imposed. In addition, the assumptions would have to be relaxed in the two- as well the three-particle analysis together.
The flow modulation for the systematic check presented is quantified by v_2 and varied by approximately 10%. The strength of the flow and the extracted two-

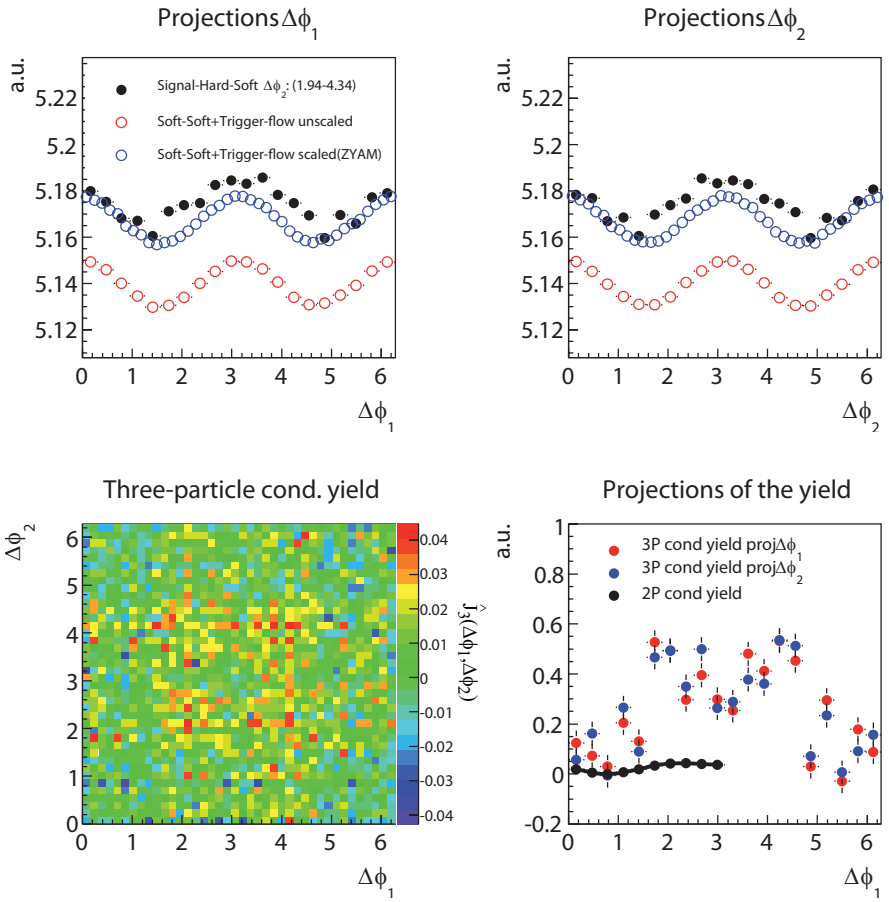

Figure 10.13: Top: Projections of Signal-Hard-Soft- (black) and Soft-Soft+Trigger-Flow contributions scaled (blue) and unscaled (red) by the ZYAM method. Trigger-Flow and Hard-Soft component are scaled by a factor of 1.1 and 0.9 respectively. Bottom: Three-particle conditional yield (left) and yield integrated on $\Delta\phi_1$ in comparison to the two-particle conditional yield (right).

particle conditional yield are assumed to be correlated such that an increasing flow modulation diminishes the integrated extracted conditional yield. In a first study the v_2 contribution is reduced by approximately 10% just scaling the Trigger-Flow distribution by 0.9. In the same way the Hard-Soft term is scaled by 1.1 (Figure 10.12).
The projection on the $\Delta\phi$-axis of the Signal subtracted by the Hard-Soft term and the Soft-Soft term added by the Trigger-Flow is shown in the top panel of the Figure 10.12. No significant difference between the Signal and the Soft-Soft+Trigger-Flow component scaled by the ZYAM method is observed. Accordingly no significant structure is observed in the three-particle conditional yield as seen before in the data. Only a slight indication of a minimum in the center of the distribution is observed.
Reducing the observed Hard-Soft term by scaling it with a factor of 0.9 and increasing the Trigger-Flow contribution by 1.1 (Figure 10.13) on the other hand, a slight enhancement of the Signal over the background components can be observed. An indication of two maxima off the diagonal and two on-diagonal maxima can be observed. In this study, the results would favor a cone like emission of the particles associated to a hard trigger particle. However, no final conclusion about a scenario underlying the three-particle correlations can be drawn.

11 Summary and Conclusions

In this chapter a brief summary of the results presented in this thesis is given. The results are discussed in the context of other experimental results at higher beam energies and with respect to limitations and improvements of the measurements at SPS energy.

Two-particle correlations

The triggered two-particle correlations are analyzed as function of centrality of the collision, for different trigger and associates p_t-ranges and different charges of the particles.
As a major result of this thesis two distinct features of the correlations appear, discriminating the near- and the away-side of the correlation function.
The near-side shows a significantly smaller yield than the away-side with a yield that is more pronounced for unlike- than for like sign combinations of the particles. On the other hand, the away-side is always more pronounced for positive particles than for negative particles independent of the trigger charge.

There is no obvious charge correlation between the trigger and the associate particles on the away-side, since the particles on the away-side are supposed to stem from a different branch of the fragmentation process. The away-side associates are supposed to be charge correlated to a possible trigger particle on the away-side which is actually not triggered on. The dominance of positive particles can be understood to arise from a combination of initial state effects reflecting the kinematics of the incoming partons, and later stages of the collisions where traversing particles interact with the surrounding medium.

Two-particle correlations: charge correlation

The charge correlation on the near-side can be understood as to arise from charge correlation in the fragmentation processes favoring the fragmentation of a positive particle following a negative and vice versa. This observation is supported by PYTHIA simulations showing similar features on the near-side as observed in the data. Not only the gross features of the enhanced unlike sign pairs of particles is reflected in the simulations, but the ratios of negative over positive particles on the near-side is in remarkable agreement with results from PYTHIA simulations. This gives strong indication that the yield on the near-side actually shows the pattern of vacuum fragmentation.

Two-particle correlations: medium response

The dominance of the yield on the away-side for positive associate particles is also shown in the PYTHIA simulations, indicating that the dominance can

partly be attributed to the large net-baryon number in the SPS regime at mid rapidity.
This net-baryon dominance is also reflected in the charge composition of the medium. Thus, from the medium as for the vacuum fragmentation, a dominance of positive associates can be expected in Pb-Au collisions at SPS energy. This results in ratios of negative over positive particles on the away-side smaller one for positive and negative triggers.
However, the magnitude of the yield ratios differ significantly for the PYTHIA simulations and the data. For positive as for negative triggers the measured yield ratios are close to the medium expectation, whereas the PYTHIA yield ratio for positive particles is significantly higher and close to the expected value of one in case of zero baryon number in case of fragmentation to the vacuum. This indicates that in contrast to the near-side the yield on the away-side shows medium properties, and thus reflects the response of the medium to the jet-particles traversing it.

Combining the results from the near- and the away-side we conclude that the vacuum properties observed on the near-side cannot be an artifact of high-p_t particles traversing the medium without interacting with it. Therefore, the observations speak in favor for a surface emission of high-p_t particles in high energy heavy ion collisions in central Pb+Au collisions at top SPS energy.

Two-particle correlations: p_t-dependence of conditional yield

Besides the magnitude of the yield on the away-side and the yield ratios close to the bulk ratios, the away-side shape of the conditional yield shows a distinct double humped shape which is a further indication of interactions of the traversing particles with the medium.
Independent of the physical mechanism, interaction of high-p_t particles with the medium leads to a transfer from high-p_t to low-p_t particles.
Assuming surface emission and no preferred direction of the emission relative to the normal to the surface, medium effects would on average be most pronounced at $\Delta\phi$=180°. Regarding the p_t dependent integrated yield on the near-side as a reference, the away-side begins to fall off steeper at approximately 1 GeV/c. This is exactly where the dip in the correlation function on the away-side appears. In this respect, the decrease of the number of associates and the change of the shape in the away-side give a consistent picture in terms of a redistribution of momenta due to interactions of particles with the medium.

Two-particle correlations: $\Delta\phi$-$\Delta\eta$ correlations

A two dimensional analysis of the correlations in $\Delta\phi$ and $\Delta\eta$ shows an elliptic shape on the near-side with an opening angle in $\Delta\eta$ of 0.25 for small trigger and associate p_t (e.g. p_t(T)=(1.0-2.5) GeV/c, p_t(A)=(0.0-0.5) GeV/c) The structure evolves to a peak at $\Delta\eta$=0.0 for higher trigger p_t however the width of staying approximately constant.
In the pair center of mass frame the observed shape shows a ringlike shape with

radius $\omega = 0.25$.
For symmetry reasons this conical shape would be expected for a fragmentation process. The opening angle in $\Delta\eta$ is close to the observations at RHIC. Albeit the limited acceptance the observed yield does not seem to approach 0 at large $\Delta\eta$ which corresponds to the observations of a ridge-like structure on the near-side as observed at RHIC. The away-side is washed out over the whole acceptance which covers $\Delta\eta$=+/-0.5. For higher associate p_t (e.g. p_t(A)=(2.5-4.0) GeV/c) the away-side as well as the near-side show flat $\Delta\eta$ distributions over the observed acceptance region.

Two-particle correlations: results in the context of other measurements

At higher beam energies, measurements of two-particle correlations show similar shapes on the near- and the away-side of the conditional yield, the magnitude however being significantly different. A comparison of the two-particle conditional yield for three different energies for the same trigger-associate p_t selection and similar centralities and colliding systems is shown in Figure 11.1.

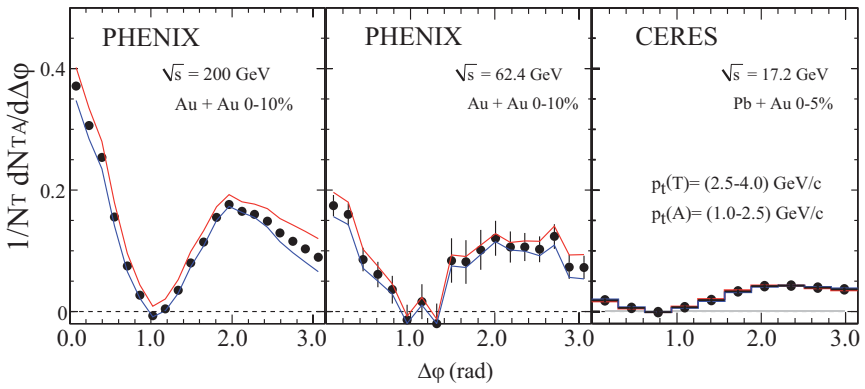

Figure 11.1: Two-particle conditional yield for RHIC [78] (left panel : PHENIX Au+Au at $\sqrt{s} = 200$ GeV. middle panel: PHENIX Au+Au at $\sqrt{s} = 62.4$ GeV) and SPS energy (right panel: CERES Au+Pb at $\sqrt{s} = 17.2$ GeV) for similar colliding systems and centralities for the same trigger and associate p_t ranges.

An increase of the order of 10 is observed for the conditional yield on the near-side going from top SPS to top RHIC energy.
The measured yield is determined by the probability to find a jet trigger in the trigger sample and the number of jet-like associates per jet-trigger in an event. If, indeed, the near-side showed the patterns of vacuum fragmentation, no pronounced difference on the near-side would be expected since the kinematics is defined by the trigger and associate p_t, not by the energy of the underlying collision.
The higher probability of finding high-p_t jets in an event at higher beam energy

could on the other hand lead to triggering on fragments from jets with p_t higher than the trigger p_t interval. This, in turn, leads to a higher yield on the near- as well as on the away-side due to the higher total energy contained in the jet. At SPS energy it is more likely that the trigger is indeed the leading hadron of the fragmentation process.
This, in combination with a possibly higher trigger probability, could lead to the observed strong increase of the measured yield on the near-side.

Two-particle correlations: limitations and improvements

Investigating the shape of the correlation function for different kinematical regions and centrality classes, it is crucial to have a well determined flow correlation as the major source of systematic uncertainty. While the relative uncertainty plays a minor role at high centralities, large systematic uncertainties arise for more peripheral collisions. A caveat of the analysis is the usage of model assumptions about the sources of correlations in the data. The ZYAM method can be justified by the large gap in the PYTHIA simulations between the near- and the away-side in p+p but stays a speculation about the true circumstances in heavy ion collisions. The impact of momentum correlations event by event could not be studied in this thesis due to the lack of statistics. Increasing the statistics and acceptance for the analysis would render it possible, on one hand, to reduce the systematical uncertainties in the flow determination, and to make the three-particle correlation analysis feasible.

Three-particle correlations

The analysis of the three-particle correlations is complicated due to the multiple sources which contribute to the observed signal, and again the model assumptions underlying the decomposition of the sources. The rule of thumb studies in chapter 3.2.4 show that based on the measured two-particle yield and basic considerations, the feasibility of the measurement depends strongly on the actual distribution of real jet triggers in the trigger sample. The results show that within the statistical uncertainties no significant three-particle jet signal can be extracted from the data. Varying systematically the background components shows the evolution of a cone like structure from the correlations in case of a slightly reduced Hard-Soft component. As is the case for the preliminary PHENIX [79],[80] results discussed in the following section, simulations resemble more closely the picture which is obtained in a cone like scenario with two distinct off-diagonal structures, in contrast to the deflected jet scenario (Figure 3.6). However, the findings do not suffice to draw a conclusion about the three-particle jet like yield.

Three-particle correlations: results in the context of other experimental results

An example of preliminary STAR results [81],[82],[83] at $\sqrt{s}$=200 GeV beam energy is given in Figure 11.2.
The analysis presented in this thesis is based on the same background subtraction method as for the STAR analysis. Trigger and associate p_t ranges

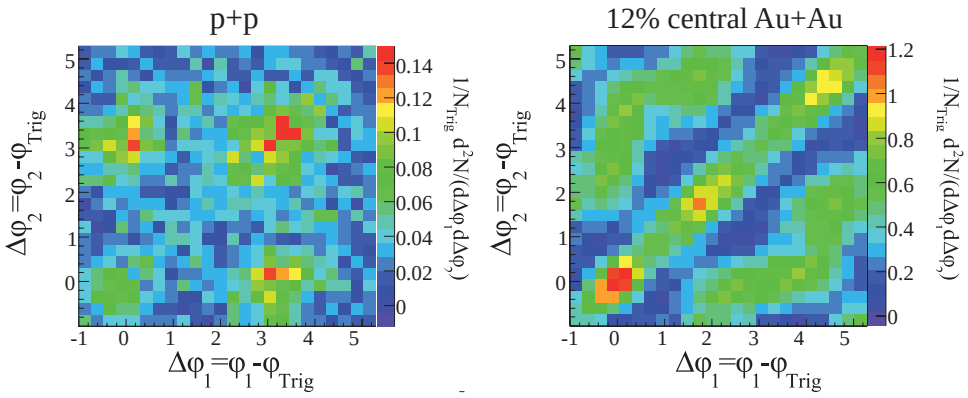

Figure 11.2: Three-particle conditional yield for p+p (left) and central Au+Au collisions (right) measured with the STAR experiment at $\sqrt{s}$ = 200 GeV beam energy [81].

(p_t(T)=(3-4) GeV/c, p_t(A)=(1-2) GeV/c) slightly deviate from the standard binning used in this thesis. For p+p collisions only one away-side peak at $(\Delta\phi_1, \Delta\phi_2) = (\pi, \pi)$ is observed in the three-particle yield. This is expected for back to back emission in the azimuthal angle and fragmentation to the vacuum. In central Au+Au collisions however, two off-diagonal peaks are observed which is consistent with conical emission in central collisions.
PHENIX uses a different coordinate system to represent the three-particle correlations. The angle θ^* represents the polar angle of one associate particle with respect to the trigger particle. This angle defines a constant radius in the two dimensional representation of the three-particle correlations as shown in Figure 11.3 (right).

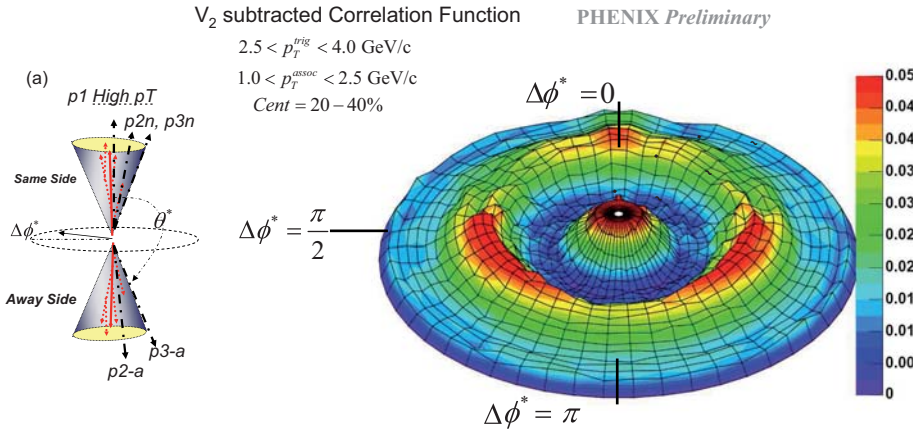

Figure 11.3: PHENIX coordinate system for the analysis of three-particle correlations (left) and preliminary flow subtracted three-particle correlation signal for mid-central Au+Au collisions at $\sqrt{s}$=200 GeV/c [79].

The second angle $\Delta\phi^*$ is the azimuthal difference of other associates with respect to the first associate in in the plane normal to the trigger direction. In case of back to back emission of jets in azimuth as well as in rapidity, conical emission would result in a ringlike structure at an angle of θ^* smaller than π. In Figure 11.3 a ring like structure is observed at $\theta^* \approx 120°$. In this preliminary analysis the Hard-Soft term is not subtracted. Simulations show a similar picture of the raw correlation function as in the data which is significantly different from a deflected scenario in which only one pronounced peak at $\Delta\phi^*=0$ is expected.

All results are still preliminary at the point of submission of this thesis and can only give an indication of how the true three-particle jet like correlation looks like.

Three-particle correlations: limitations and improvements

The limiting factor in the presented analysis is the statistics needed to measure a clear three-particle jet yield. Increasing the data sample by a factor of 10 for the presented analysis would render it possible to independently of the assumed trigger-jet probability in the trigger sample (within reasonable limits) determine the three-particle correlation signal. In combination with the measured two-particle conditional yield this would make it possible to determine the actual share of jet-like triggers in the trigger sample, and thus the total cross section of hard particle production in the collisions. This would as well give a better estimate about the impact of non jet-triggers to the overall measured signal.
An alternative to reduce the systematic uncertainties would be to increase the probability to find a jet-like trigger particle in the trigger sample.
Enhancing the data sample with triggers from hard interactions can by achieved increasing the transverse momentum of the particles. This will reduce the probability of the trigger stemming from bulk thermal particle production, however also the total cross section for particle production and therefore the overall statistics of the data sample.
Another possibility would be to determine the jet-like structure of the particles emitted around a trigger by an event-by-event analysis. Again assuming surface emission, the near-side jet could be identified by such an analysis. However the away-side cannot be analyzed on the same basis by simply counting particles as the away- side is supposed to reflect the interactions with the medium.
An improvement of the measurement could thus be obtained by identifying jet triggers event-by-event by e.g cone finding algorithms, and subsequently processing the associates again by a correlation analysis picking up all associates to the trigger in a certain kinematical range, and subtracting the background components as is done in this thesis. The feasibility of the method could be checked by comparing the near-side conditional yield as obtained by the correlation measure, to results obtained by counting the particles in the cone on the near-side in each event a jet-trigger was identified.

A Event- and track selection

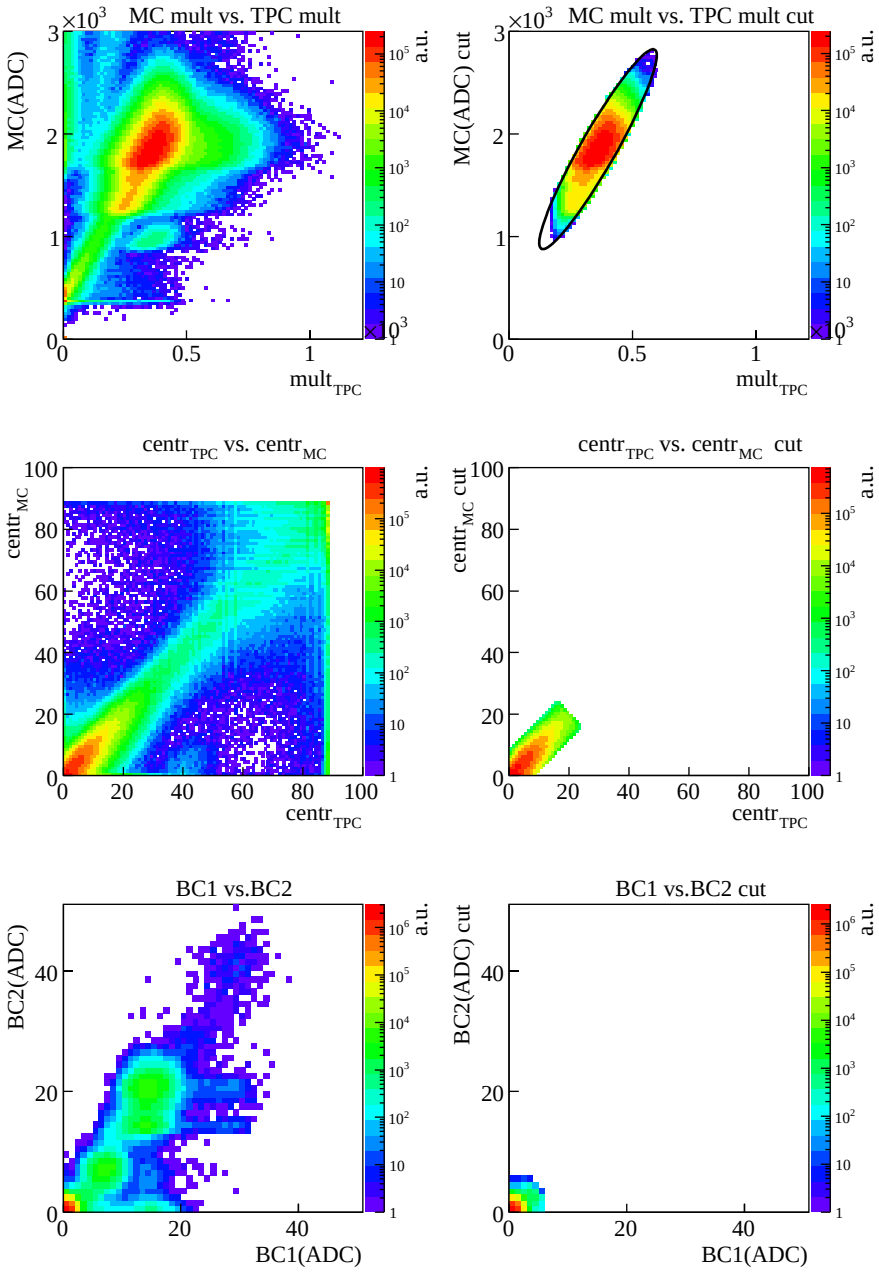

Figure A.1: Distributions of event characteristics with (right) and without (left) event cuts applied as described in section 5.1. The distributions with cuts applied correspond to all cuts applied, not only to the specific quantities displayed. The multiplicity in the MC is given in terms of the measured ADC value.

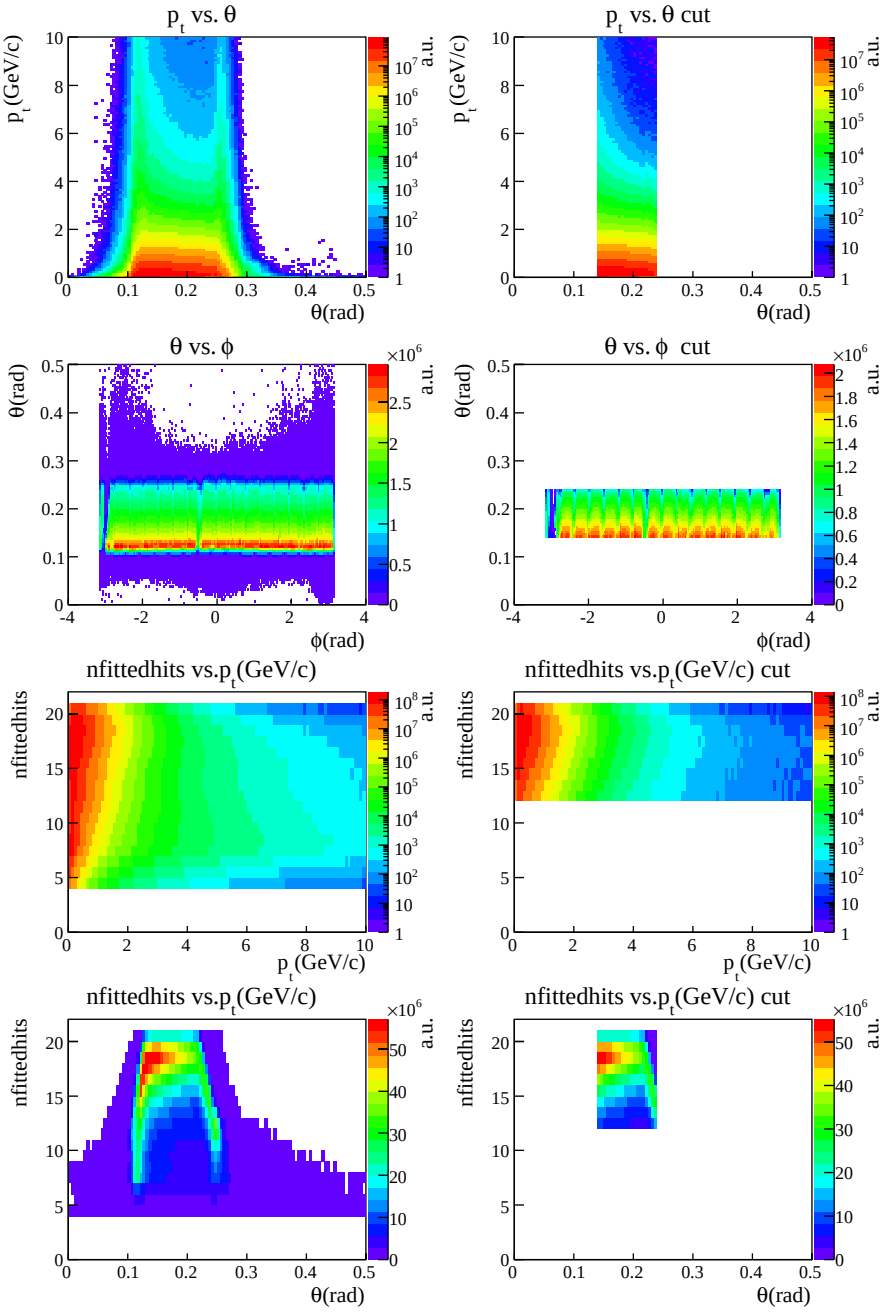

Figure A.2: Distributions of track characteristics with (right) and without (left) track cuts applied as described in section 5.2. Event quality cuts were already applied. The distributions with cuts applied correspond to all cuts applied, not only to the specific quantities displayed.

B Two-particle correlations

B.1 Charge dependence of two-particle correlations

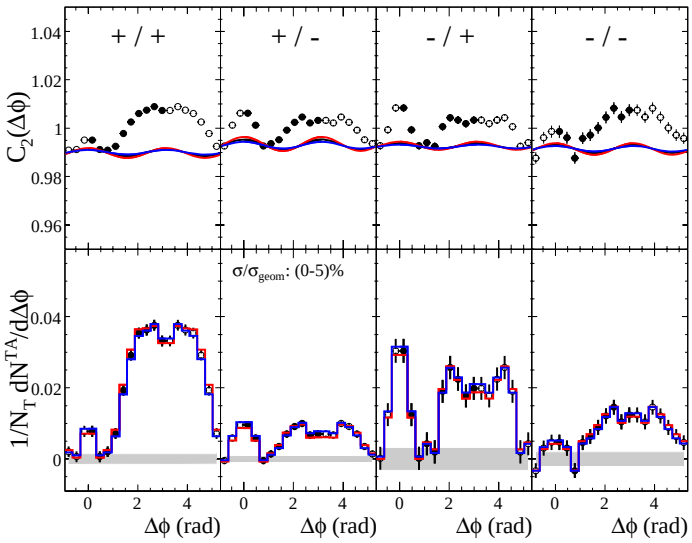

Figure B.1: Two-particle correlation function (top) and conditional yield (bottom) for different combinations of trigger and associate charge (trigger/associate) for centrality σ/σ_{geom}=(0-5)%.

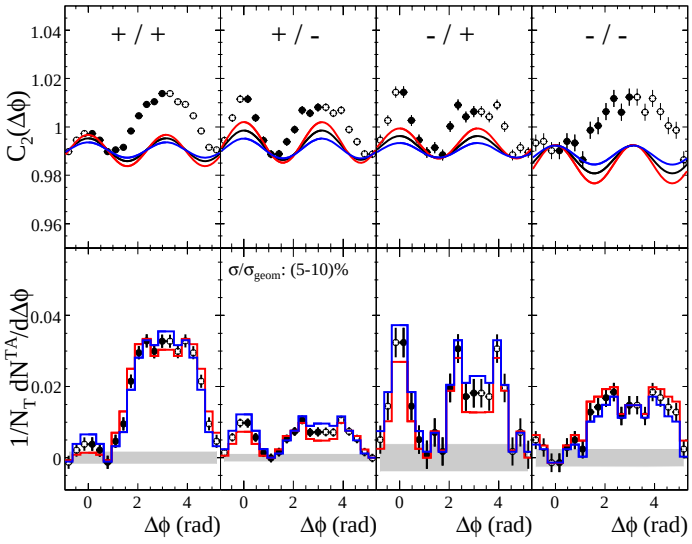

Figure B.2: Two-particle correlation function (top) and conditional yield (bottom) for different combinations of trigger and associate charge (trigger/associate) for centrality σ/σ_{geom}=(5-10)%.

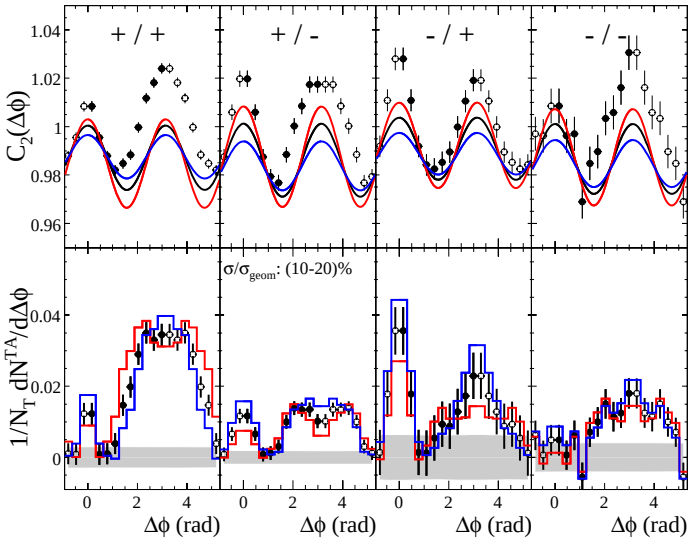

Figure B.3: Two-particle correlation function (top) and conditional yield (bottom) for different combinations of trigger and associate charge (trigger/associate) for centrality σ/σ_{geom}=(10-20)%.

B.2 p_t-scan of two-particle correlations

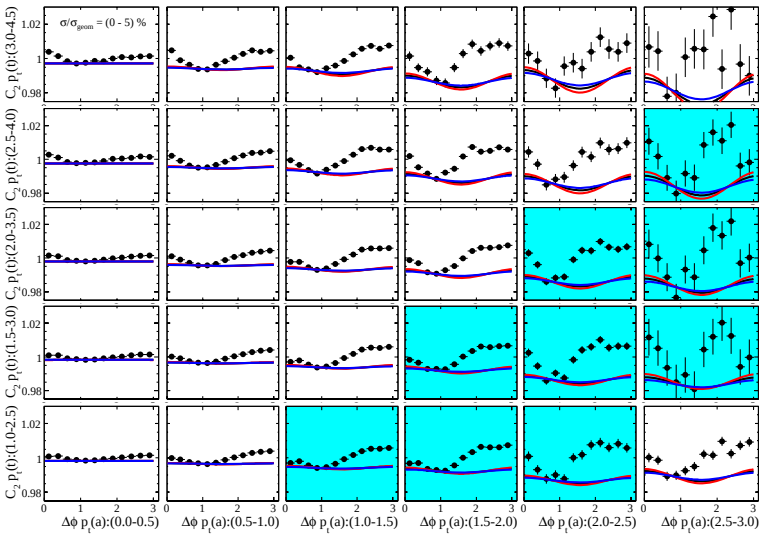

Figure B.4: p_t-depencence of the two-particle correlation function for centrality σ/σ_{geom}=(0-5)%. Shaded matches show overlapping trigger and associated p_t regions.

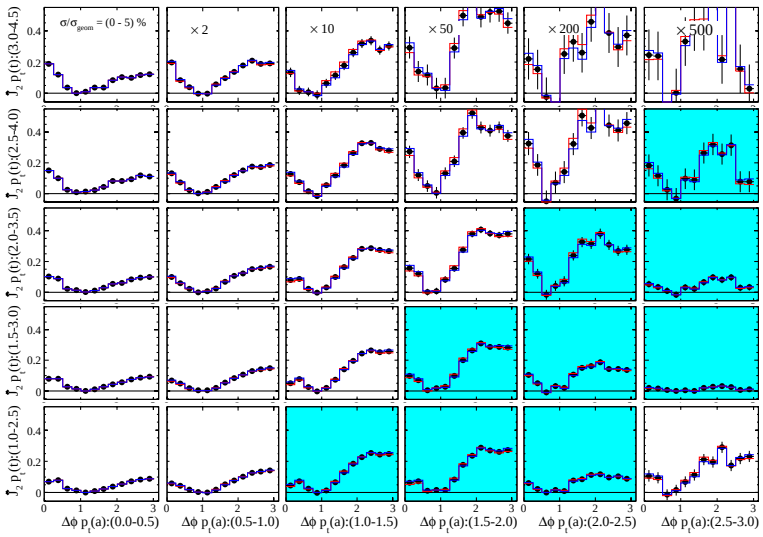

Figure B.5: p_t-depencence of the two-particle conditional yield for centrality σ/σ_{geom}=(0-5)%. Shaded matches show overlapping trigger and associated p_t regions.

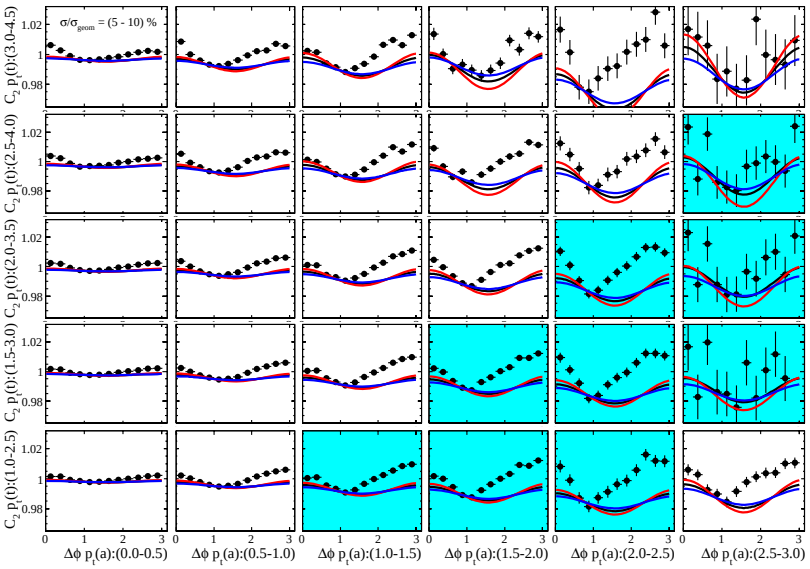

Figure B.6: p_t-depencence of the two-particle correlation function for centrality σ/σ_{geom}=(5-10)%. Shaded matches show overlapping trigger and associated p_t regions.

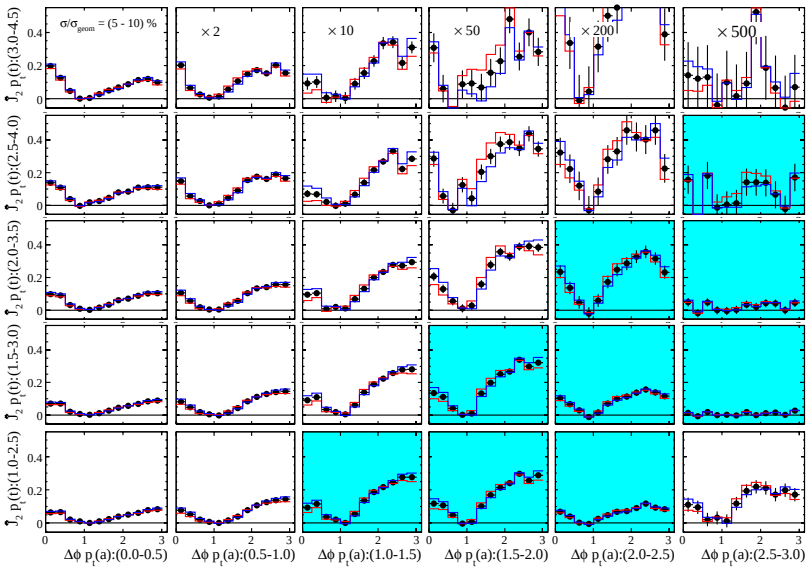

Figure B.7: p_t-depencence of the two-particle conditional yield for centrality σ/σ_{geom}=(5-10)%. Shaded matches show overlapping trigger and associated p_t regions.

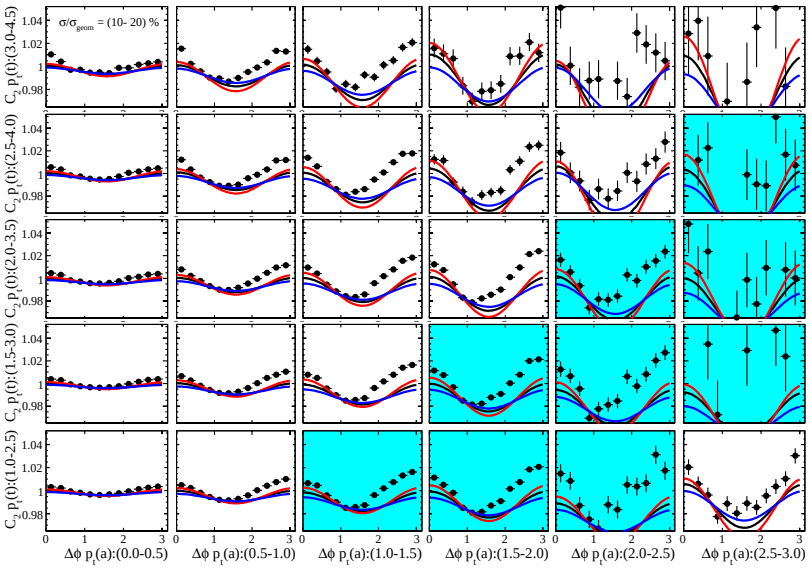

Figure B.8: p_t-depencence of the two-particle correlation function for centrality σ/σ_{geom}=(10-20)%. Shaded matches show overlapping trigger and associated p_t regions.

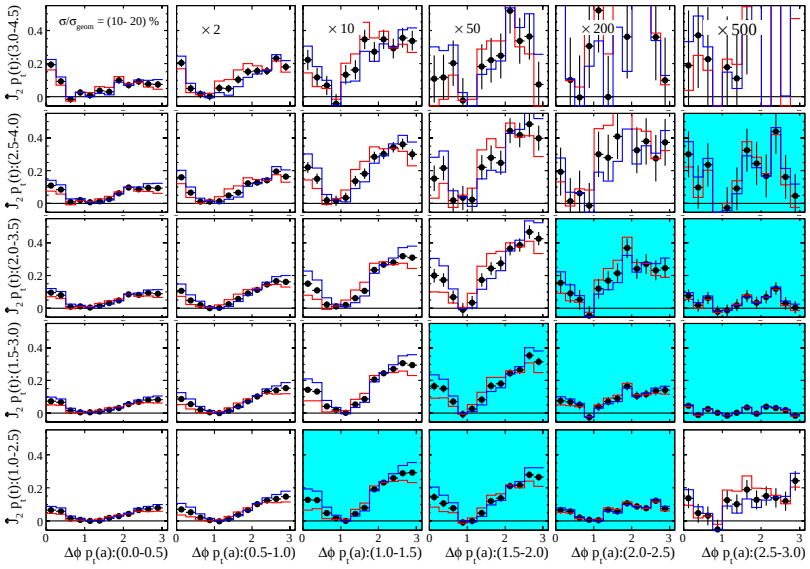

Figure B.9: p_t-depencence of the two-particle conditional yield for centrality σ/σ_{geom}=(10-20)%. Shaded matches show overlapping trigger and associated p_t regions.

B.3 p_t-scan of two-particle $\Delta\phi - \Delta\eta$ correlations

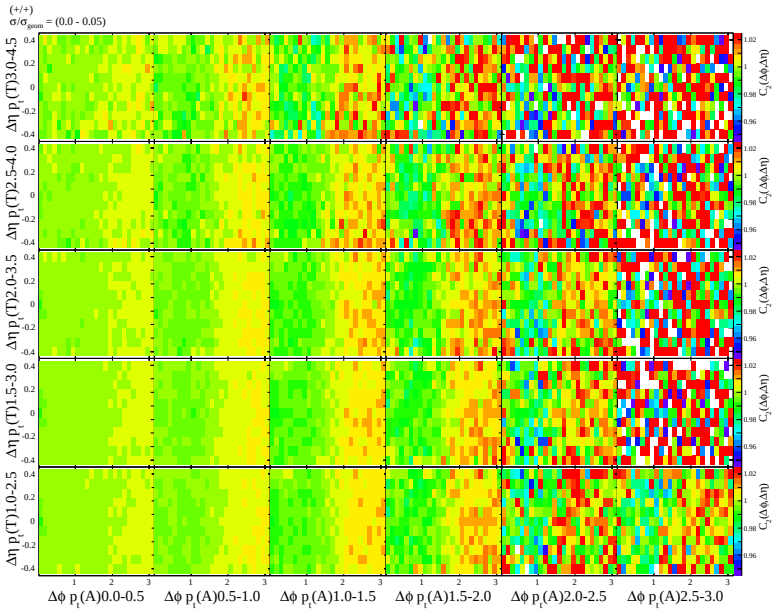

Figure B.10: $\Delta\phi$-$\Delta\eta$ correlation functions for positive triggers and associates (+/+) for centrality σ/σ_{geom}=(0-5)%. p_t given in GeV/c.

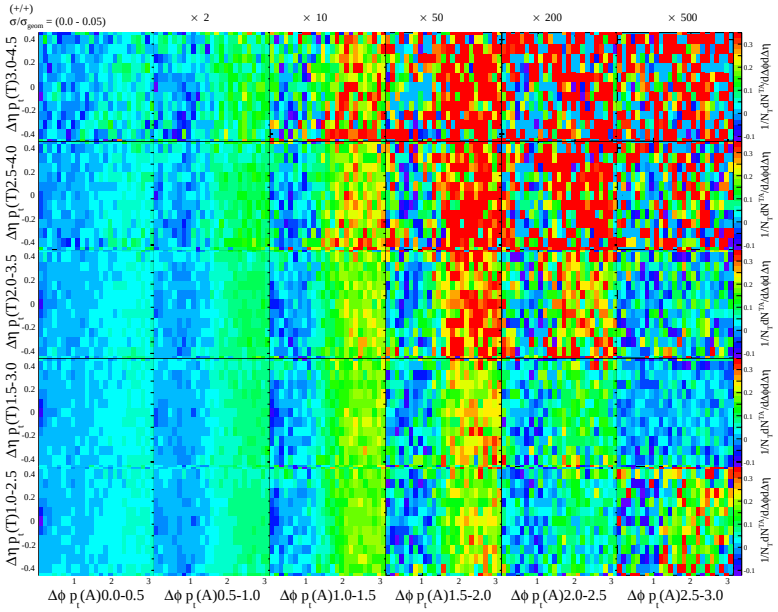

Figure B.11: $\Delta\phi$-$\Delta\eta$ conditional yield for positive triggers and associates (+/+) for centrality σ/σ_{geom}=(0-5)%. p_t given in GeV/c.

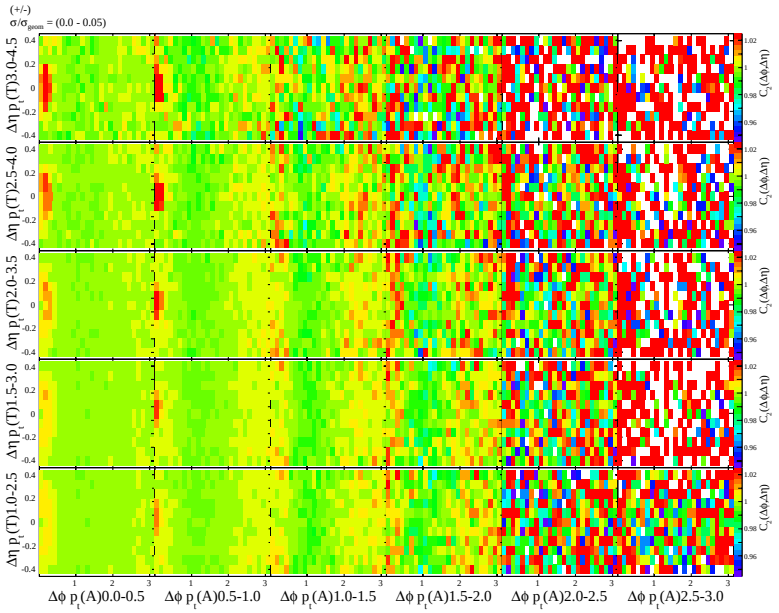

Figure B.12: $\Delta\phi$-$\Delta\eta$ correlation functions for positive triggers and negative associates (+/-) for centrality σ/σ_{geom}=(0-5)%. p_t given in GeV/c.

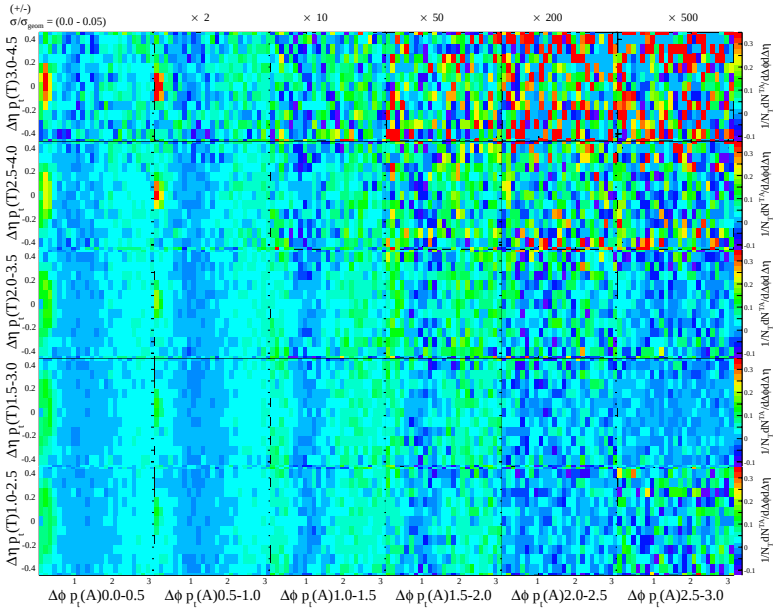

Figure B.13: $\Delta\phi$-$\Delta\eta$ conditional yield for positive triggers and negative associates (+/-) for centrality σ/σ_{geom}=(0-5)%. p_t given in GeV/c.

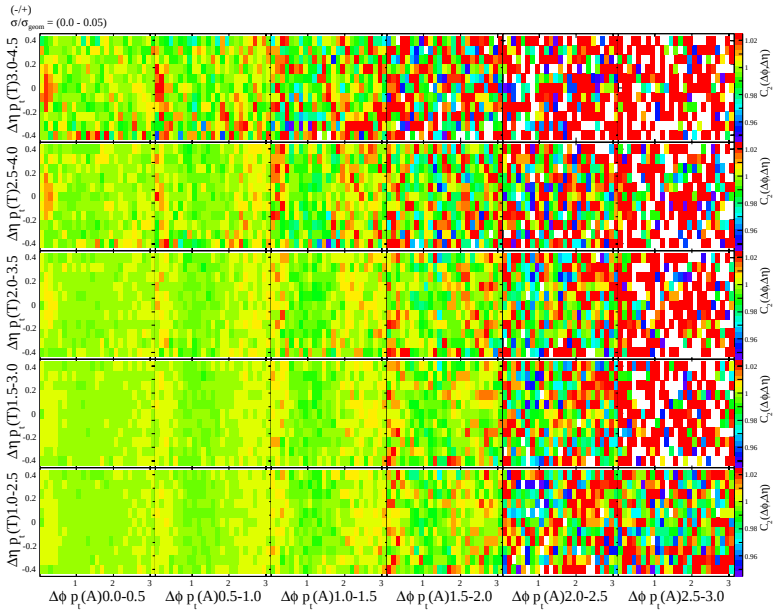

Figure B.14: $\Delta\phi$-$\Delta\eta$ correlation functions for negative triggers and positive associates (-/+) for centrality σ/σ_{geom}=(0-5)%. p_t given in GeV/c.

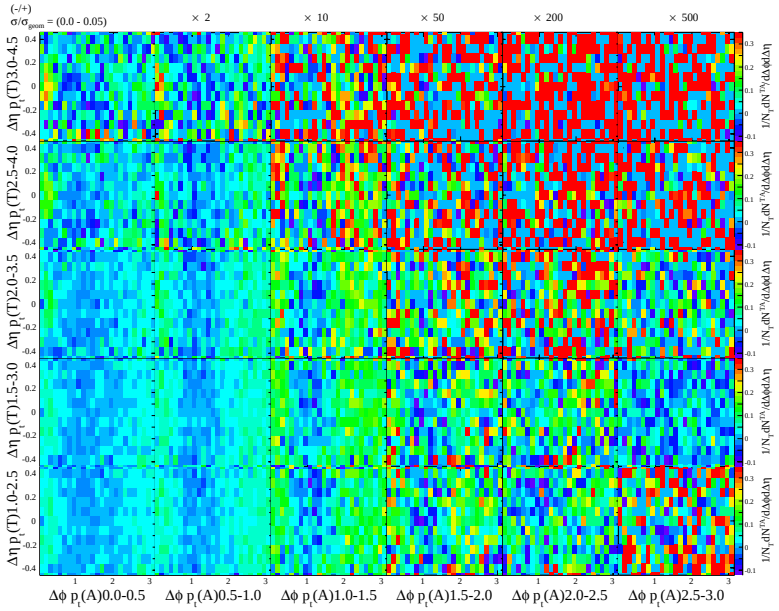

Figure B.15: $\Delta\phi$-$\Delta\eta$ conditional yield for negative triggers and positive associates (-/+) for centrality σ/σ_{geom}=(0-5)%. p_t given in GeV/c.

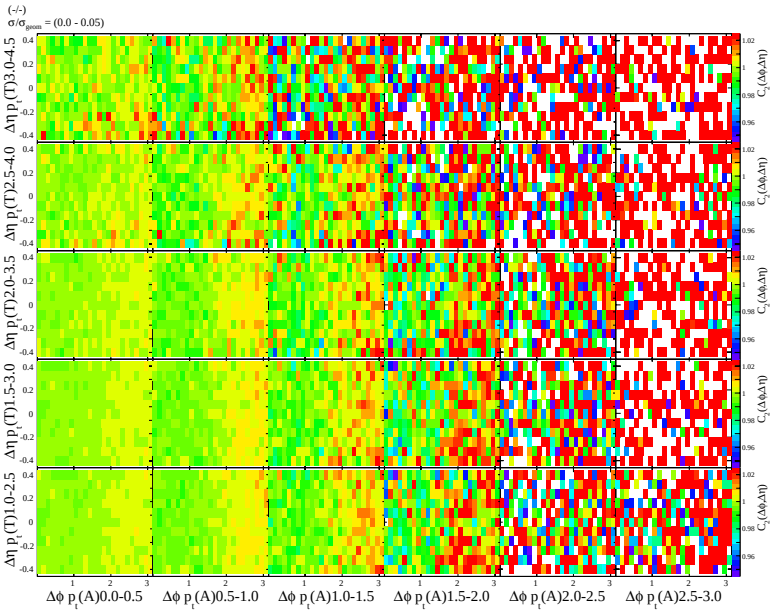

Figure B.16: $\Delta\phi$-$\Delta\eta$ correlation functions for negative triggers and associates (-/-) for centrality σ/σ_{geom}=(0-5)%. p_t given in GeV/c.

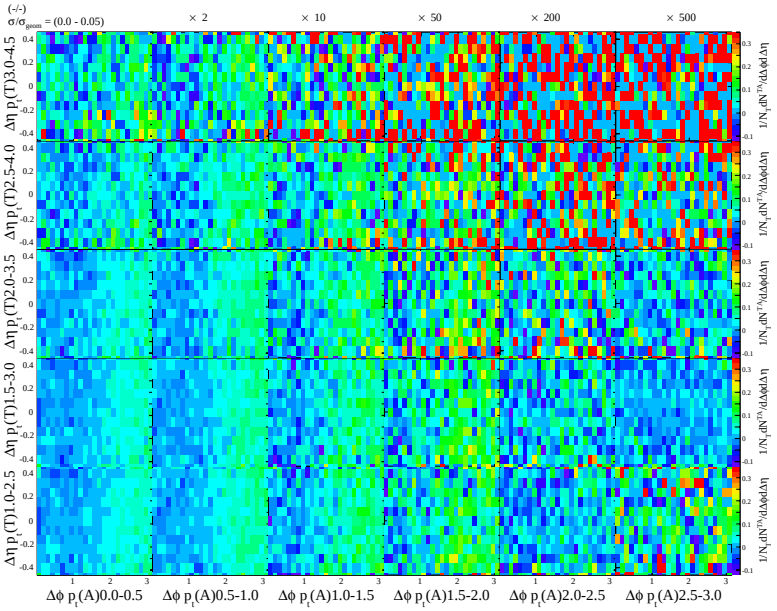

Figure B.17: $\Delta\phi$-$\Delta\eta$ conditional yield for negative triggers and associates (-/-) for centrality σ/σ_{geom}=(0-5)%. p_t given in GeV/c.

C Differential momentum resolution

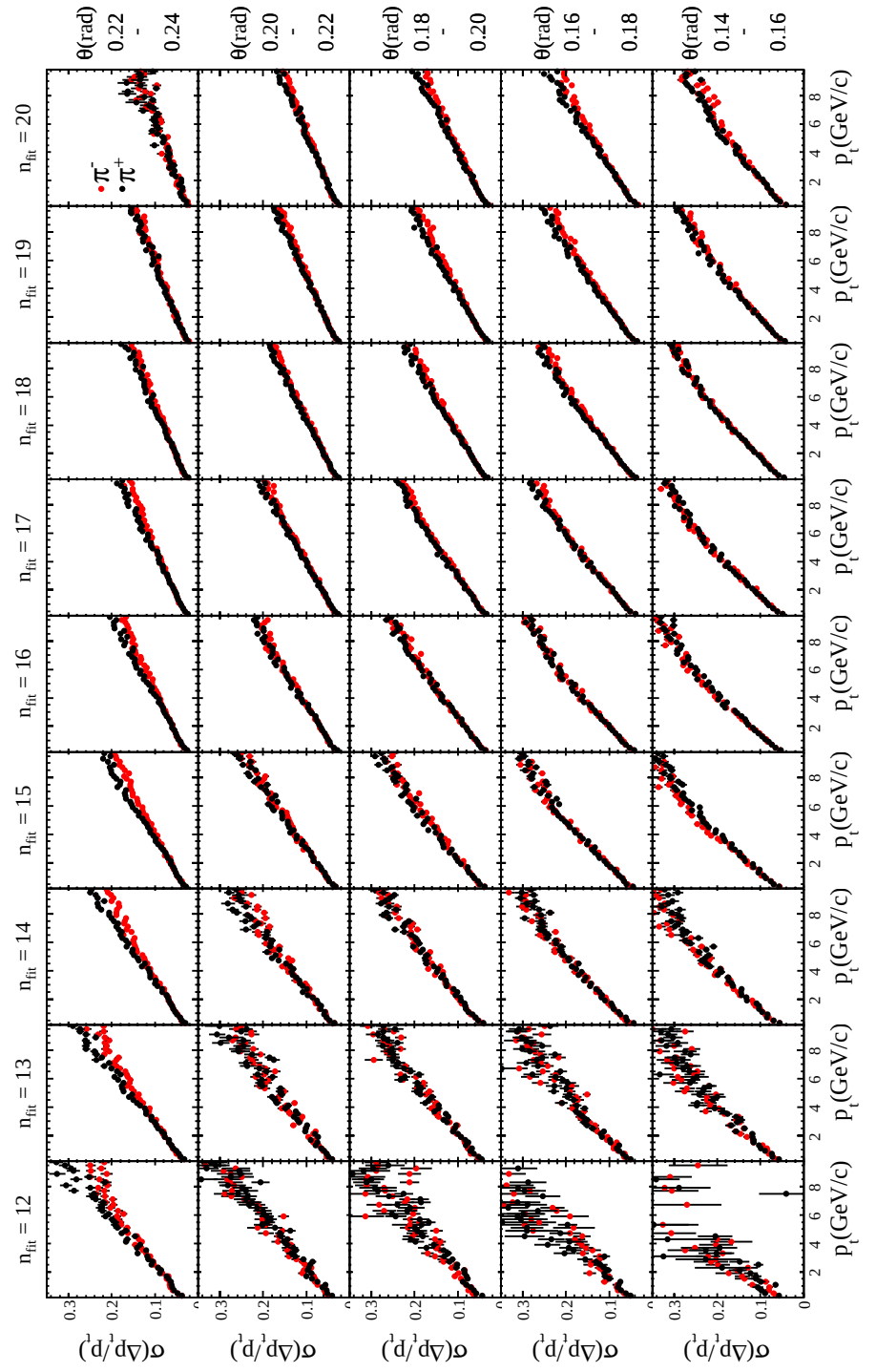

Figure C.1: p_t-depencence of the width (σ) of the distribution of the relative momentum difference ($\frac{\Delta p_t}{p_t} = \frac{p_t(rec) - p_t(mc)}{p_t(mc)}$) for positive and negative poins for different values of θ and number of fitted hits.

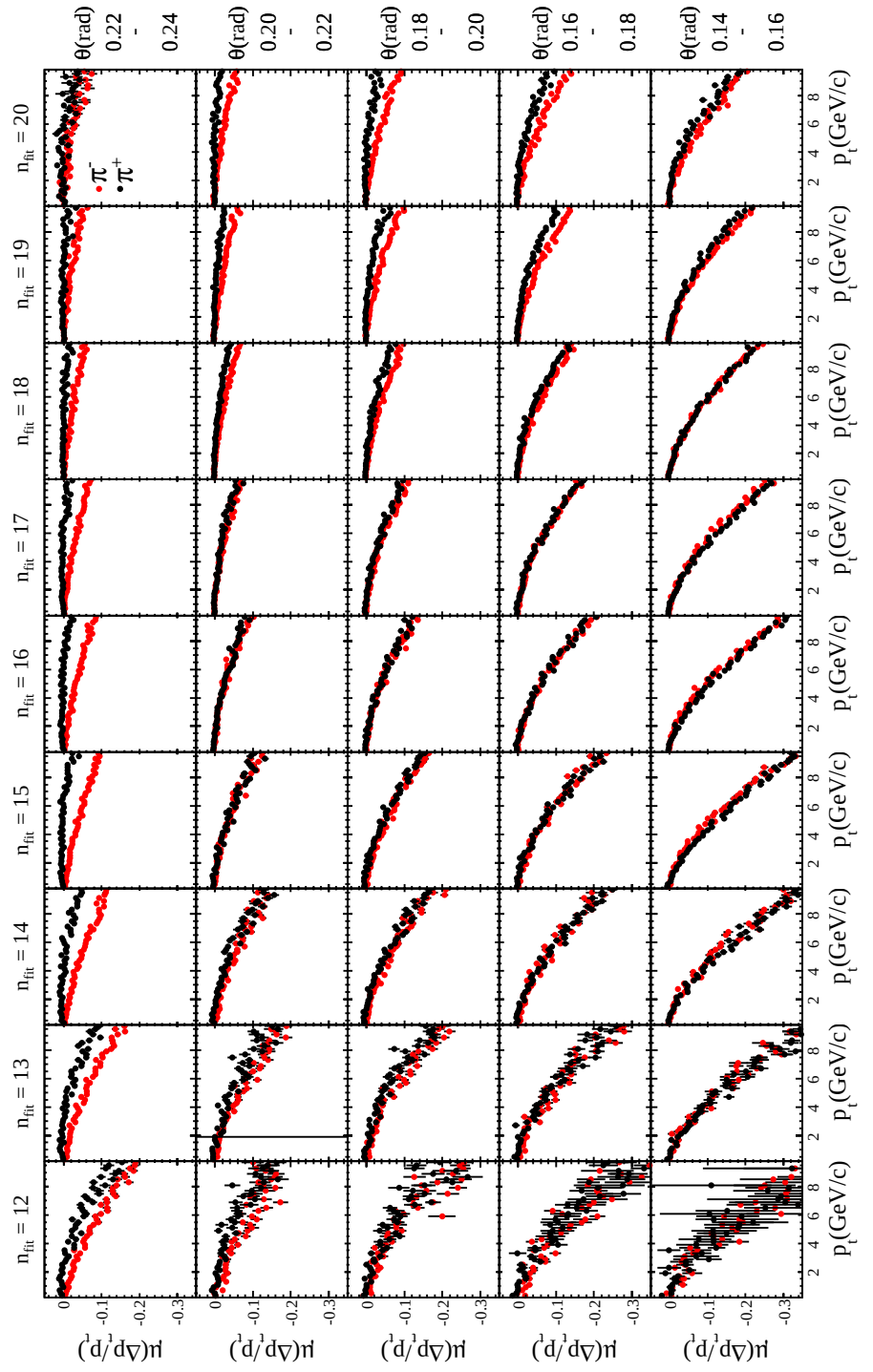

Figure C.2: p_t-depencence of the mean (μ) of the distribution of the relative momentum difference ($\frac{\Delta p_t}{p_t} = \frac{p_t(rec) - p_t(mc)}{p_t(mc)}$) for positive and negative poins for different values of θ and number of fitted hits.

D Online monitoring for the ALICE-TPC commissioning

In the course of 2006 the construction of the ALICE-TPC [84] is finished and the TPC is equipped with the Front End Electronics [85]. In a commissioning phase the electronics components and the data acquisition system (DAQ [86][87]) as it is foreseen to operate as part of the complete ALICE detector is tested for each sector of the TPC. Based on previous work [88] a program which helps to monitor online the functionality of the TPC and its components is developed. The major objective of the program is to verify the mapping and the functionality of the detector components, as well as to give an immediate coarse picture of the performance of the detector. The software package is used during the whole commissioning phase and is finally added to the official ALICE software package AliROOT [89].
After a brief discussion of the ALICE detector and its main components, the basic features of the Online Monitor as well as the final mapping of the TPC components and results from the commissioning phase are presented.

D.1 The ALICE experiment

ALICE [61] (A Large Ion Collider Experiment) is supposed to start operation in 2009 in the course of the CERN LHC (Large Hadron Collider) program. It is the only experiment at the LHC explicitly designed to study the the physics of strongly interacting matter in nucleus nucleus collisions. A variety of collision systems can be studied starting from p-p collisions up to Pb-Pb collisions in which up to about 20000 charged tracks might be produced. The initial state of the collisions is inferred to by measuring the momenta of the hadrons, leptons and photons emerging from the collisions. Key observables to be studied are e.g. particle ratios and momentum spectra of identified particles giving information about the chemical and thermal conditions at freeze-out of the system, momentum correlations of particles revealing the space time extensions of the particle emitting source, and the analysis of the energy loss of partons traversing the medium.

The experiment is embedded in the L3 magnet providing a magnetic field ranging from 0.2-0.5 T. The main tracking devices of the experiment are the Inner Tracking system (ITS) for vertex determination, a large volume Time Projection Chamber (TPC), followed by a Transition Radiation Detector (TRD) for the identification of high p_t electrons. Together with a Time of Flight detector (TOF) for particle identification up to p_t= 2.5 GeV/c, these components represent the central barrel of the ALICE detector which covers the mid rapidity

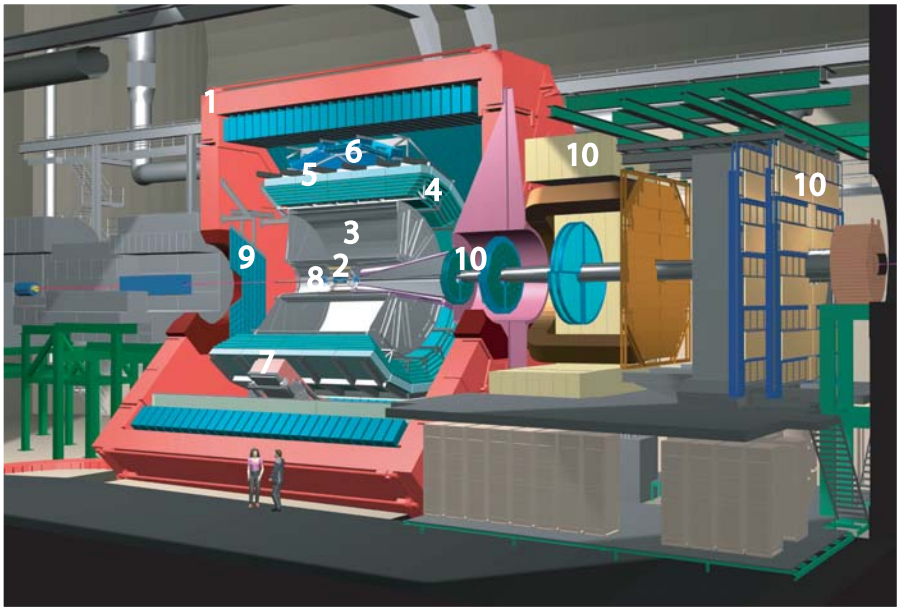

Figure D.1: The ALICE Experiment: (1) L3 Magnet, (2) ITS, (3) TPC, (4) TRD, (5) TOF, (6) HMPID, (7) PHOS, (8) FMD, (9) PMD, (10) Muon Arm.

region (-0.9<η<0.9) and has full coverage in azimuth.
Identification of hadrons up to p_t= 5 GeV/c is possible by a High Momentum Particle Identification Detector (HMPID) which covers a smaller range in pseudo rapidity (-0.6<η<0.6) and 57.6° in azimuthal angle. For photon measurements a Photon Spectrometer (PHOS) which covers the region -0.12< η <0.12 and 100° in azimuth as well as a Photon Multiplicity Detector (PMD , 2.3<η<3.5) are installed. The rapidity coverage for charged particles is increased to (-5.1<η<3.4) by a set of Forward Multiplicity Detectors (FMD) on both sides of the interaction point. A detector especially designed to measure muons as the dominant decay products of heavy quark vector mesons is installed on one side of the experiment (Muon Arm) and covers a range of -4.0<η<-2.4. This set of subdetectors makes it possible to study the dominant observables needed to examine the initial conditions of the reaction over a large range in phase space.

D.2 The ALICE-TPC

To cope with the large mid rapidity densities of the produced charged particles which are estimated to lie in the range of dn/dy= 2000-8000, a TPC is foreseen as the main tracking device of the detector. The main requirements for the TPC are a momentum resolution of a few MeV (<5) to facilitate HBT analysis, a tracking efficiency of at least 90% for measuring charged particles and a dE/dx resolution of better than 10% for particle identification. With a length of 510

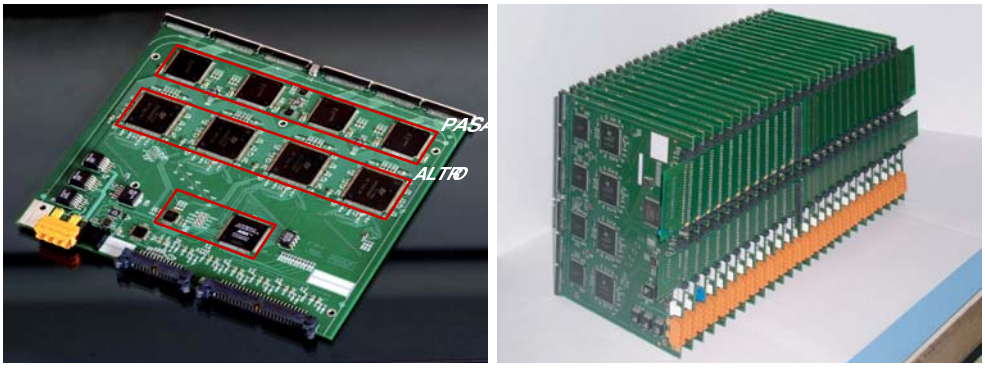

Figure D.2: Single Front end Card with PASA and ALTRO indicated (left), and FECs grouped to a readout patch by two backplanes (right).

cm and an outer radius of 250 cm it comprises a total sensitive drift volume of 88 m^3 filled with a gas mixture of $NeCO_2N_2$ (85/10/5). The drift field of 400 V/cm is provided by a central high voltage electrode and terminated by multi-wire proportional pad chambers mounted on the endcaps on both sides of the TPC.
The readout is segmented into 9 **I**nner- (**IROC**) and 9 **O**uter (**OROC**) **R**ead **O**ut **C**hambers on each side of the TPC equipped with 63 (IROC) and 93 (OROC) pad rows respectively, giving in total 557568 pads to be read out.

D.3 Front End Electronics and readout partitioning

The signals induced on the pads pass a first data processing step on the detector in the Front End Cards (FEC) which are mounted directly on a support wheel close to the endplanes of the TPC. 128 readout channels are connected via 6 capton cables to one FEC (Figure D.2) in which in a first step the electronic pulses are amplified and shaped in a Preamplifier/Shaper (PASA[90]) chip. Digitization, baseline correction, tail cancellation and zero suppression can be performed on the flight by the ALTRO chip [91] (Figure D.3) on the FEC. The

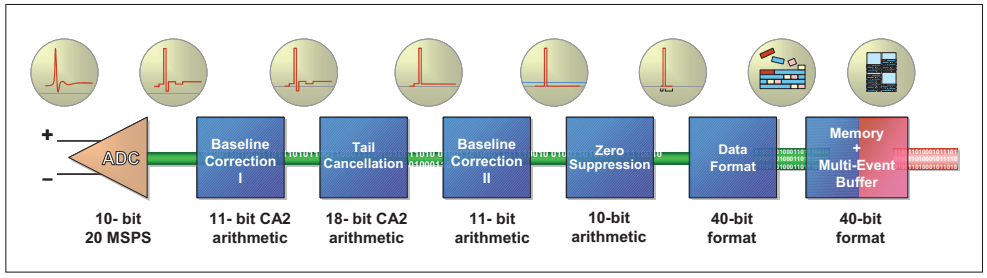

Figure D.3: Digitization, data processing, and fromatting chain in the ALTRO chip on the Front End Cards.

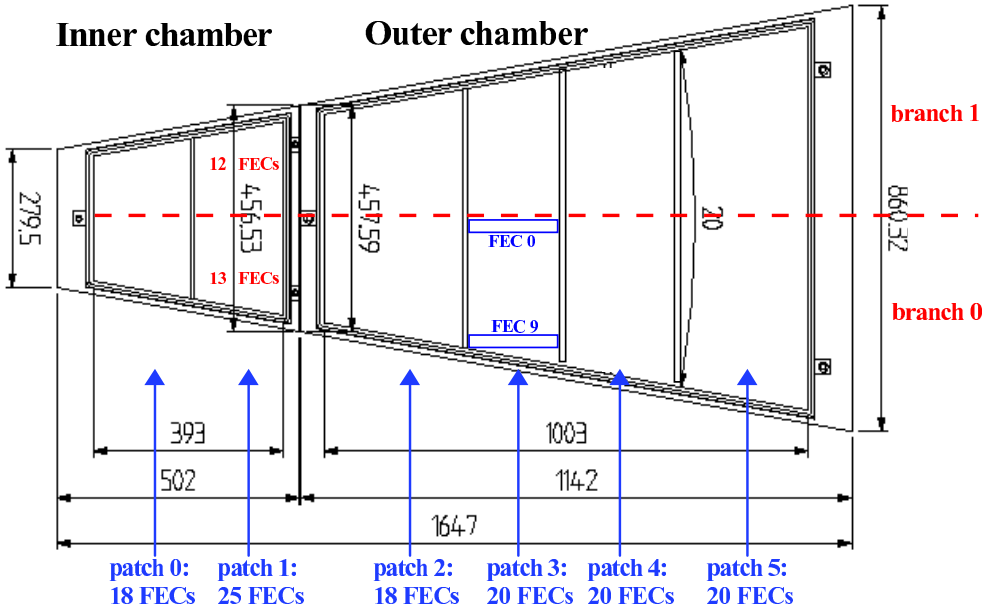

Figure D.4: Front view of a TPC sector indicating the two readout branches, the local FEC position and FEC id in a branch relevant for the determination of the complete hardware address of a single channel in one RCU.

Front End Cards are grouped in patches of 18-25 (RCU patch) cards (Figure D.4) which are read out by one Read Out Control Unit (RCU [92]). The FECs in one patch are subdivided in two branches. The local number of the FEC starts with 0 in the middle of the sector (first FEC on the backplane (Figure D.2)) and increases towards the edges. With 121 FECs in one sector and 128 channels on each card, there is a total of 15488 channels to be read out per sector.

D.4 Data format and readout chain

After the preamplification in the PASA the data are digitized in a 10 bit ADC converter in the ALTRO chip. In a first baseline correction step a pedestal pattern can be subtracted which can be read from a pedestal memory on the ALTRO chip. For this, the average baseline over several black events (without trigger signal) are calculated and read in to the pedestal memory. To check the quality of the pedestal calculation, pedestals were read in with the online monitor and subtracted from the data taken without pedestal subtraction. The long ion tail which is induced by slowly moving positive ions in the TPC is removed in the tail cancellation unit [93] in the ALTRO chip. Remaining deviations from the zero line in the signal are removed by a moving average filter. The C++ implementation of the tail cancellation filter as well as the moving average filter were implemented in the online monitor and tested but not ported to the final

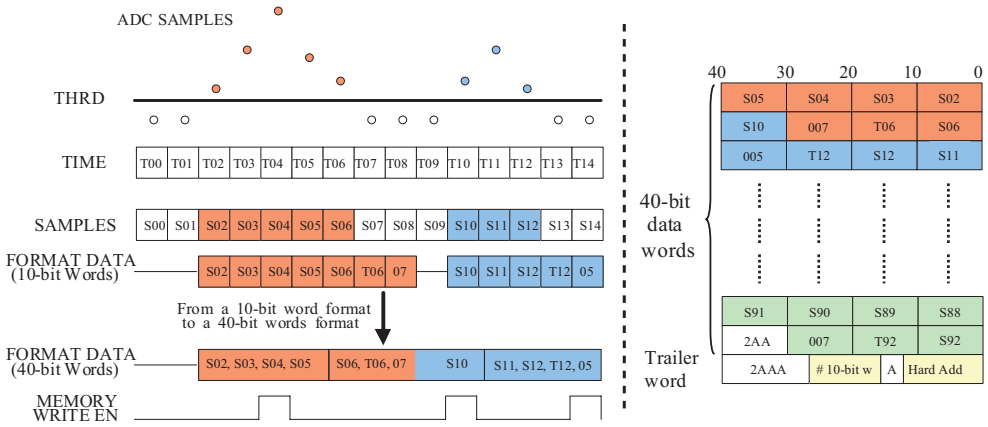

Figure D.5: Schematic picture of the data formatting using the zero suppression unit (left). The ADC information for a singal crossing the threshold are preceded by the timing information and the length of the peak and stored in 40 bit words (right). The data block for a single channel is terminated by a trailer word containing the hardware address of the channel.

implementation in AliROOT.

With a 10 bit word per time bin and channel from the ADC and a maximum of 1000 timebins per channel a full event has a size of about 500 MB. With an event design rate of a maximum of 200 Hz for A+A collisions, this exceeds by far the possible data throughput to the storage system of about 1.25 GB/s. A zero suppression unit can significantly reduce the data size by suppressing ADC values below a given threshold (Figure D.5.).
In order to better recover the full pulseshape a number of pre- and post samples (0-4) can in addition be stored. Since each word of a pulse only contains the ADC information of the peak height, an additional timestamp has to be added in order to recover the synchronization with the trigger. In addition, to distinguish the timestamp from the data words, a word indicating the total length (with timestamp and length word itself) of the data set is appended. Thus, the first data word in a set defines the position of the next data sample of a peak.

After the zero suppression the data are packed into 40-bit words and can be stored in a multi event buffer (Figure D.3.) on the ALTRO from where the date are read out by a trigger signal. Each data block for a readout channel (one pad) is terminated by a 40 bit trailer word containing the information about the hardware address of the channel and the total number of 10 bit words (Figure D.5.).

The hardware address stored in the trailer word for a channel is composed of the local channel address in an ALTRO chip (16 channels), the chip number (8 chips) on the Front End Card, the Front End Card in the branch (9-13

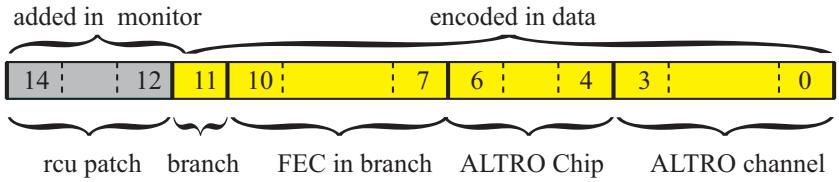

Figure D.6: The hardware address encoded in the data is composed of 12 bits storing ALTRO chip/channel number, the FEC number in a branch and the branch bit. The identification of the RCU is done via the equipment id read from the DAQ and appended to the hardware address in the monitor.

cards), and the branch bit (0-1) (Figure D.6.). The hardware address encoded in the data is thus unique only for a single rcu patch. To uniquely identify each hardware address in an entire sector the address is expanded in the monitor after reading it from the trailer word by three bits identifying the rcu patch (6 patches) of the readout partition.

The RCU reads the two branches of a patch, precedes the data by a Central Detector Header (CDH) containing information about e.g. the trigger setup and the participating sub-detectors. For each RCU the data are sent via the Detector Data Links (DDL) to the Local Data Concentrators (LDC). In this step the data are transformed to 32 bit words which is the data format of the DDL and the Data Acquisition and Test environment (DATE [94]).

D.5 DATE and ROOT data format

From the LDC level onwards the data are stored in the DATE format in 32 bit words. Each payload of a RCU patch (CDH+data from all channels) is preceded by an equipment header indicating e.g. the size and a global equipment identification number. All components read by a LDC are grouped in a sub event which is again labeled by a sub event header. On the Global Data Concentrator (GDC) level the sub events are grouped to form the global event where the event number is assigned in the event base header. Each header contains the information about the header size itself and the size of the following data sample.

In addition to reading files from tape or disk, a monitoring library makes it possible to access online the data stream from the GDCs or LDCs and monitor the data coming from the running experiment. During the commissioning the data are recorded locally in the DATE format. In addition, the data are transformed to the ROOT format and written to a ROOT TTree structure. The data structure in a RCU patch as described in D.4 is kept in this format.

The DATE as well as the ROOT format are supported by the online monitor.

Data in DATE format can be read from file or accessed online via the monitoring libraries if installed. During the compilation of AliROOT it is checked if the environment variables necessary for the DATE support are set. A warning will be issued in case DATE files are accessed without the appropriate libraries installed. ROOT files can be read locally from file or remotely via rfio from the CASTOR system if it is accessed from inside CERN.
Furthermore, access to files stored on a webserver is possible from the monitor. Early support for the U2F interface (see below) is not ported to the final version.

D.6 The commissioning phase

The first step of the commissioning is the mounting of the 4356 Front End Cards on the service support wheel of the TPC. The readout in this period is performed with the U2F [95] card which is an USB interface to the Front End Card and facilitates an easy access to each single card.
A map of the FEC positions in the TPC is created by reading the FEC identification numbers from the memory of each card and cross checking it with the bar code number printed on a label on each card. This map is used later on in the monitoring program to identify the position of single broken or malfunctioning cards.
After verifying the mapping as depicted in Figure D.4, the commissioning run starts in which different readout cycles are performed for two sectors at a time.

- The tests start with pedestal runs to check the functionality of the electronics and the noise level.
- In a second step a voltage scan is performed increasing the anode wire voltage in several steps.
- A laser run is performed from which a coarse picture of the alignment of the chambers can be obtained.
- For several sectors a calibration pulser run is performed. A signal with a defined pulse height is injected on the cathode plane wires. With this defined input signal the gain equalization of the different channels can be checked.
- Finally, a long term stability test of 8h hours for each pair of sectors is performed with a cosmic trigger setup. For this, ACCORDE counters are installed above and below the TPC to trigger on cosmic events.

D.7 The monitoring program

D.7.1 Working principle

As pointed out in section D.4, a single TPC event without zero suppression has a size of about 500 MB based on 10 bit words. Using "short" values (16 bit)

as data types for the processing of the decoded TPC data, the size would be increased by factor of 1.6 without having attributed any additional storage for the calculation of monitoring parameters and the storage of mapping tables.
Running the monitoring program with the TPC fully equipped would thus easily excess the memory of standard PCs on which the monitoring program is supposed to run.

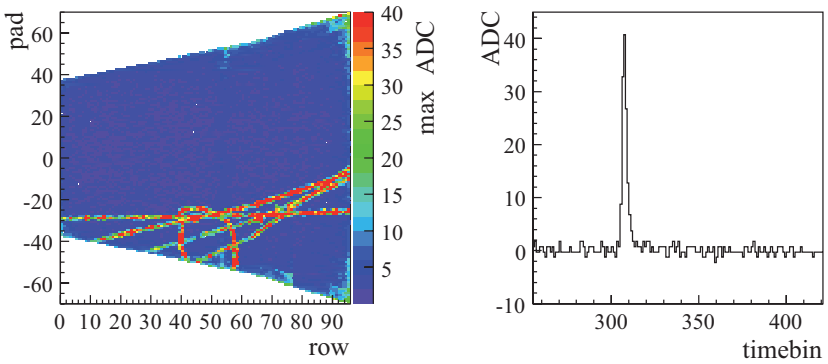

Figure D.7: Maximum ADC values for one OROC as function of the pad and row (a), and time profile for one selected pad (b). The time profile is accessed interactively in the monitor moving the mouse over a pad in the histogram in a).

In order to circumvent memory limitations a compromise between processing a full event at once and detailed monitoring capabilities for all TPC sectors is made by processing the data in two iterations.
In a first step, all available sectors are read in checking only the maximum ADC value in each channel and storing it in one global histogram for each side of the TPC. This picture can be used to fully monitor the TPC on a rather coarse basis. On a PC with 2GB RAM and a standard processor this read cycle will take about two seconds.
In a second read cycle the sector processed last is read in again calculating the baseline and the RMS for all channels in predefined windows and storing them in separate histograms. For this sector a detailed view of the maximum ADC values for each channel in IROC and OROC are dispayed in 2d ROOT histograms (Figure D.7, left).
Based on this projection of the TPC a detailed view for each channel can be started by just moving the mouse interactively over the histogram (Figure D.7,right). This calls an executable defined on the underlying TCanvas displaying the time profile of the channel the mouse is pointing at in a fraction of a second. With the link from the maximum ADC to the time profile a track can easily be followed throughout the TPC. For each channel the mapping information of the ALTRO chip, ALTRO channel, the local Front End Card in a branch and the unique Front End Card as mapped during the mounting of the cards is displayed.

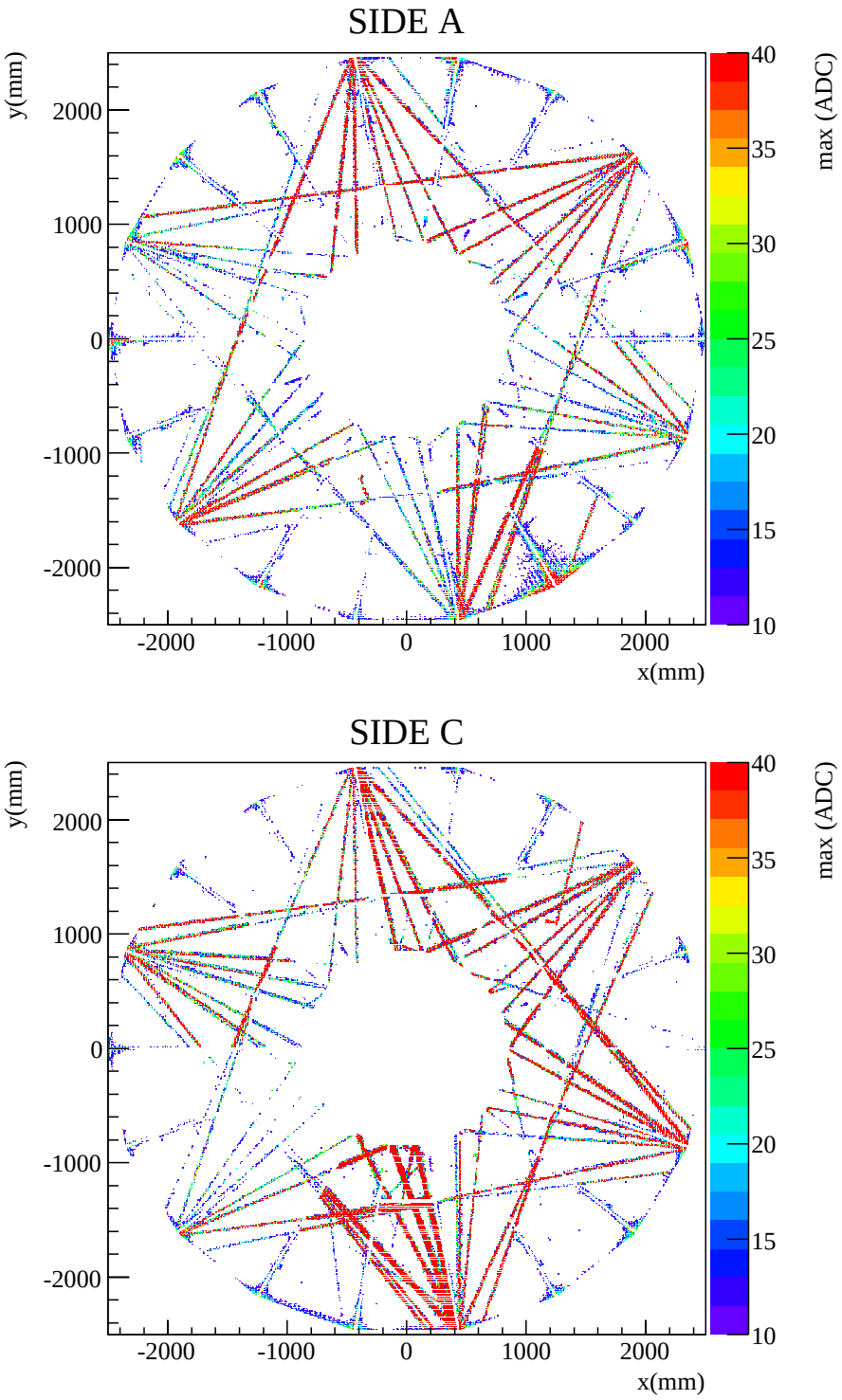

Figure D.8: Global view of the maximum ADC amplitude of each channel of the TPC with the laser setup. Only two sectors were read out at a time in the commissioning and later on merged to the global view of the TPC in this picture.

With this information displayed, the position of each single channel in the whole TPC can easily be identified by the monitoring program.

A snapshot of the monitoring program with the global view and the detailed time profile for single channels can be found at the end of this section in (Figure D.15).

D.7.2 Starting the monitoring program

The program can be started from AliROOT by loading the library and starting the Monitoring macro: start AliROOT and type:

```
root[0] .L $ALICE_ROOT/lib/tgt_linux/
        libTPCmon.so
root[1] .L $ALICE_ROOT/TPC/macros/
        TPCMonitor.C
root[2] TPCMonitor()
```

D.7.3 Main features of the monitoring program

After starting the Monitoring program a Graphical User Interface (Figure D.9.) pops up from where the monitoring program can be controlled. In the following a brief description of the first steps to access the data and the functionality behind the different buttons is given. In addition, results from the commissioning phase relevant for the different topics are discussed.

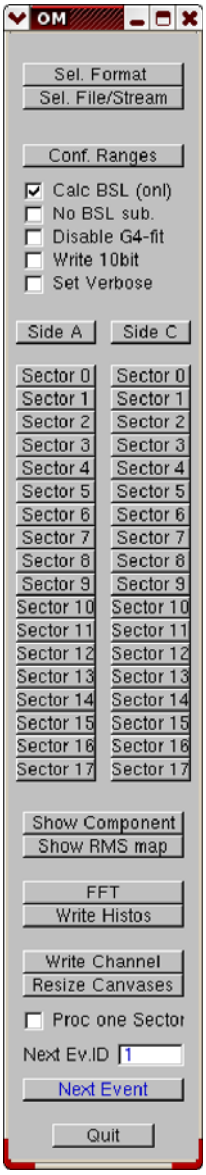

Figure D.9: Monitor GUI.

'Sel. Format'

A Window pops up offering the different formats the monitor can process: *'ROOT file'*, *'DATE file'* or *'DATE file/stream'*. As described in D.5, ROOT files can be accessed locally or remotely via *rfio* or *http* from inside CERN. Date files can be read locally choosing *DATE file* or online choosing *DATE file/stream* if the monitoring libraries are installed. Using the stream it is also possible to read in files however it is not possible to switch between events since only consecutive reading from the stream is possible. Choose one option and press 'Select Entry'.

'Sel. File'

Having chosen a format for the data to process, a file/stream to be read in can be chosen. A file dialog window will pop up displaying the last processed file/stream name. This name is stored to a file to make the access more convenient after a restart of the program. The naming convention for the DATE files/streams is as follows:

":"	local online stream
"file"	local file (both full and relative path are accepted)
"@host"	remote online on node host
"file@host"	remote file on node "host" (full path to the file should be given)
"@host1@host2"	remote online on node "host1" via the relay host "host2"
"file@host1@host2"	remote file on node "host1" via the relay host "host2" (full path to the file should be given)

Processing an Event

With the format and file set the event can be processed pushing the **'Next Event'** button which is the second to last button in the GUI. This will start the processing of all sectors in the first event that is accessible. For not zero suppressed data this can take several seconds. To increase the speed the Check-Button **'Proc one Sector'** can be pressed. This will cause the monitor only to process the last displayed sector in the next event, avoiding to fill the global histograms for all the sectors. In addition, for ROOT or DATE files a specific event can be chosen by specifying the Event Id in the field **'Next Ev. Id'**. Within an event the sector to be displayed in detail can be chosen by clicking on one of the sector buttons **'Sector 0-17'** for one side of the TPC or by double clicking on a sector in the histograms with the global view for one side.

'Conf. Ranges'

For data taken with the calibration pulser it is desired to exclude the pulse from the calculation of the baseline however the maximum should be determined in the range of the pulse. In order to meet these requirements the ranges for the baseline calculation, the maximum and the sum of the ADC channels is configurable .

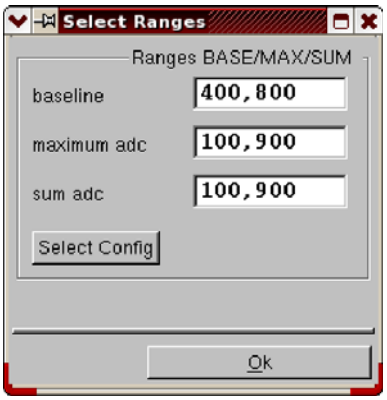

Figure D.10: Panel to configure ranges.

'Calc BSL online / No baseline sub.'

By default the baseline subtraction is calculated via the mean of the ADC values in a given time range configured via **'Conf. Ranges'**. To check if there is an offset due to floating wires or bad connections of single cards the baseline subtraction can be turned of by selecting **'No BSL sub.'**

'Disable G4 fit'

The peak around the maximum value of one channel is fit by default with a Γ4 function which is a typical function describing electronic responses. For black events this functionality can be switched off.

'Write 10 bit words'

In the monitor the data are decoded from 32 to 10 bit words and stored internally in an array. In case of the monitor not being able to properly decode the entire data block due to e.g. a corrupted trailer word of a channel, the 10 bit words can be written to a file in order to check the data structure line by line. The position of the last trailer word, the supposed next trailer position (line) as well as the file name will be piped to the console.

'Set Verbose'

Flag for verbose mode of the monitor for getting detailed information about sub routines running in the monitoring program.

'Sector 0-17'

After having read in a full event that is displayed in the global histograms, a detailed view can be obtained for single sectors by either double clicking on the position of the sector in the global histogram or selecting one of the sector buttons.

'Show component'

To check the functionality of single electronics components in the sectors a region of interest can be defined which is then mapped out of the 2d histogram displaying the max ADC value or RMS (see next item). The information displayed in the insert of the time profile histogram for a single channel can be used to identify a device. Replacing "all" in the window by the corresponding device will erase all other components but those meeting all specifications. An example for the application is shown in Figure D.12. On the left side the complete sector view for the Inner Read Out Sector is shown with a region of an enhanced baseline value. To obtain this view the baseline subtraction has to be switched off in the monitor. Moving the mouse over a single channel, the FEC number for a single channel in this region is identified and inserted in

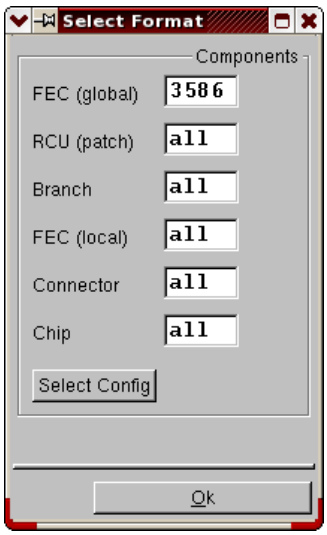

Figure D.11: Panel to select a component.

the Select Component window. Choosing "Select comp", all channels but the channels of the FEC are erased showing that the deviating channels all belong to the specified card. With the map of the Front End cards created during the installation of the FECs, the position in the branch and the RCU patch can be connected to the FEC number and can be read off the inlay of the time profile histogram. The original histogram is backed up to recover the original state by selecting "all" for the indicated components.

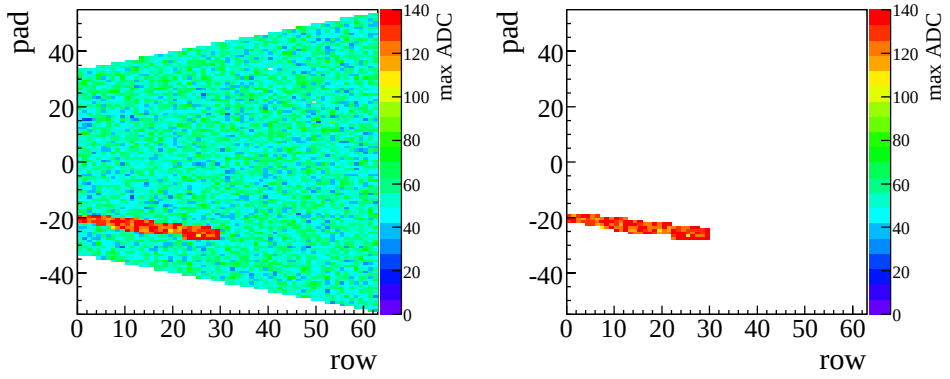

Figure D.12: Left: max ADC for one inner readout partition without baseline subtraction, indicating the malfunctioning Front End Card. Right: Malfunctioning Front End Card mapped out by the unique ID of the Card via 'Select component'.

'Show RMS map'

The performance of the TPC is strongly determined by the noise level induced on the channels during readout. Pushing **'Show RMS map'**, the width (actually σ) of the distribution of the ADC values in a predefined time range for IROC and OROC, as well as a 2d map of the RMS in the same representation as for the maximum amplitude are displayed. The same executable as for the maximum map is linked to the canvas in order to give access to the time information for each channel.

With the design value of the signal-to-noise ratio of 30:1 and a dynamic range of the Analog to Digital Converter (ADC) in the ALTRO of 2 V, the noise level σ (here named RMS since the ROOT function giving access to the σ is still called RMS) should not exceed 1 ADC count. However, at the beginning of the commissioning phase a significant fraction of pads exceeded this design value (Fig.D.13a). It could be shown that the high noise level was mainly due to the digital current arising from the synchronous readout of all channels and the insufficient cross section of the ground cables. The Front End Electronics allowes to apply a time offset in the readout to groups of channels in order to

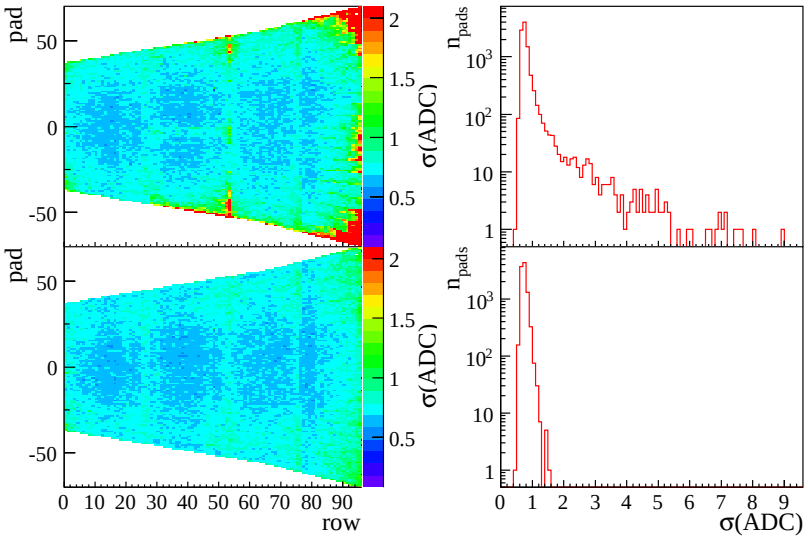

Figure D.13: Width σ of the baseline as function of pad and row (left) and the distribution (right) of the width for one OROC. The bottom right panel show the distribution after the modifications of the ground cables and the readout scheme (see text).

reduce the instantaneous digital currents. In addition, increasing the diameter of the ground cables reduced the noise level of the affected channels significantly so that the design requirements are fulfilled (Figure D.13).

'FFT'

As a measure to determine the origin of the noise a fast Fourier transformation can be performed based on Code from the GNU Scientific Library [96] which is wrapped in C++ and used in the monitor. For the last active channel the transform is calculated based on the currently displayed range of the time profile histogram which can be changed interactively.

Since the number of timebins as input for the calculation has to be an integer power of 2, the displayed range is shrunk until this requirement is met. Looking at the example of the Fourier transformation of the real component in Figure D.14, the main component of the noise has a frequency of 2.5 MHz. This corresponds to the RCU readout frequency which is identified as one of the main source of the noise described above.

'Write histos'

Writes the main histograms displayed in the monitor to a file in the current directory. The run and event number is indicated in the file name which is posted to the console.

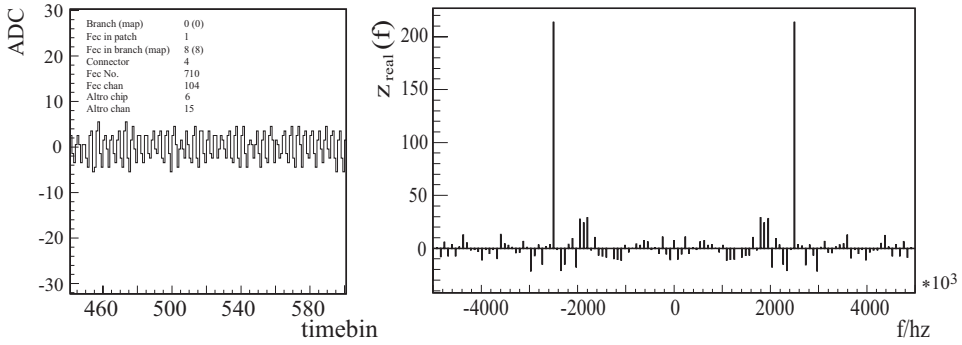

Figure D.14: Time profile of the baseline for a channel from the edge of an outer sector (right) and the real part of the Fourier transformed signal (right). The dominant frequency component corresponds to the readout frequency of the RCU (2.5 MHz).

'Resize Canvases'

The monitor is designed to have high flexibility concerning the histograms under investigation. For this reason each histogram is displayed in a separate canvas which can be changed in size and position interactively. The 'Resize Canvas' button will rescale and reposition the canvases to the default values. The default size and position of the canvases depend on the size of the master GUI D.9. The sizes as well as other default parameters controlling the behavior of the monitor can be changed in $ALICE_ROOT/TPC/AliTPCMonitorConfig.txt

'Proc one Sector'

By default, all sectors stored in the data file/stream for one event are read in. To increase speed when only investigating a particular sector for several events only the last displayed sector can be read by selecting this CheckBox.

'Next Ev. ID'

Indicating the next event ID to be processed. By default this value is increased by one after each iteration. It can be changed to step back and forth to different events. This functionality is not implemented for the online stream of data since this allows only the consecutive reading of events.

'Quit'

Terminates the application.

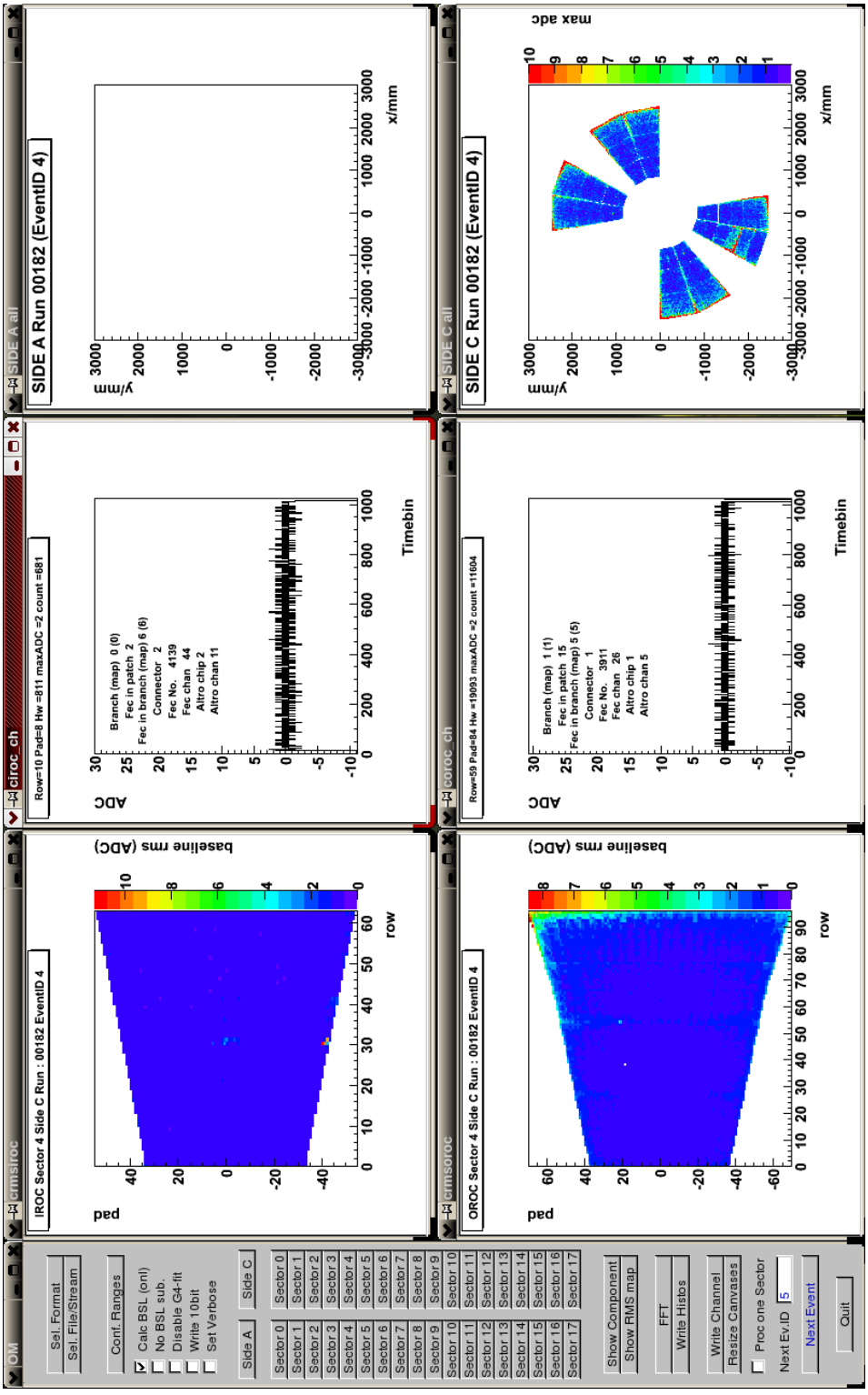

Figure D.15: Snapshot of the monitoring program.

Nomenclature

ADC	Analog-to-Digital Converter
ALICE	A Large Ion Collider Experiment
ALTRO	ALice Tpc ReadOut chip
BC	Beam Counter
CASTOR	Cern Advanced Storage System
CDH	Central Detector Header
CERES	Cherenkov Ring Electron Spectrometer
CERN	Centre Européenne pour la Recherche Nucléaire
DATE	Data Acquisition Test Environment
DDL	Detector Data Link
FEC	Front End Card
GDC	Global Data Concentrator
IROC	Inner ReadOut Chamber
LDC	Local Data Concentrator
MC	Multiplicity Counter
MD	Multiplicity Detector
OROC	Outer ReadOut Chamber
PASA	PreAmplifier Shaping Amplifier
PHENIX	Pioneering High Energy Nuclear Interaction eXperiment
QGP	Quark Gluon Plasma
RCU	Readout Control Unit
RHIC	Relativistic Heavy Ion Collider
RICH	Ring Imaging Cherenkoc Counter
RP	Reaction Plane

SDD	Silicon Drift Detectors
SE	Sub Event
SPS	Super Proton Synchrotron
STAR	Solenoidal Tracker At RHIC
TPC	Time Projection Chamber
UV	UltraViolet
VW	Veto Wall
ZYAM	Zero Yield At Minimum

Bibliography

[1] D. J. Gross and F. Wilczek. Ultraviolet Behavior of Non-Abelian Gauge Theories. *Phys. Rev. Lett.*, 30(26):1343–1346, Jun 1973.

[2] E. Laermann. Recent results from lattice QCD simulations. *Nucl. Phys.*, A610:1c–12c, 1996.

[3] F. Karsch. Lattice QCD at High Temperature and Density. *Lect. Notes Phys.*, 583:209–249, 2002.

[4] P. Braun-Munzinger. Chemical Equilibration and the Hadron-QGP Phase Transition. *Nucl. Phys.*, A(681):119–123, 2001.

[5] A. Andronic, P. Braun-Munzinger, and J. Stachel. Hadron production in central nucleus nucleus collisions at chemical freeze-out. *Nucl. Phys.*, A772:167–199, 2006, nucl-th/0511071.

[6] S. Margetis et al. Transverse energy production in Pb-208 + Pb collisions at 158 GeV per nucleon. *Phys. Rev. Lett.*, 75:3814–3817, 1995.

[7] U. A. Wiedemann and U. W. Heinz. Particle interferometry for relativistic heavy-ion collisions. *Phys. Rept.*, 319:145–230, 1999, nucl-th/9901094.

[8] R. Hanbury Brown and R. Q. Twiss. Correlation between Photons in two Coherent Beams of Light. *Nature*, 177:27, 1956.

[9] C. Alt et al. Bose-Einstein correlations of pion pairs in central Pb+Pb collisions at CERN SPS energies. *Phys. Rev.*, C77:064908, 2008, nucl-ex/0709.4507.

[10] H. Tilsner and H. Appelshäuser. Two-pion Bose-Einstein correlations at SPS energies. *Nucl. Phys.*, A715:607–610, 2003.

[11] F. Retiere and M. A. Lisa. Observable implications of geometrical and dynamical aspects of freeze-out in heavy ion collisions. *Phys. Rev.*, C70:044907, 2004.

[12] A. M. Poskanzer and S. A. Voloshin. Methods for analyzing anisotropic flow in relativistic nuclear collisions. *Phys. Rev. C*, 58:1671–1678, 1998.

[13] J. Barrette et al. Proton and pion production relative to the reaction plane in Au + Au collisions at AGS energies. *Phys. Rev.*, C(56), 1997.

[14] S. Voloshin and Y. Zhang. Flow study in relativistic nuclear collisions by Fourier expansion of Azimuthal particle distributions. *Z. Phys*, C(70), 1996.

[15] A. Adare et al. Scaling properties of azimuthal anisotropy in Au + Au and Cu + Cu collisions at $\sqrt{s_{NN}}$= 200 GeV. *Phys. Rev. Lett.*, 98:162301, 2007, nucl-ex/0608033.

[16] J. Adams et al. Particle dependence of azimuthal anisotropy and nuclear modification of particle production at moderate p(T) in Au + Au collisions at $\sqrt{s_{NN}}$ = 200 GeV. *Phys. Rev. Lett.*, 92:052302, 2004, nucl-ex/0306007.

[17] J. Adams et al. Multi-strange baryon elliptic flow in Au + Au collisions at $\sqrt{s_{NN}}$ = 200 GeV. *Phys. Rev. Lett.*, 95:122301, 2005, nucl-ex/0504022.

[18] T. Matsui and H. Satz. J/psi Suppression by Quark-Gluon Plasma Formation. *Phys. Lett.*, B178:416, 1986.

[19] R. Arnaldi et al. J/psi production in indium-indium collisions at 158 GeV/nucleon. *Phys. Rev. Lett.*, 99:132302, 2007.

[20] J. F. Owens. Large-momentum-transfer production of direct photons, jets, and particles. *Rev. Mod. Phys.*, 59:465, 1987.

[21] B. Pöttner B.A. Kniehl, G. Kramer. Fragmentation functions for pions, kaons, and protons at next-to-leading order. *Nucl. Phys.*, B(582):514–536, 2000.

[22] L. Bourhis, M. Fontannaz, J.P. Guillet, and M. Werlen. Next-to-leading order determination of fragmentation functions. *Eur. Phys. J.*, C(19):89–98, 2001.

[23] M. Arneodo. Nuclear effects on structure functions. *Phys. Rept.*, C(240):301–393, 1994.

[24] L. Apanasevich et al. *kt* effects in direct-photon production. *Phys. Rev. D*, 59(7):074007, Feb 1999.

[25] J. D. Bjorken. Energy loss of energetic partons in quark-gluon-plasma: Possible extinction of high-p_t jets in hadron-hadron collisions. *Fermilab-Pub-82/59-THY*, 1982. unpublished.

[26] M. Gyulassy and M. Plumer. Jet quenching as a probe of dense matter. *Nucl. Phys.*, A527:641–644, 1991.

[27] R. Baier, Y. L. Dokshitzer, A. H. Mueller, S. Peigne, and D. Schiff. Radiative energy loss and p(T)-broadening of high energy partons in nuclei. *Nucl. Phys.*, B484:265–282, 1997, hep-ph/9608322.

[28] J. Casalderrey-Solana and X. N. Wang. Energy dependence of jet transport parameter and parton saturation in quark-gluon plasma. *Phys. Rev.*, C77:024902, 2008, 0705.1352.

[29] R. Baier. Jet quenching. *Nucl.Phys.*, A(715):209–218, 2003.

[30] J. Adams et al. Evidence from d + Au measurements for final state suppression of high p(T) hadrons in Au+Au collisions at RHIC. *Phys. Rev. Lett.*, 91:072304, 2003.

[31] C. Adler et. al. Centrality Dependence of High-pT Hadron Suppression in $Au + Au$ Collisions at $\sqrt{s_{NN}} = 130$ GeV. *Phys. Rev. Lett.*, 89(20):202301, 2002.

[32] K. Adcox et al. Suppression of Hadrons with Large Transverse Momentum in Central Au+Au Collisions at $\sqrt{s_{NN}} = 130$ GeV. *Phys. Rev. Lett.*, 88:022301, 2002.

[33] R. Stock. Relativistic Nucleus-Nucleus Collisions and the QCD Matter Phase Diagram. 2008, nucl-ex/0807.1610.

[34] Y. Akiba. Probing the properties dense partonic matter at RHIC. *Nucl. Phys.*, A(774):403, 2006.

[35] T. Schuster A. Laszlo. High p_T Spectra of Identified Particles Produced in Pb+Pb Collisions at 158 GeV/nucleon Beam Energy. *Nucl. Phys.*, A(774):473, 2006.

[36] R. J. Fries, B. Muller, C. Nonaka, and S. A. Bass. Hadronization in heavy ion collisions: Recombination and fragmentation of partons. *Phys. Rev. Lett.*, 90:202303, 2003, nucl-th/0301087.

[37] D. d'Entrierra. Indication of suppressed high p_t hadron production in nucleus-nucleus collisions at cern-sps energy. *Phys. Lett.*, B(596):32, 2002.

[38] T. Affolder et al. Measurement of the inclusive jet cross section in p-$\overline{p}$ collisions at $\sqrt{s}$=1.8 TeV. *Phys. Rev.*, D(64):032001, 2001.

[39] C. Adler et al. Disappearance of back-to-back high p(T) hadron correlations in central Au + Au collisions at s(NN)**(1/2) = 200-GeV. *Phys. Rev. Lett.*, 90:082302, 2003.

[40] G. Agakichiev et al. Semi-hard scattering unraveled from collective dynamics by two-pion correlations in 158-A-GeV/c Pb + Au collisions. *Phys. Rev. Lett.*, 92:032301, 2004.

[41] S. S. Adler et. al. Modifications to di-jet hadron pair correlations in Au + Au collisions at $\sqrt{s_{NN}}$= 200-GeV. *Phys. Rev. Lett.*, 97:052301, 2006.

[42] A. Adare et al. Transverse momentum and centrality dependence of dihadron correlations in au+au collisions at $\sqrt{s_{NN}}$=200 gev: Jet-quenching and the response of partonic matter. *Phys. Rev.*, C(77):011901, 2008.

[43] H. Stoecker. Collective Flow signals the Quark Gluon Plasma. *Nucl. Phys.*, A750:121–147, 2005, nucl-th/0406018.

[44] I. Vitev. Large angle hadron correlations from medium-induced gluon radiation. *Phys. Lett.*, B630:78–84, 2005, hep-ph/0501255.

[45] V. Koch, A. Majumder, and Xin-Nian Wang. Cherenkov radiation from jets in heavy-ion collisions. *Phys. Rev. Lett.*, 96:172302, 2006, nucl-th/0507063.

[46] N. Armesto, C. A. Salgado, and U. A. Wiedemann. Measuring the collective flow with jets. *Phys. Rev. Lett.*, 93:242301, 2004, hep-ph/0405301.

[47] R. Hwa. High p(T) hadron correlation and no correlation. *Phys. Rev. Lett.*, A(783):57–64, 2007.

[48] N.N. Ajitanand et. al. Decomposition of harmonic and jet contributions to particle-pais correlations at ultra-relativistiv energies. *Phys. Rev.*, C(72):011902, 2005.

[49] J. G. Ulery and F. Wang. Analysis method for jet-like three-particle azimuthal correlations. *Nucl. Instrum. Meth.*, A595:502–511, 2008, nucl-ex/0609016.

[50] The CERES Collaboration. The CERES/NA45 Radial Drift Time Projection Chamber. *Nucl. Instrum. Meth.*, A593:203–231, 2008, nucl-ex/0802.1443.

[51] G. Agakichiev et al. e+ e- pair production in Pb Au collisions at 158 GeV per nucleon. *Eur. Phys. J.*, C41:475–513, 2005, nucl-ex/0506002.

[52] U. Faschingbauer et al. A doublet of 3-inch cylindrical silicon drift detectors in the CERES experiment. *Nucl. Instrum. Meth.*, A377:362–366, 1996.

[53] R. Baur et al. The CERES RICH detector system. *Nucl. Instrum. Meth.*, A343:87–98, 1994.

[54] H. Tilsner. Two-Particle Correlations at 40, 80, and 158 AGeV Pb-Au Collisions. *PhD thesis, University Heidelberg*, 2002.

[55] W. Ludolphs. Measurement of Open Charm in 158 AGeV/c Pb-Au collisions. *PdH thesis, University Heidelberg*, 2006.

[56] S. Yurevich. Electron-Pair Production in 158 AGeV/c Pb-Au Collisions from CERES. *PhD thesis, University Heidelberg*, 2006.

[57] M. Goosens et al. GEANT: Detector Description and Simulation Tool. *CERN Program Library*, long wirteup W5013, 1993. http://wwwasd.web.cern.ch/wwwasd/geant/.

[58] D. Antonczyk. Detailed Analysis of Two-Particle Correlations in Central Pb-Au Collisions at 158 GeV per Nucleon. *PhD thesis, University Heidelberg*, 2006.

[59] K. J. Eskola et al. Quark and Gluon Production in High energy Nucleus-Nucleus Collisions. *Nucl. Phys.*, B(323):38–52, 1989.

[60] D. Miskoviec. Nuclear overlap calculation. http://www-linux.gsi.de/~misko/overlap.

[61] The ALICE collaboration. ALICE : Technical proposal for a Large Ion collider Experiment at the CERN LHC. *CERN-LHCC-95-71 ; LHCC-P-3*, 1995.

[62] J. Milosevic. Investigation of Azimuthal Asymmetries in Charged and Strange Particle Distributions from CERES. *PhD thesis, University Heidelberg*, 2006.

[63] J. Barrette et al. Energy and charged particle flow in a 10.8-AGeV/c Au + Au collisions. *Phys.Rev.*, C(55), 1997.

[64] J.Y. Ollitrault. Reconstructing azimuthal distributions in nucleus-nucleus collisions. 1997, nucl-ex/9711003.

[65] J.Y. Ollitrault. Flow systematics from SIS to SPS energies. *Nucl. Phys.*, A(683):c195–c206, 1998.

[66] D. Miskowiec. List of runs taken in 2000. http://www-linux.gsi.de/~misko/ceres/analysis.html.

[67] T. Sjostrand, S. Mrenna, and P. Skands. PYTHIA 6.4 physics and manual. *JHEP*, 05:026, 2006, hep-ph/0603175.

[68] A. Adare et al. Dihadron azimuthal correlations in Au+Au collisions at $\sqrt{s_{NN}}$=200 GeV. *Phys. Rev.*, C78:014901, 2008, nucl-ex/0801.4545.

[69] J. Adams et al. Distributions of charged hadrons associated with high transverse momentum particles in p p and Au + Au collisions at $\sqrt{s_{NN}}$= 200 GeV. *Phys. Rev. Lett.*, 95:152301, 2005, nucl-ex/0501016.

[70] J. Adams et al. Delta(phi) Delta(eta) correlations in central Au + Au collisions at $\sqrt{s_{NN}} = 200$ GeV. *Phys. Rev.*, C75:034901, 2007, nucl-ex/0607003.

[71] B. Alver et al. High p_T Triggered Delta-eta,Delta-phi Correlations over a Broad Range in Delta-eta. *J. Phys.*, G35:104080, 2008, nucl-ex/0804.3038.

[72] J. Adams et al. Minijet deformation and charge-independent angular correlations on momentum subspace (eta, phi) in Au-Au collisions at $\sqrt{s_{NN}}$= 130-GeV. *Phys. Rev.*, C73:064907, 2006, nucl-ex/0411003.

[73] N. Armesto, C. A. Salgado, and U. A. Wiedemann. Measuring the collective flow with jets. *Phys. Rev. Lett.*, 93:242301, 2004, hep-ph/0405301.

[74] P. Romatschke. Momentum broadening in an anisotropic plasma. *Phys. Rev.*, C75:014901, 2007, hep-ph/0607327.

[75] C. B. Chiu, R. C. Hwa, and C. B. Yang. Azimuthal anisotropy: Ridges, recombination, and breaking of quark number scaling. *Phys. Rev.*, C78:044903, 2008.

[76] V. S. Pantuev. 'Jet-Ridge' effect in heavy ion collisions as a back splash from stopped parton. 2007, hep-ph/07101882.

[77] C.-Y. Wong. Ridge Structure associated with the Near-Side Jet in the (Delta phi)-(Delta eta) Correlation. *Phys. Rev.*, C76:054908, 2007, hep-ph/0707.2385.

[78] J. Jiangyong. How to Make Sense of the Jet Correlations Results at RHIC? 2008, nucl-ex/0810.0051.

[79] N. N. Ajitanand. Identification of exotic jet topologies via three particle correlations in PHENIX. *Acta Phys. Hung.*, A27:197–200, 2006, nucl-ex/0511029.

[80] N. N. Ajitanand. Extraction of jet topology using three particle correlations. *Nucl. Phys.*, A783:519–522, 2007, nucl-ex/0609038.

[81] J. G. Ulery. Conical Emission in Heavy Ion Collisions. *J. Phys.*, G35:104032, 2008, nucl-ex/0807.1613.

[82] J. G. Ulery. Two- and three-particle jet correlations from STAR. *Nucl. Phys.*, A774:581–584, 2006, nucl-ex/0510055.

[83] J. G. Ulery. Three-Particle Azimuthal Correlations. *Nucl. Phys.*, A783:511–514, 2007, nucl-ex/0609047.

[84] The ALICE collaboration. TPC: Technical Design Report. *CERN/LHCC 2000-001*, 2000.

[85] L. Musa et al. The ALICE TPC Front End Electronics. *Proc. of the IEEE Nuclear Science Symposium*, 2003.

[86] T. Anticic et al. The ALICE data-acquisition system. *Proc. of the IEEE Nuclear Science Symposium*, 1, 2005.

[87] The ALICE collaboration. ALICE Data Acquisition. http://ph-dep-aid.web. cern.ch/ph-dep-aid/.

[88] R. Bramm. Characterisation of the ALICE TPC readout chip. *Phd Thesis, University Frankfurt*, 2003.

[89] The ALICE collaboration. ALICE Off-line Project. http://aliweb.cern.ch/offline.

[90] PASA. http://ep-ed-alice-tpc.web.cern.ch/ep-ed-alice-tpc/PASA.htm.

[91] L. Musa et al. Alice tpc readout chip users manual, 2002. http://ep-ed-alice-tpc.web.cern.ch/ep-ed-alice-tpc/doc/ALTRO_CHIP/UserManual_draft_02.pdf.

[92] R. Esteve Bosch et al. Readout Control Unit of the Front End Electronics for the ALICE Time Projection Chamber. *Proceedings of the 8th Workshop on Electronics for LHC Experiments*, 2003.

[93] R. Mota et al. Digital Implementation of a Tail Cancellation Filter for the Time Projection Chamber of the ALICE Experiment. *Proceedings of the 6th Workshop on Electronics for LHC Experiments*, 2000. http://ep-ed-alice-tpc.web.cern.ch/ep-ed-alice-tpc/doc/papers/filter.pdf.

[94] The ALICE collaboration. Date monitoring system. http://ph-dep-aid.web. cern.ch/ ph-dep-aid/.

[95] H. Boutamine et al. USB to FEC Interface Card. Users Mamual. 2004. http://ep-ed-alice-tpc.web.cern.ch/ep-ed-alice-tpc/u2f.htm.

[96] GNU Scientific Library. http://www.gnu.org/software/gsl/.

Danksagung

Ganz besonderer Dank gilt meinem Doktorvater Herrn Prof. Dr. Harald Appelshäuser für die Aufnahme als Doktorand und die Betreuung der Arbeit. Neben der hervorragenden Infrastruktur, die er in seiner Arbeitsgruppe etabliert hat, stand er mir in persönlichen Gesprächen jederzeit für die Diskussion und Klärung inhaltlicher Fragen der Arbeit zur Verfügung. Er hat mir Möglichkeiten eröffnet, meine Ergebnisse im Rahmen mehrerer Konferenzen zu präsentieren und war stets bestrebt, dass meine Arbeit in der wissenschaftlichen Gemeinschaft wahrgenommen wird. Er hat mir insgesamt ein Umfeld geschaffen, wie ich es jedem Doktoranden nur wünschen kann.

Hervorheben möchte ich den einjährigen Aufenthalt am Europäischen Kernforschungszentrum CERN in Genf, den er mir ermöglicht hat. Für die Betreuung vor Ort bedanke ich mich bei Dr. Luciano Musa, der mir bei der Gestaltung meiner Arbeit stets freie Hand gelassen hat. Ein weiteres mal gilt mein Dank Dr. Dominik Flierl, der mir auch am CERN stets mit Rat und Tat zur Seite stand. Dr. Rainer Renfordt und Dr. Roland Bramm waren hier ebenfalls vor und während der Promotion eine große Hilfe. Prof. Appelshäuser hat mich in die Helmholtz Graduate School aufgenommen, welche hervorragende Möglichkeiten zur inhaltlichen und persönlichen Entwicklung während der Promotion geboten hat. Dem Koordinator der Schule Dr. Henner Büsching möchte ich hier besonderen Dank für die Organisation und Begleitung der Veranstaltungen der Schule aussprechen. Auch möchte ich mich bei allen Teilnehmern der Schule für die interessanten Gespräche, die Zusammenarbeit und die schönen Abende bedanken.

Dr. Mateusz Ploskon war mir zu Beginn meiner Promotion eine große Hilfe bei der Einarbeitung in das Experiment CERES und das Themengebiet der Arbeit und hat mir auch während der Promotion oft über inhaltliche und technische Hürden hinweggeholfen. Hierfür möchte ich mich ebenfalls bei Dr. Dariusz Antoncic, Dr. Oliver Busch, Dr. Dariusz Miskoviec, Dr. Ana Marin sowie bei der ganzen CERES Kollaboration bedanken.
Für die zunächst etwas angestrengte aber dann doch sehr angenehme Arbeitsatmosphäre bedanke ich mich bei meiner ehemaligen CERN-Sommerstudentin Simone Schuchmann. Ebenfalls bedanken möchte ich mich bei allen Mitarbeitern des IKF, insbesondere bei Herrn Werner Amend. Dr. Michael Mitrovski und Tim Schuster waren stets gute Begleiter wenn es um die Diskussion physikalischer sowie kulinarischer Belange ging. Tim Schuster als Mitglied der Helmholtz Schule möchte ich noch an ein mahnendes aber wohlmeinendes Wort erinnern: "Wer nicht kommt zur rechten Zeit, der muss nehmen was übrig bleibt". Er möge es mit dem gebotenen Humor zur Kenntnis nehmen.

Meiner Familie und insbesondere meiner Mutter Nora Kniege gilt ganz besonderer Dank für die Unterstützung während der Promotion. Edelgard und Edmund Mohr haben hier ebenfalls einen großen Beitrag geleistet. Bei meiner Freundin Sabrina Mohr, die während der Promotion viele Entbehrungen auf sich genommen hat und mich immer unterstützt hat, möchte ich mich besonders bedanken.